

**Naval Surface Warfare Center  
Carderock Division**  
West Bethesda, MD 20817-5700

---

---

**NSWCCD-TR-2000/010 June 2000**

Signatures Directorate  
Technical Report

**Experimental Investigation of Flow-Induced  
Cavity Resonance**

by  
Paul J. Zoccola, Jr.

NSWCCD-TR-2000/010



Approved for public release; distribution is unlimited

---

---

**20000803 108**

**DOC QUALITY INSTITUTE**

**Naval Surface Warfare Center  
Carderock Division**  
West Bethesda, MD 20817-5700

---

---

**NSWCCD-TR-2000/010** June 2000

Signatures Directorate  
Technical Report

**Experimental Investigation of Flow-Induced  
Cavity Resonance**

by

Paul J. Zoccola, Jr.

---

Approved for public release; distribution is unlimited

---

Enclosure (1)

# REPORT DOCUMENTATION PAGE

Form Approved  
OMB No. 0704-0188

Public reporting burden for this collection of information is estimated to average 1 hour per response, including the time for reviewing instructions, searching existing data sources, gathering and maintaining the data needed, and completing and reviewing the collection of information. Send comments regarding this burden estimate or any other aspect of this collection of information, including suggestions for reducing this burden, to Washington Headquarters Services, Directorate for Information Operations and Reports, 1215 Jefferson Davis Highway, Suite 1204, Arlington, VA 22202-4302, and to the Office of Management and Budget, Paperwork Reduction Project (0704-0188), Washington, DC 20503.

1. AGENCY USE ONLY (Leave blank)	2. REPORT DATE 21 June 2000	3. REPORT TYPE AND DATES COVERED Final	
4. TITLE AND SUBTITLE Experimental Investigation of Flow-Induced Cavity Resonance		5. FUNDING NUMBERS	
6. AUTHOR(S) Paul J. Zoccola, Jr.			
7. PERFORMING ORGANIZATION NAME(S) AND ADDRESS(ES) Naval Surface Warfare Center Carderock Division 9500 MacArthur Boulevard West Bethesda, MD 20817-5700		8. PERFORMING ORGANIZATION REPORT NUMBER NSWCCD-TR-2000/010	
9. SPONSORING/MONITORING AGENCY NAME(S) AND ADDRESS(ES) Naval Surface Warfare Center Carderock Division 9500 MacArthur Boulevard West Bethesda MD 20817-5700		10. SPONSORING/MONITORING AGENCY REPORT NUMBER	
11. SUPPLEMENTARY NOTES A dissertation submitted to the faculty of the School of Engineering of the Catholic University of America in partial fulfillment of the requirements for the degree Doctor of Philosophy			
12a. DISTRIBUTION/AVAILABILITY STATEMENT Approved for public release; distribution is unlimited.		12b. DISTRIBUTION CODE	
13. ABSTRACT (Maximum 200 words)  The resonant excitation of a cavity by an equilibrium turbulent grazing flow was investigated. The objectives of the research were first, to understand the dynamic processes related to the sheartones generated by vortex shedding from the upstream edge, and then to determine practical techniques for controlling the excitation and reducing the resonance. Detailed measurements of the cavity pressure and the velocity field in the opening were performed. Spectral data on cavity pressure fluctuations were analyzed over a range of speeds to determine the behavior of both the sheartones and cavity tones during non-resonant and resonant conditions. The cross-spectral properties between the velocity components and cavity pressure were also obtained. The data support the finding that the resonant and non-resonant conditions are distinguished by the behavior of the convection velocity and by the distribution of energy production in the flow field. Techniques for controlling cavity resonance were also investigated. The measurements and data analyses techniques discussed above were also performed for three practical devices. These include a technique, developed by the author, whereby fluid is diverted into the cavity from the boundary layer. The diversion technique is the most effective in reducing cavity resonance.			
14. SUBJECT TERMS Vortex Shedding      Helmholtz Resonance      Sheartone Fluid-Acoustic Interaction      Cavity Tone		15. NUMBER OF PAGES 182	
		16. PRICE CODE	
17. SECURITY CLASSIFICATION OF REPORT UNCLASSIFIED	18. SECURITY CLASSIFICATION OF THIS PAGE UNCLASSIFIED	19. SECURITY CLASSIFICATION OF ABSTRACT UNCLASSIFIED	20. LIMITATION OF ABSTRACT SAR

NSN 7540-01-280-5500

Standard Form 298 (Rev. 2-89)  
Prescribed by ANSI Std. Z39-18  
298-102

## ABSTRACT

The resonant excitation of a cavity by an equilibrium turbulent grazing flow was investigated. The mechanism causing the excitation arises from discrete vortices shed periodically from the upstream edge of the cavity opening. The shedding is controlled by feedback from the flow field near the downstream edge. The objectives of the research were first, to understand the dynamic processes related to the sheartones generated by the vortex shedding, and then to determine practical techniques for controlling the excitation and reducing the resonance.

Detailed measurements of the cavity pressure and the velocity field in the opening were performed in a quiet flow facility. Spectral data on cavity pressure fluctuations obtained for a variety of configurations were analyzed over a range of speeds to determine the behavior of both sheartones and cavity tones during non-resonant and resonant conditions. The mean and fluctuating velocity profiles as well as the cross-spectral properties between the velocity components and cavity pressure were also obtained within the cavity opening. The coherence identified the coupling while the phase was used to calculate the streamwise convection velocities across the opening. The data support the finding that the resonant and non-resonant conditions are distinguished by the behavior of the convection velocity and by the distribution of energy production in the flow field.

Techniques for controlling cavity resonance were also investigated. The measurements and data analyses techniques discussed above were also performed for three practical devices. These include a fence upstream of the leading edge, air injection near the leading edge, and a technique, developed by the author, whereby fluid is diverted into the cavity from the boundary layer. The fence and the diversion technique lower the Strouhal number of the sheartones so that resonance occurs at a higher speed. All techniques lower the resonance level. The diversion technique is the most effective in reducing cavity resonance.

## Table of Contents

List of Figures .....	viii
List of Tables .....	xvi
Nomenclature .....	xvii
Acknowledgements .....	xix
1. Introduction .....	1
1.1 Motivation for the Research .....	1
1.2 Physical Description of Flow-induced Cavity Resonance .....	2
1.2.1 Features of the Dynamic Processes .....	2
1.2.2 Discussion of Sheartones and Cavity Tones .....	3
1.3 Techniques For Reducing Flow-induced Cavity Resonance .....	7
1.4 Objectives of the Research and Outline of the Dissertation .....	8
2. Experimental Arrangement and Test Condition .....	12
2.1 Experimental Setup .....	12
2.2 Instrumentation and Data Collection .....	13
2.3 Onset Boundary Layer Measurements .....	15
3. Description of Cavity Response .....	21
3.1 Cavity Response to Acoustic Excitation .....	21
3.2 Cavity Response to Grazing Flow .....	23
3.2.1 Low Speed Cavity Pressure Spectra .....	24
3.2.2 Qualitative Description of Sheartone Behavior .....	26
3.2.3 Discussion of Level as a function of speed .....	29
3.2.4 Discussion of Frequency as a function of speed .....	31
3.3 Speed Dependent Behavior of Shear Tones In The Absence of a Cavity .....	32
3.4 Summary .....	36
4. Velocity and Cavity Pressure Correlations .....	51
4.1 Velocity Field Profiles .....	52
4.2 Velocity and Pressure Spectra .....	54

4.2.1 Pressure Spectra .....	54
4.2.2 Velocity Spectra .....	55
4.2.3 Velocity Peak Profiles .....	56
4.3 Velocity-Pressure Correlation .....	57
4.3.1 Coherence .....	57
4.3.2 Description Of Idealized Spatial Distribution Of Phase .....	59
4.3.3 Spatial Plots of Coherence and Phase .....	60
4.3.4 Convection Velocity .....	62
4.4 Summary .....	63
<b>5. Analytical Model of Flow-Acoustic Interactions .....</b>	<b>82</b>
5.1 Model of the Resonator Flow .....	82
5.1.1 Description of Processes Governing Flow-Induced Cavity Resonance .....	82
5.1.2 Features of the Flow .....	83
5.1.3 Energy Analysis .....	85
5.2 Comparisons With Experimental Data .....	86
5.2.1 Calculation of Energy Production Term .....	87
5.2.2 Results of Energy Production Term Calculations .....	87
5.2.3 Comparison of Phase Relations .....	90
5.3 Summary and Conclusions .....	91
<b>6. Techniques for Controlling Cavity Resonance .....</b>	<b>97</b>
6.1 Background .....	97
6.1.1 Passive Techniques .....	97
6.1.2 Active Techniques .....	98
6.1.3 Objectives of Control Technique Investigation .....	100
6.2 Cavity with Fence .....	101
6.2.1 Cavity Pressure Results .....	101
6.2.2 Results of Flow Field Measurements .....	103
6.2.3 Discussion .....	105
6.3 Cavity with Air Injection .....	106
6.3.1 Cavity Pressure Results .....	106
6.3.2 Results of Flow Field Measurements .....	108

6.3.3 Discussion .....	110
6.4 Cavity with Boundary Layer Diversion.....	111
6.4.1 Cavity Pressure Results.....	112
6.4.2 Results of Flow Field Measurements .....	113
6.5 Comparison of Techniques Investigated .....	115
6.5.1 Comparison of Cavity Pressure Results .....	115
6.5.2 Comparison of Phase.....	117
7. Summary and Conclusions.....	147
7.1 Summary.....	147
7.2 Conclusions .....	151
7.3 Suggestions for Future Research .....	153
Appendix 1 - Frequency And Level Of Speed Dependent Tones.....	155
Bibliography.....	157

## List of Figures

Figure 1.1: Dynamic processes of flow-induced cavity resonance.....	11
Figure 2.1: Schematic of Low Noise Flow Facility (LNFF).....	18
Figure 2.2: Section view of installed cavity.....	18
Figure 2.3: Drawing of custom x-probe 1243BE-20 .....	19
Figure 2.4: Mean streamwise velocity profile measured with right angle probe normalized by wall variables .....	19
Figure 2.5: Streamwise turbulence intensity profiles.....	20
Figure 2.6: Wall-normal turbulence intensity profiles.....	20
Figure 3.1: Schematic of arrangement for measuring cavity response to acoustic excitation.....	37
Figure 3.2: Frequency response of cavity with $L=1"$ and $d=5.5"$ .....	37
Figure 3.3: Measured Helmholtz resonance frequency normalized by calculated Helmholtz resonance frequency.....	38
Figure 3.4: Cavity pressure spectrum at 6.8 m/s with $L=1"$ , $d=5.5"$ .....	38
Figure 3.5: Cavity pressure spectrum at 6.9 m/s with $L=2"$ , $d=2.75"$ .....	39
Figure 3.6: Cavity pressure spectrum at 6.8 m/s with $L=0.5"$ , $d=2.75"$ .....	39
Figure 3.7: Comparison of Helmholtz frequency due to acoustic excitation and turbulent rumble as a function of cavity geometry.....	40
Figure 3.8: Cavity pressure spectra at 12 speeds for $L=1"$ , $d=5.5"$ .....	40
Figure 3.9: Cavity pressure spectra at 12 speeds for $L=2"$ , $d=2.75"$ .....	41
Figure 3.10: Cavity pressure spectra at 12 speeds for $L=0.5"$ , $d=2.75"$ .....	41
Figure 3.11: Comparison of normalized level of first speed dependent tone for deep and shallow cavities as a function of speed for $L=1"$ .....	42

Figure 3.12: Comparison of normalized level of first speed dependent tone for deep and shallow cavities as a function of speed for L=1.5"	42
Figure 3.13: Comparison of normalized level of first speed dependent tone for deep and shallow cavities as a function of speed for L=2"	43
Figure 3.14: Comparison of normalized level of second speed dependent tone for deep and shallow cavities as a function of speed for L=1"	43
Figure 3.15: Comparison of normalized level of second speed dependent tone for deep and shallow cavities as a function of speed for L=1.5"	44
Figure 3.16: Comparison of normalized level of second speed dependent tone for deep and shallow cavities as a function of speed for L=2"	44
Figure 3.17: Comparison of frequency of first speed dependent tone for deep and shallow cavities as a function of speed for L=1"	45
Figure 3.18: Comparison of frequency of first speed dependent tone for deep and shallow cavities as a function of speed for L=1.5"	45
Figure 3.19: Comparison of frequency of first speed dependent tone for deep and shallow cavities as a function of speed for L=2"	46
Figure 3.20: Comparison of frequency of second speed dependent tone for deep and shallow cavities as a function of speed for L=1"	46
Figure 3.21: Comparison of frequency of second speed dependent tone for deep and shallow cavities as a function of speed for L=1.5"	47
Figure 3.22: Comparison of frequency of second speed dependent tone for deep and shallow cavities as a function of speed for L=2"	47
Figure 3.23: Comparison of Strouhal number of first speed dependent tone at all values of L for d=2.75"	48
Figure 3.24: Strouhal number of speed dependent tones just prior to resonance as a function of $\delta/L$	48
Figure 3.25: Cavity pressure spectra at 11 speeds for L=1", no cavity	49
Figure 3.26: Comparison of Strouhal number of first speed dependent tone for L=1" and L=1.5" with no cavity as a function of speed	49
Figure 3.27: Comparison of Strouhal number of first speed dependent tones with and without cavity as a function of speed	50

Figure 3.28: Comparison of $fL/U_0(\theta/L)^{1/7}$ of first speed dependent tone for various values of $L$ with and without cavity as a function of speed.....	50
Figure 4.1: Comparison of streamwise mean velocity profiles for 30, 13, and 6.9 m/s at 3 streamwise locations .....	65
Figure 4.2: Comparison of streamwise mean velocity profiles at $x=0.85"$ and $x=-0.1"$ ....	65
Figure 4.3: Comparison of streamwise mean velocity profiles at $x=0.935$ to hyperbolic tangent profile .....	66
Figure 4.4: Comparison of streamwise turbulence intensity profiles for 30, 13, and 6.9 m/s at 3 streamwise locations .....	66
Figure 4.5: Comparison of wall-normal turbulence intensity profiles for 30, 13, and 6.9 m/s at 3 streamwise locations .....	67
Figure 4.6: Comparison of Reynolds stress profiles for 30, 13, and 6.9 m/s at 3 streamwise locations .....	67
Figure 4.7: Cavity pressure spectrum for 30 m/s, 331 Hz first sheartone resonant condition, with $L=1"$ , $d=5.5"$ .....	68
Figure 4.8: Cavity pressure spectrum for 13 m/s, 345 Hz second sheartone resonant condition, with $L=1"$ , $d=5.5"$ .....	68
Figure 4.9: Cavity pressure spectrum for 6.9 m/s non-resonant condition with $L=1"$ , $d=5.5"$ .....	69
Figure 4.10: Velocity spectra at 2 locations for 30 m/s, 331 Hz first sheartone resonant condition .....	70
Figure 4.11: Velocity spectra at 2 locations for 13 m/s, 345 Hz second sheartone resonant condition .....	71
Figure 4.12: Velocity spectra at 2 locations for 6.9 m/s non-resonant condition .....	72
Figure 4.14: Profiles of velocity spectral levels of 662 Hz 2 <sup>nd</sup> harmonic of first sheartone resonance .....	73
Figure 4.15: Profiles of velocity spectral levels of 993 Hz 3 <sup>rd</sup> harmonic of first sheartone resonance .....	73
Figure 4.16: Coherence between $v-p$ at 2 locations for 3 speeds.....	74
Figure 4.17:Coherence between $u-p$ at 2 locations for 3 speeds.....	75

Figure 4.18: Description of behavior of velocity components of discrete vortex as it passes an x-probe .....	76
Figure 4.19: Idealized description of phase between velocity components and cavity pressure as a discrete vortex convects along the cavity opening at a constant speed .....	76
Figure 4.20: Spatial plot of phase and coherence between u-p of first sheartone resonance at 30 m/s.....	77
Figure 4.21: Spatial plot of phase and coherence between v-p of first sheartone resonance at 30 m/s.....	77
Figure 4.22: Spatial plot of phase and coherence between u-p of non-resonant first sheartone at 13 m/s .....	78
Figure 4.23: Spatial plot of phase and coherence between v-p of non-resonant first sheartone at 13 m/s .....	78
Figure 4.24: Spatial plot of phase and coherence between u-p of second sheartone resonance at 13 m/s.....	79
Figure 4.25: Spatial plot of phase and coherence between v-p of second sheartone resonance at 13 m/s.....	79
Figure 4.26: Phase between v-p along vortex path for sheartones at 30, 13, and 6.9 m/s .	80
Figure 4.27: Normalized convection velocity of vortex for sheartones at 30, 13, and 6.9 m/s.....	80
Figure 4.28: Normalized convection velocity of vortex for first sheartones at 30, 13, and 6.9 m/s.....	81
Figure 4.29: Normalized convection velocity of vortex for second sheartones at 13 and 6.9 m/s.....	81
Figure 5.1: Dynamic processes of flow-induced cavity resonance.....	93
Figure 5.2: Spatial plots of rms vorticity and mean energy production term of 331 Hz tone at 30 m/s.....	93
Figure 5.3: Spatial plots of rms vorticity and mean energy production term of 345 Hz tone at 13 m/s .....	94
Figure 5.4: Spatial plots of rms vorticity and mean energy production term of 191 Hz tone at 13 m/s.....	94

Figure 5.5: Spatial plots of rms vorticity and mean energy production term of 111 Hz tone at 6.9 m/s.....	95
Figure 5.6: Spatial plots of rms vorticity and mean energy production term of 207 Hz tone at 6.9 m/s.....	95
Figure 5.7: Filtered time records of u and v at 5 streamwise locations along 1 cycle of cavity pressure oscillations of 331 Hz tone at 30 m/s compared to predicted records.....	96
Figure 5.8: Filtered time records of u and v at 5 streamwise locations along 1 cycle of cavity pressure oscillations of 191 Hz tone at 13 m/s compared to predicted records.....	96
Figure 6.1: Schematic of cavity with fence installed.....	119
Figure 6.2: Cavity pressure spectra at 30 m/s for configuration 2d with $\frac{1}{4}$ " fence, $\frac{1}{8}$ " fence, and no fence .....	119
Figure 6.3: Comparison of normalized level of first sheartone for cavity configuration 2dd with $\frac{1}{4}$ " fence, $\frac{1}{8}$ " fence, and no fence .....	120
Figure 6.4: Comparison of normalized level of first sheartone for cavity configuration 2d with $\frac{1}{4}$ " fence and no fence.....	120
Figure 6.5: Comparison of Strouhal number of first sheartone for cavity configuration 2d with $\frac{1}{4}$ " fence, $\frac{1}{8}$ " fence and no fence .....	121
Figure 6.6: Comparison of normalized level of Helmholtz resonance cavity tone for cavity configuration 2d with $\frac{1}{4}$ " fence, $\frac{1}{8}$ " fence, and no fence .....	121
Figure 6.7: Comparison of normalized level of Helmholtz resonance cavity tone for cavity configuration 4d with $\frac{1}{4}$ " fence, $\frac{1}{8}$ " fence, and no fence.....	122
Figure 6.8: Comparison of streamwise mean velocity profiles at 30 m/s for configuration 2d with and without $\frac{1}{4}$ " fence .....	122
Figure 6.9: Comparison of streamwise turbulence intensity profiles at 30 m/s for configuration 2d with and without $\frac{1}{4}$ " fence.....	123
Figure 6.10: Velocity spectra at 30 m/s at 2 locations for configuration 2d with $\frac{1}{4}$ " fence .....	124
Figure 6.11: Coherence between u-p at 30 m/s for 3 locations for configuration 2d with $\frac{1}{4}$ " fence .....	125

Figure 6.12: Coherence between v-p at 30 m/s for 3 locations for configuration 2d with 1/4" fence .....	126
Figure 6.13: Spatial plot of phase and coherence between v-p of first sheartone resonance at 30 m/s for configuration 2d with 1/4" fence .....	127
Figure 6.14: Spatial plot of phase and coherence between u-p of first sheartone resonance at 30 m/s for configuration 2d with 1/4" fence .....	127
Figure 6.15: Spatial plot of rms vorticity and mean energy production term of first sheartone resonance at 30 m/s for configuration 2d with 1/4" fence .....	128
Figure 6.16: Configuration and drawing of air injection manifold.....	128
Figure 6.17: Cavity pressure spectra at 30 m/s for configuration 2d, with 0, 4.6, and 7 SCFM fluid injection .....	129
Figure 6.18: Cavity pressure spectra for configuration 2d, with 7 SCFM fluid injection at 0, 12, and 27 m/s.....	129
Figure 6.19: Normalized level of Helmholtz resonance at 30 m/s for cavity configuration 2d as a function of fluid injection rate .....	130
Figure 6.20: Normalized level of Helmholtz resonance for cavity configuration 2d at 5 values of fluid injection rate .....	130
Figure 6.21: Flow-rate normalized level of Helmholtz resonance for cavity configuration 2d at 5 values of fluid injection rate .....	131
Figure 6.22: Frequency of Helmholtz resonance for cavity configuration 2d at 5 values of fluid injection rate .....	131
Figure 6.23: Streamwise mean velocity profile at 29.5 m/s for configuration 2d with 4.6 SCFM air injection at 3 streamwise locations .....	132
Figure 6.24: Comparison of streamwise mean velocity profiles at 30 m/s for configuration 2d with and without 4.6 SCFM air injection .....	132
Figure 6.25: Comparison of streamwise turbulence intensity profiles at 30 m/s for configuration 2d with and without 4.6 SCFM air injection .....	133
Figure 6.26: Velocity spectra at 29.5 m/s at 2 locations for configuration 2d with 4.6 SCFM air injection.....	134
Figure 6.27: Coherence between u-p at 29.5 m/s for 2 locations for configuration 2d with 4.6 SCFM air injection.....	135

Figure 6.28: Coherence between v-p at 29.5 m/s for 2 locations for configuration 2d with 4.6 SCFM air injection.....	135
Figure 6.29: Spatial plots of phase and coherence between v-p of first sheartone resonance at 29.5 m/s for configuration 2d with 4.6 SCFM air injection.....	136
Figure 6.30: Spatial plots of phase and coherence between u-p of first sheartone resonance at 29.5 m/s for configuration 2d with 4.6 SCFM air injection.....	136
Figure 6.31: Spatial plots of rms vorticity and mean energy production term of first sheartone resonance at 29.5 m/s for configuration 2d with 4.6 SCFM fluid injection .....	137
Figure 6.32: Schematic of boundary layer diversion implementation.....	137
Figure 6.33: Cavity pressure spectra at 29 m/s for configuration 2d, with and without boundary layer diversion .....	138
Figure 6.34: Cavity pressure spectra at 12 speeds for configuration 2d, with boundary layer diversion.....	138
Figure 6.35: Comparison of normalized level of first sheartone for cavity configuration 2d with and without boundary layer diversion .....	139
Figure 6.36: Comparison of Strouhal numbers of first sheartone for deep cavity ( $d=5.5"$ ) at various values of $L$ with and without boundary layer diversion.....	139
Figure 6.37: Comparison of normalized level of first sheartone for cavity configurations 2d and 2dd with and without boundary layer diversion.....	140
Figure 6.38: Comparison of normalized level of Helmholtz resonance tone for cavity configuration 2dd with and without 3.6 SCFM air injection .....	140
Figure 6.39: Comparison of streamwise mean velocity profiles at 30 m/s for configuration 2d with boundary layer diversion and with 4.6 SCFM air injection.....	141
Figure 6.40: Comparison of streamwise turbulence intensity profiles at 30 m/s for configuration 2d with boundary layer diversion and with 4.6 SCFM air injection .....	141
Figure 6.41: Velocity spectra at 29.9 m/s at 2 locations for configuration 2d with boundary layer diversion .....	142
Figure 6.42: Coherence between u-p at 29.9 m/s at 2 locations for configuration 2d with boundary layer diversion .....	143

Figure 6.43: Coherence between v-p at 29.9 m/s at 2 locations for configuration 2d with boundary layer diversion .....	143
Figure 6.44: Spatial plots of phase and coherence between v-p of first sheartone at 29.9 m/s for configuration 2d with boundary layer diversion .....	144
Figure 6.45: Spatial plots of phase and coherence between u-p of first sheartone at 29.9 m/s for configuration 2d with boundary layer diversion .....	144
Figure 6.46: Spatial plots of rms vorticity and mean energy production term of first sheartone at 29.9 m/s for configuration 2d with boundary layer diversion ..	145
Figure 6.47: Phase between v-p along vortex path of first sheartones for configuration 2d with boundary layer diversion, 4.6 SCFM air injection, $\frac{1}{4}$ " fence, and no control .....	145
Figure 6.48: Convection velocity of vortex of first sheartones for configuration 2d with boundary layer diversion, 4.6 SCFM air injection, $\frac{1}{4}$ " fence, and no control .....	146

## **List of Tables**

Table 2.1 Cavity Configurations Tested .....	13
Table 2.2 Boundary Layer Parameters.....	16
Table 3.1 Cavity Helmholtz Resonance Frequencies and Loss Factors .....	22
Table 3.2 Boundary Layer Properties .....	34
Table 4.1 X-Probe Measurement Locations .....	52

## Nomenclature

a	circle radius; average absorption coefficient
A	area of cavity opening
c	speed of sound
$C_f$	coefficient of skin friction
d	cavity depth
E	internal energy
f	frequency
$G_{12}$	forward transfer function
$G_{21}$	backward transfer function
h	fence height
H	shape factor, $\delta^*/\theta$ ; enthalpy
k	wavenumber, $\omega/c$
l	thickness of cavity wall at the cavity opening
$l'$	effective thickness of air slug in cavity opening
L	streamwise length of cavity opening
$L_p$	sound pressure level
$L_w$	sound power level
m	sheartone order index
M	Mach number
p	fluctuating pressure
q	dynamic head, $1/2\rho U_0^2$
$q_i$	dynamic head based on effective fluid injection velocity
$Q_b$	$U_0 \times A$
$Q_i$	volume flow rate of injected fluid
R	room constant
$r_c$	vortex core radius
Re	Reynolds number
$R_r$	radiation resistance of cavity opening
S	area of room
St	Strouhal number, $fL/U_0$
T	period, $1/f$
u	streamwise velocity
$\mathbf{u}$	velocity vector
$u^+$	streamwise velocity scaled on inner variables
$U_0$	free stream velocity
$U_c$	convection velocity
$u_\tau$	shear velocity
v	wall normal velocity
$\mathbf{v}$	solenoidal component of velocity vector

$V$  volume of cavity  
 $W_a$  acoustic energy loss from cavity opening  
 $W_v$  net energy production in cavity opening  
 $W_{vv}$  vortex energy loss from cavity opening  
 $x$  streamwise coordinate  
 $y$  wall normal coordinate  
 $y+$  wall normal coordinate scaled on inner variables

$\delta$  boundary layer thickness  
 $\delta^*$  displacement thickness  
 $\theta$  momentum thickness  
 $\rho$  density  
 $\sigma$  standard deviation  
 $\omega_n$  natural frequency, rad/s  
 $\Omega$  vorticity vector  
 $\Omega_3$  vorticity in z-direction  
 $\xi$  loss factor

$\overline{(\ )}$  mean value or time average  
 $( \ )_{rms}$  root mean square value  
 $( \ )'$  fluctuating component

## Acknowledgements

This research effort would not have been possible without the support of a great many people. Dr. Mario Casarella worked into his retirement as my major advisor, teaching me what it means to conduct original research in an academic environment. I am grateful beyond words for his encouragement and friendship. The efforts of Dr. Theodore Farabee and Dr. J. Steven Brown, who served as readers, are greatly appreciated as well. Dr. Farabee is also a colleague who over the years has taught me much about conducting experiments, and whose career has served as a model for my own; I am most grateful. The friendly help of Mrs. Ruth Hicks and Mr. Don Smolley are also appreciated.

The support of the Carderock Division of the Naval Surface Warfare Center was essential to this work. Financial support was provided by the Extended Term Training Programs of the Division and of the Signatures Directorate, as well as by the Research Ventures Program and the Independent Research Program. The encouragement and flexibility of my Department Head, Dr. Paul Shang, made it possible for me to take the time needed to complete this effort. Other colleagues too numerous to mention were helpful in ways big and small. My thanks to all.

Most important of all was the support I received from my family. I depended on, and am deeply grateful for, the love and sacrifice of my lovely wife, Mary, and my wonderful daughters, Alison and Katherine, throughout. I am also thankful for the love and support throughout my life of my parents, especially my father, Paul J. Zoccola, who passed before this work was completed. He nurtured my curiosity and love of science from a tender age. To him I dedicate this work.

# 1. Introduction

## 1.1 Motivation for the Research

When fluid flows over a surface with an aperture that is the opening to a fluid-filled cavity, it may, under certain conditions result in pressure fluctuations within the cavity, which may be quite high in amplitude. This condition will usually radiate sound from the cavity opening. Typically, the frequency spectrum of the radiated sound shows one or two narrow tones with frequencies associated with the inherent resonance frequency of the cavity. This phenomenon may be referred to as *flow-induced cavity resonance*. In some applications the pressure fluctuations are desired, for example in the case of the flute or other musical instruments. There are many applications, however, where these fluctuations are undesirable and may cause harm. These include flow tones produced by flow over openings in naval vessels, cavity pressure fluctuations in the interior of automobiles with open sunroofs or windows, and noise in aircraft with open landing gear wells or bomb bays.

Many passive techniques have been implemented to reduce the unwanted pressure fluctuations. These have included leading edge spoilers, trailing edge ramps, and slatted louvers. Techniques which may be described as semi-active have also been tried. For example, fluid injection, continuous or with a fixed period and amplitude of oscillation, either upstream of the opening or at the base of the cavity. More recently, active (feedback) control of flow-induced cavity resonance has been studied. The sensor is typically a microphone in the cavity, while a variety of actuators have been tried. The reduction techniques have met with varying degrees of success. Most have been effective in reducing, if not eliminating, the tonal levels. Some have other undesirable effects such as increased drag or obstructed flow through the cavity opening.

The present investigation has the primary objective of contributing to the understanding of the fluid dynamic and acoustic processes that cause flow-induced cavity resonance. It is hoped that this research will establish the foundation for developing both active and passive techniques for reducing or eliminating flow-induced cavity resonance.

## 1.2 Physical Description of Flow-induced Cavity Resonance

### 1.2.1 Features of the Dynamic Processes

A physical description of the dynamics of a flow excited cavity is given based on the work by Nelson, Halliwell, and Doak(1981,1983). A turbulent boundary layer flow grazing over a cavity produces an unstable free shear layer over the open region of the cavity. This arrangement is shown in figure 1.1(a). Under certain conditions, the instability of the shear layer causes it to roll up into vortices, which are shed with period  $T$  and frequency  $f=1/T$ . In the absence of a resonant cavity, this frequency is proportional to the free stream velocity,  $U_0$  of the flow and inversely proportional to the length of the opening,  $L$ . The Strouhal number, or non-dimensional frequency,  $fL/U_0$ , is then a constant. When the frequency of the vortex shedding approaches the so-called resonance frequency of the cavity, feedback between the flow in the opening and the resonance of the cavity result in the cavity being strongly excited by the grazing flow. High amplitude pressure fluctuations will then exist in the cavity.

The interaction between the fluid dynamics in the cavity opening and the cavity resonance is of primary interest. Figure 1.1(b) is an illustration based on flow visualization and LDV velocity measurements from Nelson, et al (1981). Based on these measurements, the following dynamical model has been proposed for this complex interaction. The vortex develops during the first half period in the upstream half of the opening. It then convects along the downstream half of the opening during the second half period at a convection velocity of about one half of  $U_0$ , the grazing flow speed. The vortex exhibits solid body rotation in a core of radius  $r_c$ . The cavity pressure is at a minimum at the beginning of this process, and the air is being displaced into the cavity during the first half period. The cavity pressure reaches a maximum when the vortex is at the midpoint of the cavity opening and air is being displaced outward during the second half of the process. When the vortex reaches the downstream edge it is ejected from the cavity and accelerates to approximately  $U_0$ . After ejection the vortex appears “stretched” in shape.

This dynamic process results in the generation of acoustic energy flowing into the cavity from near the downstream edge. Some of this energy is absorbed by the interaction in the upstream half of the opening. The remaining energy excites the cavity to radiate. The acoustic velocity at the opening due to this radiation enhances the vortex shedding at the upstream edge. This process continues until the net energy produced by the vortex interaction is balanced by the energy extracted by the acoustic radiation and the vortices ejected from the opening.

The description given above relates particularly to the arrangement tested in the present research. Flow-induced cavity resonance can occur under other conditions as well. For example, the grazing boundary layer flow need not be turbulent. Elder(1978) and DeMetz and Farabee(1977) have described resonances under laminar flow. Elder(1978) gives a description of flow-induced cavity resonance based on the oscillations of instability wave in the shear layer rather than discrete vortices. Bruggemann(1997) proposed a criteria that determines the conditions under which discrete vortices will form. Both Bruggemann and Elder also describe a separate phenomenon where the broadband turbulent boundary layer (TBL) fluctuations excite the cavity resonance.

Also, while the description above relates to Helmholtz resonator-like cavities, where the opening is an aperture in a much larger upper surface of the cavity, a broad class of applications, and a correspondingly significant amount of research, is related to so-called rectangular cavities, where the opening is the upper boundary of the cavity. Work in the aircraft industry and in piping systems relate primarily to this configuration. Differences between the physics of flow-induced cavity resonance in rectangular cavities and in Helmholtz resonator-like cavities have not been clearly established. Significant work in rectangular cavities has been done by Tam and Block(1978), Heller and Bliss(1975), and Rossiter(1964). The review paper by Komerath, Ahuja, and Chambers(1987), while covering both types of cavities, relates largely to rectangular cavities.

### **1.2.2 Discussion of Sheartones and Cavity Tones**

To understand the physical processes of flow-induced cavity resonance, it is useful to first study the behavior of a free shear layer with and without the presence of any

downstream edge. Michalke (1965) describes the process by which small disturbances in a free shear layer with no downstream edge result in periodic oscillations in the wall normal direction. He derives an equation that may be solved to give the eigenvalues and eigenvectors of possible modes of oscillation. Rockwell and Knisely (1979) performed an experiment in which velocity fluctuation measurements were made in a shear layer with and without a downstream edge present. The results show that in the absence of a downstream edge, there is significant variability in both the frequency and amplitude of autocorrelation traces taken at an approximately 800 cycle separation. When the same measurements are made with a downstream edge in place, there is no detectable variation in frequency, and amplitudes are the same to within approximately 30%. This implies that the downstream edge causes the flow to become strongly organized with discrete oscillations. The frequency of these so-called *sheartones* depends on the distance to the downstream edge.

Two important processes must be studied in order to understand the formation of sheartones. One is near the upstream edge of the opening, where the vortex shedding process (or instability wave) is influenced by disturbances from other locations. The other is the interaction downstream between the vortex (or transverse shear layer fluctuations) and the downstream edge of the opening. This interaction may create the disturbance that directly or indirectly affects the fluctuations at the upstream edge, causing the formation of a sheartone. Taken together, these processes form a feedback loop between the interaction at the downstream edge and the vortex formation process at the upstream edge.

It is important to recognize that sheartones exist over a wide range of flow speeds and are not always associated with cavity resonance. A tone may be generated without the cavity being excited to resonate. It is only when the frequency of a sheartone is near a resonant frequency that the cavity may be excited. The frequencies then coincide, and the resulting tone may then be called a *cavity tone*. The distinction between these types of tones is made clear by Elder (1978).

In this section, the downstream edge interaction is discussed, followed by the vortex formation process near the upstream edge. Finally, the use of these models in predicting the frequency of both cavity tones and sheartones is discussed.

## Downstream Edge Interaction

Elder (1978) analyzed the interaction at the downstream edge by presenting a functional description of the shear layer oscillations and then showing how those oscillations resulted in a volume source near the downstream edge. Mast and Pierce (1995) base their model of the downstream edge interaction on the work of Tang and Rockwell (1983), who describe the dipole radiation pattern that results when a vortex impinges on and is swept past a corner. Kook & Mongeau (1997) show how fluctuating excitation pressures result from the uneven pressure distribution associated with the convection of discrete vortices. In the paper by Bruggemann (1997), et al., the interaction described is not necessarily confined to the downstream edge region. Rather, they use the equation by Howe (1980) to calculate the power due to a convected vortex in the presence of an acoustic field. This equation is an integral over the area of non-vanishing vorticity. This power must be positive and greater than energy losses in order for the cavity to resonate. Nelson, et al.(1983) start with the energy balance equation from Doak (1974) and derive an equation similar to Howe's for the power generated by the vortex interacting with the flow field. They show that for a fully resonant cavity, energy is produced near the downstream edge and absorbed nearer to the upstream edge. The net energy production is positive and agrees reasonably well with the measured far field radiation. This model will be discussed in detail in Chapter 5.

## Vortex Formation Process

The timing and the strength of the vortex shed from the upstream edge of the opening is controlled by an external disturbance. The general case of vortex shedding in a free shear layer due to an external disturbance is discussed in the review papers by Wygnanski and Petersen (1987), and Ho and Huerre (1984). For a sheartone, the disturbance results from the interaction of the previously shed vortex near the downstream edge. Howe (1979) describes the influence of the downstream interaction on the upstream edge by showing how the energizing of the unsteady flow associated with the vorticity is necessary to satisfy the Kutta condition. This condition requires that the velocity leaving the surface at the upstream edge be tangential to the surface.

A more physically based description of the processes near the upstream edge is given by Nelson, et al.(1983) They start with the momentum equation and show that the Coriolis

force due to the cross product of the mean vorticity and the acoustic particle velocity is unbalanced. As a result, when the acoustic particle velocity is into the cavity, this force acts on fluid particles in the opposite direction from the mean flow. This causes the shear layer to roll up into discrete vortices. This effect will be described in detail in Chapter 5.

### Frequency Prediction of Sheartones and Cavity Tones

An understanding of the disturbance produced at the downstream edge and how it reaches the upstream edge may be used to predict the flow speeds and frequencies at which a flow excited cavity may resonate. The simplest and perhaps most useful equation is given by Rossiter (1964):

$$L/U_c + L/c = m/f,$$

where  $f$  is the frequency of the tone, and  $m$  is a positive integer denoting the "order" of the tone, or, in the case where discrete vortices are formed in the shear layer, the number of vortices present in the opening. The length of the cavity opening in the streamwise direction is given by  $L$ , the speed of sound by  $c$ , and the speed at which the vortices convect along the opening by  $U_c$ . We see, then, that the left side of the equation is the time for a vortex to travel downstream along the opening,  $L/U_c$ , summed with the time for a disturbance propagating at the speed of sound to travel back to the upstream edge,  $L/c$ . If there is only one vortex present, this time is the period,  $T=1/f$ . If  $m$  vortices are present at a time, it is  $m*T$ , or  $m/f$ . The assumption in the Rossiter equation, then, is that the vortex shedding at the upstream edge is controlled by a disturbance propagating at the speed of sound from the downstream edge.

This may not be the case, particularly when the cavity is resonating. Elder (1978) used a root locus technique to solve the equation  $G_{12} = 1/G_{21}$ , where  $G_{12}$  is the forward transfer function describing how the volume velocity of the cavity response influences the disturbance in the cavity opening.  $G_{21}$  is the backward transfer function, describing how the disturbance in the cavity opening excites the cavity. The solutions of the equation are the resonant frequencies of the flow excited cavity, and agreed well with experimental values.

Mast and Pierce (1995) derived a different forward transfer function but otherwise used the same equation as Elder to calculate resonant frequencies of a flow excited cavity. Kook

and Mongeau (1997) derived yet another forward transfer function but also used the same equation to calculate frequency. Both also reported good agreement with experimental data.

It should be noted that the forward transfer function essentially describes the interaction at the downstream edge, as discussed above. When the cavity is resonant, the disturbance produced downstream affects the upstream edge indirectly, through the acoustic response of the cavity.

### 1.3 Techniques For Reducing Flow-induced Cavity Resonance

Various techniques, both active and passive, have been employed to reduce the levels of flow-induced cavity resonance. Most of these techniques may be viewed as modifying the upstream or downstream flow regions, or both. Some passive techniques are discussed by Rockwell and Naudascher (1978). In their review paper, they describe the work of Ethembabaoglu (1973), in which the use of leading and trailing edge ramps resulted in as much as a 20 dB reduction in the tonal levels. Shaw (1979) used a leading edge spoiler and a trailing edge ramp to achieve a 20 dB reduction as well. Sarohia and Massier (1977) showed that fluid mass injection at the base of the cavity of between 5 and 15 % of the freestream mass  $\rho A U$ , where  $A$  is the area of the cavity opening, could result in as much as 12 dB reduction the cavity resonance tone. Sarno and Franke (1990) tested a static fence (similar to the spoiler used by Shaw (1979)) and a pulsating fence, as well as steady and pulsating fluid injection at the upstream edge of the cavity. Of these, the most effective technique was the static fence. A static fence with a height of 1 boundary layer thickness reduced the level by more than 30 dB at supersonic Mach numbers and by about 10 dB at  $M=0.62$ . Mendoza and Ahuja (1996) used fluid injection in the wall upstream of the opening to reduce levels by as much as 30 dB.

The techniques described above were all tested on rectangular cavities and at Mach numbers mostly greater than 0.2. The effectiveness of these techniques at lower Mach numbers and/or on Helmholtz resonator-like cavities has not been demonstrated. The only known passive technique demonstrated on Helmholtz resonator-like cavities at very low Mach numbers is the use of slatted louvers over the cavity opening. The use of these louvers is described by Bruggemann, et al. (1991).

Active control techniques have also been applied to reduce the levels of flow-induced cavity resonance. Sunyach and Ffowcs Williams (1986) used a loudspeaker in the base of the cavity and feedback from a microphone inside the cavity to reduce the levels in a Helmholtz resonator by 25 dB at 15 m/s. Kestens and Nicoud (1998) performed a numerical simulation of the use of a loudspeaker in the base of a rectangular cavity with an adaptive control technique to reduce the tonal level by about 8 dB at Mach 0.2.

Cattafesta, et al. (1997) used feedback control with a piezo-electric actuated flap at the upstream edge of a rectangular cavity to reduce levels by as much as 20 dB under some conditions. Mongeau, et al. (1998) use feedback control with a mechanically actuated flap at the upstream edge of Helmholtz resonator to reduce levels at  $M < 0.1$  by up to 20 dB.

Shaw (1998) tested pulsed fluid injection at the upstream edge and dynamic actuation of a leading edge flap on a rectangular cavity at high Mach numbers. The pulsing frequency varied, but was well below the frequency of the cavity tone (~500 Hz) and was preset (no feedback control). The pulsating flow was also tested at angles of 0 degrees (parallel to flow) and 90 degrees. The dynamic leading edge required an amplitude of 20 degrees to be effective and was most so at a frequency of 5 Hz. The pulsed fluid injection was most effective at an angle of 90 degrees and its effectiveness increased with mass flow rate and frequency up to the maximums tested (0.5 lb/s and 100 Hz). Reductions in tonal amplitude of up to 25 dB with the pulsed fluid ejection are shown.

Raman, et al. (1999) tested the use of pulsed fluid injection from the base of a rectangular cavity at an angle of 90 degrees. Measurements were performed at high subsonic Mach numbers. They designed a miniature fluidic oscillator capable of producing oscillating waveforms with frequencies up to 3000 Hz. The actuator was tested at both the upstream and downstream ends of the cavity. Testing using the downstream location showed no effect. Using the upstream location, reductions of as much as 10 dB were achieved with mass flow rates of about 0.12% of the freestream flow.

## **1.4 Objectives of the Research and Outline of the Dissertation**

We have seen how a flow-induced cavity resonance may result when the frequency of vortex shedding due to unsteady flow over an opening in a flow surface coincides with a resonance frequency of the cavity. Prior research has focused on the physical processes near

the upstream edge and near the downstream edge. Understandings of these processes have been used to predict the frequency of cavity resonance tones. We have also reviewed some of the control techniques, active and passive, that have been applied to reduce cavity resonance.

The goal of this research is to enhance our understanding of the complex flow-acoustic interactions in the cavity opening so that techniques for controlling cavity flow-induced resonances may be developed. To do this, we first examine the behavior of the speed dependent sheartones generated by flow over a cavity, looking at both the behavior of the sheartones under non-resonant conditions, as well as how these interact with the resonant response of the cavity to become cavity tones. We then study how these phenomena are altered by the use of cavity resonance control techniques. The combined results will enhance our understanding of the mechanisms of flow-induced cavity resonance. This understanding will lead to the development of better control techniques.

The approach taken to address these issues is to perform a series of experiments directed at these fundamental questions:

1. What are the distinct features of the sheartones under both non-resonant and resonant flow speed conditions?
2. What are the basic criteria by which established control techniques are effective?

Two distinct types of experiments are performed to collect the data required to address these issues. The first experiment consists of cavity pressure fluctuation data obtained over a broad speed range for a range of cavity parameters. The analysis of these data focuses on studying the behavior of the frequency and the level of the measured tones as a function of speed. The second experiment is a series of detailed measurements of the velocity field in the cavity opening obtained simultaneously with the cavity pressure fluctuations for selected speeds and cavity configurations. The mean and fluctuating velocity fields, and the correlation between the velocity components and the cavity pressure are analyzed to show some aspects of the flow field processes in the cavity opening. Both types of experiments were performed for the unaltered cavity, as well as for the cavity with the application of three different control techniques.

In Chapter 2, the experimental arrangements and instrumentation used to obtain the measurements are described. In Chapter 3, the results of the cavity pressure measurements for a range of geometries are presented, and the response of the cavity to grazing flow excitation is described in detail. Measurements for flow over a wall aperture (no cavity present) are also obtained and serve to increase our understanding of the frequency behavior. In Chapter 4, detailed measurements of the velocity and pressure performed at several speeds for a single cavity configuration are reported. Particular emphasis is placed upon the phase relationship between the velocity components and the cavity pressure.

In Chapter 5, the model proposed by Nelson, et al. (1983) is described in detail and terms derived in the model are calculated using the acquired experimental data. These calculations allow an evaluation and validation of this model, which provides a better understanding of the complex flow-acoustic interaction that exists at resonance.

In Chapter 6, measurements are reported for two established cavity resonance control techniques, as well as for a new technique developed by the author as part of this research. The data analysis techniques applied to the uncontrolled cavity are used here also. The results are compared to the uncontrolled cavity, enhancing our understanding of both. Finally, in Chapter 7, the findings of this research are summarized and directions for future research are discussed.

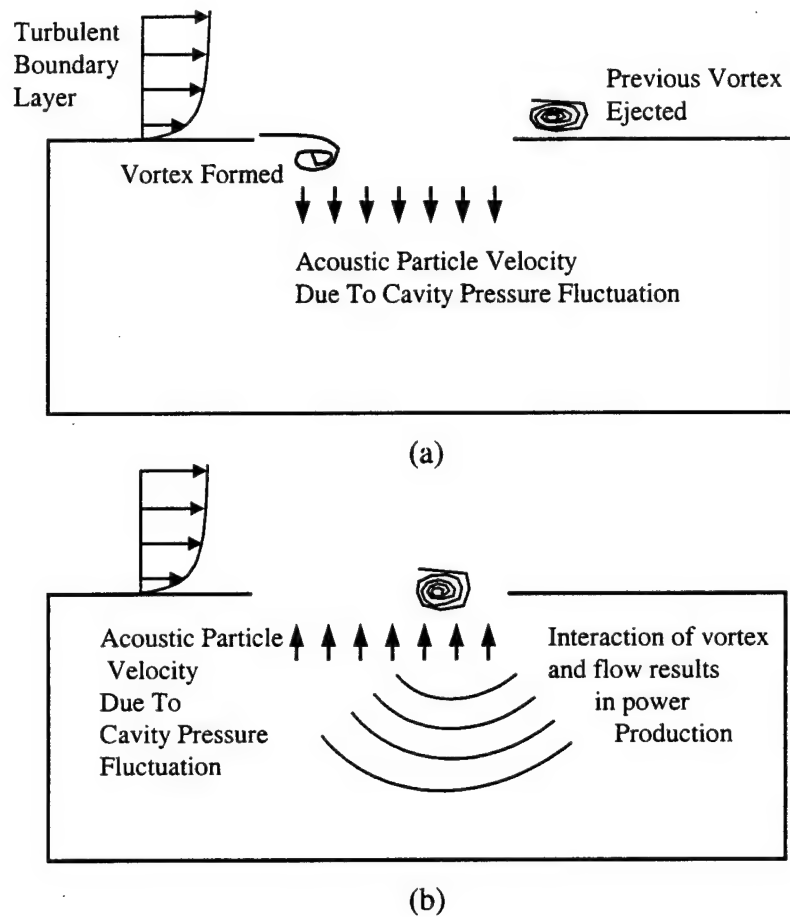


Figure 1.1: Dynamic processes of flow-induced cavity resonance

## 2. Experimental Arrangement and Test Condition

### 2.1 Experimental Setup

The measurements performed for this investigation were made in the Low Noise Flow Facility (LNFF) at the Catholic University of America (CUA). The LNFF was designed to be a quiet wind tunnel for making measurements of fluctuating wall pressures and velocity. A detailed description is given by Farabee (1986) and a schematic of the facility is shown in figure 2.1. The test section is 2.4 m long with a 0.6 m x 0.6 m cross section. The inlet includes a series of turbulence management screens followed by a 16:1 contraction section. The profile of this section was designed to prevent regions of local separation. The diffuser has an expansion angle of 7 degrees and is acoustically treated to reduce noise. Flow is generated by a low speed centrifugal blower driven by a 20 hp dc motor; both are located in a separate room. Acoustic mufflers are located upstream and downstream of the blower. Air drawn through the tunnel is discharged into the room housing the inlet, contraction, test, and diffuser sections.

The tunnel may be operated at flow speeds between approximately 3 and 30 m/s. At 28 m/s, noise levels above 50 Hz in the test section are below 80 dB re  $1\mu\text{Pa}^2\text{s}$ . Levels below 50 Hz are contaminated by blower generated acoustic standing waves. The free stream turbulence intensity level is approximately 0.2%.

A section view of the cavity used in this research is shown in figure 2.2. The cavity body is a 9" wide x 10" high x 2" thick piece of polyurethane with a 4.5" square opening in the center constituting the cavity volume. A flange allows the cavity to be fitted into a 7.5" x 10.5" opening in the side wall of the test section. A base plate is screwed onto the back of the cavity body to close the cavity. The depth of the cavity,  $d$ , may be increased by placing spacers of varying number and thickness between the cavity body and the base plate.

A top cover is mounted on the face of the cavity. This cover comprises the flow surface and is faired to the test section wall to ensure that the entire flow surface is smooth. The opening to the flow surface is milled out of the cover plate and spans with width of the cavity. The streamwise length of the opening,  $L$ , is varied by using cover plates with

different opening lengths. Table 2.1 lists the values of  $d$  and  $L$  for nine cavity configurations that were tested as part of this research. Four values of the cavity opening length were tested at each of two depths. A distinction between the two cavity depths tested is indicated in the configuration number by the use of  $s$  and  $d$  to indicate shallow and deep cavities, respectively. An additional, very deep, cavity, denoted by  $dd$ , was also tested.

Table 2.1 Cavity Configurations Tested

Configuration No.	$d$ (in.)	$L$ (in.)
1s	2.75	0.5
2s	2.75	1
3s	2.75	1.5
4s	2.75	2
1d	5.5	0.5
2d	5.5	1
3d	5.5	1.5
4d	5.5	2
2dd	18	1

## 2.2 Instrumentation and Data Collection

Measurements of cavity pressure and of the flow field in the opening were made using a  $\frac{1}{2}$ " microphone and a constant temperature anemometer (CTA), respectively. The microphone used was Brue & Kjaer model 4134, serial number 152774, with a sensitivity of  $-41.7$  dB re  $(V/Pa)^2$ . The microphone was powered by a Brue & Kjaer model 2619 pre-amp and a type 2807 power supply. It was mounted in the center of the base of the cavity with a polyurethane mounting block.

The microphone was calibrated using a Brue & Kjaer model 4220 pistonphone. The pistonphone produces a known sound pressure level. The microphone sensitivity can then be calculated by dividing the SPL by the voltage from the microphone.

The anemometer used to make velocity measurements was a TSI model IFA-300 with two channels of anemometry installed. This unit uses proprietary bridge optimization circuitry and is controlled by an Intel based PC using an RS232 interface and the TSI

ThermalPro software package. Temperature compensation is also performed automatically using temperature measurements from a thermocouple inserted into the test section of the tunnel downstream of the cavity.

The ThermalPro software automatically calculates the calibration coefficients of the probe and performs the linearization of the output from the anemometer. The calibration of the cross wire probes used in this research is based on measurements at 12 speeds between 0 and 30 m/s, and at 5 yaw angles.

Measurements of the velocity field in the opening were made using a TSI model 1243BE-20 probe and a model 1155 probe support. The probe, shown in figure 2.3, was custom designed so that measurements could be made inside the cavity at locations close to the downstream edge of the opening. The probe and probe support were mounted inside the tunnel test section on a motorized traverse system which was used to control the location of the probe.

Ideally, the prongs of the probe that support the sensor wires would be oriented in-line with the mean flow. However, to be able to measure the flow field within the entire opening, the prongs of the 1243BE are oriented perpendicular to the flow. To address the issue of whether this affected the results, preliminary measurements were made with a model 1243-T1.5 probe. This probe was designed for boundary layer measurements and could not make measurements below the opening of the cavity in the downstream half of the opening, but it was useful for qualifying the 1243BE probe. The results of the comparison between measurements made with both probes are given in the next section.

The freestream velocity during all experiments was monitored using a pitot-static probe with a Datametrics type 538-3 differential pressure transducer and a Datametrics model 1174 electronic manometer. Atmospheric temperature and pressure were monitored with a mercury thermometer and barometer. Free stream velocity was calculated from Bernoulli's equation using the measured pitot-static difference and the atmospheric density calculated using the perfect gas law with the atmospheric temperature and pressure.

Data were collected and stored using UEI ADCWIN-16 Analog to Digital (A/D) converter card installed in an Intel based PC. The A/D functions were controlled by the

ThermalPro software. Data were collected and stored as formatted files. Processing of data was done using MATLAB and the MATLAB Signal Processing Toolbox.

A Hewlett Packard 3562A dynamic signal analyzer was used to monitor the frequency spectra of the data during the measurements. This analyzer was also used to measure the cavity frequency response discussed in Chapter 3.

### **2.3 Onset Boundary Layer Measurements**

Measurements of the boundary layer profile upstream of the cavity opening were made and compared to similar measurements performed in the same facility by other researchers. This was done in order to, first, establish that an equilibrium turbulent boundary layer (TBL) exists upstream of the opening, and second, to establish the validity of data measured using the 1243BE probe with the IFA 300 anemometer and acquisition system.

Table 2.2 shows the calculated boundary layer parameters measured at 13.88 m/s with the model 1243-T1.5 probe and at 15.09 m/s with the 1243 BE-20 probe. Shown for comparison are data from Kammeyer (1995) measured at 16.13 m/s using a TSI model 1249A-10 miniature x probe. Acceptable agreement is seen between the parameters measured with the two probes used in this research and between these parameters and those measured by Kammeyer. The variation that is observed may be attributed to the different geometries of the various probes used and to slight irregularities in the flow surface upstream of the measurement location used in the current research.

Table 2.2 Boundary Layer Parameters

	Boundary Layer Properties w/ 1243-T1.5	Boundary Layer Properties w/ 1243BE-20	Boundary Layer Properties from Kammeyer
$U_0$	13.88 m/s	15.09	16.13
$u_\tau$	0.57 m/s	0.62 m/s	0.64 m/s
$u_\tau/U_0$	0.041	0.041	0.040
$\delta$	3.43 cm (1.349 in)	3.38 cm (1.332 in)	2.95 cm
$\delta^*$	0.49 cm (0.192 in)	0.48 cm (0.189 in)	0.46 cm
$\theta$	0.34 cm (0.134 in)	0.34 cm (0.134 in)	0.32 cm
$Re_\theta$	3259	3626	3358
$H$	1.4317	1.4319	1.4193
$C_f$ (calculated)	0.00301	0.00293	0.00304
$C_f$ (measured)	0.00340	0.00338	0.00318

Figure 2.4 shows the mean streamwise velocity profile measured with the 1243BE probe normalized by viscous wall variables and plotted against the low-law reference line given by the equation  $U^+=4.44\ln y^+ + 4.9$ . The profile shows adequate log-law behavior. This plot, along with the measured properties shown in the table, demonstrates that the boundary layer is indeed an equilibrium TBL.

It should be pointed out that an equilibrium turbulent boundary layer is not required for flow-induced cavity resonance to occur; the phenomenon occurs under laminar boundary layers and disturbed turbulent boundary layers as well. These boundary layer properties are discussed only to establish a general understanding of the flow conditions under which the cavity measurements were made.

Figures 2.5 and 2.6 show profiles of  $u_{rms}$  and  $v_{rms}$ , respectively, measured with the same probes for which results are shown in table 2.1. Also plotted on each figure is the corresponding data from Russell (1997). Note that the 1243BE probe, which has the prongs oriented at right angles to the flow, shows lower levels of both  $u_{rms}$  and  $v_{rms}$  than the 1243

probe, which has its prongs oriented in line with the flow. This is consistent with Kassab, et al. (1985), who found that values of the fluctuating components measured with a right angled probe were 5-10 % lower than those measured with an in-line probe.

In addition to boundary layer measurements, both probes were also used to make measurements of the velocity field in the opening of the cavity. Spectra of the velocity components and cross-spectral properties between  $u$  and  $v$  and between the velocity components and the cavity pressure, were compared. The spectral results were consistent with the rms results in that the spectra spectral levels measured with the right angled probe were generally several dB lower than those measured with the in-line probe at frequencies above about 400 Hz. However, this did not affect the measured levels of cavity tones, which were clearly observed with both probes. The phase between  $u$ - $v$  and between the velocity components and the cavity pressure were also equivalent for both probes.

There was some concern that the insertion of the  $x$  probe into flow field in the cavity opening would disrupt the fluid dynamic processes that govern flow-induced cavity resonance. A comparison of cavity pressure spectra for locations of the velocity probe within and far away from the opening established that no disruption occurred. Finally, calculations of the energy production term, which is discussed in detail in Chapter 5, made from data taken with both probes, agreed well given the constraints on available measurement locations imposed by the in-line probe. These results clearly establish the validity of using the model 1243BE probe for the velocity field measurements reported in this investigation.

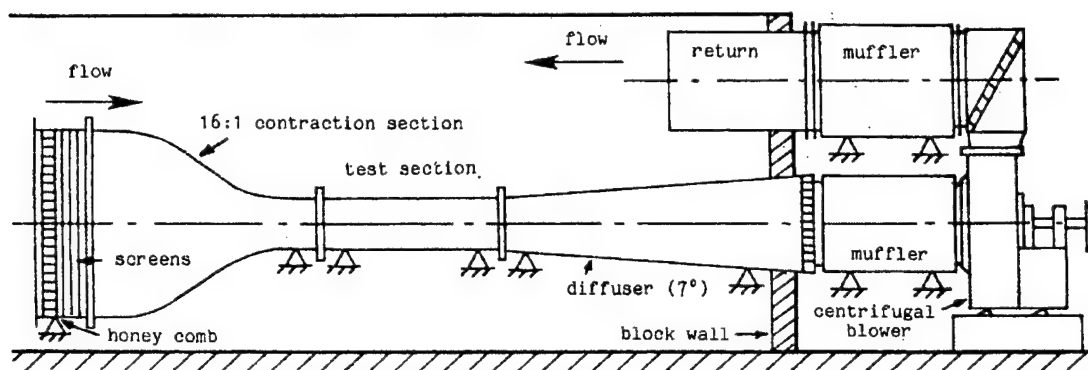


Figure 2.1: Schematic of Low Noise Flow Facility (LNFF)

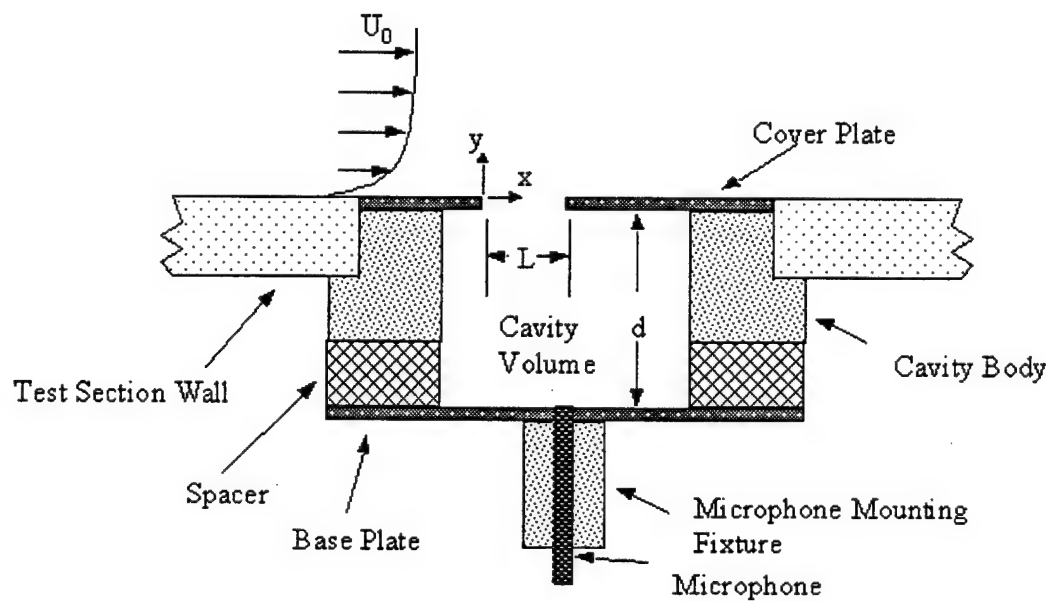


Figure 2.2: Section view of installed cavity

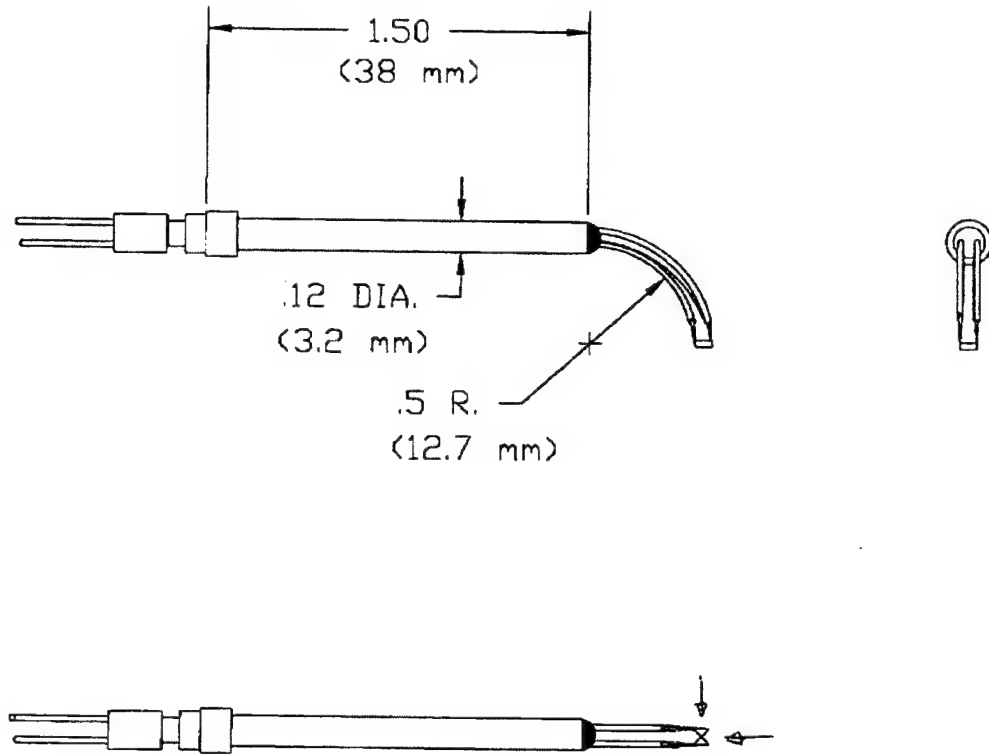


Figure 2.3: Drawing of custom x-probe 1243BE-20

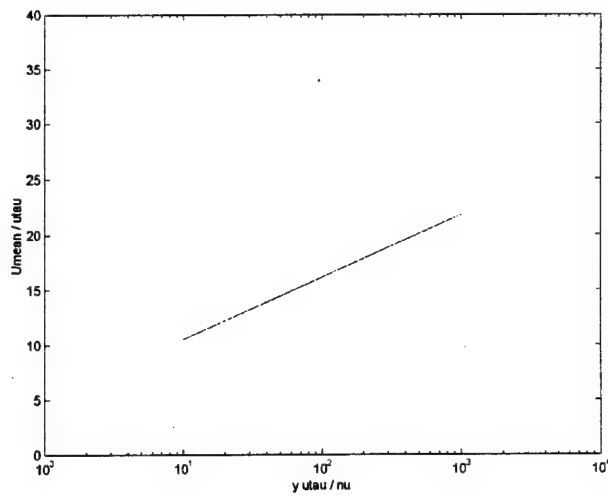


Figure 2.4: Mean streamwise velocity profile measured with right angle probe normalized by wall variables

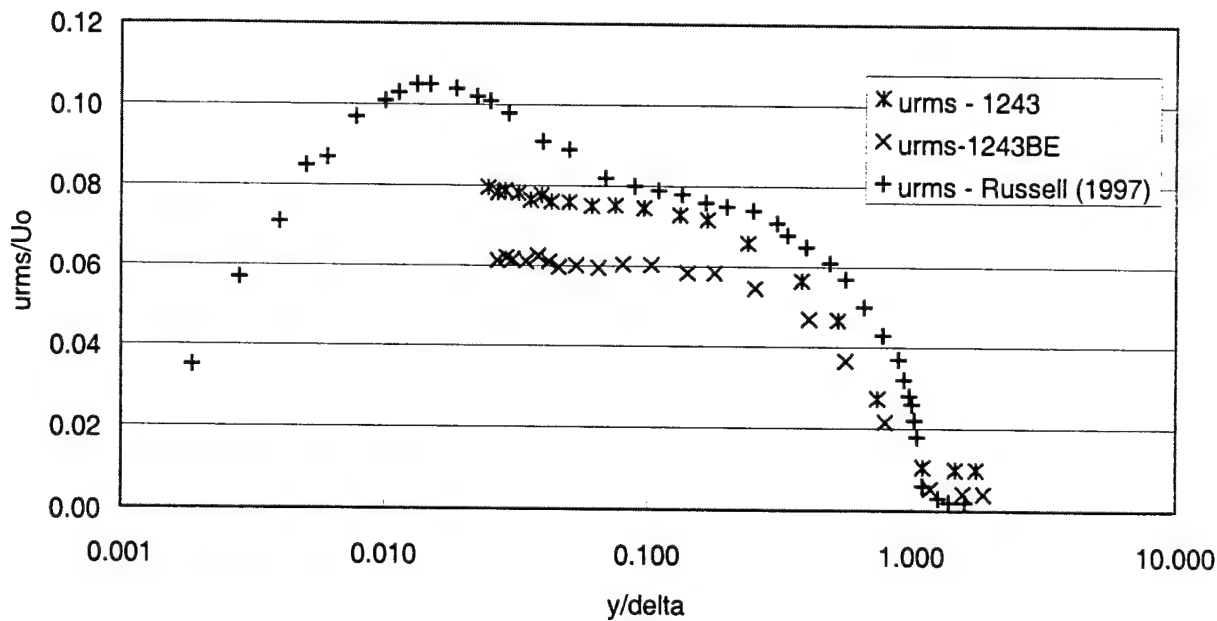


Figure 2.5: Streamwise turbulence intensity profiles

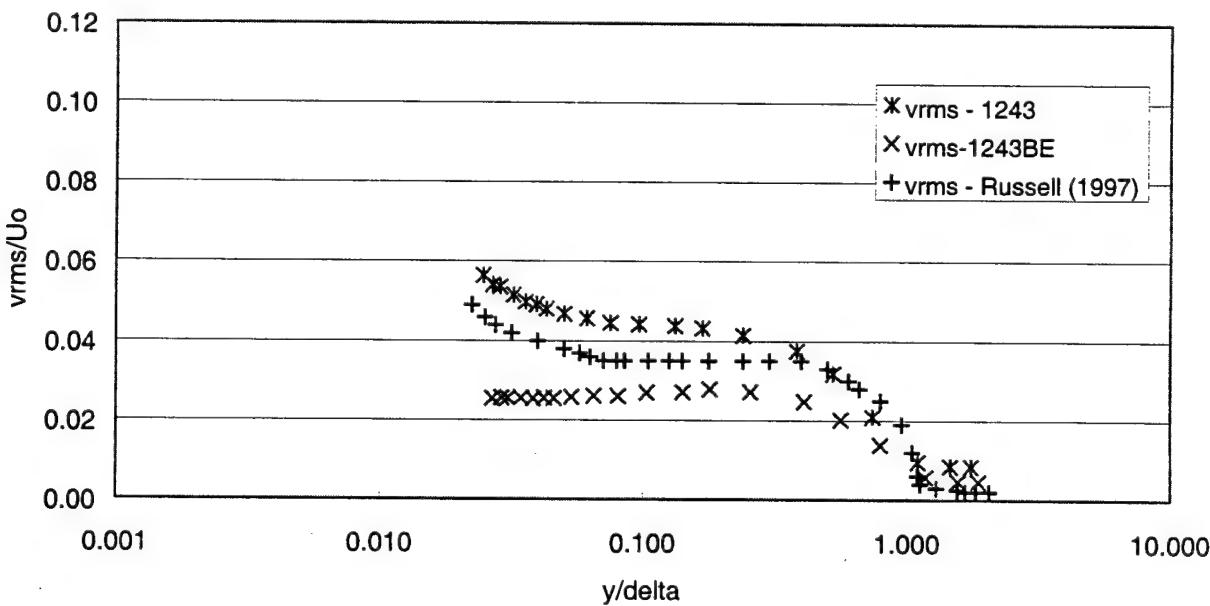


Figure 2.6: Wall-normal turbulence intensity profiles

### 3. Description of Cavity Response

In this chapter, the response of a cavity to flow excitation is described by analyzing measurements of the pressure fluctuations inside of a cavity over a range of speeds and for varied values of the cavity depth,  $d$ , and opening length,  $L$ . The first section describes the results of measurements of acoustic excitation of the cavity and compares these measurements to theoretical predictions. In the second section, cavity pressure spectra due to grazing flow over a cavity are described qualitatively. Detailed results of cavity response to grazing flow over a range of speeds are also discussed. In the third section, measurements of flow over an opening with no cavity backing are described and compared to the results from the prior section in order to further explain how the cavity response depends on cavity properties and boundary layer quantities. These results are summarized in the fourth section.

#### 3.1 Cavity Response to Acoustic Excitation

The cavity used in this research responded as a Helmholtz resonator. A Helmholtz resonance is modeled as a simple damped spring-mass oscillator, where the mass is the slug of fluid in the cavity opening and the spring is the volume of compressible fluid in the cavity. Damping comes from acoustic radiation and viscous losses. The resonance frequency of the cavity may be given by  $f_n = c/2\pi \sqrt{A/l'V}$ , where  $c$  is the speed of sound,  $A$  is the area of the cavity opening,  $V$  is the volume of the cavity, and  $l'$  is the effective thickness of the fluid slug in the opening. For the cavity used in the present research, the thickness was calculated using  $l' = l + 1.2a$ , where  $l$  is the actual thickness of the wall at the cavity opening, and  $a$  is the radius of a circle having the same area as the cavity opening. A more detailed explanation of Helmholtz resonance may be found in textbooks on acoustics, including Kinsler, et al. (1982).

The frequency response of the cavity Helmholtz resonance to fluctuating pressure at the opening was measured using an arrangement shown in figure 3.1. This arrangement was similar to that of Nelson, et al. (1981). A speaker was positioned approximately 1 ft from

the cavity opening and oriented facing the cavity opening. A  $\frac{1}{2}$  " microphone was mounted in the base of the cavity, and a 1" microphone was positioned outside the cavity, adjacent to the top surface. A periodic chirp signal was supplied to the speaker, which served to ensonify the cavity opening with an acoustic plane wave. The frequency response function, defined as the ratio of the acoustic power inside the cavity to that at the opening, was calculated using the measured signals from the microphones.

This measurement was performed for the cavity configurations listed in table 3.1. The configurations are numbered according to the values of L and d. The numbers 1 thru 4 correspond to the increasing values of L listed, and s and d correspond to two classifications of shallow ( $d=2.75"$ ) and deep ( $d=5.5"$ ) cavities. An 18" deep cavity, denoted by dd, was also tested. Also listed is the measured Helmholtz resonance frequency and loss factor for each configuration. Loss factor was calculated using the 3 dB down points on either side of the peak frequency. In figure 3.2, the frequency response for the  $L=1"$ ,  $d=5.5"$  cavity is plotted. This response is typical. Also plotted is the frequency response calculated based on the center frequency and loss factor. Agreement in the region near the resonance frequency is excellent. Above the resonance frequency, the measured response is limited by a loss of signal-to-noise, while the calculated response falls off at a rate of  $(1/f)^2$ .

Table 3.1 Cavity Helmholtz Resonance Frequencies and Loss Factors

Configuration No.	d (in.)	L (in.)	$f_h$ – Resonant frequency under acoustic excitation (Hz)	$\xi$ – loss factor based on acoustic measurements
* 1s	2.75	0.5	436.2	0.207
2s	2.75	1	527.5	0.0096
3s	2.75	1.5	572.5	0.0044
* 4s	2.75	2	636.2	0.0069
1d	5.5	0.5	312.5	0.0249
* 2d	5.5	1	346.2	0.01673
3d	5.5	1.5	396.2	0.0096
4d	5.5	2	416.2	0.00447
** 2dd	18	1	131.0	.03695

\* Section 3.2 contains an in-depth discussion of these configurations

\*\* Results of this configuration are discussed in Chapter 6

In figure 3.3, the measured Helmholtz resonance frequency normalized by the calculated frequency,  $c/2\pi \sqrt{A/l'V}$ , for all cavities are plotted against the streamwise length of the cavity opening,  $L$ . A value of 1 indicates agreement between measured and calculated values. For most of the cavity configurations, measured values are within about 5% of predicted values. These results show that the cavity configurations used in this research behave like a classical Helmholtz resonator.

The values tabulated in Table 3.1 of Helmholtz resonance frequency for the various cavity configurations illustrate how the frequency depends on the values of  $L$  and  $d$ . A larger value of  $d$  corresponds to a larger cavity volume. Since frequency decreases with increasing volume, the resonance frequency decreases with increasing  $d$ . Also, Helmholtz frequency increases with  $A$  but decreases with  $l'$ . A larger value of  $L$  corresponds to a proportionally larger opening area,  $A$ , but also to a larger value of  $l'$ , the thickness of the mass slug in the opening. The relationship between  $l'$  and  $L$  is approximately a  $1/2$  power relation. Thus the resonance frequency increases with  $L$ , but not as strongly as it decreases with  $d$ .

### 3.2 Cavity Response to Grazing Flow

Grazing flow over a cavity opening results in the creation of tones observable in the cavity pressure spectrum. These speed dependent tones, referred to as sheartones, are produced by the interactions of discrete vortices shed from the upstream edge of the opening. As speed is increased, the first and second sheartones increase in frequency. The first sheartone corresponds to the presence of one vortex in the cavity opening, while the second sheartone corresponds to two vortices and has a frequency greater than, but less than two times, the first. When the frequency of the second sheartone becomes sufficiently close to the cavity resonance frequency, the second sheartone locks in to the cavity resonance and becomes a cavity tone. The level of the tone then begins to increase rapidly with speed. When the speed has increased sufficiently that the frequency of the cavity tone is greater than the resonant frequency, the level decreases rapidly to near its original level. The

process is repeated at still higher speeds when the frequency of the first sheartone becomes sufficiently close to the cavity frequency and becomes resonant.

In this section, the response of a cavity to turbulent grazing flow over the opening is discussed. The focus is on the behavior of the sheartones, over a range of speeds and how those tones interact with the various resonances of the cavity. However, other features of the cavity pressure spectra are also discussed. The first subsection discusses the various tones seen in the cavity pressure spectrum excited by low speed grazing flow and deals in a general way with how the frequencies of the tones depend on the geometry of the cavity, specifically, the values of  $L$  and  $d$ . The second subsection describes how the first and second sheartones behave with increasing speed, including their interaction with the resonance of the cavity. The third subsection discusses the spectral level of those tones as a function of speed, while the fourth subsection discusses the frequency of those tones as a function of speed and helps to quantify the relationship between frequency and the values of  $L$  and  $d$ .

### 3.2.1 Low Speed Cavity Pressure Spectra

Cavity response to excitation by grazing flow is more complex than response to acoustic excitation. Three different cavity configurations are examined. These are labeled 2d, 4s, and 1s in table 3.1. Spectral data will be presented to illustrate the behavior of the sheartones for each of these configurations.

The response of a deep cavity configuration (2d) to flow of 6.8 m/s is shown in figure 3.4. This configuration has a Helmholtz resonance frequency of 346 Hz. The peaks at 108 Hz and 193 Hz are speed dependent tones that are of interest in this study and will be discussed in detail in the following section. The peak at 280 Hz is the half-wavelength standing wave of the tunnel cross section. This resonance was observed under nearly all conditions and was often excited by the sheartones at the appropriate speeds. However, this resonance is different from the cavity resonance and is not the focus of this research.

Data below 50 Hz are contaminated by facility related tones and are not shown. The peak at 333 Hz is the Helmholtz resonance response of the cavity to turbulent boundary

layer (TBL) excitation. Elder et al. (1982) refer to this mode of excitation as turbulent rumble. A description of the turbulent rumble phenomenon is also given by Bruggeman, et al. (1997). In their model, they assume that the opening is excited by turbulent boundary layer pressure fluctuations having the same wavenumber frequency spectrum as exists on the wall upstream of the opening. They also assume that the air in the opening responds like a rigid piston and use a model of the turbulent boundary layer given by Chase (1987) to describe the forcing. A comparison between the calculated response and their measurements shows both having roughly the same shape, but the calculated values are low by about 20 dB. This was attributed to the inapplicability of the Chase model to their experiment.

In figure 3.5, the cavity pressure spectrum for a shallow cavity configuration (4s) due to excitation by flow at 6.9 m/s is shown. The Helmholtz resonance frequency for this configuration is 636 Hz. For this case, the speed dependent tones are seen at 58 Hz and 104 Hz. They are narrower than the speed dependent tones for the deep configuration (2d) and they are also higher in amplitude. The TBL excited Helmholtz resonance for configuration 4s is 554 Hz. This frequency is lower than its Helmholtz resonance frequency. This discrepancy will be discussed at the end of this subsection. It should be noted that the frequencies of the sheartones for this configuration are approximately half of those for configuration 2d. This is due exclusively to the value of  $L$  being doubled; the value of  $d$  has no effect. This dependence will be shown in detail later in this section.

In figure 3.6, the cavity pressure spectra due to flow of 6.8 m/s for shallow cavity configuration (1s) is shown. This configuration has a smaller opening length,  $L$ , than configurations 4s and 2d. Its Helmholtz resonance frequency is 436 Hz. For configuration 4s, speed dependent tones are seen at 58 Hz and 104 Hz. For this case, only the first sheartone, at 185 Hz is seen. This tone is broader and lower in amplitude than the first sheartones for both configurations 2d and 4s. The second sheartone is beginning to excite the Helmholtz resonance, though this is difficult to discern without looking at the spectra at a series of speeds. The TBL excited Helmholtz resonance is seen at 416 Hz. This value is lower than that for 4s and is again attributable to the dependence of Helmholtz resonance frequency on  $L$  and  $d$ ; the lower value of  $L$  has the effect of reducing the frequency from

that seen in 4s. The higher value of the first sheartone is again attributable to the lower value of L.

The difference between the acoustically excited Helmholtz resonance frequency and the observed TBL excited resonance frequency for each of the configurations requires further examination. In figure 3.7, the normalized measured frequencies of the turbulence excited Helmholtz at a nominal flow speed of 7 m/s for all cavity configurations listed in table 3.1 are compared to those of the acoustically excited cavity. In all cases, the turbulence excited resonant frequency is lower than the acoustically excited resonant frequency. It is hypothesized that the lower frequencies are due to differences in the excitation. The acoustically excited cavity is excited by a plane wave at normal incidence. The turbulent rumble tone is excited by boundary layer turbulence convecting across the opening, which is roughly equivalent to plane wave excitation at grazing incidence.

### **3.2.2 Qualitative Description of Sheartone Behavior**

In this section, the behavior of the tones over the speed range of the tunnel for the three configurations discussed above are described. The intent is to describe qualitatively how the sheartones behave with speed, with an emphasis on how they interact with the cavity resonance.

Figure 3.8 is a tiling of plots of the pressure spectrum inside the cavity for configuration 2d at 12 different speeds over the range of 6.8 m/s to 29.2 m/s. What follows is a description of the speed dependent tones observed in these plots.

At 6.8 m/s, peaks at 108 and 193 Hz are due to the first and second sheartones, respectively. These tones, measured at the base of the cavity, are due to strong vortical flow in the shear layer formed in the cavity opening. These frequencies of the disturbances in the shear layer are sufficiently far from the resonant frequency of the cavity that they do not produce a cavity resonant tone. At 9.6 m/s, the frequency of the first sheartone has increased to 148 Hz. The frequency of the second sheartone has also increased, and it is now near coincident with the standing wave in the tunnel at 278 Hz. Note that the

turbulence excited cavity resonance changed character somewhat between these two speeds. This is attributed to the influence of the second sheartone.

At 12.4 m/s, the second sheartone and the Helmholtz resonance tone have merged: the second order tone is now coincident with the cavity resonant tone. The vortex shedding in the shear layer and the resonance of the cavity are now sympathetically driving each other in a resonant manner. This phenomenon will be referred to as "lock-in". Note that the first order sheartone is still present and continues to increase in frequency with speed.

The second sheartone has decreased in amplitude at 14.4 m/s as its frequency is now 30 Hz greater than the turbulence excited resonant frequency of the cavity, but it is still exciting the resonance and is the strongest tone at this speed. The first sheartone continues to increase in frequency, but is now somewhat less distinct as it approaches the standing wave resonance.

As the speed is increased to 16.9 m/s, the second sheartone is still weakly exciting the cavity resonance at 375 Hz. At this speed, the tone appears similar to the turbulent rumble seen at low speed, but the increase in frequency of the tone with speed indicates that it is still sheartone driven. The first sheartone has now almost completely locked in to the standing wave resonance of the tunnel, and is the highest peak in the spectrum. At the next speed, 18.6 m/s, the first sheartone is fully locked in to the standing wave, while the second sheartone is still exciting the Helmholtz resonance.

At 20.7 m/s, the first sheartone has separated from the standing wave resonance and is now beginning to excite the Helmholtz resonance. Note that at this speed, the frequency of the sheartone excited Helmholtz resonance is well below the frequency due to turbulence or acoustic excitation. However, this sheartone frequency is higher than the frequency that would exist in the absence of a nearby resonant response frequency. The response of the cavity is altering the sheartone, resulting in a higher frequency, while at the same time, the interaction of the sheartone and the cavity is exciting the cavity to resonate.

The second sheartone is no longer in the spectrum at 22.7 m/s. The first sheartone at this speed has increased in level and frequency; a tone now also appears at the second harmonic of the sheartone.

At speeds of 25.0 and 27.1 m/s, the Helmholtz resonance, excited by the first sheartone, continues to increase in speed and in level. The second and third harmonics of this tone are also present in the spectrum. These harmonics arise from the non-sinusoidal nature of the signal at the resonance frequency and should not be confused with the higher order sheartones. The resonance reaches a maximum value at 28.5 m/s and decreases slightly at 29.2 m/s.

Spectra over the speed range for configuration 4s are shown in figure 3.9. Here, the effect of the higher Helmholtz resonance frequency and the lower (for a given speed) sheartone frequencies are evident. The effect is that the speed limit of the wind tunnel is reached before the first or second sheartone reaches a high enough frequency to excite the cavity to resonate. At speeds of 22.5 and 24.8 m/s, the Helmholtz resonance appears to be weakly excited. Based on the dependency of sheartones with flow speed, it is conjectured that this excitation is due to the existence of a third sheartone. However, the third sheartone is not observed in any spectra in a non-resonant condition; it is observed only when it is exciting the cavity to resonate.

Spectra over the speed range for configuration 1s are shown in figure 3.10. Here, the second sheartone weakly excites the cavity resonance at the three lowest speeds, 6.8, 9.7, and 12.4 m/s. At 14.4 m/s, the first sheartone takes over and continues to interact with the resonance over the rest of the speed range, reaching a maximum at 22.5 m/s. For this configuration, the value of L of 0.5" has the effect of increasing the frequency of the sheartone at a given speed, and the result is that, despite the Helmholtz frequency being higher than that for configuration 2d, the cavity is excited by both sheartones at lower speeds. In fact, the data suggest that at speeds just above the speed limit of the wind tunnel, both sheartones will be beyond the Helmholtz resonance so that it is no longer excited.

Based on the description of the data discussed above, we can summarize how these tones behave as a function of speed. When the sheartones are sufficiently far away from the cavity resonant frequency, their frequencies increase linearly with speed. However, near a cavity resonance frequency, the feedback mechanism controlling the sheartone changes from being due a disturbance propagating directly from the downstream edge, to being associated directly with the Helmholtz response of the cavity. At this point, the sheartone is said to be

locked in to the resonance. It is still increasing in frequency with speed, but more slowly, and therefore it deviates from the linear relationship. When speed has increased enough, the tone breaks free of the cavity resonance and again increases nearly linearly with speed at the original rate. It should be pointed out, however, that in this experiment, sheartones were not actually observed in the cavity pressure spectra at speeds greater than those where they are locked in to the Helmholtz resonance. The behavior at speeds above those where the cavity is excited is inferred from the behavior of the sheartones in exciting the standing wave resonance of the wind tunnel test section.

It is also worth noting that the flow speed at which flow excited cavity resonance occurs depends strongly on the geometry of the cavity. Lower values of  $L$  will result in resonance at lower speeds, while lower values of  $d$  will cause resonance to occur at higher speeds. This is important because selection of the appropriate values of  $L$  and  $d$ , where possible, is the simplest way to avoid flow-induced cavity resonance in a practical design.

Appendix 1 lists frequency and level for all speed dependent tones for all values of  $L$  and  $d$ . The following sections contain detailed discussions of the behavior of these tones.

### 3.2.3 Discussion of Level as a function of speed

In this section, the behavior of the amplitude of sheartones observed in the cavity pressure spectra as a function of speed, and how this behavior illustrates the interaction of the sheartones with the cavity Helmholtz resonance, are discussed. This is done by analyzing plots of the normalized level of the sheartones as a function of speed for all combinations of  $L$  and  $d$ . The intent is to show the behavior of sheartones prior to lock-in with cavity resonance does not depend on  $d$ , and to observe how the level of the tone changes as it locks in to the cavity resonance. In the legends of the figures shown in this section,  $L1$  and  $L2$  denote the normalized level of the first and second sheartones, respectively.

Figures 3.11, 3.12, and 3.13, are plots of level of the cavity pressure spectra, normalized by the dynamic head,  $q=1/2\rho U_0^2$ , at the frequency of the first sheartone as a function of speed for  $L=1"$ ,  $L=1.5"$ , and  $L=2"$ , respectively. In each of these plots, the  $d=2.75"$  and  $d=5.5"$  cavities are compared. It can be seen that the normalized levels at low speeds are

nearly constant and are essentially the same for both cavity depths. When the speed is sufficiently high for the sheartone of the deep cavity to lock in to the cavity resonance, the level begins to increase rapidly. Speeds where the sheartone was judged to have locked in to the cavity resonance are indicated on the figures. The sheartone can be seen locking in to the cavity resonance for the smaller openings ( $L=1"$  and  $L=1.5"$ ). However, only for  $L=1"$  (figure 3.11) is a maximum value reached. This value is about 50 dB above the low speed level.

It should be noted that for  $L=1.5"$  and  $L=2"$  (figures 3.12 and 3.13), the first sheartone can also be seen to be influenced by the resonant second sheartone at speeds where the second sheartone is resonant. This is also indicated on the figures. This phenomenon was identified by noting that the behavior of the non-dimensional frequency, or Strouhal number,  $St = fL/U_0$ , of the first sheartone is altered and the frequency of the first sheartone becomes almost exactly equal to half of the frequency of the resonant second sheartone. Essentially, when the second sheartone locks in to the cavity resonance, it forces the first sheartone to be a sub-harmonic of the second sheartone.

Figures 3.14, 3.15, and 3.16, are plots of level of the cavity pressure spectra at the frequency of the second sheartone as a function of speed for cavity openings of  $L=1"$ ,  $L=1.5"$ , and  $L=2"$ , respectively. In each of these plots, the deep and shallow cavities are compared. As was observed for the first sheartone, the levels at low speeds are essentially constant and independent of  $d$ . When the sheartone begins to lock in to the cavity resonance, the level rises rapidly, reaches a peak value about 50 dB above the low speed value, and then declines to the low speed value. For  $L=2"$ , the speed limit of the tunnel is reached before the decline in level can be observed.

The behavior of the level as the sheartone locks in to the cavity resonance is more apparent for the second sheartone because resonance is reached at a lower speed. For both sheartones it can be seen that the normalized levels at low speeds are nearly constant with speed and independent of the depth of the cavity. For some cavity configurations, the speed where the sheartones lock-in to cavity resonance is marked by a rapid increase in normalized level to a peak of about 50 dB above the low speed value, followed by a rapid decline to the original low speed value.

### 3.2.4 Discussion of Frequency as a function of speed

In this section, the relationship between the frequencies of the sheartones and the grazing flow speed is examined by comparing plots of the frequency as a function of speed. Also, the effect of the thickness of the boundary layer just upstream of the opening is considered by examining the non-dimensional frequency, of Strouhal number,  $St=fL/U_0$ , as a function of speed. In the legends of the figures shown in this section,  $F_1$  and  $F_2$  denote the frequency of the first and second sheartones, respectively;  $S_1$  and  $S_2$  denote the Strouhal number of the first and second sheartones, respectively.

Figures 3.17, 3.18, and 3.19, are plots of the frequency of the first sheartone as a function of speed for cavity openings of  $L=1"$ ,  $L=1.5"$ , and  $L=2"$ , respectively. In each of these plots, the deep and shallow cavities are compared. Data points where the sheartones are determined to have locked in to the cavity resonance are identified in the figures. The determination was made based on the behavior of the plots of normalized level shown in the previous section. For all of these results, it can be seen that at the low speeds, the frequency has an essentially constant slope for a given value of  $L$ . In general, as the frequency approaches the Helmholtz frequency of the cavity, the slope then begins to decrease with speed. This happens at a lower speed for the deep cavity due to the lower resonance frequency of the cavity. In fact, for  $L=1.5"$  and  $L=2"$ , the first sheartone never excites the resonance of the shallow cavity. Also, in figures 3.18 and 3.19, speeds where the frequency of the first sheartone are forced to the half frequency of the resonant second sheartone, thus becoming sub-harmonics of the second sheartone, are indicated. This phenomenon was also noted in the discussion of normalized level.

Figures 3.20, 3.21, and 3.22, are plots of the frequency of the second sheartone as a function of speed for cavity openings of  $L=1"$ ,  $L=1.5"$ , and  $L=2"$ , respectively. In each of these plots, the deep and shallow cavities are compared. Again, in these figures it can be seen that at the low speeds, the slope is essentially the same for a given value of  $L$ . And again, in general, the slope begins to decrease after the sheartone has locked in to a resonance. Because the second sheartone is at a higher frequency than the first sheartone, the

effect of lock-in may be most easily observed for the smaller openings ( $L=1$  and  $L=1.5$ ) at both depths of the cavity.

It would be useful to compare the values of the Strouhal number for different sized openings. The constant slope of the frequency plots seen at the lower speeds implies that the Strouhal number has a constant value at those speeds. In figure 3.23, Strouhal number as a function of speed is shown for all values of  $L$  with the shallow cavity. It can be seen that in the low speed region, Strouhal number is highest for  $L=2"$  and decreases for smaller openings. This observation agrees with the results reported by DeMetz and Farabee (1977). They observed that Strouhal number at the onset of resonance, defined as the speed where the peak of the speed dependent tones are at least 10 dB above the continuum, is inversely proportional to  $\delta/L$ . Since  $\delta$  is relatively constant with respect to speed, Strouhal number increases with increasing  $L$ . In figure 3.24, the data of both DeMetz and Farabee and Dunham (1962) for Strouhal number at resonance onset are plotted against  $\delta/L$ . Also plotted are the same data from the current research and lines fitted through the data points representing the first and second sheartones. Excellent agreement is seen among all of the experimental data.

In this section it has been shown that the Strouhal numbers of the first and second sheartones at speeds below lock-in are essentially constant and independent of the cavity depth,  $d$ . The value of the Strouhal number is, however, dependent on the boundary layer thickness. The issue of Strouhal number dependence on boundary layer thickness is examined in more detail in the next section.

### 3.3 Speed Dependent Behavior of Shear Tones In The Absence of a Cavity

In the previous section, it was seen that the Strouhal number of the sheartones was independent of the volume of the cavity. This suggests that the cavity is not involved in the feedback process between the downstream edge and upstream edge interactions that control the frequency of the non-resonant sheartone. It was also seen that Strouhal number did depend on the ratio,  $\delta/L$ . In this section, confirmation that the cavity is not involved in the

feedback process controlling the non-resonant sheartones is sought. Also, the dependence of the Strouhal number on the boundary layer thickness is quantified. This is done by examining pressure fluctuations resulting from flow over a wall aperture in the absence of a cavity.

The walls of the cavity were removed and the microphone suspended in the same position it was when the walls were present. It should be noted that the tunnel test section pressure is lower than atmospheric pressure. Hence, these measurements are complicated by the fluid flow into the tunnel through the open wall aperture. However, advantage of this inflow is taken by using measurements of the thicker boundary layer that results to extend the study of Strouhal number dependence on boundary layer properties discussed in the previous section.

Figure 3.25 shows the pressure spectra at various speeds measured with an  $L=1"$  cavity opening but without the cavity present. It can be seen that three closely spaced speed dependent tones are present. These tones are seen at 59, 98, and 158 Hz at 12.1 m/s and increase to 75, 183, and 258 Hz at 22.2 m/s. These tones are fairly broad and are less than 5 dB above the background levels.

As will be seen, the highest frequency tone has a Strouhal number similar to what would be expected from the first sheartone in a closed cavity, and will be considered the first sheartone in the analyses reported. The two tones at lower frequencies may be due to other modes of the instability wave of the shear layer. In fact, the frequency of the middle tone, when normalized by  $U_0$  and inflow momentum thickness,  $\theta$ , agrees well with the Strouhal number for the neutral disturbance of the unstable shear layer calculated by Michalke (1965).

In figure 3.26, the Strouhal number of the highest frequency tone measured for the no-cavity condition is plotted as a function of speed for  $L=1"$  and  $L=1.5"$ . The curves for both values of  $L$  are nearly identical.

A test of the hypothesis that the Strouhal number behavior of this tone and of the first sheartones measured with the closed cavity is the same is desired. In figure 3.27, Strouhal number as a function of speed for the no-cavity condition is compared to the same data for the shallow cavity. The value of  $St$  for the no-cavity condition with  $L=1"$  is about 5 %

below the value for the  $L=1"$   $d=2.75"$  condition. However, recall that  $St$  is a function of  $\delta/L$ . Also, significant mass inflow is present in the no-cavity condition, meaning that we cannot expect the boundary layer to be similar to that with a closed cavity present.

Boundary layer profiles were measured 0.25" upstream of the opening for the no-cavity condition at two speeds with  $L=1"$  and  $L=2"$ . Mass inflow through the aperture made it difficult to identify where  $u$  asymptotically equals  $0.99U_0$ . Hence consideration was given to integral boundary layer length scales instead. Estimates of displacement thickness,  $\delta^*$ , and momentum thickness,  $\theta$ , were calculated and are shown in table 3.4. Also shown are similar measurements made 0.25" upstream of the cavity opening with the cavity in place. The displacement thickness for the no-cavity condition is as much as 10 times the displacement thickness with no mass inflow.

Table 3.2 Boundary Layer Properties

No-Cavity Condition			
$U_0$ (m/s)	$L$ (in.)	$\delta^*$ (in.)	$\theta$ (in.)
9.7	1	.9	.42
25	1	.82	.39
9.8	2	1.6	.88
26	2	1.3	.63
Closed Condition			
$U_0$ (m/s)	$\delta$ (in.)	$\delta^*$ (in.)	$\theta$ (in.)
9.4	0.938	0.16	0.115
19.9	1.252	0.194	.0141
25.8	1.094	0.179	.0129

From these results, it is reasonable to believe that the discrepancy between  $St$  for the no-cavity condition, and that for the closed cavity shown in figure 3.27, exists because the thicker boundary layer results in a higher  $\delta/L$ . This translates to a lower value of  $St$  based on the results shown in figure 3.24.

An increased understanding of this result can be gained by studying the Rossiter equation. This equation was introduced in Chapter 1 and is re-written in the form

$$f = m / [L/U_c + L/c].$$

For a first sheartone,  $m$  may be set equal to 1. Both sides may then be multiplied by  $L/U_0$  to obtain

$$fL/U_0 = 1/[U_0/U_c + M],$$

where  $M$  is the Mach number of the free stream flow. Thus it is seen that when  $M \ll 1$ ,

$$fL/U_0 \approx U_c/U_0.$$

To successfully predict Strouhal number,  $fL/U_0$ , Rossiter's equation must be modified by replacing  $m$  with  $m-\beta$ , where represents a "phase lag" in the feedback process. However, even with this modification, it can still be seen that  $fL/U_0 \propto U_c/U_0$ .

It can be difficult to measure  $U_c$ . Instead,  $U_c$  may be related to the boundary layer thickness. In discussing the effect of  $\delta/L$  on the ratio  $U_c/U_0$ , Bruggeman (1997) suggests that  $U_c/U_0$  decreases with increasing  $\delta/L$ . Schlichting (1968) describes the velocity profile of a turbulent boundary layer on a smooth flat plate by the equation  $u/U_0 = (y/\delta)^{1/7}$ . While this equation is not meant to describe the behavior of a free shear layer, it is suggests the following relation between boundary layer thickness and convective velocity:

$$U_c/U_0 \propto (\delta/L)^{-1/7}.$$

Momentum thickness,  $\theta$ , is proportional to boundary layer thickness,  $\delta$ . Therefore,  $\delta$  is replaced with  $\theta$  to give

$$U_c/U_0 \propto (\theta/L)^{-1/7}.$$

This idea is applied to the measured data in figure 3.28, where, for several values of  $L$ , with and without a cavity present, the quantity  $fL/U_0(\theta/L)^{1/7}$  is plotted as a function of speed. It is seen that this quantity is a nearly constant 0.275 for all cavity configurations and speeds.

These results show that the speed dependent tone with the highest frequency measured without the cavity is characteristically the same as the first sheartone that is present with a cavity. This confirms that the feedback mechanism between the upstream and downstream edges of the opening for non-resonant sheartones does not involve the cavity.

### 3.4 Summary

In section 3.1 the response to acoustic excitation was considered. This allowed an understanding of the behavior of the resonance frequency of the cavity with respect to the geometry of the cavity, and demonstrated that for acoustic excitation, the cavity behaves as a classical Helmholtz resonator.

In section 3.2, the response to a grazing flow over the opening was examined. The mechanisms governing resonance of this condition are the major focus of this investigation. It was seen that flow over the opening generates sheartones, which are detectable in the cavity pressure spectrum. When the frequencies of these tones are sufficiently below the Helmholtz resonance frequency of the cavity, they behave independently of the Helmholtz resonator and have frequencies proportional to the speed of the flow and inversely proportional to the length of the opening. Also, under these conditions, the levels of the tones in the cavity normalized by the dynamic head,  $q$ , are constant with respect to speed. This is referred to as the non-resonant condition.

When the flow speed is such that the frequency of a sheartone approaches the Helmholtz frequency of the cavity, the feedback mechanism controlling the sheartone changes abruptly and becomes associated directly with the Helmholtz response of the cavity. This state is identifiable by a sudden increased in the normalized level of the tone, and also by a decrease in the Strouhal number,  $fL/U_0$  of the tone. This is referred to as the resonant, or lock-in, condition.

The effect of cavity opening  $L$  and cavity depth  $d$  were studied. It was found that below resonance, the frequencies of the sheartones were independent of the depth of the cavity. They were, however, dependent on the ratio of the boundary layer thickness to the opening length.

In section 3.3, measurements made with the cavity removed helped to quantify that dependence and also confirmed that the frequencies away from resonance are independent not just of the depth of the cavity, but of the presence of the cavity. This establishes that the feedback mechanism discussed in Chapter 1 for the non-resonant sheartone does not involve the cavity.

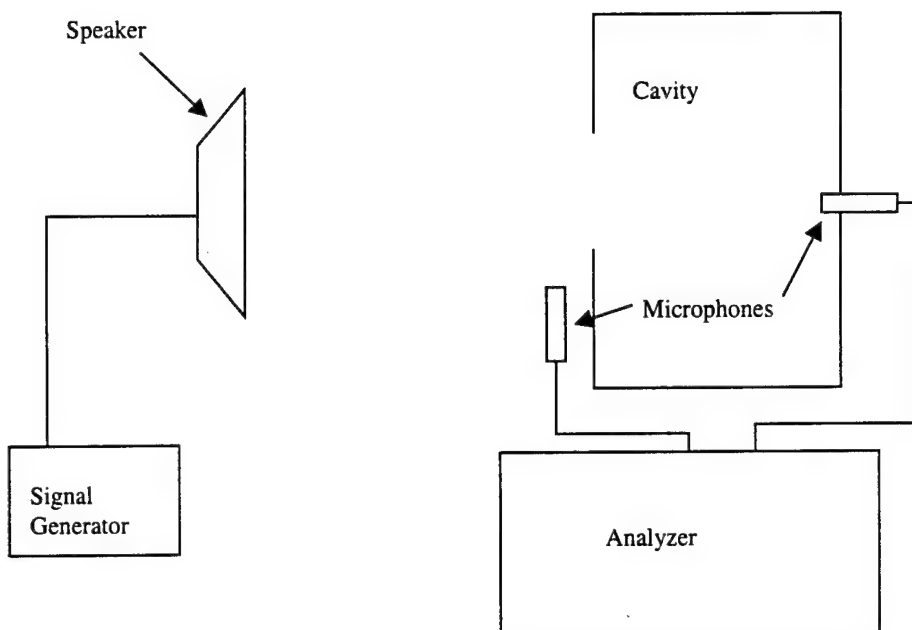


Figure 3.1: Schematic of arrangement for measuring cavity response to acoustic excitation

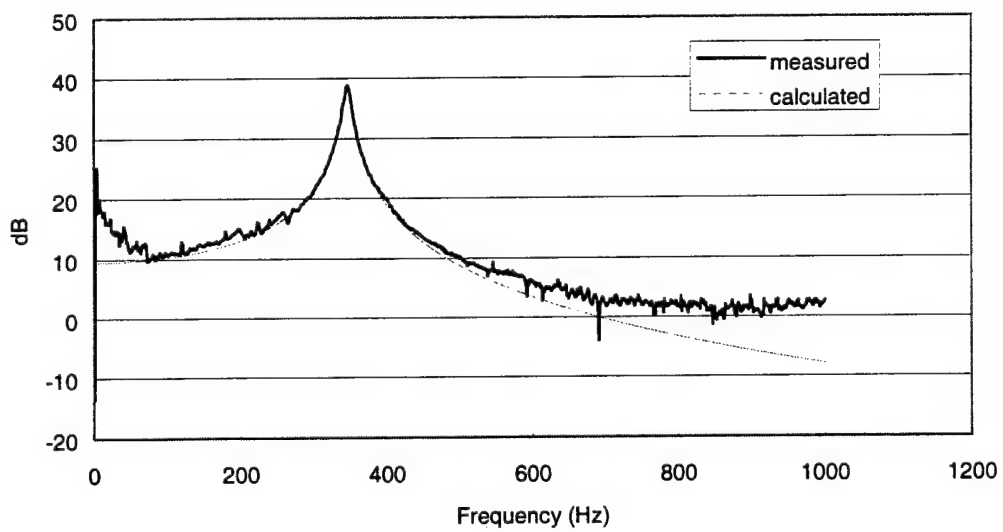


Figure 3.2: Frequency response of cavity with  $L=1"$  and  $d=5.5"$

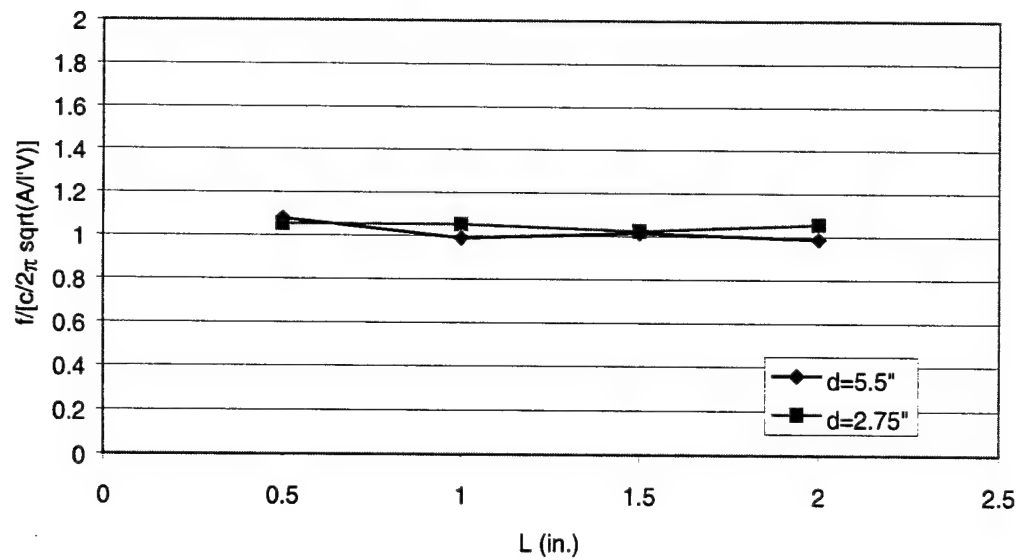


Figure 3.3: Measured Helmholtz resonance frequency normalized by calculated Helmholtz resonance frequency

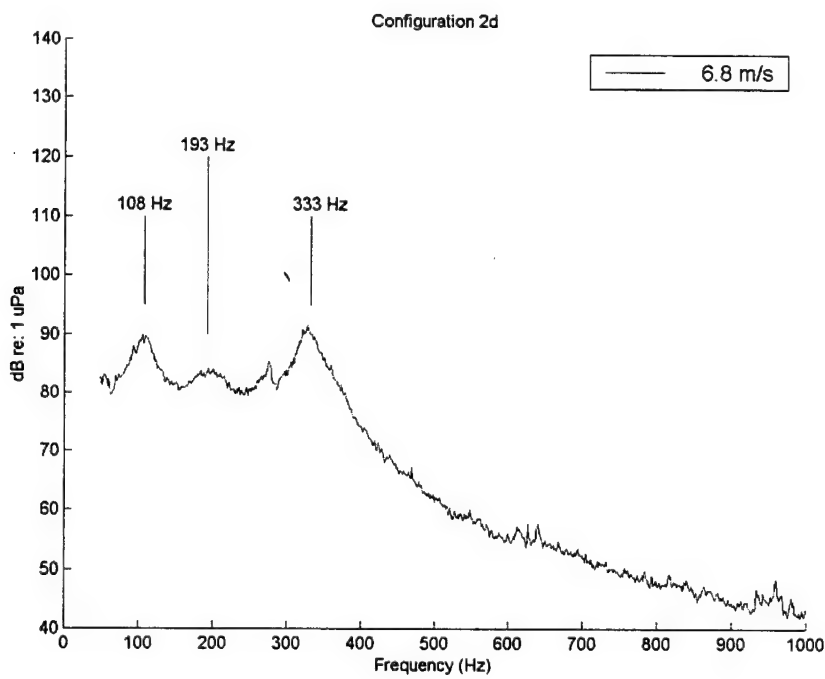


Figure 3.4: Cavity pressure spectrum at 6.8 m/s with L=1", d=5.5"

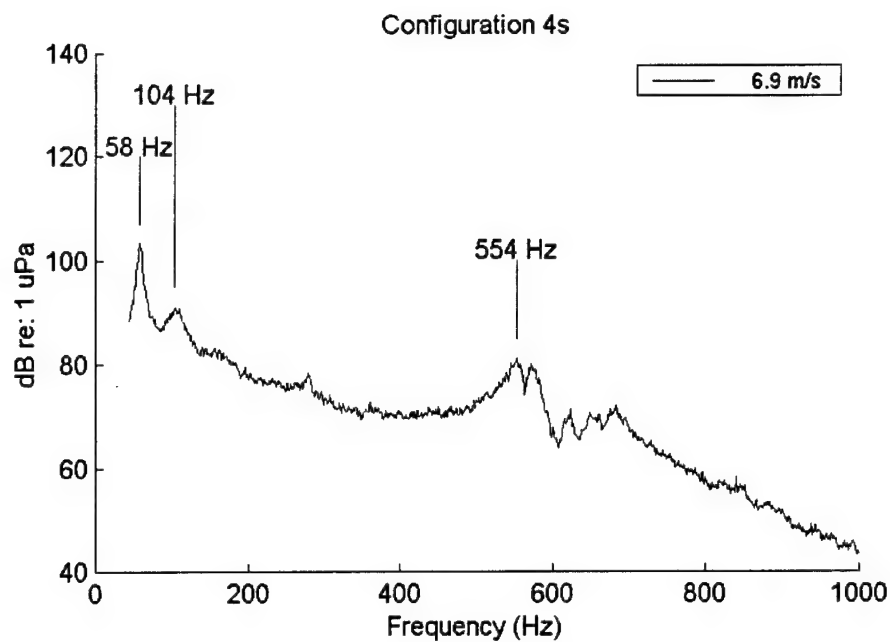


Figure 3.5: Cavity pressure spectrum at 6.9 m/s with  $L=2"$ ,  $d=2.75"$

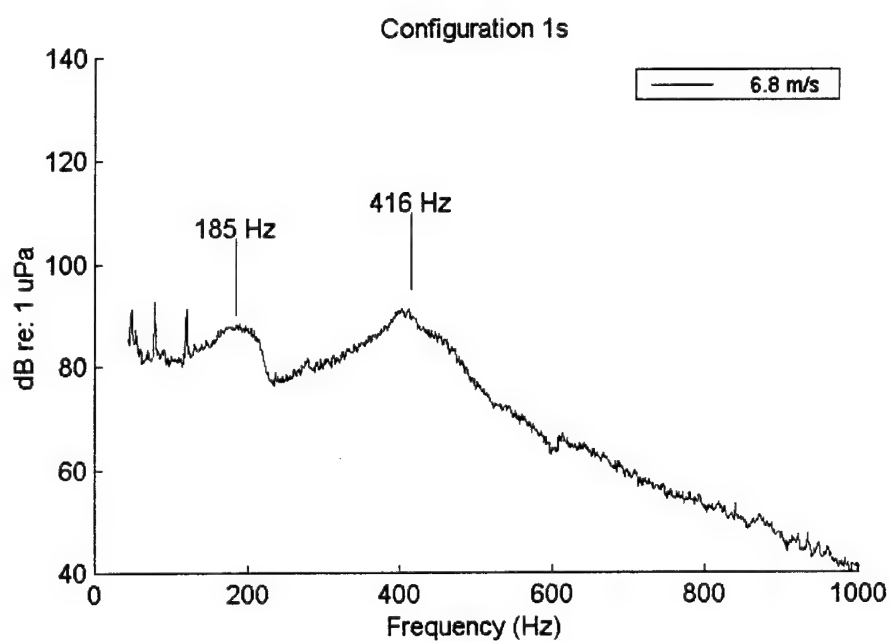


Figure 3.6: Cavity pressure spectrum at 6.8 m/s with  $L=0.5"$ ,  $d=2.75"$

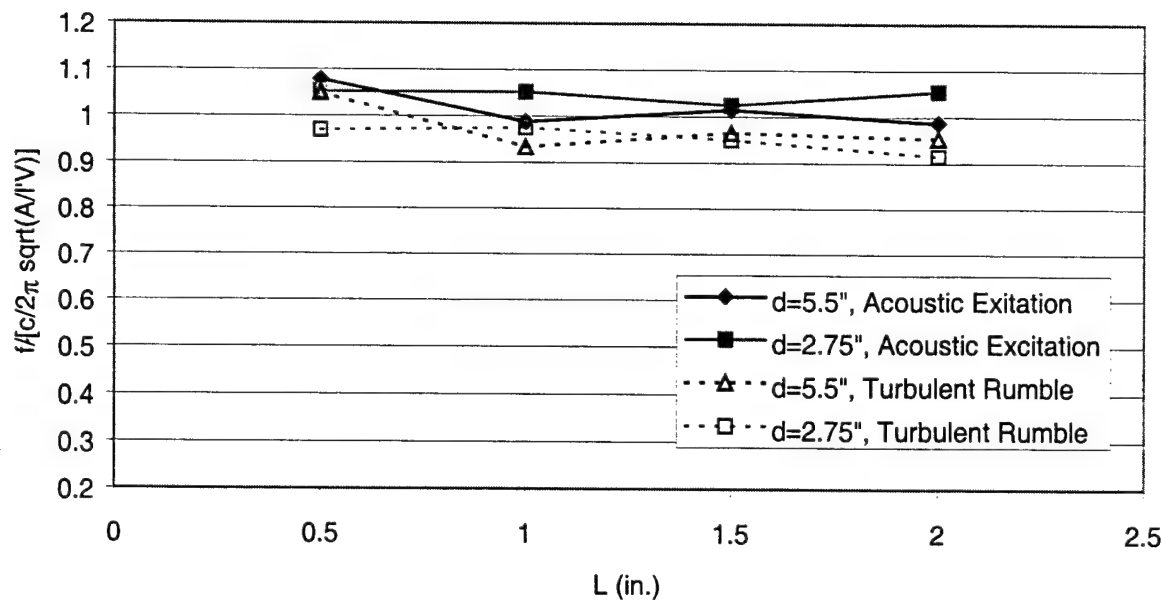


Figure 3.7: Comparison of Helmholtz frequency due to acoustic excitation and turbulent rumble as a function of cavity geometry

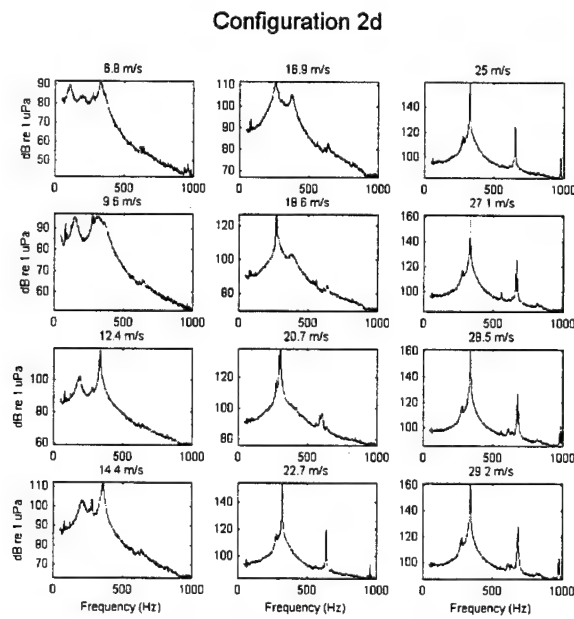


Figure 3.8: Cavity pressure spectra at 12 speeds for  $L=1"$ ,  $d=5.5"$

### Configuration 4s

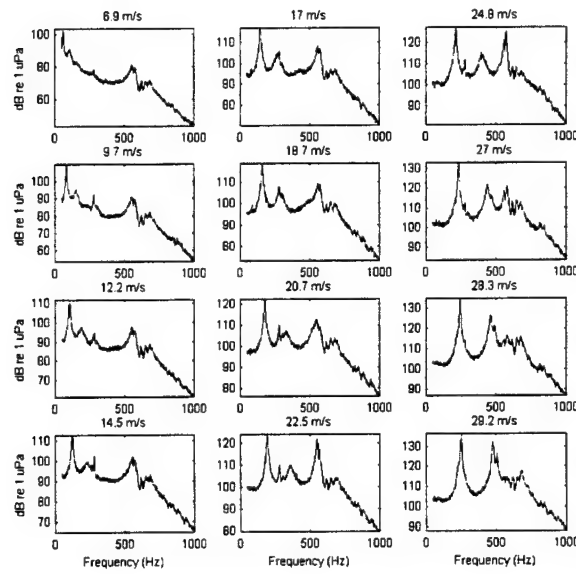


Figure 3.9: Cavity pressure spectra at 12 speeds for  $L=2"$ ,  $d=2.75"$

### Configuration 1s

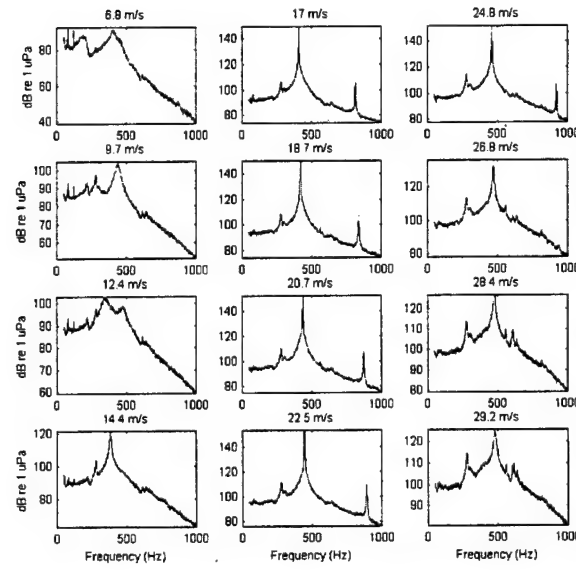


Figure 3.10: Cavity pressure spectra at 12 speeds for  $L=0.5"$ ,  $d=2.75"$

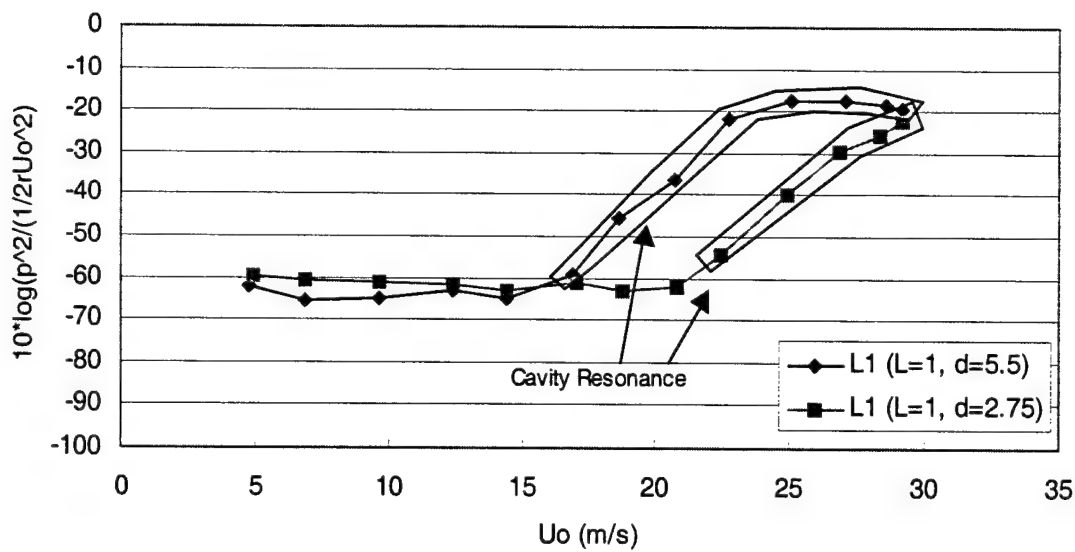


Figure 3.11: Comparison of normalized level of first speed dependent tone for deep and shallow cavities as a function of speed for  $L=1"$

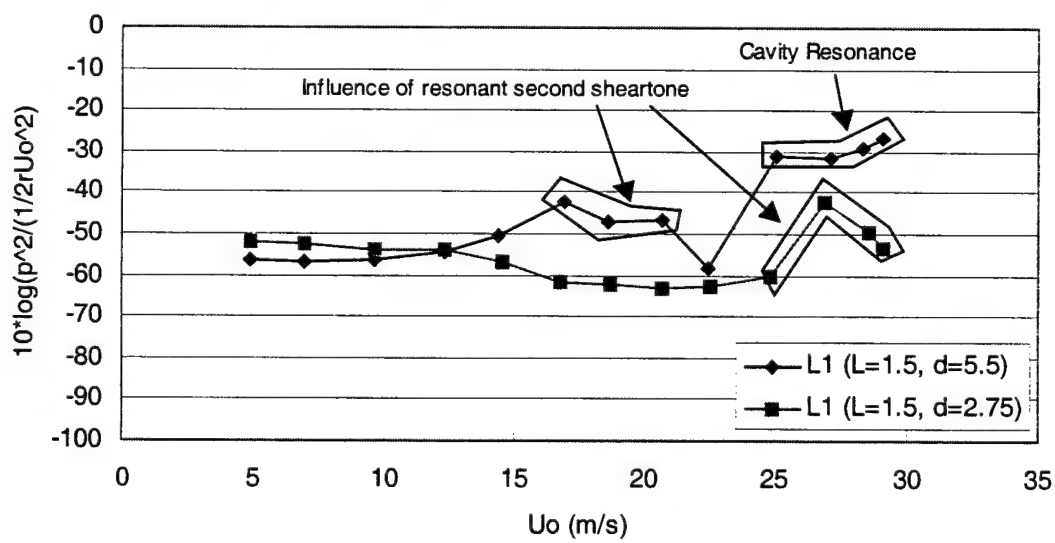


Figure 3.12: Comparison of normalized level of first speed dependent tone for deep and shallow cavities as a function of speed for  $L=1.5"$

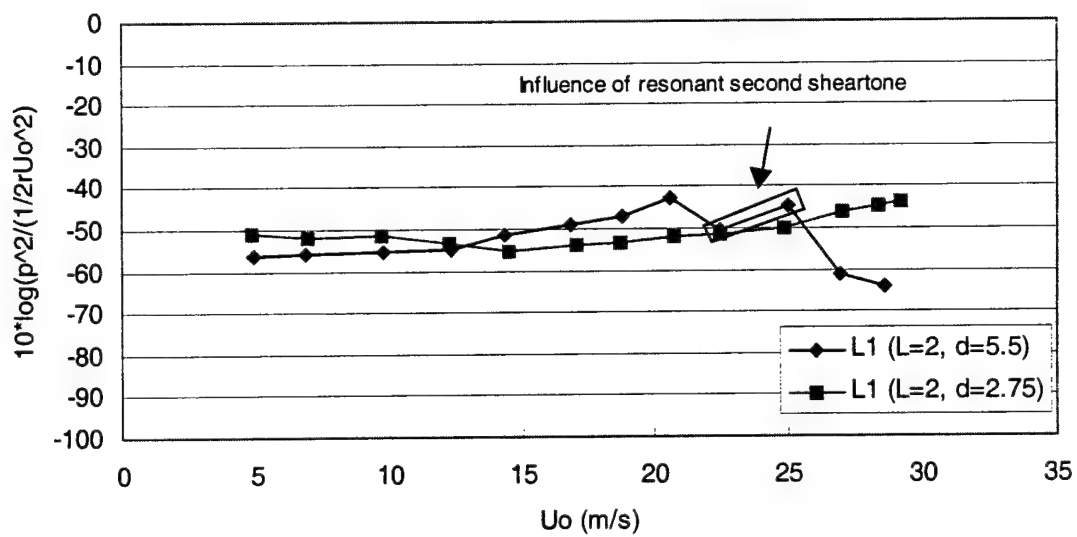


Figure 3.13: Comparison of normalized level of first speed dependent tone for deep and shallow cavities as a function of speed for  $L=2"$

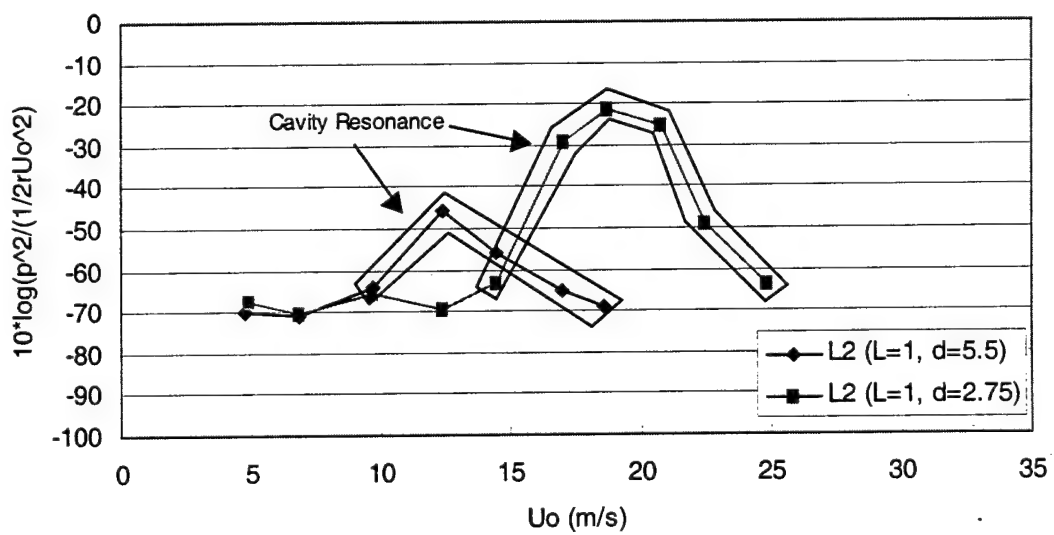


Figure 3.14: Comparison of normalized level of second speed dependent tone for deep and shallow cavities as a function of speed for  $L=1"$

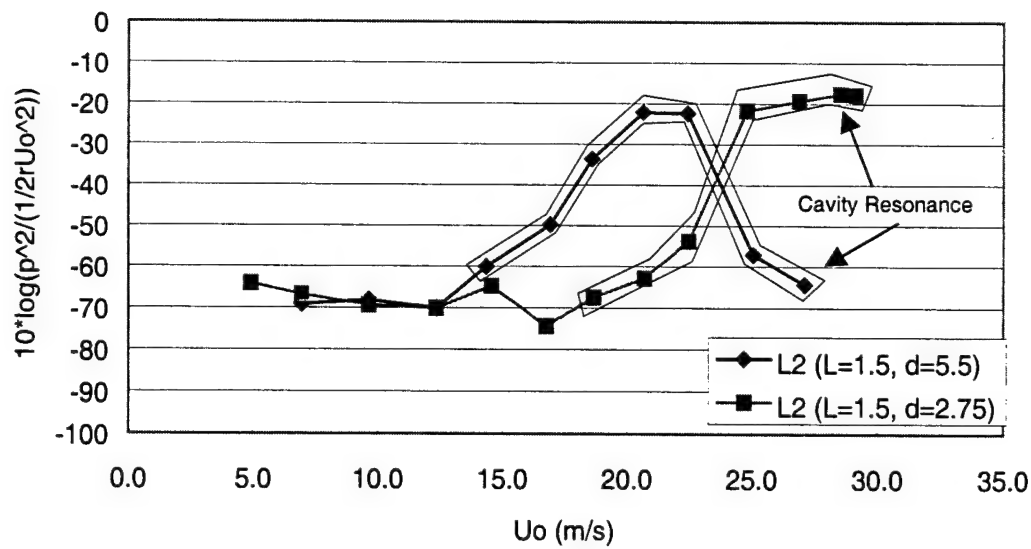


Figure 3.15: Comparison of normalized level of second speed dependent tone for deep and shallow cavities as a function of speed for  $L=1.5"$

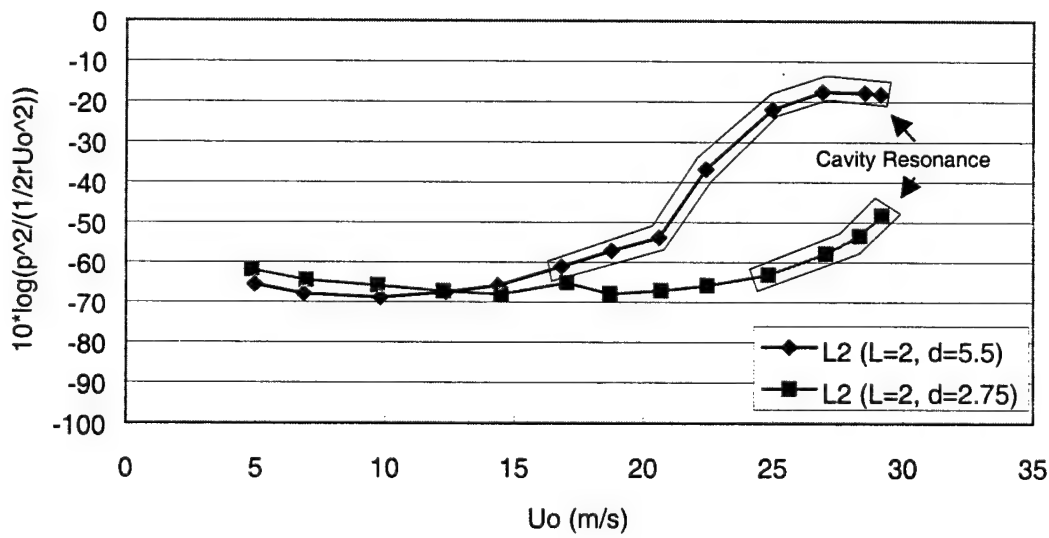


Figure 3.16: Comparison of normalized level of second speed dependent tone for deep and shallow cavities as a function of speed for  $L=2"$

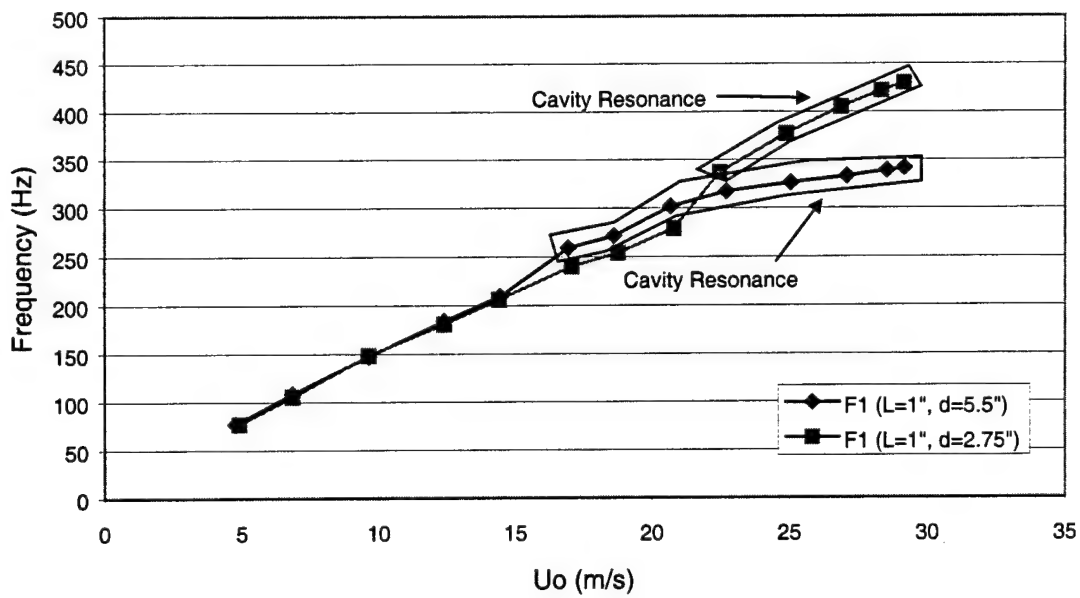


Figure 3.17: Comparison of frequency of first speed dependent tone for deep and shallow cavities as a function of speed for  $L=1"$

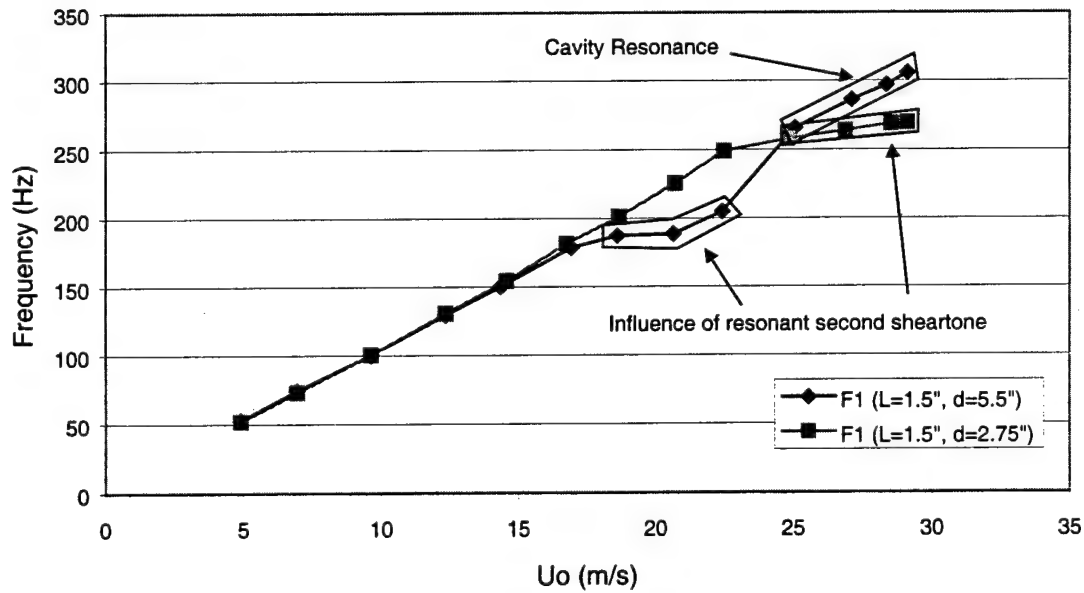


Figure 3.18: Comparison of frequency of first speed dependent tone for deep and shallow cavities as a function of speed for  $L=1.5"$

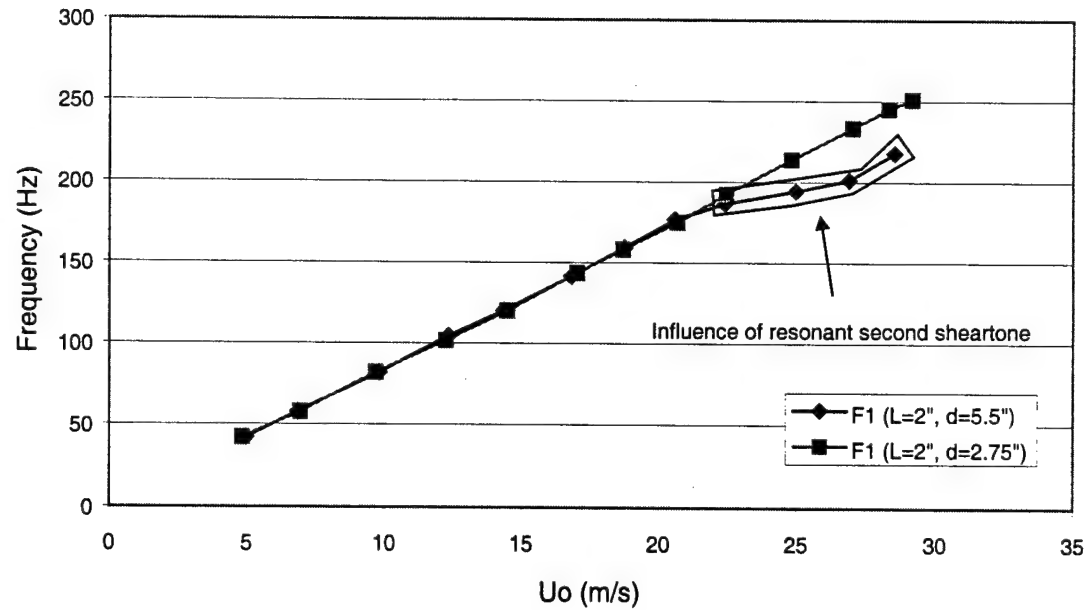


Figure 3.19: Comparison of frequency of first speed dependent tone for deep and shallow cavities as a function of speed for  $L=2"$

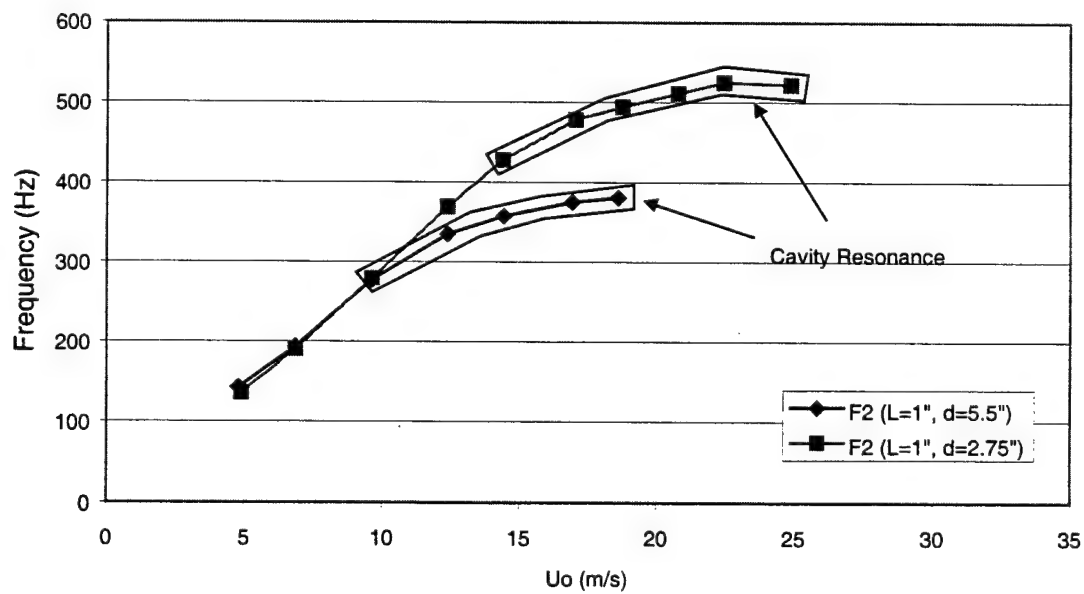


Figure 3.20: Comparison of frequency of second speed dependent tone for deep and shallow cavities as a function of speed for  $L=1"$

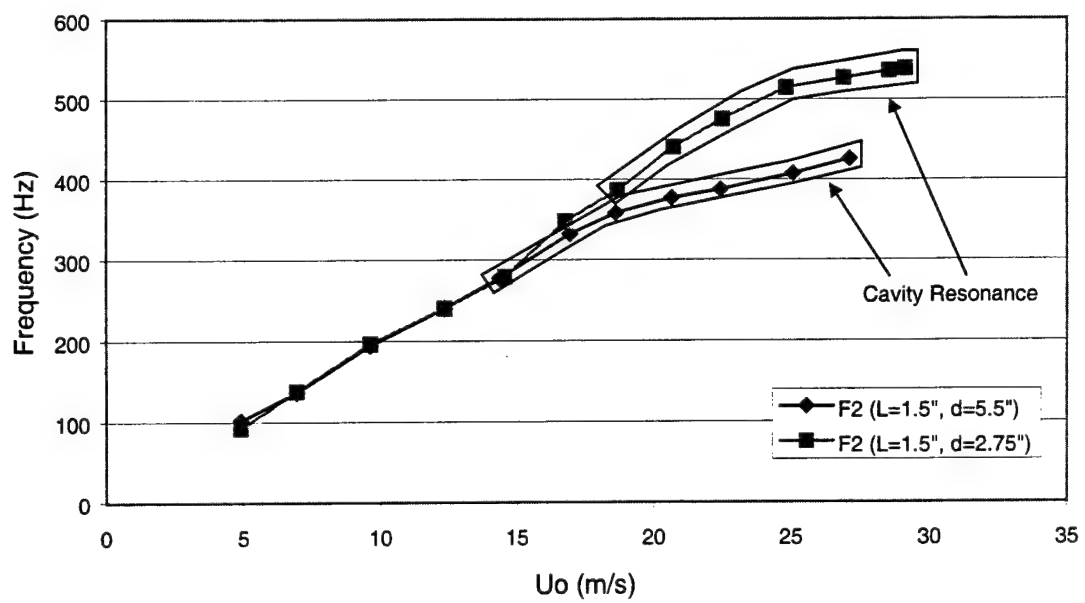


Figure 3.21: Comparison of frequency of second speed dependent tone for deep and shallow cavities as a function of speed for  $L=1.5"$

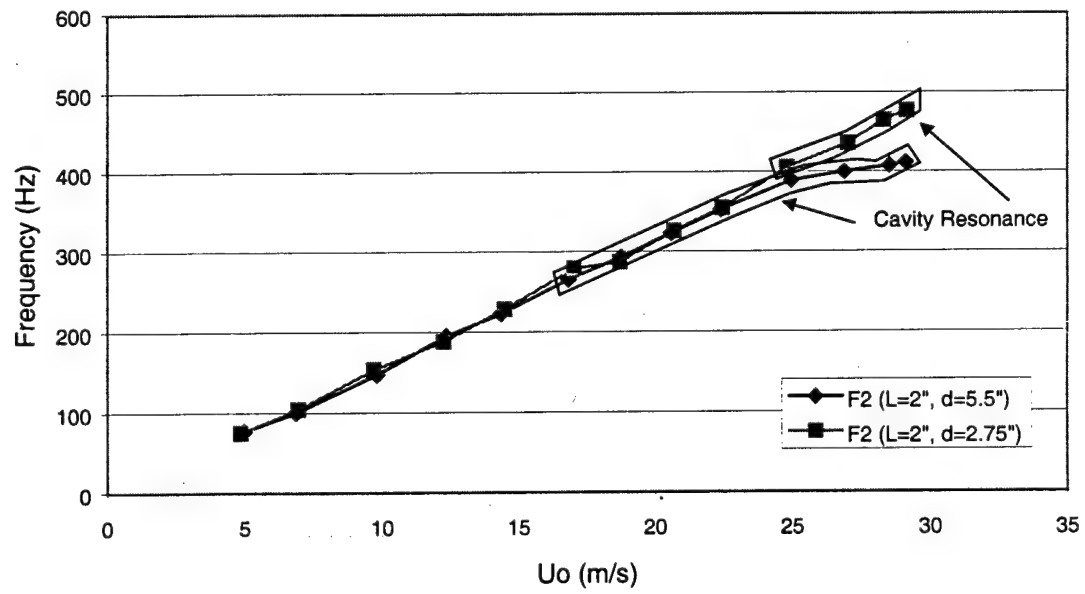


Figure 3.22: Comparison of frequency of second speed dependent tone for deep and shallow cavities as a function of speed for  $L=2"$

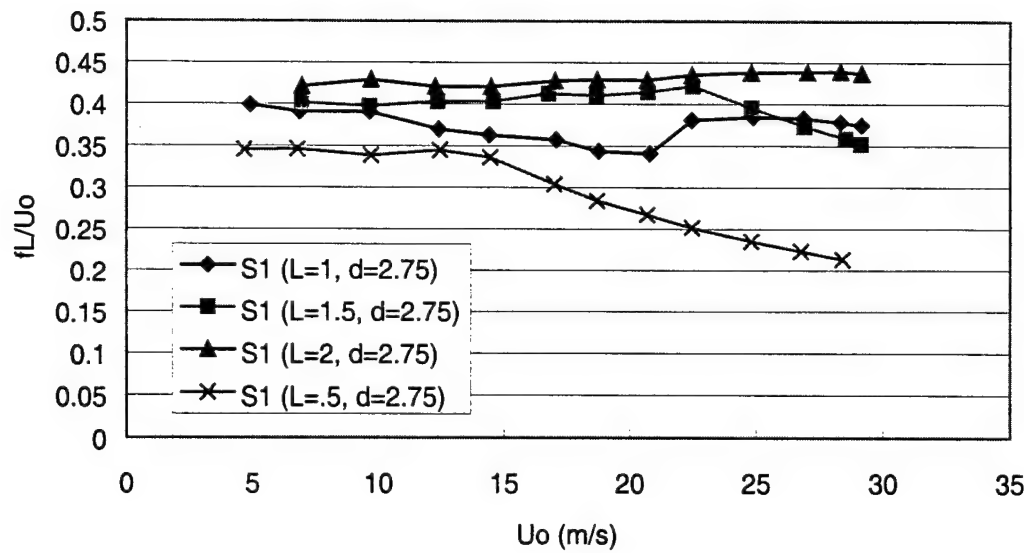


Figure 3.23: Comparison of Strouhal number of first speed dependent tone at all values of  $L$  for  $d=2.75"$

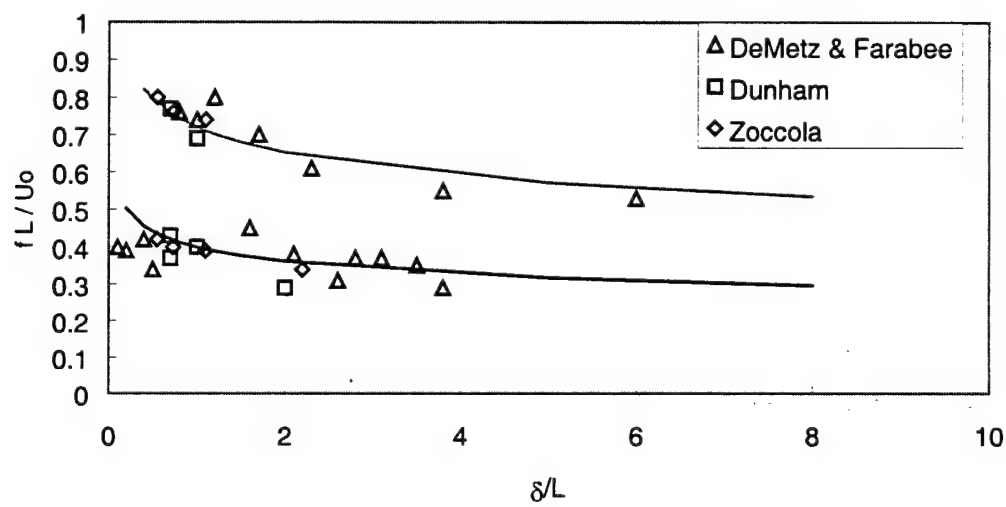


Figure 3.24: Strouhal number of speed dependent tones just prior to resonance as a function of  $\delta/L$

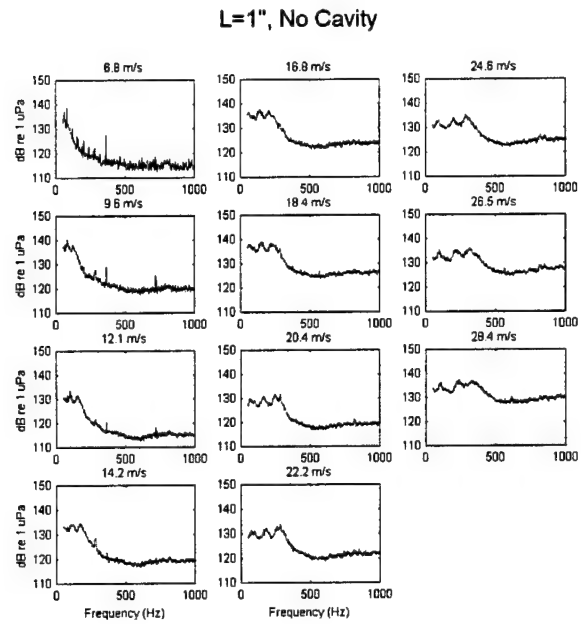


Figure 3.25: Cavity pressure spectra at 11 speeds for L=1", no cavity

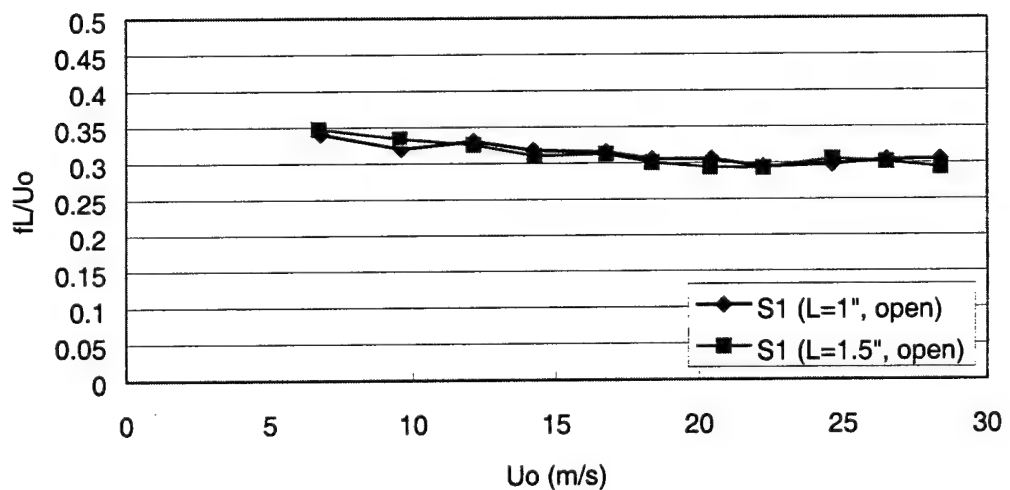


Figure 3.26: Comparison of Strouhal number of first speed dependent tone for L=1" and L=1.5" with no cavity as a function of speed

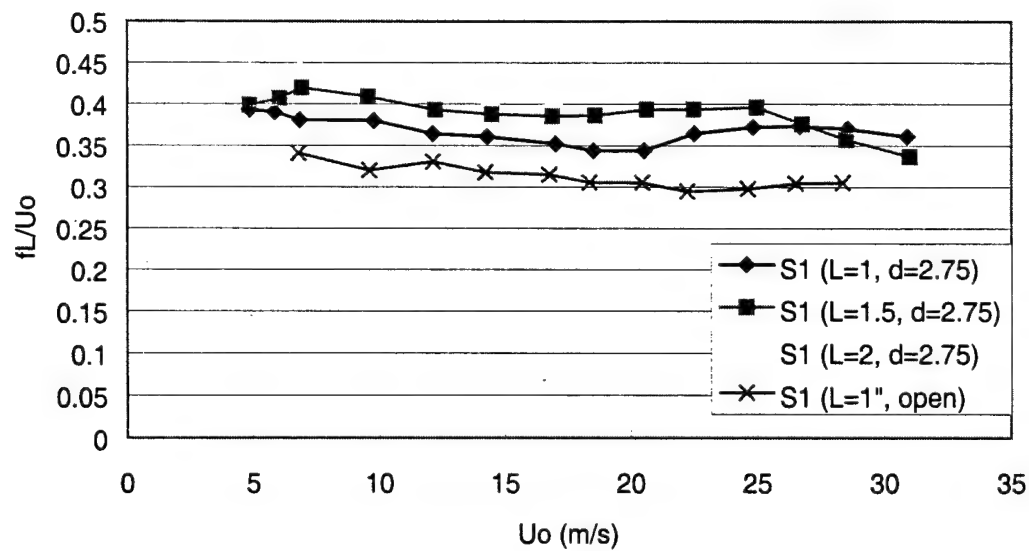


Figure 3.27: Comparison of Strouhal number of first speed dependent tones with and without cavity as a function of speed

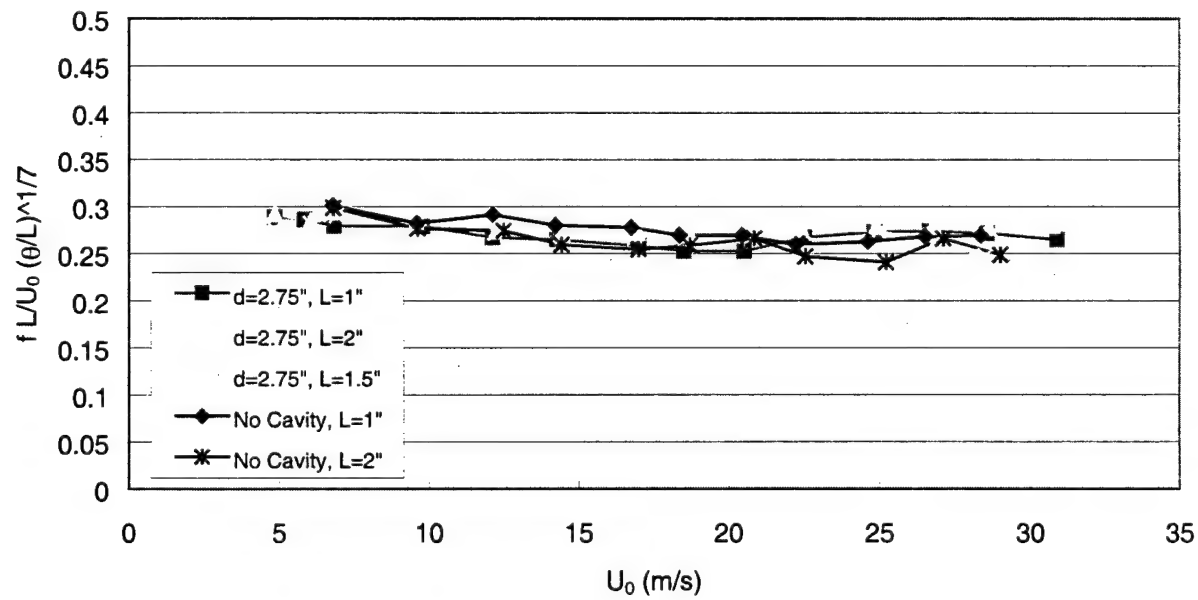


Figure 3.28: Comparison of  $fL/Uo(\theta/L)^{1/7}$  of first speed dependent tone for various values of  $L$  with and without cavity as a function of speed

## 4. Velocity and Cavity Pressure Correlations

Cavity pressure and u and v components of velocity were recorded simultaneously at 288 different locations in the cavity flow field for each of 3 speeds. Table 4.1 is a listing of locations at which the measurements were obtained. The origin is taken to be on the flow surface at the upstream edge of the cavity. The x coordinate is increasing along the flow direction. The y coordinate is increasing normal to the flow surface. For all of these locations, the probe was located at the mid-span of the cavity opening.

Note that about half of these locations are below the cavity opening, and some of these are very near the upstream edge, where little mean flow would be expected. Measurements made with an x-wire probe generally require mean flow in order to be valid. For the ThermalPro software, this translates to a requirement that the direction of the fluid velocity vector be less than 45 degrees from the direction of the presumed mean flow. When the direction of the flow vector is not sufficiently less than 45 degrees, the ThermalPro software cannot resolve the values of the velocity components. In this case, it returns a value of -1 for u, the component of velocity in the x direction, and 0 for v, the component in the y direction. Therefore, the presence of sufficient mean flow may be established by calculating the percentage of records where u is greater than zero for each measurement location. It was found that at all speeds and at most locations, the percentage was greater than 99%. (Note that regardless of the mean flow speed, turbulent velocity fluctuations may combine to make the effective flow direction at a given instant approach 45 degrees from the freestream flow direction, resulting in a value of -1 for u.) The region just below the upstream edge showed a lower percentage, but was still generally better than 90%. The presence of sufficient mean flow below the cavity opening is attributed to mean flow circulation within the cavity. These results establish that, while flow in the region just below the upstream edge of the opening, and in some other regions under certain flow conditions, were not ideal for x-wire measurements, data measured at most locations are significant and are used to indicate actual flow conditions.

Table 4.1 X-Probe Measurement Locations

x locations (in.)	0.085	0.135	0.0185	0.235	0.285	0.335	0.385	0.435	0.485	0.535	0.585	0.635	0.685	0.735	0.785	0.835	0.885	0.935
y locations (in.)	0.535	0.375	0.255	0.175	0.115	0.075	0.035	-0.005	-0.045	-0.085	-0.125	-0.165	-0.225	-0.285	-0.365	-0.465		

The cavity used to make the measurements reported in this chapter was configuration 2d ( $L=1"$  and  $d=5.5"$ ). This configuration was chosen because it has a low Helmholtz resonance frequency, which allows all of the types of sheartone behavior discussed in Chapter 3 to be observed over the speed range of the tunnel. At low speeds, non-resonant first and second sheartones are observed. At high speeds, the first sheartone is resonant. And in the middle of the speed range, the second sheartone is resonant while the first sheartone is observable and non-resonant.

Data reported in this chapter were obtained for three speeds:

- 30 m/s, where the first sheartone is resonant
- 13 m/s, where the second sheartone is resonant and the first is not
- 6.9 m/s, where both sheartones are non-resonant

In section 1, the mean and fluctuating velocity data are presented. In section 2, frequency spectra of the velocity and pressure fields are discussed. And in section 3, the correlations between the velocity components and the pressure are discussed.

## 4.1 Velocity Field Profiles

Profiles of  $\bar{u}$ , the normalized mean velocity in the x direction, at  $x=0.135"$ ,  $x=0.485"$ , and  $x=0.885"$  for all three speeds are shown in figure 4.1. The profiles at  $x=0.085"$  are compared in figure 4.2 to the onset boundary layer profile measured 0.1" upstream of the cavity opening. They are similar above the opening, and near zero below the opening. Note, however, that for the high speed, the mean velocity below the opening, while very small, is noticeably higher than that of the other two speeds. This suggests the presence of mean circulation within the cavity caused by flow at 30 m/s, but apparently not at the lower speeds. Also, note that at  $x=0.485$  and  $x=0.885$ , the mean velocity below the opening is significantly higher for the high speed.

In figure 4.3, profiles of  $\bar{u}$  for the three speeds measured at  $x=0.935"$  are compared to a hyperbolic tangent profile. This profile was used by Michalke in his analysis of shear layer instability. Variations between the measured profiles and the hyperbolic tangent profile exist because the profile was intended to model an unbounded flow with no downstream reattachment.

Profiles of  $u_{rms}$  at  $x=0.135"$ ,  $x=0.485"$ , and  $x=0.885"$  are shown in figures 4.4. These profiles are rather dissimilar among the speeds. Speed comparisons of  $v_{rms}$  at the same three locations are shown in figure 4.5. At the two most downstream locations it is noted that the profile of the highest speed is distinctly different from the two lower speeds, which are very similar. Profiles of the Reynolds stress coefficient,  $-\langle uv \rangle$ , at the same  $x$ -locations are shown in figure 4.6. At  $x=0.135"$ , and  $x=0.485"$ , the two lower speeds have very similar profiles, while the high speed shows a very sharp peak with a value more than twice that of the lower speeds. At  $x=0.885"$ , the peak values of the highest and lowest speed are noticeably higher than that of the middle speed.

Care must be taken in interpreting the profiles of fluctuating velocity components, since we have seen in Chapter 3 that the pressure spectra are generally dominated by a small number of distinct tones in the spectrum. And as we shall see, this is also true in some instances for the velocity spectra. This is particularly true at the resonant speed condition of 30 m/s. Nonetheless, comparisons of the profiles of rms velocities and of Reynolds stress coefficient are instructive. The  $u_{rms}$  and the Reynolds stress profiles near the upstream edge show a strong, narrow peak near  $y=0"$  for the 30 m/s case that is not present for the two lower speeds. The comparison of Reynolds stress among the three speeds seems to show that they would otherwise have a similar shape except for that peak. This suggests that the vortex formation process begins further upstream at 30 m/s, where there is a strongly excited cavity resonance, than it does at the other speeds.

There are also significant differences near the downstream edge between the 30 m/s profile and the profiles of the two lower speeds. In the  $u_{rms}$  profiles, the peak value occurs at a higher value of  $y$  for the 30 m/s case. And in the Reynolds stress comparison, the profile is split into twin peaks. Again, this suggests a different physical process occurring near the downstream edge when a strongly excited cavity resonance is present.

Overall, it is clear that the velocity field at 30 m/s, where there is a fully resonant first sheartone, is distinctly different than the velocity fields at 13 m/s, where the second sheartone is resonant and the first is not, and 6.9 m/s, where the first and second sheartones are non-resonant. This illustrates the ways in which the differences between the physical processes governing a resonant cavity tone and those governing a non-resonant sheartone are observable in the fluctuating velocity field of the cavity opening. It also suggests that the physical processes for the resonant second sheartones are fundamentally different from those of a resonant first sheartone in some fundamental way. This issue will be explored further in Chapter 5.

## 4.2 Velocity and Pressure Spectra

### 4.2.1 Pressure Spectra

Spectra of cavity pressure fluctuations at various speeds and cavity configurations were shown and discussed in the previous chapter. Pressure spectra shown here are consistent with these results and are repeated in this chapter so that the velocity spectrum calculations may be properly interpreted. Figures 4.7, 4.8 and 4.9 are plots of spectra for 30 m/s, 13 m/s and 6.9 m/s, respectively. As previously stated, these three speeds correspond to the conditions where the first sheartone is resonant, the second sheartone is resonant, and both sheartones are non-resonant, respectively.

The spectrum at 30 m/s is dominated by the cavity resonance at 331 Hz. The second and third harmonics of this resonance at 662 Hz and 993 Hz are also observed. It should be noted that these harmonics are the result of the non-sinusoidal nature of the waveform at 331 Hz and should not be confused with second or third sheartones. At 280 Hz, the standing wave resonance of the tunnel can be seen as well.

At 13 m/s, the cavity resonance is seen at 345 Hz and is excited by the second sheartone rather than the first, as was the case at 30 m/s. The first sheartone is seen here as a somewhat broader peak at about 191 Hz.

At 6.9 m/s, the cavity does not resonate. The first sheartone is seen at about 111 Hz and is somewhat narrower than the first sheartone observed at 13 m/s. The second sheartone is

seen at 207 Hz. This tone is noticeably broader than the first sheartone. It is likely that this peak would not be identified as a tone if its behavior as a function of speed as discussed in Chapter 3 had not been observed. The cavity is weakly excited by the TBL at 333Hz.

#### 4.2.2 Velocity Spectra

Spectra of the u and v components of velocity are plotted in figure 4.10 for 30 m/s at locations of ( $x=0.335"$ ,  $y=-0.085$ ) and ( $x=0.735"$ ,  $y=-0.085$ ). The 331 Hz cavity resonance caused by the first sheartone is seen in the u and v spectra at all locations as a very narrow tone at least 15 dB above the continuum. The level of the tone is higher downstream at ( $x=0.735"$ ,  $y=-0.085$ ). The second harmonic is present at both locations. The third harmonic is not present upstream at ( $x=0.335"$ ,  $y=-0.085$ ) but is downstream at ( $x=0.735"$ ,  $y=-0.085$ ).

Spectra of the u and v components of velocity are plotted in figure 4.11 for 13 m/s at the same x locations ( $x=0.335"$ ,  $y=-0.085$  and  $x=0.735"$ ,  $y=-0.085$ ). The 345 Hz cavity resonant tone caused by the second sheartone is seen in the v spectrum as a small peak at both x locations. In the u spectra it was seen only at the upstream location. Note that the fact that the tone is not present at a particular location is attributed not to its absence, but to the fact that its level is below that of the broadband part of the signal. The first sheartone at 191 Hz is barely observable in the v spectrum at  $x=0.735"$ .

Spectra of the u and v components of velocity are plotted in figure 4.12 for 6.9 m/s at the same x locations used previously ( $x=0.335"$ ,  $y=-0.085$  and  $x=0.735"$ ,  $y=-0.085$ ). At  $x=0.735"$ , the first sheartone is barely observable in the v spectrum. For all other spectra in figure 4.12, the sheartones are not observable in the velocity spectra. As with 13 m/s, this is attributed to the fact that its level is below that of the broadband part of the signal. While the presence of the sheartones in the individual velocity spectra is not demonstrated by these figures, they are known to be present in the velocity signals by virtue of their presence in the coherence functions between the velocity signal and the pressure signal. This feature will be discussed in a later section.

#### 4.2.3 Velocity Peak Profiles

Higher order harmonics were observed in the velocity spectra only for the resonant first sheartone at 30 m/s. An examination of the spatial variation of the levels of the second and third harmonics for this condition may be helpful in understanding the dynamic processes governing the resonant condition.

The absence of any harmonics means that a signal is purely sinusoidal, while increasing levels of increasing numbers of harmonics mean an increasingly non-sinusoidal wave form. To study the varying levels of the harmonics, including the first, it is preferable to look at the velocity peak profiles. To generate these profiles, the levels of the cavity tone from the velocity spectra at the frequency corresponding to the peak in the pressure spectra are plotted as a series of y profiles at each x location. The velocity peak profiles for the first harmonic of the resonant first sheartone at 30 m/s are shown in figures 4.13. The peak profiles for the second and third harmonics are shown in figures 4.14 and 4.15, respectively.

In contrast to the first harmonic, which, in the u spectrum, has a high peak value right from the upstream edge that decreases slightly as the downstream edge is approached, the second and third harmonics have no peak near the upstream edge. A peak does develop and grow, however, as the middle of the aperture is approached. Also, the "twin peaks" character of the profile that was seen in the fluctuating velocity profiles is seen here, particularly in the third harmonic. Similar behavior is observed in the v spectra of the second and third harmonics.

It may be said, then, that the velocity fluctuations are nearly sinusoidal near the upstream edge, and then become increasingly non-sinusoidal approaching the mid-point of the aperture. This observation may be attributed to the vortex formation process. It is significant that this non-sinusoidal behavior is observed only for the resonant first sheartone. This reinforces the observation made in section 4.1, where it was noted that the fluctuating velocity profiles for the resonant first sheartone at 30 m/s were distinctly different from the resonant second sheartone and the non-resonant first sheartone at 13 m/s.

## 4.3 Velocity-Pressure Correlation

The coherence and the phase of the cross spectra between the cavity pressure  $p$ , and the  $u$  and  $v$  velocity components, are useful in understanding the downstream behavior of the vortex in the cavity opening. In section 4.3.1, the coherence spectra at two representative locations are discussed. In section 4.3.2, the behavior of the phase at the frequencies of the sheartones as a function of space is discussed for an idealized case of a vortex convected along a cavity opening. This is done in order that the measurements made on a real cavity may be understood. These measurements, shown in section 4.3.3, show the spatial variation of phase at a single frequency – the frequency corresponding to the resonant and non-resonant sheartones – for each of several flow speeds. Finally, in section 4.3.4, a convection velocity, calculated from the spatial distribution of the phase, is presented and discussed.

### 4.3.1 Coherence

In order to be certain that we may use a phase value of the cross spectrum at a single frequency, we must first determine that the coherence is high enough for the phase to have acceptable statistical error. For the data shown here, 256 averages were used in calculating the cross spectra. Using the equation given by Bendat and Piersol (1980), for 256 averages and a coherence of 0.1, the standard deviation of the phase due to random error in the data is 7.6 degrees. This level of error is considered acceptable. Also, it is noted that the standard deviation of the phase is inversely proportional to the square root of the coherence. Therefore, measurements with higher coherence have lower error bounds.

Coherence between the vertical velocity component and pressure ( $v-p$ ) is shown in figure 4.16 for 30, 13, and 6.9 m/s at two locations ( $x=0.335, y=-.085$ ) and ( $x=0.735, y=-.085$ ). The measurements at these locations are generally representative of the results at other locations. For 30 m/s, coherence is approximately 1 at the cavity tone frequency of 331 Hz. The second harmonic is seen with a coherence greater than 0.9 at both the upstream and the downstream location. The third harmonic has coherence greater than 0.8 downstream, but is not seen at the upstream location.

At 13 m/s, the 345 Hz tone and the 191 Hz tone exhibit significant coherence at both locations. Coherence for the 345 Hz tone has a peak value of about 0.5 at both locations. The 191 Hz tone has a coherence of about 0.25. The 191 Hz tone is generally broader in frequency than the 345 Hz tone. No harmonics of either tone are observed.

The 111 Hz tone at 6.9 m/s has a coherence of about 0.25 at both locations. It is similar in both maximum coherence level and in frequency width to the 191 Hz tone at 13 m/s. The 207 Hz tone is just detectable in the coherence spectrum at the upstream location. At the downstream location, it is not discernable in the spectrum.

The coherence between the streamwise velocity component and the pressure (u-p) are shown in figure 4.17 for 30, 13, and 6.9 m/s and at locations ( $x=0.335, y=-0.085$ ) and ( $x=0.735, y=-0.085$ ). The spectra for 30 m/s are essentially the same as for the v-p spectra: high coherence at the 331 Hz cavity resonance frequency and second harmonic at both locations, and high coherence for the third harmonic at the downstream location only.

At 13 m/s, the coherence is lower for the u-p spectra than for the v-p spectra. The 345 Hz tone has significant coherence at the upstream location, but has much lower coherence at the downstream location. The 191 Hz tone appears only as a broad region of low coherence distinguishable only because at most other frequencies it is lower still. The tone is effectively not discernible.

Likewise, both tones in the 6.9 m/s spectra are lower in the u-p spectra than in the v-p spectra. The 111 Hz tone is discernible at the downstream location. At the upstream location it is much like the 191 Hz tone at 13 m/s – if you weren't looking for it, you wouldn't see it. The 207 Hz tone is not discernible.

In summary, we can say that the coherence in the v-p spectra at 30 and 13 m/s are high enough to provide error bounds satisfactory for confidence in the phase data. This is also true for the 111 Hz tone at 6.9 m/s. The u-p spectra also have sufficient coherence for 30 Hz and for the 345 Hz tone at 13 m/s. In other cases, coherence is low and the error should be evaluated on a case by case basis.

### 4.3.2 Description Of Idealized Spatial Distribution Of Phase

The spatial distribution of phase relationships in the neck of the cavity opening can be understood by considering an idealized model based on the observations of Nelson, et al. First consider a vortex with solid body rotation moving along a straight line at a constant speed. Examine the values of  $u$  and  $v$  that would be measured by an  $x$  probe slightly above the vortex path as the vortex passes the probe. This is illustrated in figure 4.18. At time 1, with the vortex somewhat upstream of the probe, the  $u$  velocity is positive and increasing, while the  $v$  velocity is negative with decreasing amplitude. At time 2, when the vortex has moved to directly below the probe, the  $u$  velocity has its maximum value, and the  $v$  velocity is now zero. After the vortex has moved downstream of the probe at time 3, the  $u$  velocity is now decreasing and the  $v$  velocity is now positive and increasing.

This means that the  $u$  velocity measured at a probe will be at its maximum when the vortex is directly beneath the probe, and that the  $v$  velocity will be crossing zero with positive slope at the same time. Now use this knowledge to see what this says about a vortex in a cavity opening.

Nelson et al. observed that the time for a vortex to travel the length of the cavity opening is approximately one period of the cavity pressure oscillation. They also observed that when the vortex is initially formed at  $x=0$ , the pressure in the cavity is at a minimum. The phase between the  $u$  and  $v$  velocity components and the cavity pressure can then be determined by considering velocity measurements made at various streamwise location over one period, starting when the cavity pressure is at a minimum.

In figure 4.19, the cavity pressure,  $u$  velocity, and  $v$  velocity are plotted for 5 streamwise locations of the  $x$  probe. The vortex is assumed to travel along a straight line at a constant speed. The probe is assumed to be just above the vortex path. At all 5 locations the pressure is sinusoidal with the minimum value occurring at  $t=0$ . Thus a time interval of one period plotted along the horizontal axis corresponds to the position of the vortex, located at  $x=0$  at  $t=0$ , and at  $x=L$  at  $t=1$ .

From the above consideration of velocity measured by the probe, we know that the  $u$  velocity is a maximum when the vortex center is at the probe location and the  $v$  velocity is

zero and increasing at the same time. If we assume, as is reasonable based on the work of Nelson, that the velocity signals are sinusoidal, we can plot the velocity signals with the proper phase based on the probe location. In figure 4.19, the horizontal position corresponding to the probe location is indicated by the vertical dotted line. We know from above that the maximum value of  $u$  and the positive sloped zero crossing of  $v$  should be at the same  $x$  location as the probe, and we use this to plot the velocity signals with the proper phase. The values of the phase between the quantities are then obtained by comparing the plots.

We see that the phase  $u-p$  and  $v-p$  are increasing with time (and streamwise distance,  $x$ ), but are 90 degrees out of phase with each other. If, as assumed here, the speed of the vortex is constant, the increase is linear. The phase goes through a complete 360 cycle along the length of the opening. If the probe is located below the path of the vortex, it can be seen that the phase  $u-p$  would change by 180 degrees. This idealized understanding of the spatial distribution of phase will be compared to measurements in the next section.

#### 4.3.3 Spatial Plots of Coherence and Phase

In this section, plots of the spatial distribution of the correlation properties between the quantities extracted from the data are shown. The coherence and phase for those frequencies corresponding to the tones observed in the pressure spectra are plotted spatially in the  $xy$  plane of the cavity opening. The coherence plots are shown in order to establish the acceptability of the measured phase. The trends of how the phase varies spatially are compared to those predicted in the previous section. This comparison attempts to establish the vortex nature of the flow field in the cavity opening. The phase variation may then be used to calculate the convection speed of the vortex. A comparison between the measured and predicted values of the phase will also help in establishing the validity of the observations made by Nelson, et al. concerning the phase of the vortex shedding with respect to pressure fluctuations in the cavity. This issue will be examined in Chapter 5.

Two-dimensional plots showing the spatial distribution of coherence and phase between  $u-p$  and  $v-p$  at the first sheartone cavity resonance frequency of 331 Hz at  $U_0 = 30$  m/s are shown in figures 4.20 and 4.21, respectively. The phase along the vortex path, which is

approximately equal to the line  $y=0$ , is of interest. Along this path, the phase between  $v-p$  is observed to increase along the streamwise direction and to be essentially constant in the  $y$  direction, in accordance with the idealized description. Note that the phase values are wrapped, so that the change from 180 degrees to  $-180$  degrees appears as a sudden change in shade.

The phase between  $u-p$  also shows a continuous increase in value in the streamwise direction, as predicted, above the vortex path. Below the path, however, the phase appears to be relatively constant. That a variation from the predicted behavior is seen in the  $u-p$  but not in the  $v-p$ , phase behavior, suggests that the behavior of the  $u$  velocity component below the vortex path differs from the predicted behavior.

Somewhat different results are seen in the spatial phase plots for the first sheartone at the lower speed. Plots of  $u-p$  and  $v-p$  phase for the 191 Hz tone at  $U_0 = 13$  m/s are shown in figures 4.22 and 4.23, respectively. Here, the spatial behavior for the  $u-p$  and  $v-p$  phase is as predicted. The same behavior is also seen for the 111 Hz tone at  $U_0=6.9$  m/s, and therefore these data are not shown.

Finally, plots of the spatial distribution of  $u-p$  and  $v-p$  phase for the second sheartone driven cavity tone of 345 Hz at 13 m/s are shown in figures 4.24 and 4.25, respectively. The idealized description in the previous section regarding the first sheartone assumed 1 vortex in the opening at a time. For a second sheartone, a discrete vortex travels only half the length of the opening during 1 cycle of the tone. At that point another vortex is shed, and so there are two vortices in the opening at a time. This means that the  $u-p$  and  $v-p$  phase plots should go through about 2 cycles along the length of the opening rather than 1. And indeed, this is what is observed.

It is likely that the variations from the predicted results discussed above for the  $u-p$  phase at 30 m/s occur because the model upon which the prediction is based is overly simplistic. It offers no prediction of how the phase might change as a function of distance from the vortex path. Despite these variations, the phase results shown are sufficient to establish that the fluctuating velocity field at the frequencies of the tones being studied is consistent with the presence of discrete vortices propagating along the opening of the cavity. The speed at which they propagate is discussed in the next section.

#### 4.3.4 Convection Velocity

As mentioned above, the rate of change of the phase between  $v-p$  with  $x$  may be used to calculate the phase speed of the disturbance in the shear layer. This is equivalent to the convection velocity,  $U_c$ , of the vortex in the shear layer. The slope of the phase curve,  $d\phi/dx$ , is effectively the wavenumber,  $k$ , of the disturbance in the direction along which the derivative is taken. Wavenumber may be related to frequency by  $k = \omega/c$ , where  $c$  is the phase speed. We can then write  $d\phi/dx = \omega/U_c$ . This can be rearranged to give  $U_c = 2\pi f/(d\phi/dx)$ .

The phase speed was calculated using the phase between  $v-p$  along the presumed path of the vortex. The presumed path of the vortex was determined by following the path of maximum vorticity in the  $y$  direction along the  $x$  direction. The vorticity which is calculated in section 5.2 and shown in figures 5.2 – 5.6, was used to determine this path. The resulting phase data, shown in figure 4.26, were somewhat irregular. Therefore, a 5<sup>th</sup> order polynomial was fit through the phase curve and the result used to calculate the phase speed. The 5<sup>th</sup> order curve fit to each phase is shown in the figure as the fine dashed line.

The statistical error of the phase was considered. The equation given by Bendat and Piersol for calculating the standard deviation,  $\sigma$ , of the phase based on the coherence and the number of averages. For all data shown here 256 averages were used. This number and the coherence corresponding to the phase at each frequency and location were used to calculate the standard deviation for each phase curve. The  $\pm 1\sigma$  curves are shown on the figure as the coarse dashed line. For the 207 Hz tone at 6.9 m/s, where the coherence is the lowest, the standard deviation is within about 10 degrees. This was considered to be acceptable.

In figure 4.27, the phase speed normalized by the freestream velocity is shown for all of the tones discussed in this chapter. The mean phase speed of each of the tones averaged over the  $x$  direction is about  $0.4U_0$ , which is similar to the results reported by other researchers (Kook and Mongeau, 1997).

However, the detailed behavior as a function of location is more interesting. In figures 4.28 and 4.29, the speed is plotted separately for the first and second sheartones, respectively. For the first sheartone, it is clear that the 30 m/s first sheartone, which excites

the cavity resonance, is distinctly different from the first sheartones at non-resonant speeds of 13 m/s and 6.9 m/s. The resonant sheartone shows a dip in  $U_c$  in the region  $0.2 < x/L < 0.5$ , while the non-resonant first sheartones show peaks in the same region. The resonant second sheartone also shows reaching a local minimum value of  $U_c$  in roughly the same region, where the non-resonant second sheartone at 6.9 m/s has  $U_c$  reaching a local maximum. This suggests that resonant sheartones may be distinguished from non-resonant sheartones by the presence of a local minimum in the convection velocity in the upstream half of the opening.

All of the sheartones show deceleration in the downstream region. This agrees with the results of Rockwell and Knisely (1979), who showed that when a vortex impinges on a corner, the influence of the corner causes the vortex to decelerate starting at about  $4\theta$  upstream of the corner, where  $\theta$  is the momentum thickness at separation. For the data shown here, that corresponds to a location of about  $x/L=0.6$ . This is what is observed for the first sheartone at 30 m/s. For both second sheartones, and for the first sheartone at 6.9 m/s, deceleration begins at about  $x/L=0.75$ . Data for  $U_c$  extend only to  $x/L = 0.885$ .

#### 4.4 Summary

In this chapter measurements of the  $u$  and  $v$  velocity components in the flow field of the cavity opening, together with cavity pressure data, were analyzed. Profiles of the mean and fluctuating velocity fields were discussed in section 4.1. It was seen that for all of the quantities considered, there was a significant difference between the profiles at 30 m/s and those at the other two speeds. This was particularly true near the downstream edge of the opening.

Consideration of the velocity spectra in section 4.2 showed that the non-resonant sheartones were essentially not observable. The resonant sheartones were observable, but the second sheartone at 13 m/s had much lower signal to noise than the first sheartone at 30 m/s. Also, in both the pressure and velocity spectra, higher order harmonics were observed only for the resonant first sheartone at 30 m/s. In the velocity spectra, these harmonics are not present near the upstream edge but appear and gradually increase along the streamwise

direction. In the middle of the opening, the second and third harmonics also show variation in the y direction, with peaks above and below  $y=0$ .

In section 4.3, cross spectral properties were computed and the spatial variation of the phase was considered. A comparison between the spatial variation of phase for an idealized case of a vortex convecting along the opening at a constant speed and the measured phase confirmed the vortex nature of the disturbance in the cavity opening associated with sheartones at both resonant and non-resonant conditions.

The variation of the phase along the vortex path was used to calculate the convection velocity of the vortex. A distinct difference was found between convection velocities of the resonant sheartones and those of the non-resonant sheartones in the upstream region of the opening. As they approached the downstream edge, both appeared to be decelerating.

Distinct differences are seen in the velocity profiles, the velocity spectra, and the behavior of the convection velocity between the various types of tones. The resonant first sheartone has important differences in the velocity profiles and in the velocity spectra. In the convection velocity, both the resonant first and second sheartones show behavior different from that of the non-resonant sheartones. These differences may be used to distinguish the types of tones from one another and may be considered in more detail to understand the physics of the flow-induced cavity resonance process.

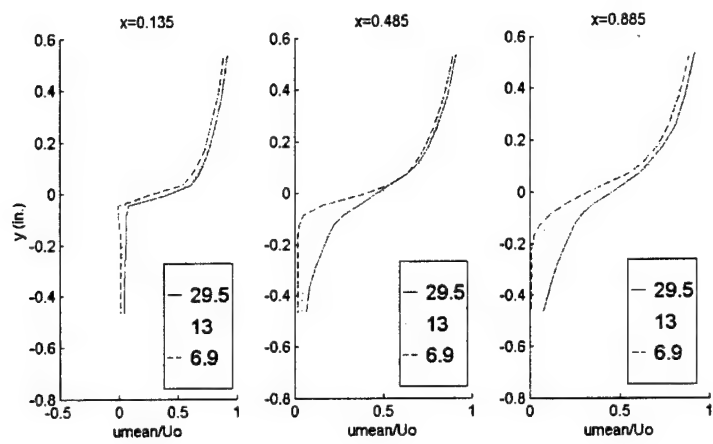


Figure 4.1: Comparison of streamwise mean velocity profiles for 30, 13, and 6.9 m/s at 3 streamwise locations

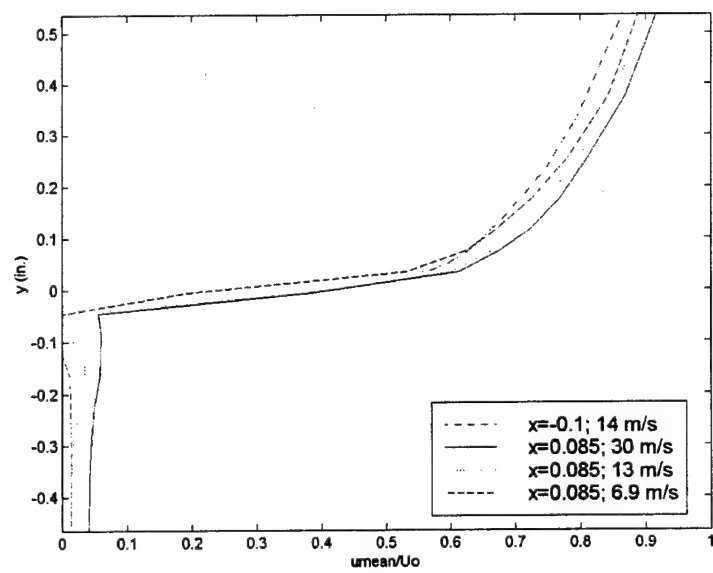


Figure 4.2: Comparison of streamwise mean velocity profiles at  $x=0.85''$  and  $x=-0.1''$

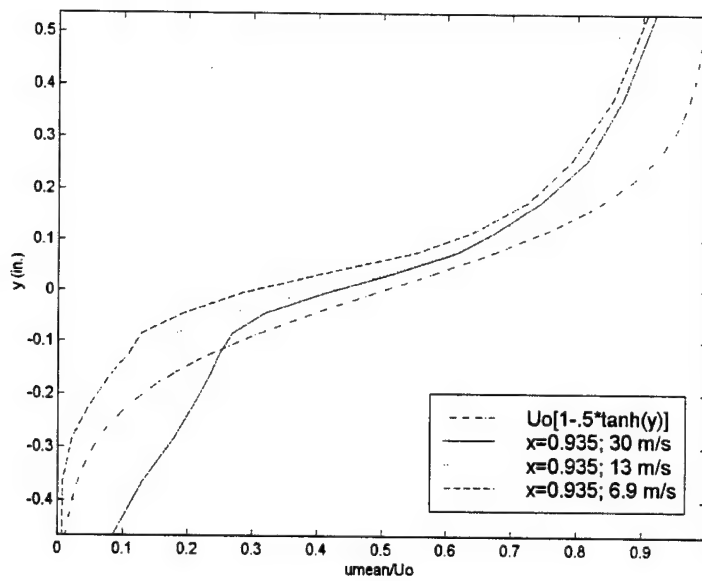


Figure 4.3: Comparison of streamwise mean velocity profiles at  $x=0.935$  to hyperbolic tangent profile

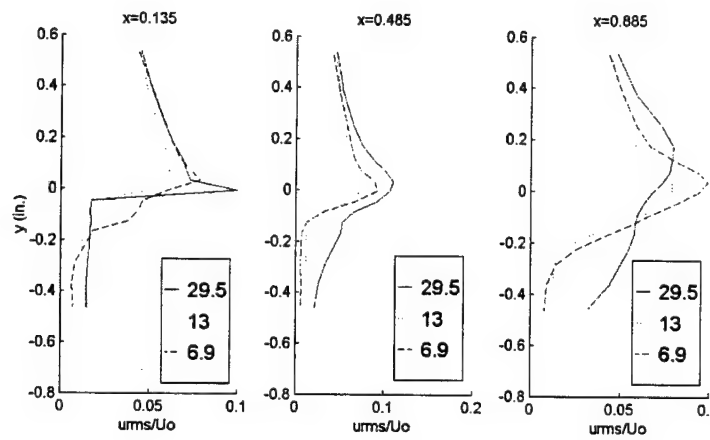


Figure 4.4: Comparison of streamwise turbulence intensity profiles for 30, 13, and 6.9 m/s at 3 streamwise locations

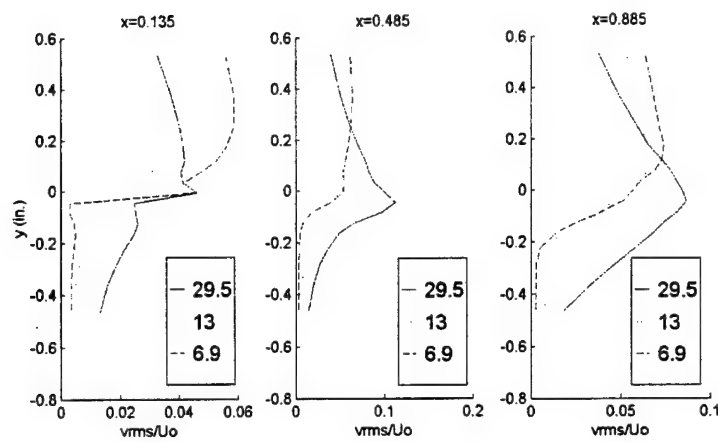


Figure 4.5: Comparison of wall-normal turbulence intensity profiles for 30, 13, and 6.9 m/s at 3 streamwise locations

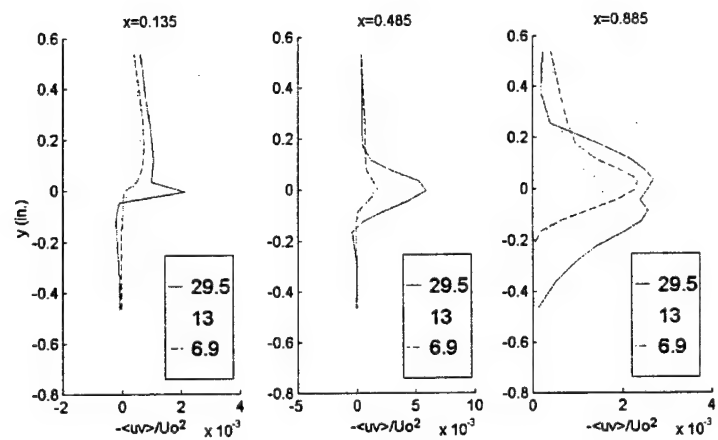


Figure 4.6: Comparison of Reynolds stress profiles for 30, 13, and 6.9 m/s at 3 streamwise locations

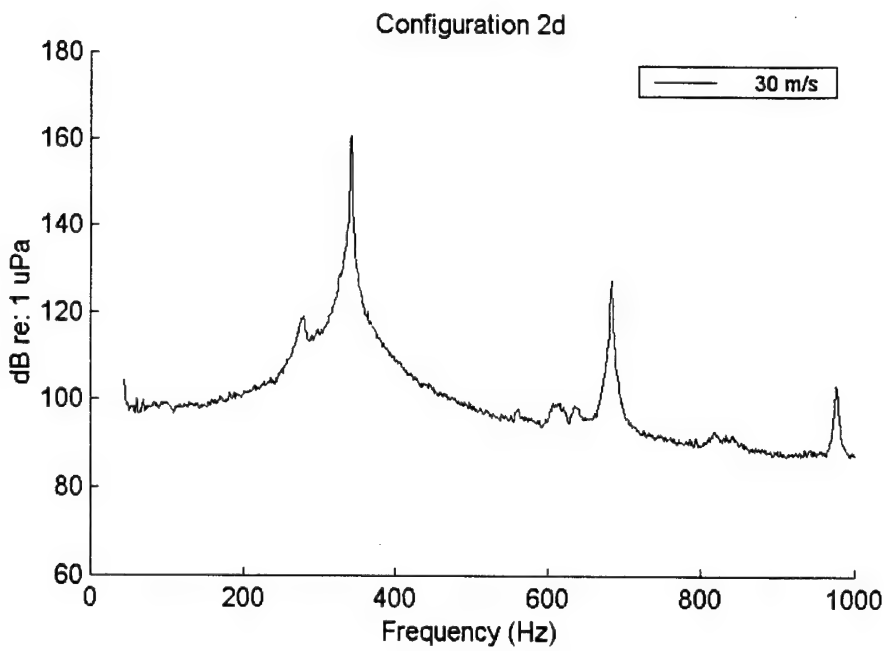


Figure 4.7: Cavity pressure spectrum for 30 m/s, 331 Hz first sheartone resonant condition, with  $L=1"$ ,  $d=5.5"$

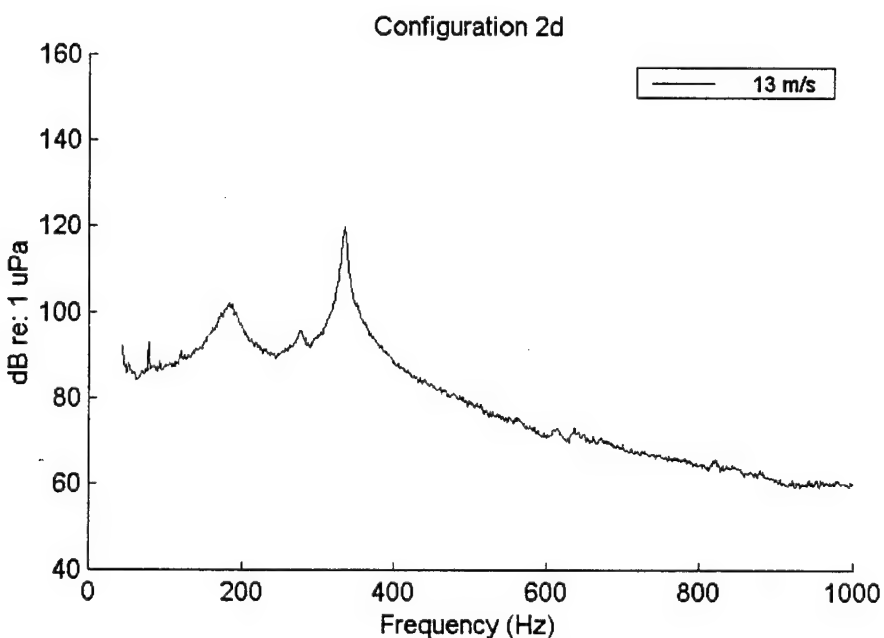


Figure 4.8: Cavity pressure spectrum for 13 m/s, 345 Hz second sheartone resonant condition, with  $L=1"$ ,  $d=5.5"$

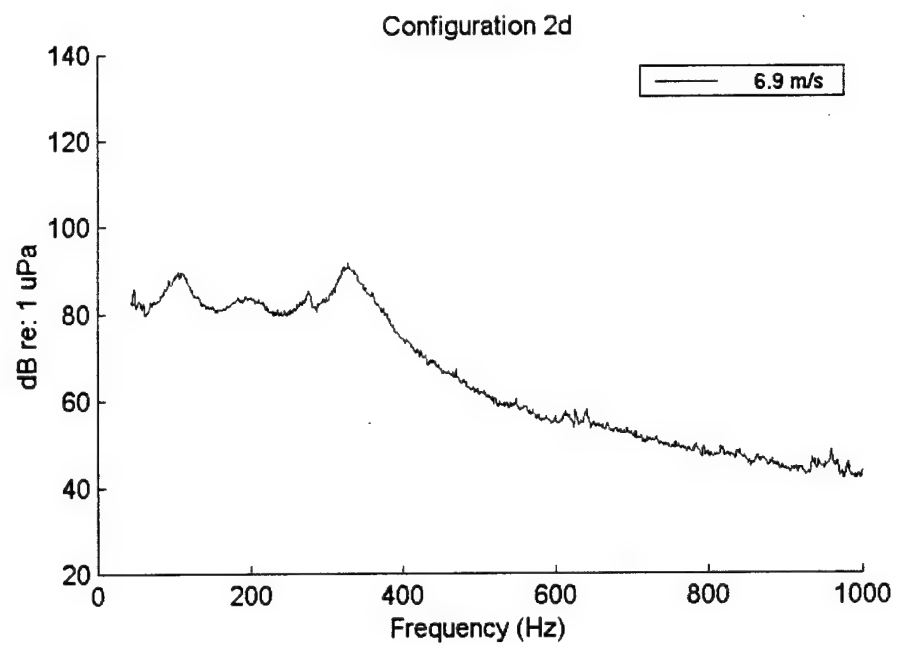


Figure 4.9: Cavity pressure spectrum for 6.9 m/s non-resonant condition with  $L=1"$ ,  $d=5.5"$

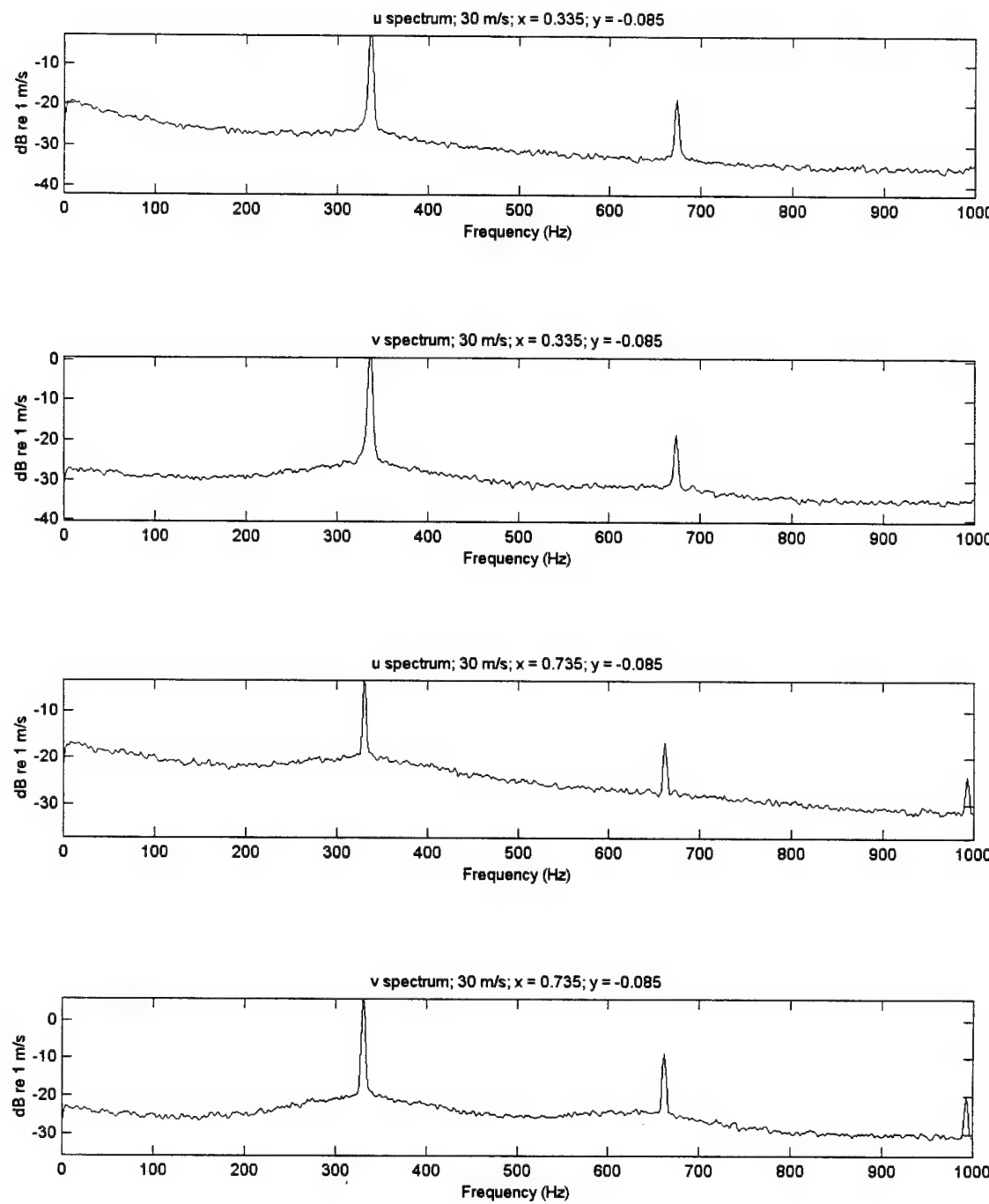


Figure 4.10: Velocity spectra at 2 locations for 30 m/s, 331 Hz first  
sheartone resonant condition

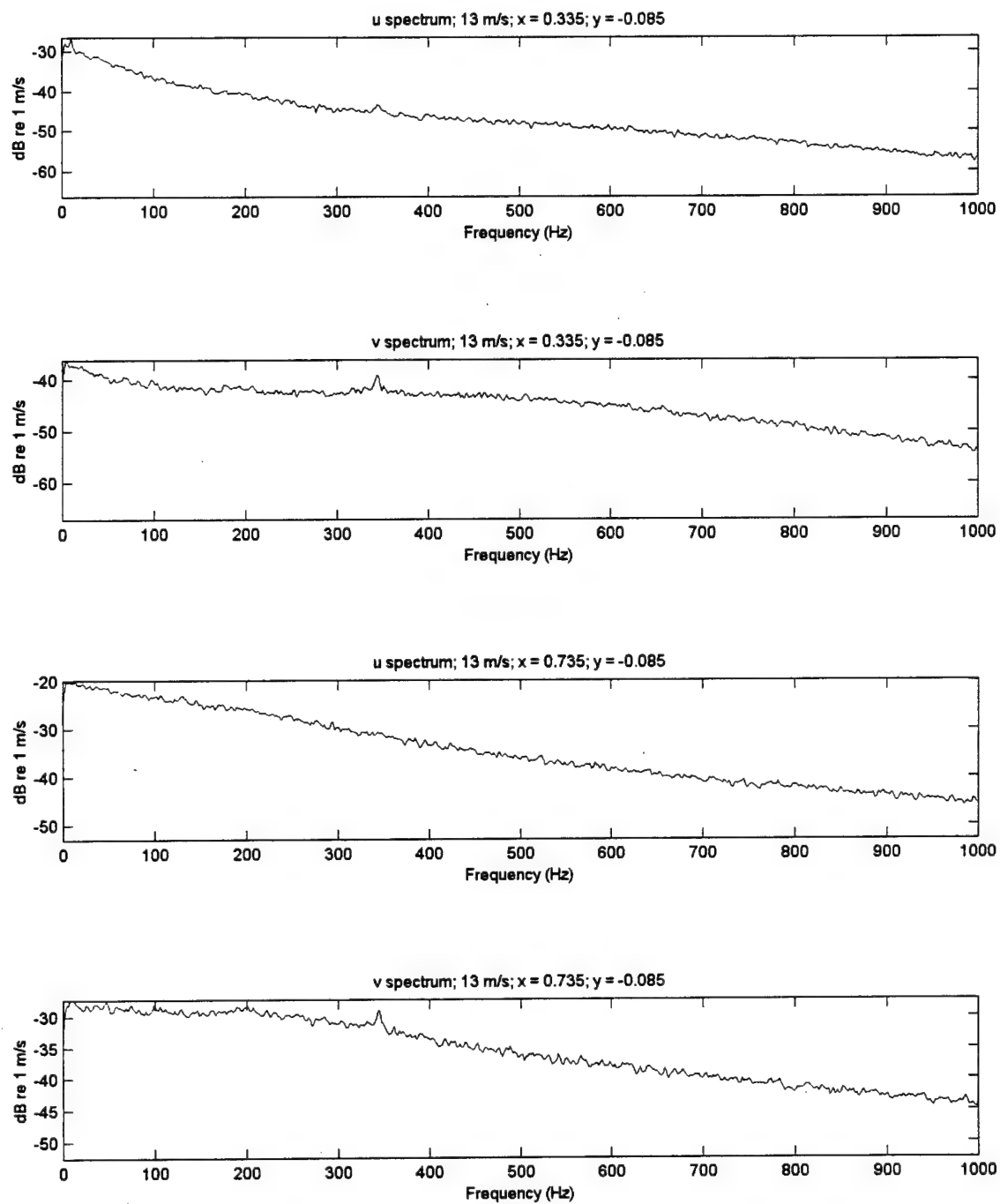


Figure 4.11: Velocity spectra at 2 locations for 13 m/s, 345 Hz second sheartone resonant condition

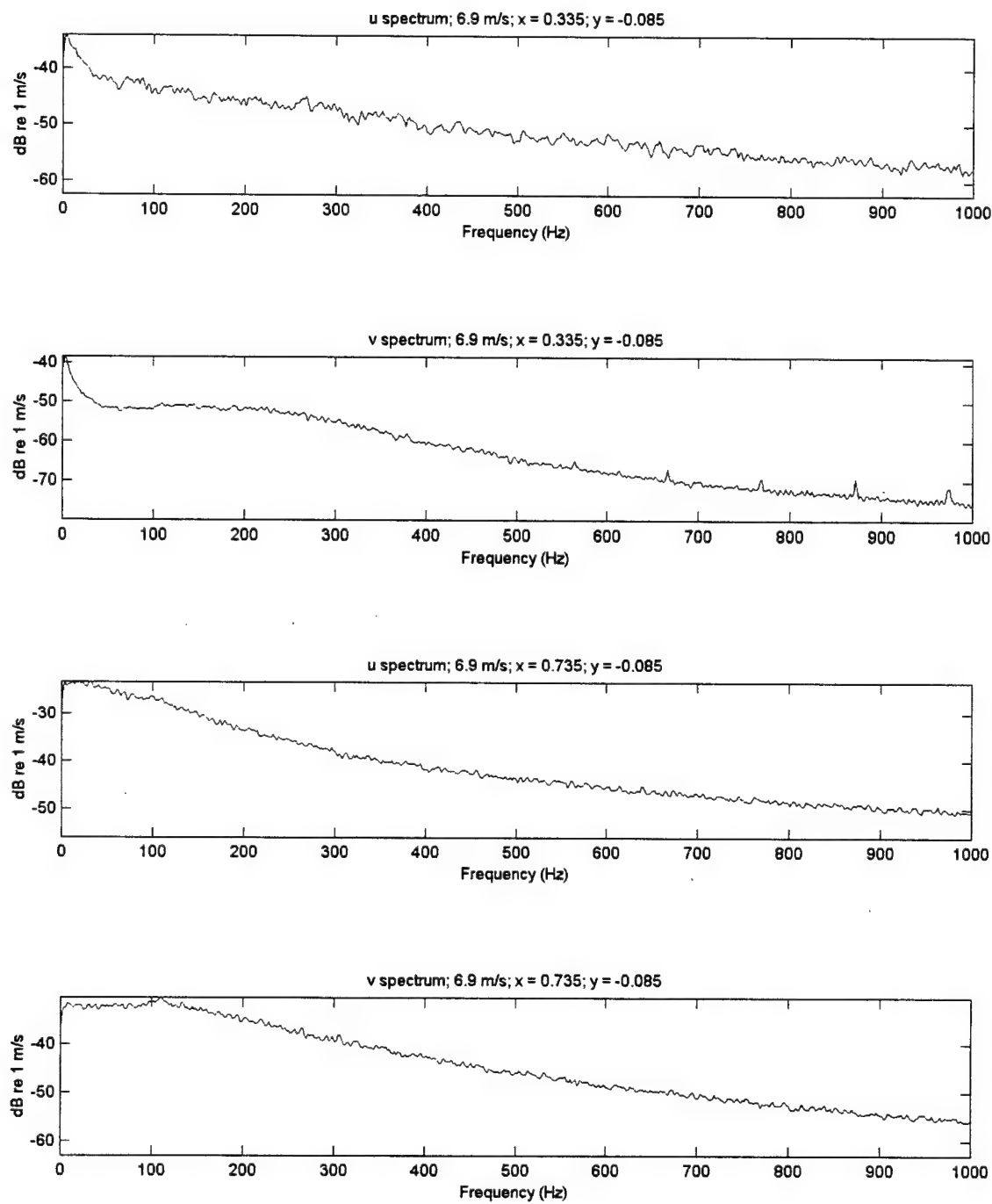


Figure 4.12: Velocity spectra at 2 locations for 6.9 m/s non-resonant condition

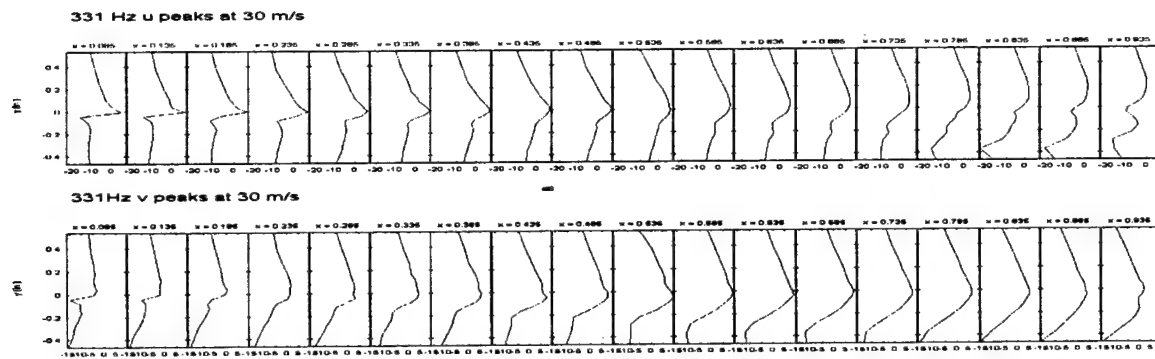


Figure 4.13: Profiles of velocity spectral levels of 331 Hz first sheartone resonance

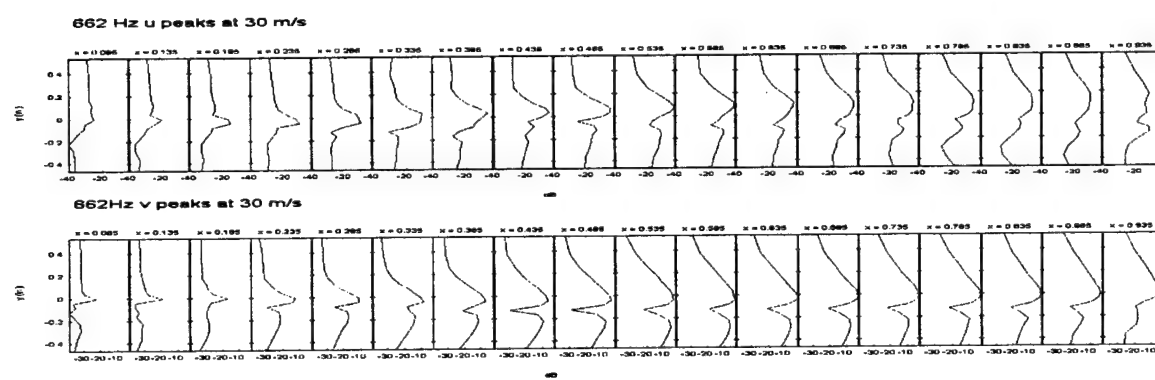


Figure 4.14: Profiles of velocity spectral levels of 662 Hz 2<sup>nd</sup> harmonic of first sheartone resonance

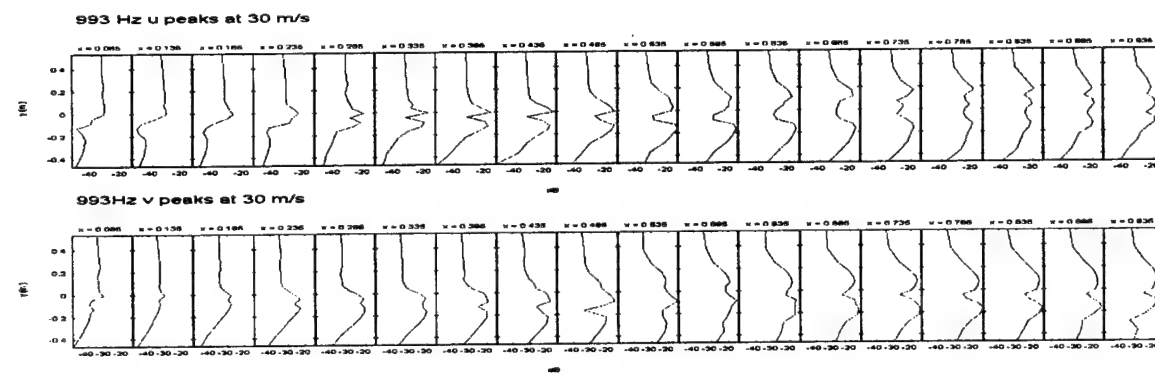


Figure 4.15: Profiles of velocity spectral levels of 993 Hz 3<sup>rd</sup> harmonic of first sheartone resonance

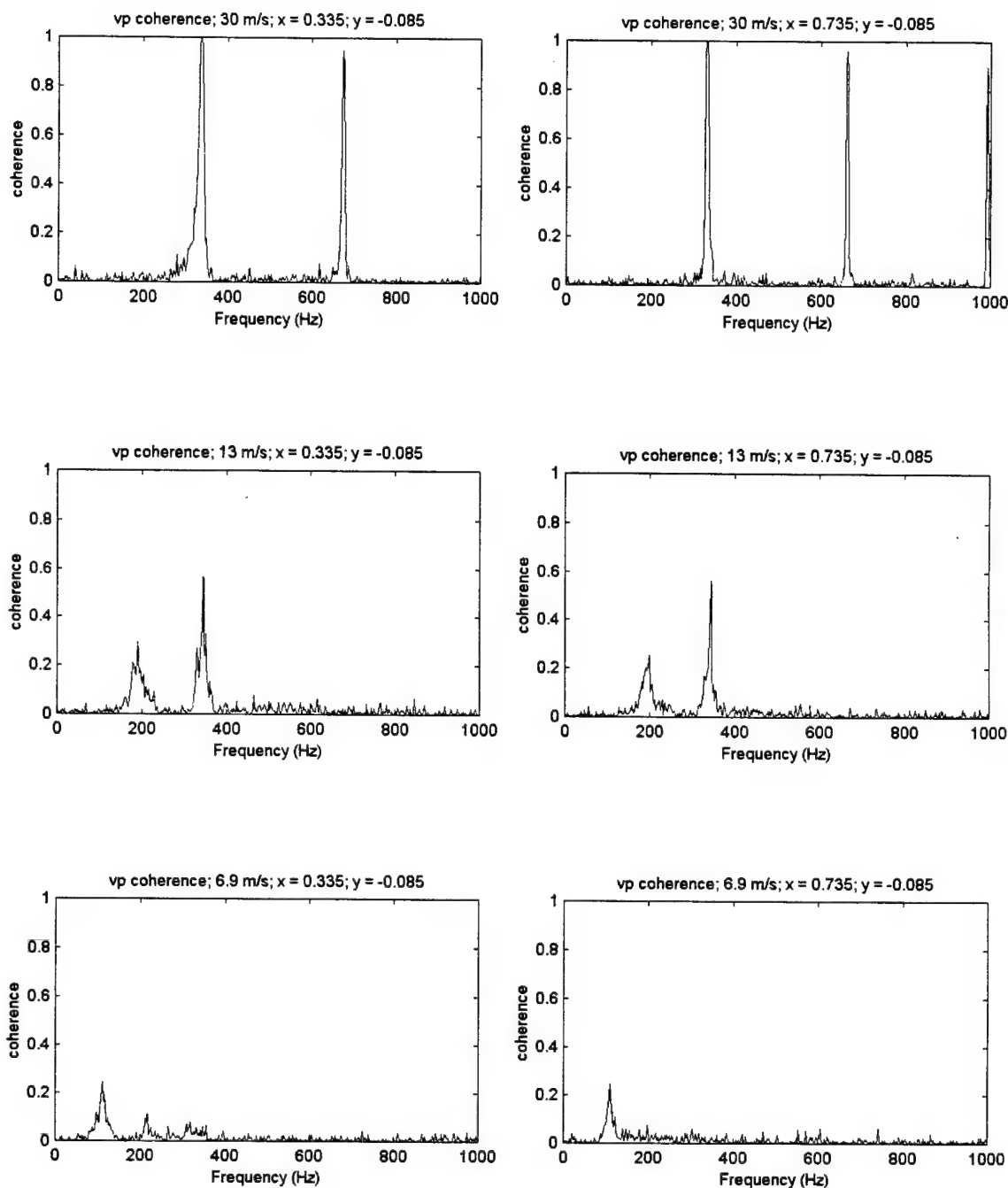


Figure 4.16: Coherence between v-p at 2 locations for 3 speeds

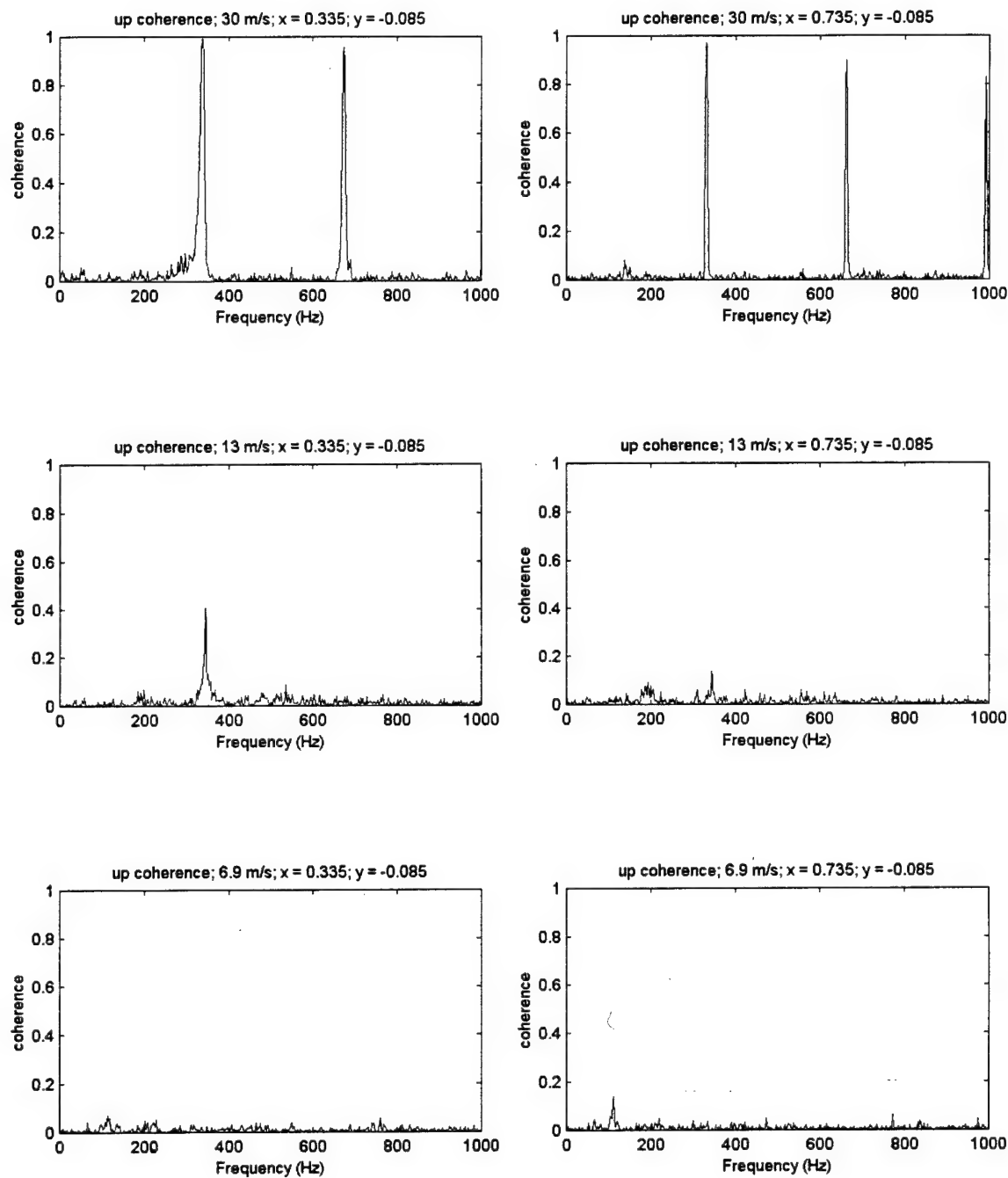
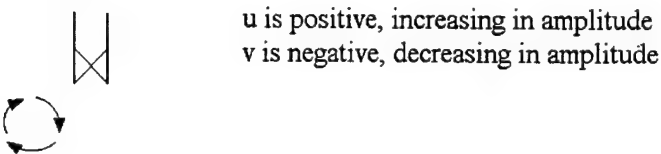
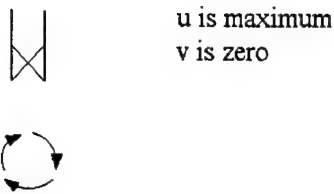


Figure 4.17: Coherence between  $u$ - $p$  at 2 locations for 3 speeds

Time 1



Time 2



Time 3

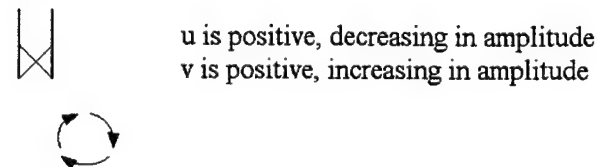


Figure 4.18: Description of behavior of velocity components of discrete vortex as it passes an x-probe

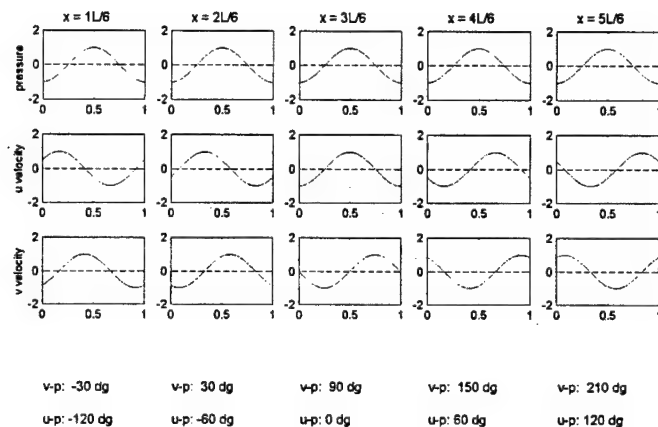


Figure 4.19: Idealized description of phase between velocity components and cavity pressure as a discrete vortex convects along the cavity opening at a constant speed

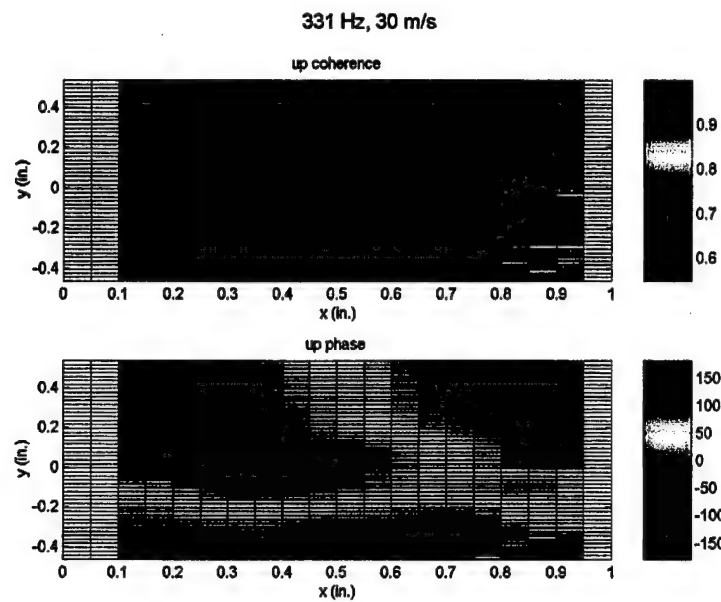


Figure 4.20: Spatial plot of phase and coherence between u-p of first sheartone resonance at 30 m/s

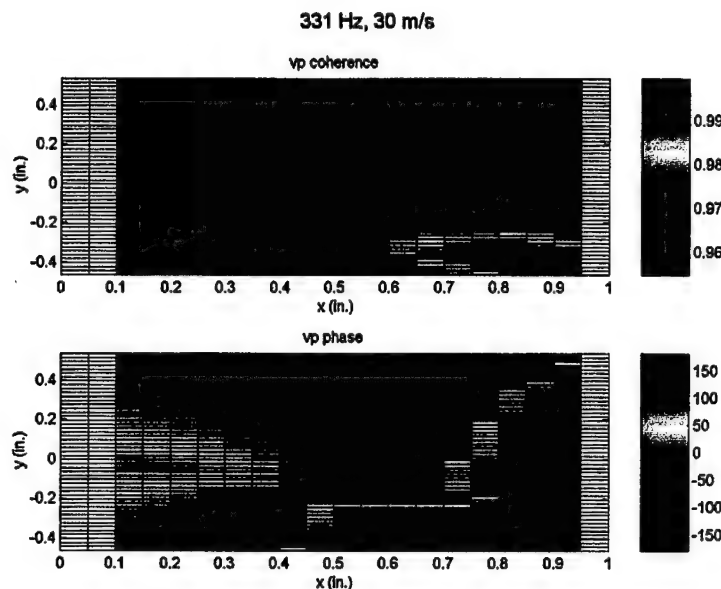


Figure 4.21: Spatial plot of phase and coherence between v-p of first sheartone resonance at 30 m/s

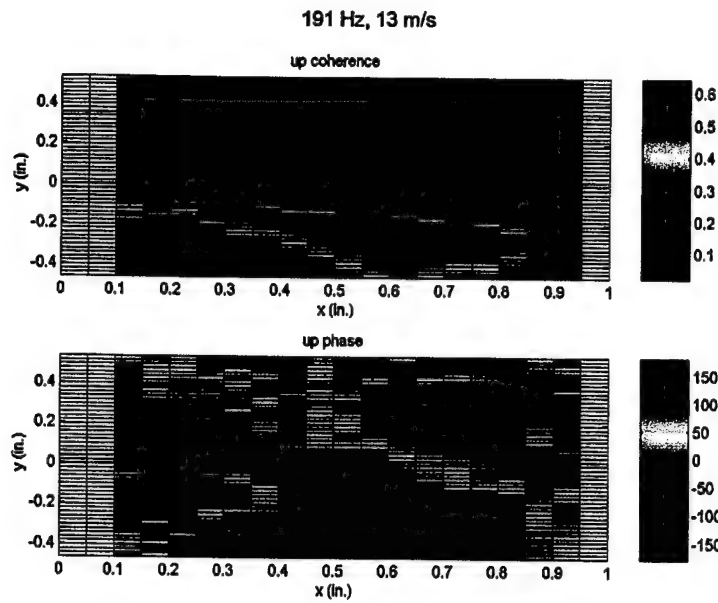


Figure 4.22: Spatial plot of phase and coherence between u-p of non-resonant first sheartone at 13 m/s

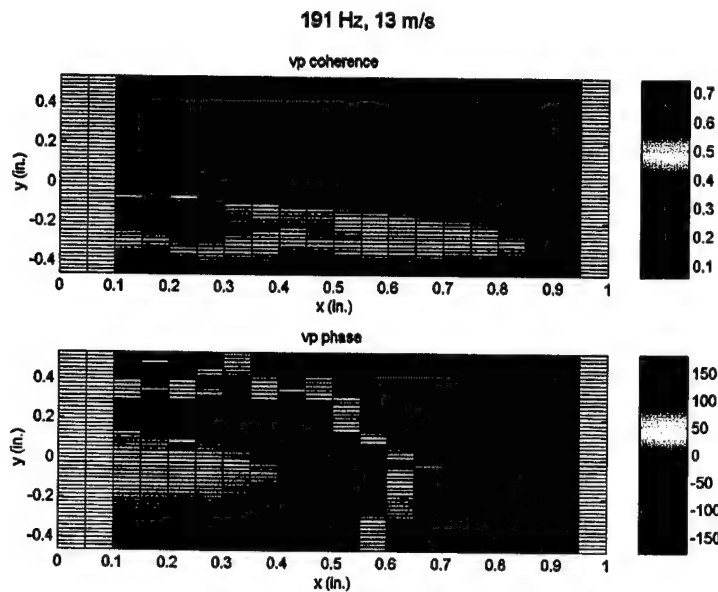


Figure 4.23: Spatial plot of phase and coherence between v-p of non-resonant first sheartone at 13 m/s

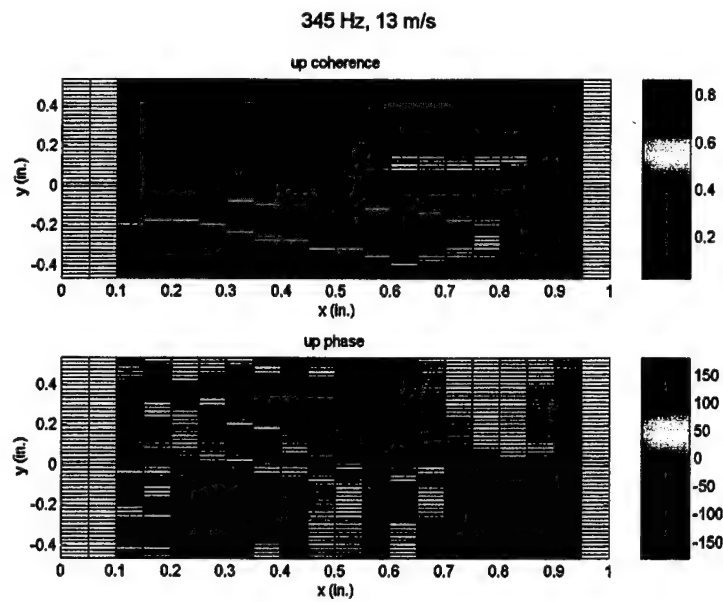


Figure 4.24: Spatial plot of phase and coherence between u-p of second sheartone resonance at 13 m/s

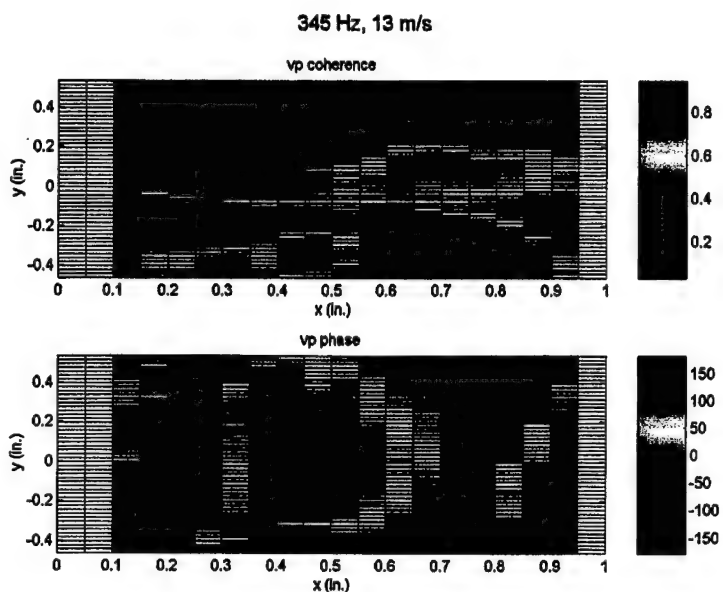


Figure 4.25: Spatial plot of phase and coherence between v-p of second sheartone resonance at 13 m/s

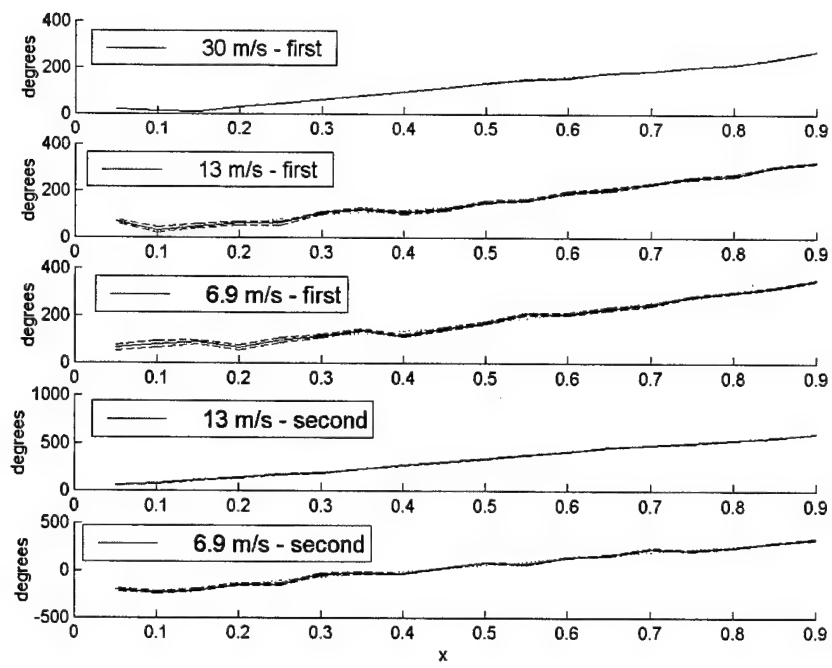


Figure 4.26: Phase between v-p along vortex path for sheartones at 30, 13, and 6.9 m/s

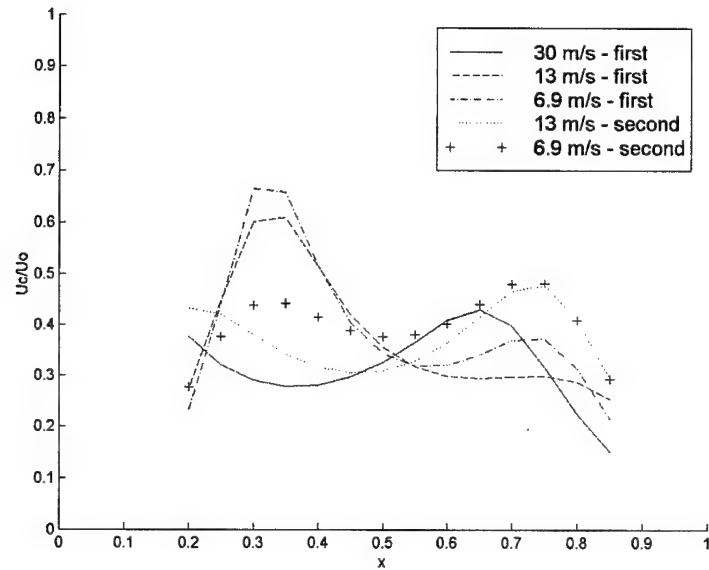


Figure 4.27: Normalized convection velocity of vortex for sheartones at 30, 13, and 6.9 m/s.

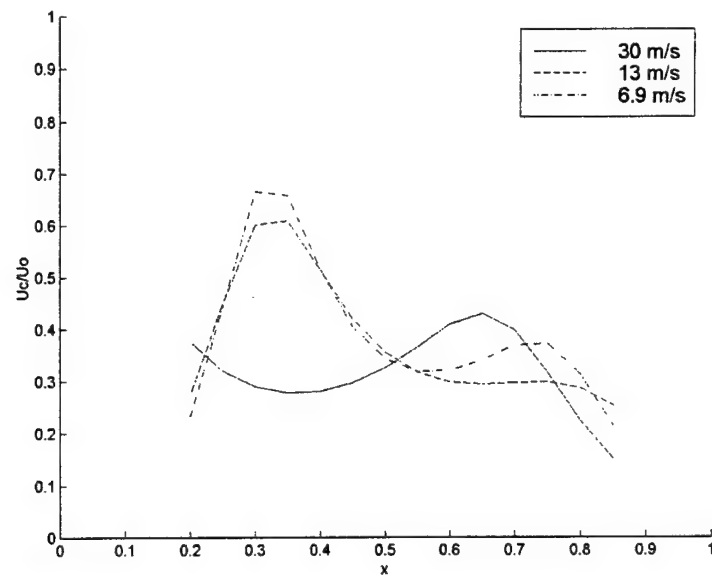


Figure 4.28: Normalized convection velocity of vortex for first sheartones at 30, 13, and 6.9 m/s

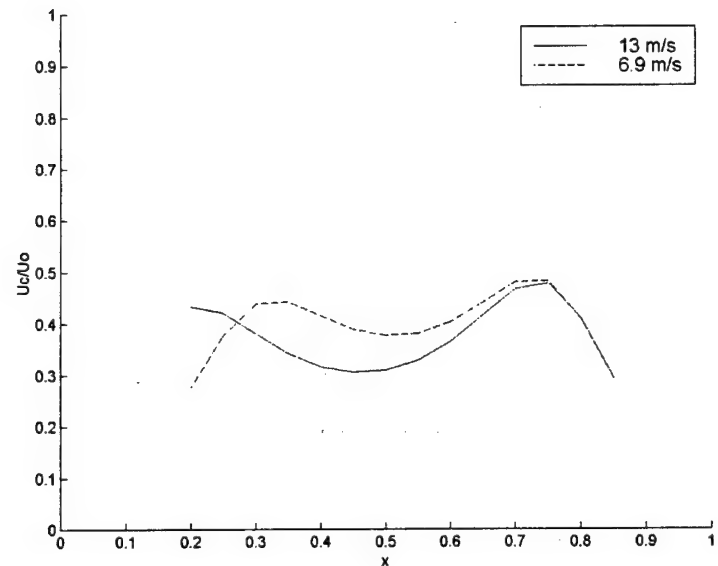


Figure 4.29: Normalized convection velocity of vortex for second sheartones at 13 and 6.9 m/s

## 5. Analytical Model of Flow-Acoustic Interactions

In this chapter, the model given by Nelson, et al. (1981, 1983) for a flow-excited resonant cavity is used as the basis for studying the resonant and non-resonant cavity tones measured as part of this research. In the first section, the relevant features of that model are described. In the second section, the data from Chapter 4 are used to calculate the energy production term derived in the model and the results are compared to predictions made by the model. Also, the description given by the model of the phase relationship between the cavity pressure fluctuations and the location of the vortex is compared with the measured data. In the final section, the results are summarized and conclusions are drawn.

### 5.1 Model of the Resonator Flow

The dynamics of a flow excited cavity at maximum resonance level are described by Nelson, et al. They explain the flow acoustic interaction in the opening of the cavity in terms of the momentum and energy balances in the fluid. Detailed measurements of the flow field in the opening of a first sheartone excited cavity at its maximum resonance level are used to develop a kinematic model of the flow in the opening. The momentum and energy balances are evaluated using this model.

A summary of the processes governing flow-excited cavity resonance based on Nelson's model is given. This is followed by a review of some of the features of the flow seen in the experimental data and then by a review of the energy balance analysis, including the derivation of the energy production term.

#### 5.1.1 Description of Processes Governing Flow-Induced Cavity Resonance

Figure 5.1 is an illustration of the processes governing flow induced cavity resonance. The flow upstream of the cavity opening is assumed to be a classical fully developed turbulent boundary layer. While upstream laminar flows yield similar results, the interest in this study is turbulent flows. As the turbulent boundary layer passes over the cavity

opening, a free shear layer forms. The fluid acoustic interactions that lead to resonance are dictated by the nature of the free shear layer, which is inherently unstable. As a result of this shear layer instability, vortices are shed with period  $T$ , corresponding to the frequency of the cavity resonance,  $f = 1/T$ . The vortex develops during the first half of the period as it convects along the upstream half of the opening. Then, during the second half period, it convects along the downstream half of the opening at a convection velocity of about one half of  $U_0$ , the grazing flow speed. The vortex exhibits solid body rotation in a core of radius  $r_c$ . The cavity pressure is at a minimum at the beginning of this process, and increases as fluid is displaced into the cavity during the first half period. The cavity pressure reaches a maximum when the vortex is at the midpoint of the cavity opening at which point air begins being displaced outward during the second half of the process. When the vortex reaches the downstream edge it is ejected from the cavity opening and accelerates to the local mean flow velocity,  $U_0$ . After ejection the vortex appears "stretched" in shape in the streamwise direction.

Interaction between the fluctuating vorticity, mean flow, and acoustic particle velocity result in an acoustic energy balance in which acoustic energy flows into the cavity near the downstream edge. Some of this energy is absorbed by interactions in the upstream half of the opening. The remaining energy is dissipated by some combination of acoustic radiation and energy carried away by the vortices.

### 5.1.2 Features of the Flow

Flow visualization was performed by releasing oil mist into the flow and using a stroboscope light triggered by the cavity pressure signal to illuminate the flow so that photographs could be taken. It was noted that the shear layer at the upstream edge leaves the edge tangential to the upper surface of the resonator. This is taken to mean that the Kutta condition is satisfied.

Based on a series of photographs taken at phase increments of 30 degrees, it was possible to deduce the following about the flow in the shear layer: "A discrete vortex is formed during the first half of the cycle after the cavity pressure reaches a minimum.

During this period the cavity pressure is increasing and the air below the neck is being displaced into the cavity. The vortex reaches the mid-point of the resonator neck on completion of the first half cycle. At this stage the cavity is at its maximum downward displacement. During the next half cycle, as the cavity pressure falls and the air below the neck is displaced upwards, the vortex convects towards the downstream lip." The vortex is then ejected from the neck. The convection velocity of the vortex appears to increase on ejection.

LDV measurements of the  $u$  and  $v$ , the streamwise and vertical components of velocity, respectively, in the region of the cavity opening were also performed. The presence of discrete vortices is confirmed by the  $180^\circ$  phase difference in streamwise velocity fluctuations between the upper and lower halves of the shear layer. The vertical location of this change defines the path along which the vortices travel. The streamwise velocity fluctuations seemed to be consistent with the passage of vortices having a solid body rotation in their core.

The mean shear layer thickness was observed to grow linearly in the downstream direction. It was also observed that the amplitude of fluctuating streamwise velocity is highest at the upstream edge of the opening and decreases as the vortex convects downstream. This implies that the unstable shear layer rolls up into discrete vortices very early in the cycle and is followed by a spreading of the vortices as they convect downstream, in accordance with the growth of the mean shear layer.

Measurements of the phase of the vertical velocity fluctuations in the middle of the neck show that they lag the cavity pressure by about  $90^\circ$ . The phase between cavity pressure and velocity in the opening can be calculated from the impedance of the cavity opening. Measurements made by exciting the cavity opening with a speaker allowed the impedance of the opening to be determined. Calculations using these values give a phase of  $84^\circ$  at the resonant frequency, which is in reasonable agreement with observations of the flow excited resonance.

### 5.1.3 Energy Analysis

Nelson, et al. describe a kinematic model of the flow field in the cavity opening based on their experimental observations. In this model, the velocity field,  $\mathbf{u}$ , is considered to consist of the superposition of two flows: a solenoidal component,  $\mathbf{v}$ , and a purely irrotational component,  $\nabla\phi$ , so that

$$\mathbf{u} = \mathbf{v} - \nabla\phi.$$

The vorticity vector  $\boldsymbol{\Omega}$ , is given by

$$\boldsymbol{\Omega} = \nabla \times \mathbf{u} = \nabla \times \mathbf{v}.$$

The velocity,  $\mathbf{u}$ , is also considered to consist of a mean part and a fluctuating part, so that

$$\mathbf{u} = \bar{\mathbf{v}} - \nabla\bar{\phi} + \mathbf{v}' - \nabla\phi',$$

where the overbar denotes time average and the prime denotes the fluctuating component.

Interaction between the vorticity and the potential flows is analyzed by studying the energy balance. This analysis, taken directly from Nelson, starts with the energy transport equation developed by Doak (1974),

$$(\partial/\partial t)(\rho E + \frac{1}{2} \rho \mathbf{u}^2) + \nabla \cdot (H\rho \mathbf{u}) = 0,$$

where  $\mathbf{u}$  is the velocity vector,  $E$  is internal energy, and  $H$  is stagnation enthalpy,  $E + p/\rho_0 + \frac{1}{2} \mathbf{u}^2$ .

For stationary energy density,  $(\rho E + \frac{1}{2} \rho \mathbf{u}^2)$ , the time average of the equation reduces to

$$\nabla \cdot (\bar{H}\rho \mathbf{u}) = 0,$$

which can be written as

$$\nabla \cdot (\bar{H}\rho \mathbf{u}) + \nabla \cdot (\bar{H}'(\rho \mathbf{u}')) = 0.$$

The first term represents the mean energy flux associated with the mean momentum. The second term represents the mean energy associated with the fluctuating momentum. This equation shows that a local generation of energy due to the fluctuating flow must be balanced by a loss of energy from the mean flow. The mechanism by which energy is transferred from the mean flow to the fluctuating flow is the mean work done by a fluctuating Coriolis force. This is illustrated by considering momentum equation in the form,

$$\partial \mathbf{u}'/\partial t + (\mathbf{\Omega} \times \mathbf{u}') + \nabla H' = 0.$$

Taking the scalar product of  $(\rho \mathbf{u})'$  with this equation leads to

$$(\rho_0 \mathbf{u})' \cdot \partial \mathbf{u}' / \partial t + (\rho \mathbf{u})' \cdot (\mathbf{\Omega} \times \mathbf{u}') + (\rho \mathbf{u})' \cdot \nabla H' = 0.$$

Since  $(\rho \mathbf{u})' \cdot \nabla H' = \nabla(H'(\rho \mathbf{u})') - H' \nabla \cdot (\rho \mathbf{u})'$ , and  $\nabla \cdot (\rho \mathbf{u})' = 0$  for an incompressible flow, the time average of the equation reduces to

$$\nabla \cdot (\overline{H'(\rho \mathbf{u})'}) = -\overline{(\rho \mathbf{u})' \cdot (\mathbf{\Omega} \times \mathbf{u})'}$$

Thus the mean energy flux associated with fluctuating momentum is due to action of a fluctuating Coriolis force on the fluctuating flow. Total power outflow,  $W_v$  may be calculated by integrating

$$W_v = \int_v -\overline{(\rho \mathbf{u})' \cdot (\mathbf{\Omega} \times \mathbf{u})'} dV.$$

The dot product can be expanded to give

$$-(\rho \mathbf{u})' \cdot (\mathbf{\Omega} \times \mathbf{u})' = -(\rho_0 \mathbf{u})' \cdot (\overline{\mathbf{\Omega}} \times \mathbf{u}') - (\rho_0 \mathbf{u})' \cdot (\overline{\mathbf{\Omega}' \times \mathbf{u}}').$$

The first term on the right side is zero, so the only part of the Coriolis force available to produce energy flux is that associated with the fluctuating and not the mean vorticity. Thus based on the two dimensional model of flow in the opening that has been developed, the integral may be reduced to

$$W_v = \int_v -\rho_0 \overline{\mathbf{u}} \cdot \overline{\mathbf{\Omega}'_3 \mathbf{v}'} dV.$$

The quantity being integrated is referred to as the *energy production term*.

Values from the kinematic model were used by Nelson to calculate a contour plot of the energy production term. The result shows a source near the downstream edge and an energy sink in the upstream half of the opening. Integrating the contour plot would show zero net energy production. However, the kinematic model fails to account for the vortex formation process in the upstream half of the opening. In practice, the sink will absorb less energy than is produced by the source, resulting in net energy production.

## 5.2 Comparisons With Experimental Data

In this section, the energy production term from Nelson's model will be calculated using the data obtained in this investigation. Calculations are made for the three cases discussed in Chapter 4, the resonant first sheartone, the resonant second sheartone, and a non-resonant

speed. Also, Nelson's observations on the phase of the vortex shedding process with respect to cavity pressure are compared to the measured data for both the resonant and non-resonant sheartones.

### **5.2.1 Calculation of Energy Production Term**

The term  $\Omega_3 = \partial v / \partial x - \partial u / \partial y$  is the component of the vorticity vector in the z direction. An estimate of vorticity can be calculated from measurements of the u and v components of velocity at three locations. For the data presented here, vorticity was calculated for each measurement location for which measurements also existed at the next position in the x direction and at the next position in y direction. Those measurements were used to calculate  $\Delta v / \Delta x$  and  $\Delta u / \Delta y$ . An estimate of vorticity is then obtained by taking the difference,  $\Delta v / \Delta x - \Delta u / \Delta y$ . The measurements at the various locations were not simultaneous. However, the nature of the cavity resonance process is such that the velocity at any point will always have the same phase relationship with the pressure in the cavity at the frequency of a given tone. Based on this, the pressure and velocity signals were filtered with a 40 Hz wide filter centered on the frequency of the tone, and the signal from the microphone in the cavity was used to synchronize velocity measurements performed at different times in different locations.

The energy production term,  $-\rho_0 \bar{u} \overline{\Omega'_3 v'}$ , described in the previous section, may then be calculated. The vorticity,  $\Omega_3$ , is calculated as described above, and its fluctuating part at each time multiplied by the fluctuating vertical velocity component,  $v'$ , at each time. The time average of these products is multiplied by  $-\rho_0 \bar{u}$ . The results of calculations of both of these terms are described in the next section.

### **5.2.2 Results of Energy Production Term Calculations**

In this section, the energy production term is calculated for the resonant sheartones at speeds of 30 m/s, 13 m/s, and 6.9 m/s for the cavity configuration 2d ( $L=1"$ ,  $d=5.5"$ ). The

data that was discussed in Chapter 4 was used to make the calculations. The distribution and the net energy produced are compared to the predicted results for a resonant first sheartone given by Nelson, et al. The energy production is also calculated for resonant second sheartone at 13 m/s and for the non-resonant sheartones at 13 and 6.9 m/s.

A spatial plot of the energy production term for the resonant first sheartone of 331 Hz at 30 m/s is shown in figure 5.2. For this tone, distinct regions of strong energy production and strong energy absorption exist, as described by Nelson, et al. However, unlike Nelson's calculations, the measured regions are above and below each other in the y direction as well as downstream and upstream from each other. The positive area is at a 0.2" higher location in the y direction, and its center is about 0.2" downstream. Integration of the term yields a net energy production of about 1.2 Watts/meter.

The distributions of the energy production term for the resonant second sheartone of 345 Hz and the non-resonant first sheartone of 191 Hz at 13 m/s are shown in figures 5.3 and 5.4. The distribution for the second sheartone resonance is distinctly different from that of the first sheartone resonance, but very similar to that of the non-resonant tone at 13 m/s. The net energy produced by the second sheartone and the non-resonant tone is about 1/40<sup>th</sup> that of the first sheartone resonance at the higher speed. Also, no region of energy absorption is observed at the two lower speed tones. The location of maximum energy production in both of these tones is at about  $x/L = 0.75$ , well downstream of the maximum energy production location for the first sheartone resonance.

The presence or absence of the negative energy production region appears to be associated with patterns in the vorticity distribution. When the negative region is present, the vorticity is high near the upstream edge of the opening. When no negative region is present, the vorticity is seen to increase gradually across the opening. This result should be considered with the expression for the energy production term,  $-\rho_0 \bar{u} \bar{\Omega}_3' v'$ . The phase and magnitude of the term depend on  $\bar{\Omega}_3' v'$ , the product of the fluctuating vorticity and the fluctuating wall normal velocity. The presence of the negative region upstream of the positive region requires that the two fluctuating terms be in phase near the upstream edge and out of phase near the downstream edge. The magnitude of the vorticity also affects the energy production. It is difficult with the available data to determine whether a low

magnitude of energy production is due to low amplitudes of the fluctuating quantities or due to the phase between them being near +/- 90 degrees. It should also be noted that the resonant first sheartone has a higher normalized cavity pressure level than the resonant second sheartone. Thus, the presence of the negative energy production region is associated with a stronger resonance.

In figures 5.5 and 5.6, the energy production term for the non-resonant 111 Hz first sheartone and 207 Hz second sheartone at 6.9 m/s are plotted. The regions of energy production for these tones are in the same location as those observed for both tones at 13 m/s. The net energy produced by these tones is about one half and one quarter of that produced by the first and second sheartones, respectively, at 13 m/s. Results at 6.9 m/s are consistent with those at 13 m/s.

A rough attempt was made to compare the acoustic radiation from the resonant cavity to the net value of energy production. Measurements were made of the sound pressure level,  $L_p$ , in the room housing the wind tunnel for the 331 Hz resonant first sheartone at 30 m/s and for the 345 Hz resonant second sheartone at 13 m/s. A microphone located in the vicinity of the inlet to the wind tunnel was used for these measurements. For comparison purposes, the room was considered to be a reverberant room. Because of the geometry of the room and the wind tunnel, this is very much an approximation.

For the resonant first sheartone, the net energy production was 1.194 W/m from a 0.114 m wide opening. This translates to a sound power level,  $L_w$ , of -8.6 dB re 1 W.

The equation relating sound power and sound pressure levels in a reverberant room is

$$L_p = L_w - 10 \log R + 32.2 \text{ dB},$$

where  $R$  is the room constant in  $\text{m}^2$ ,  $L_p$  is in dB re 1 Pa, and  $L_w$  is in dB re 1 W.  $R$  may be calculated from the equation

$$R = S * a / (1-a),$$

where  $S$  is the area of the room and  $a$  is the average absorption coefficient. The surface area of the room and its contents was estimated to be  $1650 \text{ m}^2$ . The absorption coefficient was estimated to be about 0.2. Using these values, the value of  $L_p$  based on the net energy production, is -1 dB re 1 Pa. The measured sound pressure level was -8.3 dB re 1 Pa. This

is about 7 dB below the value predicted using the net energy production. This implies that about a quarter of the net energy produced is being radiated acoustically from the cavity.

For the 345 Hz resonant second sheartone at 13 m/s, the net energy production of 0.0222 W/m translates to a sound power level of -25.9 dB re 1 W. Using the equation for a reverberant room, the equivalent sound power level is -18.3 dB re 1 Pa. The measured sound power level was -47.1 dB re 1 Pa. This is well below the estimate based on the net energy production and suggests that only a very small fraction of that energy production is being radiated.

A possible explanation for the difference in the relationship between the measured sound pressure level and that estimated from the net energy production is based on the energy balance discussed by of Nelson et al. A resonating flow excited cavity has achieved a balance between the energy produced and the energy carried away. The net energy production term is the source of energy produced. Energy is carried away both as acoustic energy,  $W_a$ , and as energy associated with the vortices ejected from the cavity,  $W_{vv}$ . Calculations for a fully resonant first sheartone driven cavity using their kinematic model shows that the value of  $W_a$  is slightly less than  $W_{vv}$ . This would equate to the measured  $L_p$  being about 3 dB lower than the  $L_p$  that would be calculated from the net energy production. This is similar to what was observed. For the second sheartone driven cavity resonance, however, the difference between observed and calculated  $L_p$  suggests that  $W_{vv}$  is much greater than  $W_a$ .

### 5.2.3 Comparison of Phase Relations

In section 5.1, the statement of Nelson, et al., regarding the vortex formation process was quoted. Their statement implies that in the upstream half of the aperture, possibly right at the upstream edge, the phase between  $v$  velocity and cavity pressure is such that the velocity of fluid "below the neck" by some unspecified distance would be just becoming negative when the cavity pressure was at a minimum. This requires a phase of -90 degrees between  $v-p$  at the upstream edge and was used as the basis for the predicted values of phase between

the various quantities given in figure 4.19. In that chapter, the way in which the phase varies spatially was compared to the predicted spatial variation. In this section, the measured values of phase are compared to the predicted values.

Figure 5.7 shows sample time traces of one period of the resonant first sheartone of 331 Hz tone at 30 m/s measured with the probe at locations along the vortex path and spaced by about  $L/6$ . For all traces, the pressure, shown as a solid line, starts and ends at its minimum value. The measured  $u$  and  $v$  traces, shown with the dashed line, are shown on the top and bottom rows, respectively. Also plotted with each trace is the predicted value of the velocity component for that location based on the idealized vortex propagation discussed in Chapter 4 and shown in figure 4.19. Since only the phase was predicted, the amplitudes of the predicted traces is made equal to those of the measure traces, and only phase may be compared. Very good agreement is seen for both components at all locations except for the  $u$  component at  $x = 5L/6$  which varies from the predicted value by more than 90 degrees. All other traces vary from the prediction by less than 45 degrees.

The same data for the non-resonant first sheartone of 191 Hz tone at 13 m/s are shown in figure 5.8. Here, poor agreement is seen for the  $u$  component. Indeed, the measured traces are close to 180 degrees out of phase from the predicted traces. However, the traces for the  $v$  component show somewhat better agreement.

### 5.3 Summary and Conclusions

In the first section of this chapter, the model describing flow-induced cavity resonance of Nelson, et al., was described. In the second section, measurements, observations, and calculations based on that model and its underlying experiment were compared to the same quantities based on the results from the experiment performed in this investigation.

It was seen that, as predicted by the model, the first sheartone resonance data show regions of positive and negative energy production in the opening of the flow excited cavity. The positive region was centered near  $x/L$  of about 0.65 and the negative region near  $x/L$  of about 0.45. These locations are similar to those predicted by the model. Also, when the energy production is integrated over the measurement region, a positive value of power was obtained, as predicted. This value was used to estimate a sound pressure level and that

sound pressure level compared to the sound pressure level measured in the room. The results suggested that a significant fraction, about  $\frac{1}{4}$ , of the power was radiated from the cavity.

Time traces of the velocity components measured at this speed at the resonant frequency were compared to a prediction based on an idealized model of discrete vortex propagation. The comparison confirmed the observations of Nelson, et al. regarding the phase between the vortex shedding and the cavity pressure.

The energy production term was also plotted for the resonant second sheartone and the non-resonant first sheartone at 13 m/s, and for the non-resonant first and second sheartones at 6.9 m/s. In no other case were regions of negative energy production exhibited. Also, a comparison of the sound pressure level estimate from the integrated energy production term of the second sheartone driven cavity tone with the measure sound pressure level suggested that only a very small fraction of the integrated power was being radiated.

In conclusion, it can be said the measured distribution of the energy production term of the resonant cavity tone caused by the first sheartone agree with the calculations by Nelson, et al. The measured distributions for the resonant second sheartone and for the non-resonant sheartones are similar to each other, but distinctly different from the results of the resonant first sheartone at 30 m/s. The differences suggests that, while it was established earlier that the feedback mechanism for the resonant sheartones involves the Helmholtz resonance of the cavity, some fundamental difference exists between the feedback mechanisms of the first and second sheartone driven resonance. Consideration of the expression for energy production suggests that this difference is related to differences in the phase and amplitude of the fluctuating vorticity across the opening.

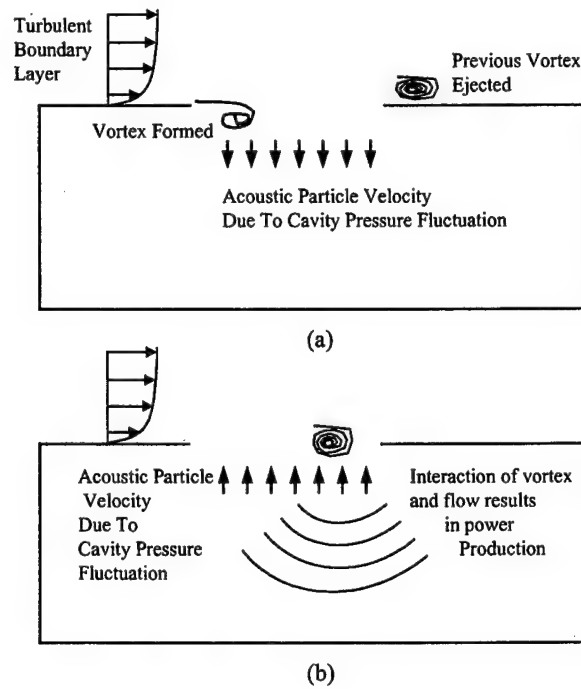


Figure 5.1: Dynamic processes of flow-induced cavity resonance

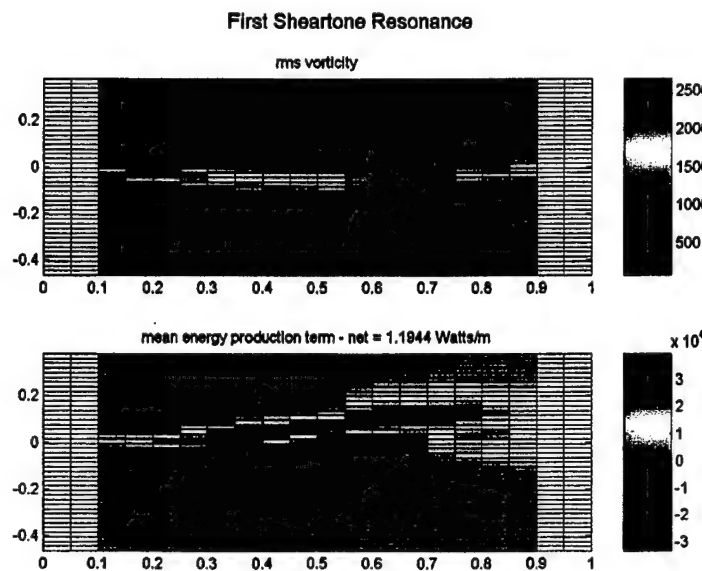


Figure 5.2: Spatial plots of rms vorticity and mean energy production term of 331 Hz tone at 30 m/s

**Second Sheartone Resonance**

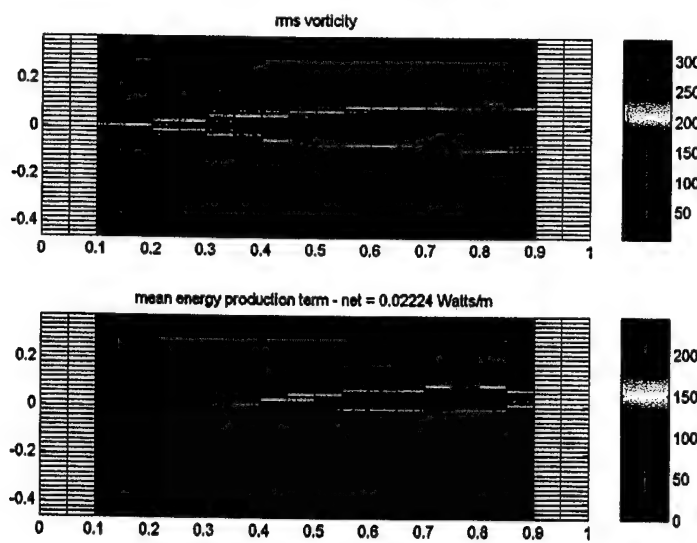


Figure 5.3: Spatial plots of rms vorticity and mean energy production term of 345 Hz tone at 13 m/s

**Non-resonant First Sheartone**

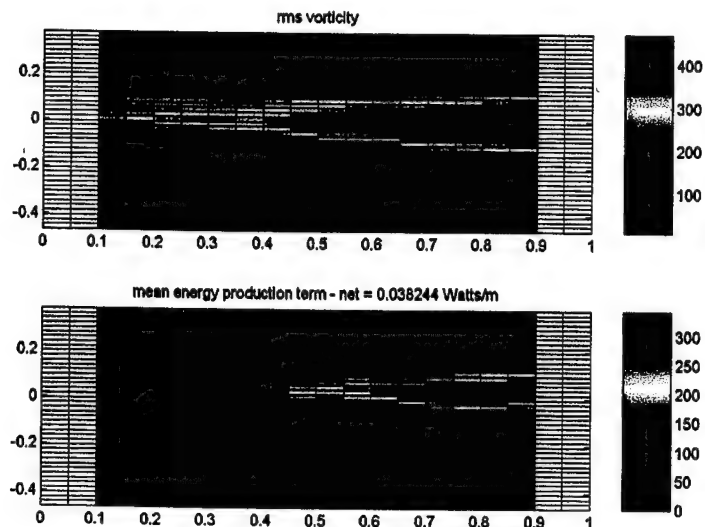


Figure 5.4: Spatial plots of rms vorticity and mean energy production term of 191 Hz tone at 13 m/s

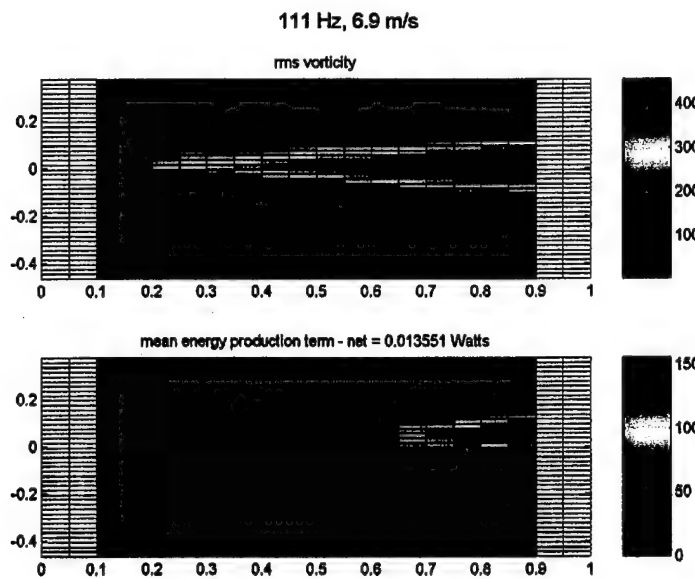


Figure 5.5: Spatial plots of rms vorticity and mean energy production term of 111 Hz tone at 6.9 m/s

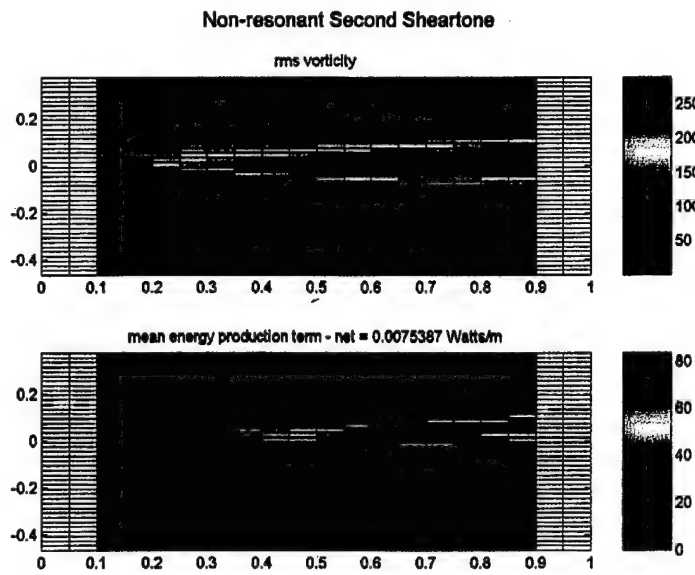


Figure 5.6: Spatial plots of rms vorticity and mean energy production term of 207 Hz tone at 6.9 m/s

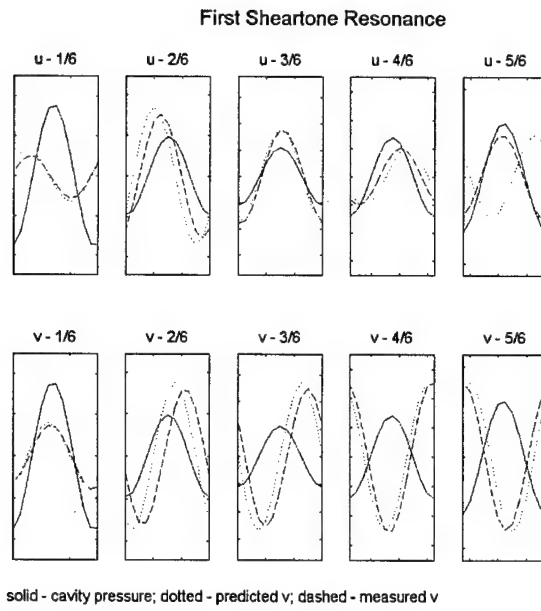


Figure 5.7: Filtered time records of  $u$  and  $v$  at 5 streamwise locations along 1 cycle of cavity pressure oscillations of 331 Hz tone at 30 m/s compared to predicted records

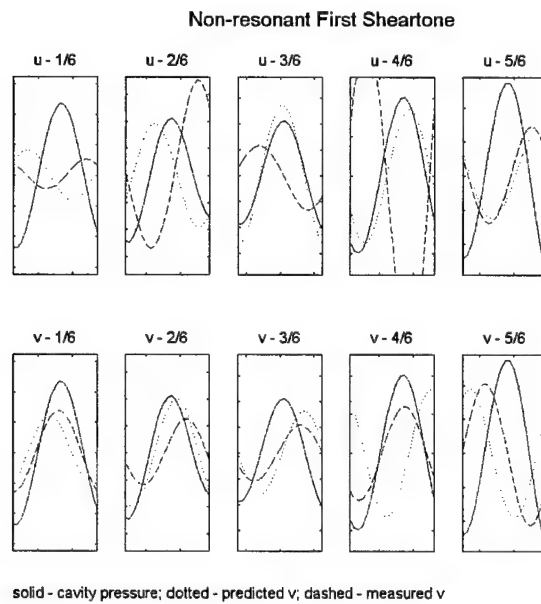


Figure 5.8: Filtered time records of  $u$  and  $v$  at 5 streamwise locations along 1 cycle of cavity pressure oscillations of 191 Hz tone at 13 m/s compared to predicted records

## 6. Techniques for Controlling Cavity Resonance

### 6.1 Background

As discussed in Chapter 1, various techniques, both active and passive, have been tried to reduce or eliminate flow-induced cavity resonance with varying degrees of success.

Passive techniques found in the literature can generally be divided into two categories: those that alter the geometry at or near the upstream or downstream edges of the cavity opening, and those using fluid mass injection. Active techniques are more difficult to categorize, but may be divided into those that use feedback from a sensor measuring the disturbance in some way, and those that do not. The latter may also be referred to as semi-active techniques.

#### 6.1.1 Passive Techniques

Passive techniques that alter the geometry near the upstream edge include the use of a fence or spoiler just upstream of the upstream edge, and the use of a ramped (or beveled) downstream and/or upstream edge. A ramp at the downstream edge is effective by altering the interaction between the shear layer and the edge, reducing the disturbance created there (Rockwell and Naudascher 1978). Alterations at the upstream edge are effective because they alter the resulting shear layer in the cavity opening. Recall from Chapter 3 that the Strouhal number of a sheartone is weakly dependent on the momentum thickness of the inflow boundary layer. This may provide some insight into understanding the details of this effect.

The fence tested by Sarno and Franke (1990) was varied in height up to approximately two boundary layer thicknesses, and was installed at about one boundary layer thickness upstream. The testing was done at Mach numbers between 0.6 and 1.5. The fence reduced the cavity pressure at all speeds tested, but was most effective at Mach numbers above 1.25.

The downstream edge ramp test by Shaw (1979) was a 45 degree bevel on the downstream edge of the opening of the rectangular cavity. The depth of the ramp was about

2 boundary layer thicknesses. The ramp reduced the cavity pressure level of the resonance by about 15 dB, but did not eliminate it. When the ramp was combined with a spoiler upstream, the resonance was nearly eliminated.

Fluid mass injection techniques tried were quite varied. They included fluid injection at the base of the cavity, fluid injection into the boundary layer on the flow surface upstream of the cavity, and fluid injection at the upstream edge of the opening at several angles relative to the free stream flow direction.

Sarohia and Massier (1977) measured the effect of fluid injection into the base of an axisymmetric rectangular cavity. At  $M=0.35$ , they found that the radiated noise was reduced by as much as 25 dB, depending on the direction. The mass flow rate required was less than 20% of the freestream  $\rho U_0$ . Fluid injection at the base of the cavity is effective by stabilizing the motion of the shear layer near the downstream edge.

Mendoza and Ahuja (1996) injected fluid upstream from a Coanda surface. Testing was conducted on a rectangular cavity at Mach numbers of 0.36, 0.44, and 0.55. They found that the boundary layer thickness and hence the shear layer thickness increased, resulting in greater than 20 dB reduction in levels at all Mach numbers. They note that at a boundary layer thickness to cavity length ratio ( $\delta/L$ ) of about 0.07, cavity tones are significantly reduced.

Sarno and Franke (1990) injected fluid at the leading edge of a rectangular cavity at Mach numbers between 0.6 and 1.5. Two different nozzles were used, one that provided fluid parallel to the free stream flow, and another that provided fluid at 45 degrees. Injection at 45 degrees was generally found to be more effective. The results of Mendoza and Ahuja (1996) suggest that the effectiveness of fluid injection at the leading edge is a result of thickening of the shear layer. However, Sarno and Franke do not report any measurements of shear layer thickness.

### 6.1.2 Active Techniques

Non-feedback active techniques tested involve oscillations of some element of the system, such as the upstream edge, at a predetermined frequency and amplitude. The fence

of Sarno and Franke (1990) described above was oscillated at frequencies up to 120 Hz. The intent was to alter the frequency of the disturbance in the shear layer. The effect was that the levels at the forced oscillation frequency were comparable to the level of the original tone. That original tone was, however, reduced by about 20 dB.

Sarno and Franke (1990) also used pulsation with the fluid injection described above. Pulsation frequencies of up to 80 Hz are reported. They found that pulsing the flow had little effect on cavity pressure oscillations.

Shaw (1998) tested an oscillating leading edge flap on a rectangular cavity at Mach numbers of 0.85 and 1.05. Oscillation frequencies of up to 100 Hz were tested. An oscillation amplitude of 20 degrees from a neutral angle of 20 degrees at 5 Hz provided 10 dB reduction. All other amplitudes and frequencies were less effective or not effective at all. The maximum deflection of the most effective condition was about one boundary layer thickness.

Shaw (1998) also tested pulsating fluid injection at the leading edge on the same cavity at the same speeds. Angles of 0 degrees (parallel to the free stream flow), and 45 and 90 degrees (into the free stream flow) were tested at pulsation frequencies up to 120 Hz. A 20 dB reduction was found with a 90 degree injection angle at 100 Hz.

Feedback active control with an upstream edge flap as the actuator was tested by Cattafesta, et al. (1997) on a rectangular cavity at low Mach numbers ( $M < 0.2$ ) and by Kook and Mongeau (1997) on a Helmholtz resonator at speeds up to about 30 m/s. Both reported reductions of up to 20 dB. Cattafesta, et al. measured the shear layer profiles under controlled and uncontrolled conditions and found that the mean shear layer was unchanged. Reductions in the fluctuating velocity profiles were found.

Sunyach and Ffowcs Williams (1986) used feedback control with a speaker in the base of a Helmholtz resonator as an actuator. Testing was done at 15 m/s. A reduction of greater than 20 dB was shown.

### 6.1.3 Objectives of Control Technique Investigation

The most commonly tested and most effective techniques make use of fluid injection or of an alteration at the upstream edge of the cavity, such as a fence, or an oscillating flap. The earlier investigations focused primarily on the effectiveness of those techniques. To the extent that the various researchers did explore why their control techniques were effective, most speculate that it was because of a change in the shear layer, generally a thickening. These past studies were primarily on rectangular cavities and at high ( $M>0.2$ ) Mach numbers.

In this chapter we seek to focus primarily on the mechanism(s) by which some of these techniques were effective. This will be done with the benefit of the insights gained in the previous chapters, and will, it is hoped, add depth to the understanding gained in those chapters. Another objective of this chapter is to determine whether these techniques are effective on cavities other than rectangular ones, and if they are effective at the low Mach numbers characteristic of automotive and naval applications.

Two established techniques were investigated in depth. They are the fence, and fluid injection at the upstream edge. In addition, the results of a third technique are presented. This technique, which was developed as part of this research effort, is a variation on the fluid injection technique. The difference from traditional fluid injection is that rather than supplying the fluid from an external source using external power, the fluid is diverted from the boundary layer.

Measurements are primarily of cavity configuration 2d ( $L=1"$ ,  $d=5.5"$ ) that was used for the measurements reported in Chapter 4. Where appropriate, measurements were also made for values of  $L$  of 1.5" and 2". Also, limited measurements were made with  $d=18"$  for reasons that are discussed. Data include cavity pressure over a range of speeds, similar to that in chapter 3, and measurements of the flow field in the cavity opening recorded simultaneously with cavity pressure, similar to that reported in Chapters 4 and 5.

Section 6.2 reports the results of measurements with a fence installed. Section 6.3 reports the results of measurements with fluid injection. Section 6.4 reports the results with a

vane installed to divert fluid from the boundary layer. Finally, in section 6.5, the findings of the various sections are compared.

## 6.2 Cavity with Fence

Two different fences were installed:  $1/8''h \times 1/8''w$  and  $1/4''h \times 1/4''w$ . Both fences were placed with the downstream edge  $1/4''$  upstream of the cavity opening. A schematic of the cavity with an installed fence is shown in figure 6.1. For each fence, cavity pressure data were collected over the speed range of the tunnel for the 5.5" deep cavity, with  $L=1''$  and  $L=1.5''$ . In addition, simultaneous with the cavity pressure data, velocity data were also obtained in a manner similar to that discussed in Chapter 4, were recorded for the  $1/4''h \times 1/4''w$  fence at 30 m/s.

### 6.2.1 Cavity Pressure Results

The cavity pressure spectrum for  $L=1''$  at the first sheartone resonant speed of 30 m/s for the no fence condition, is shown in figure 6.2, along with the spectra for the  $1/4''$  fence and  $1/8''$  fence. It is readily observed that both the level and frequency of the cavity resonance tone decrease as the fence height is increased. At frequencies below the cavity resonance, increasing fence height results in increased broadband noise levels and increased levels of the tunnel acoustic resonance at 278 Hz. At frequencies above the cavity resonance, the levels with the  $1/4''$  fence are somewhat lower than the other two.

It is instructive to examine the behavior of the various fences over the speed range studied. In figure 6.3, the normalized level of the first sheartone is plotted as a function of speed for the  $1/8''$  fence,  $1/4''$  fence, and the no fence condition of the  $L=1''$  cavity. With the  $1/4''$  fence installed, the sheartone was observed only when exciting the cavity to resonate, and thus only at the higher speeds. At the lowest speeds, it is seen that the normalized levels for the first sheartone are basically unchanged by the  $1/8''$  fence. But the  $1/8''$  fence has the effect of delaying the speed at which the tone begins to lock in to the cavity resonance, increasing it from about 15 m/s to about 22.5 m/s. Also, the peak level is lower.

Data for the  $\frac{1}{4}$ " fence are shown over a limited speed range because sheartones were observed only at higher speeds, but they appear to show similar behavior, with the resonance interaction occurring at a higher speed and with a lower overall level. The curve for the  $\frac{1}{4}$ " fence suggests that the cavity pressure levels would continue to increase with speed. Due to the upper limit of the tunnel speed, it is not possible to examine the performance of the  $\frac{1}{4}$ " fence at its peak condition. To study the  $\frac{1}{4}$ " fence at maximum performance, a Helmholtz resonator with a lower resonant frequency is needed. An 18" deep cavity, with a Helmholtz resonance frequency of 131 Hz, was installed. This cavity is referred to in table 3.1 as configuration 2dd. Data for this configuration were collected over the speed range of the tunnel with and without the  $\frac{1}{4}$ " fence installed. The results are shown in figure 6.4. They show that with the  $\frac{1}{4}$ " fence installed, the behavior of the cavity resonance over the speed range is similar to that without, except that the peak resonance occurs at a higher speed (15 m/s vs. 12 m/s) and at a lower level (about 5 dB less).

This higher speed of lock-in between the first sheartone and the cavity resonance may be understood by considering the data shown in figure 6.5. In this figure, the Strouhal numbers of the first sheartones at the three conditions are plotted. At speeds below about 25 m/s, data with the  $\frac{1}{8}$ " fence show a lower Strouhal number than seen for the no fence condition. As a result, a higher speed must be achieved before the sheartone locks in to the cavity resonance. Once the lock-in condition is reached, the Strouhal numbers are much closer but with the  $\frac{1}{8}$ " fence still slightly lower. Data for the  $\frac{1}{4}$ " fence are only available at the lock-in condition, and they are slightly lower in Strouhal number than the  $\frac{1}{8}$ " data. However, it is likely that were the first sheartone with the  $\frac{1}{4}$ " fence observable at speeds below resonance, its Strouhal number would be lower than that of the  $\frac{1}{8}$ " fence data.

Another perspective on the effectiveness of the  $\frac{1}{8}$ " and  $\frac{1}{4}$ " fences is provided by considering the normalized level of the cavity tone. By cavity tone it is meant the peak in the frequency spectrum that is most clearly due to the Helmholtz resonance response of the cavity, regardless of whether it is excited by broadband turbulence, or a sheartone of any order. This level is plotted as a function of speed for the 330 Hz Helmholtz resonance frequency with  $L=1$ " in figure 6.6 and for the 395 Hz Helmholtz resonance frequency with  $L=2$ " in figure 6.7.

In figure 6.6, the cavity with no fence and  $L=1"$  is excited to resonance by the second sheartone at 13 m/s. That resonance is completely eliminated by the  $1/8"$  fence and by the  $1/4"$  fence. In figure 6.7, the cavity with  $L=2"$  and no fence resonates at 18 m/s, apparently due to excitation by the third order sheartone. This resonance is completely eliminated by the  $1/8"$  and  $1/4"$  fences. However, these fences do not have the same effect on the second sheartone resonance. With no fence, the second sheartone is fully resonant between about 25 and 30 m/s. The fences have the same effect on this resonance that they had on the first sheartone resonance with the  $L=1"$  cavity. That is, they significantly reduce, but do not eliminate, the resonance. This suggests a scaling relationship among the fence height, opening length, flow speed, and fence effectiveness. A more detailed examination of the scaling issue is beyond the scope of this research.

### 6.2.2 Results of Flow Field Measurements

Flow field measurements were made for  $1/4"$  high fence installed on the cavity with  $L=1"$  and  $d=5.5"$ . This configuration was selected because of the greater contrast seen in the cavity pressure data compared to the uncontrolled configuration. The results of these measurements are described in this section.

In figure 6.8, the fence and no fence mean velocity profiles at 30 m/s are plotted. It is seen that the profiles with a  $1/4"$  high fence are displaced upward by about 0.4". The additional upward displacement is attributed to the separation of the flow as it passes over the fence.

Profiles of  $u_{rms}$  with and without the fence are shown in figure 6.9. The most significant difference observed is that the profiles in the downstream part of the opening with the  $1/4"$  fence has two distinct peaks, one at around  $y=0.5"$  and one at around  $y=0.0"$ . The profiles with no fence hint at the presence of a secondary peak below the primary one, however, as we examine the coherence and phase between the velocity components and the cavity pressure, we will see that something distinctly different is happening with the fence installed.

In figure 6.10, the  $u$  and  $v$  velocity spectra are shown at  $(x=0.885, y=0.55)$ ,  $(x=0.885, y=0.25)$ , and  $(x=0.885, y=0.01)$ . These locations were chosen to correspond most closely to the locations of the two peaks in the  $u_{rms}$  profiles and the minimum between them. As with the spectra shown in Chapter 4, it is difficult to discern peaks in the velocity spectra. However, it is possible, and we see that the peaks are lower or non-existent at the location corresponding to the minimum in the profiles. More useful are the coherence plots between the velocity components and the cavity pressure, which are shown in figures 6.11 and 6.12. We see that for  $v-p$ , the coherence is very high at the upper peak location, lower, but still significant at the lower peak location, and nearly zero at the minimum location. The difference is less pronounced for the  $u-p$  coherence, but still, at the minimum location, the coherence is lower than at the two peak locations.

The underlying reality of the two peaks in the  $u_{rms}$  profiles is revealed by the spatial phase and coherence plots between  $v$  velocity and cavity pressure, shown in figure 6.13. Recall from Chapter 4 that for a vortex convecting along the opening, we expect the phase between  $v-p$  to be increasing in the  $x$  direction and essentially constant along the  $y$  direction. What we see in figure 6.13 is that the phase is increasing in the  $x$  direction, but there is a discontinuity in the  $y$  direction. The values of the phase above and below the discontinuity differ by about 180 degrees. This is what we expect the phase between  $u-p$  to do for a single vortex convecting along the opening. But this is the  $v-p$  phase, so we must have a vortex pair convecting along the opening. Both are shed at the resonance frequency of 321 Hz, but they are shed a half cycle apart from each other, so they appear in the phase plot to be 180 degrees out of phase. They also, of course, travel on two separate paths, one above the fence top, and one below. The line dividing them is seen in the spatial coherence plot as a line of very low coherence separating two regions of rather high coherence.

The spatial distribution of phase between  $u-p$ , shown in figure 6.14, confirms the twin vortex nature of the flow. For a single vortex, the  $u-p$  phase plot would look similar to the  $v-p$  phase plot discussed above. However, for the vortex pairs described above, the plot should have an inner region, centered on the dividing line between the paths, increasing in phase, and two outer regions, increasing in phase, but 180 degrees out of phase with the inner region. Though less distinct than the  $v-p$  phase plot, this is essentially what is seen.

The data shown in the figure shows that the two vortices are separate, but they are not equal. It is clear from the spatial coherence plots that the lower vortex is weaker than the upper one. It is made clearer so by the rms vorticity and mean energy production term plots in figure 6.15. It is difficult to discern the presence of vorticity along the lower vortex path because it is so much less than the vorticity of the upper vortex. And, as a consequence, the mean energy production appears to come entirely from the upper vortex.

### 6.2.3 Discussion

It is clear from the data that a fence can be an effective way of reducing cavity resonance. However, the effectiveness of the fence depends on several parameters, including fence height, cavity opening length, flow speed, and cavity resonance frequency. A detailed examination of the scaling laws for these parameters is outside the scope of this research, but we can offer several hypotheses suggested by the data.

Reduction in level of the cavity resonance tone increases with fence height,  $h$ . It is likely that the reduction would scale with some boundary layer property, such as displacement thickness,  $\delta^*$ . The relative effectiveness of the two fences tested was quite different for the two values of  $L$  tested. Therefore it is also likely that the ratio  $h/L$  is significant. It is less clear what the dependence is on flow speed. Because the fence lowers the Strouhal number of the sheartones, peak resonance occurs at a higher speed with the fence installed. This should be accounted for in designing a fence for use in a specific application.

The flow field results are less clear, but more interesting. The vortex pairing nature of the unsteady flow field is somewhat similar to vortex shedding from a cylinder or a trailing edge. Application of flow visualization to this problem would likely be illuminating.

The plot of the mean energy production term is contrary to expectations. Most of the literature talks about the mechanisms of flow-induced cavity resonance in terms of interaction with the downstream edge of the opening. And in Chapter 5, the data suggested that energy production at all speeds, resonant and non-resonant, was associated with the downstream edge. However in figure 6.15, it is seen that the energy production is

concentrated in a region well above the cavity opening, and well above the fence height. This is a result that invites further examination.

### 6.3 Cavity with Air Injection

Measurements were made with air injection into the cavity just below the upstream edge of the opening. Air was supplied by a ProAir PRF5530 air compressor with a 30 gallon tank and a 5.5 HP motor. The pressure at which air was supplied to the cavity was controlled by a Cambell Hausfeld MP5148 regulator and the volume flow rate was measured using a Cole-Parmer spring loaded direct reading flowmeter installed upstream of the regulator. Air from the regulator was supplied through 3/16 ID Tygon tubing to a manifold installed inside the cavity just below the upstream edge of the opening. The manifold design and installation arrangement are shown in figure 6.16.

Volume flow rates of air injection of 2, 3.6, 4.2, 4.6, 5, 5.5, 6, and 7 SCFM were tested at 30 m/s. Also, flow rates of 3.6, 4.6, 5.5, and 7 SCFM were tested over the speed range of the tunnel. Finally, detailed measurements of the flow field were made at 30 m/s with 4.6 SCFM of fluid injection. All of these measurements were performed for cavity configuration 2d ( $L=1"$ ,  $d=5.5"$ ).

#### 6.3.1 Cavity Pressure Results

In figure 6.17, the cavity pressure spectra at a free stream velocity of 29.6 m/s with no injected flow, 4.6 SCFM of injected flow, and 7 SCFM of injected flow are shown. It is seen that 4.6 SCFM of flow injection reduces the level of the cavity resonance by about 10 dB, while a flow rate of 7 SCFM reduces the level by about 25 dB. However, increasing flow rates of air injection also result in increasing broadband noise levels at frequencies away from the tone. In fact, at 7 SCFM, the broadband noise levels at frequencies away from the tone are completely controlled by the noise from the air injection. This is illustrated in figure 6.18, where the cavity pressure spectra with 7 SCFM of air injection are shown for free stream velocities of 0, 12 m/s, and 27 m/s. These spectra are essentially the same except for the cavity tone (and tunnel acoustic resonance) seen at 27 m/s. It should be

noted that no attempt was made to quiet the flow injection system. It is likely that with significant modifications to the design, broadband noise could be reduced.

The effect on the cavity resonance level of the rate of fluid injection is shown in figure 6.19. Here, the normalized level of the cavity tone is plotted as a function of the volume flow rate of fluid injection into the cavity. It is seen that 2 SCFM of fluid injection actually increases the level of the tone slightly. At 3.6 SCFM, the tone is back down to the no flow injection level, and from 4.2 SCFM to 6 SCFM, the level declines steeply to about 21 dB below the no flow injection level. Increasing the flow to 7 SCFM reduces the tone by another dB or so. Clearly, however, the range of flow rates between 4.2 and 5 SCFM is a critical region in which a small increase or decrease in the flow rate has a significant impact on the tonal level.

It will be helpful to consider the flow rate of fluid injection relative to the properties of the flow over the cavity. It is reasonable to hypothesize that the flow injection rate required for a given amount of reduction is proportional to the free stream velocity. However, because the fluid injection rate,  $Q_i$ , is in units of volume/time, it must be scaled by a quantity with the same units. It is therefore suggested that  $U_0$  multiplied by  $A$ , the area of the cavity opening, which we will call  $Q_b$ , be used to scale the injection rate. This quantity will be referred to as  $Q_b$ . For the data in figure 6.18,  $U_0$  was 29.6 m/s. The corresponding value of  $Q_b$  is therefore 182 CFM. Thus the ratios of injection flow rate,  $Q_i/Q_b$ , that were tested range from 0.011 to 0.038. The center of the critical region was at a ratio of approximately .026. Use of this ratio is suggested as a starting point for possible future efforts to examine the scaling laws governing the use of fluid injection to reduced cavity resonance.

In no case were sheartones observed in the cavity pressure spectra with air injection occurring. Therefore, it is not possible to plot the levels of speed dependent tones. Instead, in figure 6.20, the levels of the cavity resonance normalized by  $q$  are plotted as a function of  $U_0$  for 4 flow rates as well as for the no fluid injection condition. Because the ratio  $Q_i/Q_b$  varies with speed, data shown as a function of  $U_0$  are labeled by absolute flow rate rather than the ratio. The second sheartone excited resonance seen at about 13 m/s with no flow is not seen with air injection at any flow rate. At speeds below about 20 m/s, it is seen that the

normalized level is decreasing with speed. This is because the levels at these speeds are controlled in part or completely by the rate of fluid injection. Note how the levels also increase with increasing fluid injection rates.

It therefore makes more sense for speeds well below resonance to normalize the levels by  $q_i$ , the dynamic pressure corresponding to the effective velocity of the air being injected into the cavity. This effective velocity is determined by multiplying the volume flow rate,  $Q_i$ , by the area of the manifold opening from which the fluid is injected into the cavity. Data normalized this way are shown in figure 6.21. These normalized levels collapse onto each other rather well and are essentially constant up to about 18 m/s. This demonstrates that the level of the cavity tone at these speeds is controlled primarily by the injection flow rate, not the freestream tunnel velocity, and that the level is proportional to  $q_i$ .

At speeds above about 18 m/s, the cavity begins to resonate. At flow rates of 4.6 SCFM and 5.5 SCFM, the tone peaks at a speed of about 26 m/s then begins to decrease. At flow rates of 3.6 SCFM and 7 SCFM, the level is still increasing when the upper speed limit of the wind tunnel is reached.

Because no sheartones are observed, the frequency, not the Strouhal number, of the cavity tones are plotted as a function of speed. This plot is shown in figure 6.22, where frequency of the cavity tone as a function of speed is given for 4 values of fluid injection, as well as for the no flow condition. The no fluid injection condition shows the presence of excitation by the second sheartone between 10 and 20 m/s. No particular trend is seen below 22 m/s with flow applied, but above that speed, the cavity resonance frequency for all conditions is seen to increase with speed with roughly the same slope. The values of frequency with fluid injection present are essentially the same, regardless of flow rate, but the frequency with no fluid injection is distinctly higher.

### 6.3.2 Results of Flow Field Measurements

Flow field measurements were made on the  $L=1"$ ,  $d=5.5"$  cavity with fluid injected at a rate of 4.6 SCFM. This rate was chosen because it is in the center of the critical region,

where the reduction in the level of the flow-induced resonance is most sensitive to changes in fluid injection rate.

In figure 6.23, mean velocity profiles at  $x=0.135"$ ,  $0.485"$ , and  $0.935"$  are shown. The effect of the fluid injection is seen very clearly in the profile at  $x=0.135"$ , where the mean velocity is seen to decrease between  $y=0.5"$  and  $y=0.0"$ , then increase again due to the fluid injection. The peak due to the fluid injection peaks at about  $0.4U_o$  at  $y=-0.2"$ , then quickly decreases. This peak is completely gone by the  $x=0.485"$  profile.

In figure 6.24, mean profiles with fluid injection are compared to those without fluid injection at the same speed, which were discussed in Chapter 4. We see that at all locations shown other than the region immediately downstream of the injection point, the mean velocity is lower with fluid injection present, suggesting that fluid injection thickens the shear layer. We also see in figure 6.25 that fluid injection reduces the  $u_{rms}$  levels everywhere except near the point of injection. It is unclear whether this is the cause of the reduced cavity tone level, or the result of it.

Spectra of  $u$  and  $v$  at  $(x=0.485, y=0.035)$  and  $(x=0.685, y=0.075)$  are shown in figure 6.26. At both locations, the cavity resonance tone at 330 Hz stands at least 20 dB above the background levels in both the  $u$  and  $v$  spectra. The second harmonic is also present and is slightly stronger at the more downstream location.

Coherence between  $u-p$  and  $v-p$  are plotted for both locations in figures 6.27 and 6.28, respectively. The coherence is essentially perfect for both components at both locations. The second harmonic also appears strongly in the coherence spectra and is slightly higher at the downstream location for the  $u-p$  spectra.

The spatial distribution of coherence and phase is shown in figure 6.29 for the  $v-p$  pair and in figure 6.30 for the  $u-p$  pair. For both pairs, the phase follows the predicted behavior discussed in Chapter 4, with the exception of a region near the point of fluid injection. Fluid injection has the effect of altering the phase and slightly lowering the coherence in this region. Apart from this region however, there is no substantial difference between these plots and the plots for the 30 m/s no-flow condition shown in Chapter 4.

Plots of spatial distribution of the energy production term with fluid injection, shown in figure 6.31, and without fluid injection, shown in figure 5.2, may be compared. Both show

regions of negative and positive energy production in roughly the same spatial arrangement. However, with fluid injection, the magnitude of the peak positive energy production is more than twice that of the peak negative energy production. Without injection, those magnitudes were nearly equal. Also, the results for the resonant second sheartone, shown in figure 5.3, and the resonant first sheartone with the fence installed, shown in figure 6.15, show no region of negative energy production. The levels of these cavity resonance tones are also much lower. This suggests that the relative strength of regions of negative energy production is an indication of the strength of a cavity resonance and that the presence or absence of such regions indicate a fundamental difference between resonances that do and do not exhibit such a region.

### 6.3.3 Discussion

It is not surprising that the effect of air injection underneath the leading edge on the cavity resonance tone depends on the rate of injection. The interesting result is the non-linear nature of the effect as a function of injection rate. It suggests that there is a "critical rate" at which a significant change in the flow field in the opening occurs.

The flow field data, which were taken for a flow rate in the critical region, can be examined for clues to what happens in the flow field to reduce the cavity tone. Some differences between the velocity field with and without air injection are noted. First, the mean velocity in the measured region is noticeably lower with injection, except in the area just in front of the injection point. It is also the case that  $u_{rms}$  is lower with injection except in the region just downstream of the point of injection. However, the phase between the velocity components and the cavity pressure show the same general trends with injection as without, except in the region of the injection point.

Perhaps the most interesting, however, is the distribution of the mean energy production term. Here is seen what appears to be the beginning of a shift, from a pattern for the fully resonant first sheartone condition, where there are positive and negative regions of nearly equal magnitude, to one more like the non-resonant first sheartone, where there is no region of negative energy production. This suggests that in the critical region, increasing fluid injection rate corresponds with a decrease in amplitude of the negative energy production

region from being approximately equal to the positive region, to being non-existent. These results also suggest that there may be a fundamental difference between cavity resonance tones that have a region of negative energy production, and those that do not.

#### 6.4 Cavity with Boundary Layer Diversion

In the previous section, the injection of fluid at the upstream edge of the opening was seen to be an effective technique for significantly reducing or eliminating flow-induced cavity resonance. It is, however, neither simple nor inexpensive to implement in a practical design. Fluid injection requires an external source of compressed air and an extensive piping system, terminating in a potentially complex manifold. Also, if low broadband noise levels are desired, care must be taken in to design a quiet system.

An alternative way of delivering fluid into the cavity is to divert it from the flow field. A device (Zoccola 1999) for taking air from the inflow boundary layer and injecting it just below the upstream edge of the cavity opening was installed in the cavity, and is illustrated in figure 6.32. This device was simple to implement, and was not a significant source of broadband noise.

The genesis for this device was the suggestion that a slit just upstream of the cavity opening would result in fluid being diverted into the cavity and that this fluid might result in a reduction in cavity resonance similar to that seen with fluid injection. This idea was tested, and it was found that, while some fluid was diverted into the cavity, the peak resonance level was reduced only about 1 dB.

To increase the amount of fluid diverted into the cavity, a design was produced similar to the slit, but with the downstream edge of the slit opening raised. A height of 1/8" was selected because it was approximately equal to the momentum thickness. As initially implemented, this left the upstream edge of the cavity opening 1/8" higher than the downstream edge. In order to avoid confusion over whether the results with diversion were due to the effect of the diverted fluid or due to the difference in elevation between the upstream and downstream edges of the opening, the downstream edge was also raised in the final design. Figure 6.32 is an illustration of this design.

It is instructive to compare the rate at which fluid is diverted into the cavity with boundary layer diversion to the rate with fluid injection. For fluid injection, it was possible to directly measure flow rate. For boundary layer diversion, the flow rate could not be measured directly, so an estimate of the volume flow into the cavity was made based on the measured boundary layer profile. The profile was numerically integrated from 0 to 1/8" and the result was used to calculate the volume flow rate into the cavity. It was estimated that at a free stream velocity of 30 m/s, the volume flow rate was 12.4 SCFM. This is significantly higher than the rates of external fluid injection described in the previous section. However, unlike fluid injection, this flow rate will be roughly proportional to the freestream velocity. Thus at  $U_0 = 15$  m/s, the flow rate would be approximately 6.2 SCFM. Also, the results with fluid injection suggested that flow rates greater than 7 SCFM would be only slightly more effective.

In this section, measurements made with the boundary layer diversion device installed are discussed. Comparisons between boundary layer diversion and fluid injection are made for the flow field, as well as for the cavity pressure results.

#### 6.4.1 Cavity Pressure Results

In figure 6.33, the cavity pressure spectra at 30 m/s,  $L=1"$ ,  $d=5.5"$ , with and without boundary layer diversion are plotted. It can be seen that the cavity resonance tone is completely eliminated. Similar results were found for all values of  $L$  tested.

Unlike the air injection condition, the first sheartone was observed at all speeds for  $L=1"$  and greater with boundary layer diversion. These can be seen in figure 6.34, where spectra for the  $L=1"$  opening at 12 speeds are plotted. The level and frequency of these tones were tabulated for  $L=1"$ ,  $L=1.5"$ , and  $L=2"$ . The normalized level of the first sheartone for  $L=1"$  as a function of speed is plotted in figure 6.35. Also plotted are corresponding levels for the no boundary layer diversion condition. It is seen that the levels with boundary layer diversion are in all cases lower than without. In fact, the levels with diversion are nearly constant, while the levels without are constant at low speed, but increase rapidly when the sheartone locks in to the cavity resonance.

The frequencies were used to calculate Strouhal numbers,  $fL/U_0$ , which were plotted as a function of speed in figure 6.36. Also shown are the Strouhal numbers of the corresponding no diversion conditions. It is seen that the Strouhal numbers with boundary layer diversion are significantly lower for all values of  $L$ . Since the values of  $L$  and  $U_0$  are the same, this means that the frequencies are lower and thus it may be that cavity resonance does not occur because the sheartone frequency is well below the cavity Helmholtz resonance frequency. This suggests that at speeds beyond the speed limit of the wind tunnel, the cavity would still resonate with boundary layer diversion, as it did with the  $\frac{1}{4}$ " fence.

The maximum speed of the tunnel is fixed. To determine whether the cavity can be excited to resonate with boundary layer diversion installed, cavity configuration 2dd, with  $d=18$ " and a Helmholtz resonance frequency of 131 Hz, was used. This would allow the cavity to be excited at a lower speed. Measurements with this cavity were made, and normalized cavity pressure level as a function of speed is plotted in figure 6.37 for  $L=1$ " both with and without boundary layer diversion. It is seen that the cavity with the diversion does indeed resonate. Because of the reduced Strouhal number effect of boundary layer diversion, the resonance occurs at a higher speed with diversion than without, 20 m/s vs. 12 m/s. Although resonance does occur, the peak cavity pressure level is 20 dB lower with the boundary layer diversion than without for the  $d=18$ " cavity. Additionally, the peak pressure level is 10 dB lower than the peak level for the  $d=5.5$ " cavity with no diversion.

This reduced Strouhal number effect is not observed with air injection. This is confirmed by the data in figure 6.38. In this figure, normalized levels for the  $d=18$ " cavity are plotted with and without air injection. In this case we see that air injection greatly lowers the peak cavity resonance level, but the peak occurs at the same speed with and without injection.

#### 6.4.2 Results of Flow Field Measurements

Flow field measurements were made at 30 m/s with boundary layer diversion. In figure 6.39, mean velocity profiles are compared to those with air injection reported in section 6.3. Also shown are profiles with no control implemented. It can be seen that the peak in the

mean profile due to the diverted fluid, seen at  $y = -0.2"$  on the  $x=0.135"$  location, is somewhat higher than the corresponding peak for air injection. However, the difference is less than might be expected based on the difference in volume flow rate of fluid into the cavity. The estimated volume flow rate for injection at 30 m/s was 12.4 SCFM, which is nearly 3 times the 4.6 SCFM of fluid injection. This difference may be accounted for, at least in part, by the greater span (4.5") over which the boundary layer fluid is diverted compared to the injected fluid (3.75").

Profiles of  $u_{rms}$  for boundary layer diversion and for air injection are plotted together in figure 6.40, along with the profile with no control. For both of the control techniques, the peak in the upstream profile at  $y=-0.2$  is due to turbulence associated with the fluid jet. It can be seen that, unlike the air injection case, for diversion the peak persists further downstream and is still present at  $x=0.885$ . The peak just above  $y=0.0"$  is associated with the free shear layer and is stronger for diversion than for injection. However, both techniques show a substantial reduction in turbulence intensity compared to the uncontrolled case.

Spectra of  $u$  and  $v$  at  $(x=0.335", y=-0.085")$  and  $(x=0.735", y=-0.085")$  are shown in figure 6.41. At this speed, the first sheartone was observed in the cavity pressure spectrum with a frequency of 229 Hz. This tone is not seen in the velocity spectra, which have essentially no tonal character. Broadband energy associated with this tone is seen in the coherence between  $u-p$  and  $v-p$ , the spectra of which are shown in figures 6.42 and 6.43, respectively.

Spatial plots of phase and coherence are shown in figure 6.44 and 6.45 for  $v-p$  and  $u-p$ , respectively. Coherence is seen to be greater than 0.1 in a sufficient number of locations to make the  $v-p$  phase results meaningful. The phase between  $v-p$  is in all respects similar to the expected behavior described in Chapter 4 and to the  $v-p$  phase plot for the 191 Hz first sheartone at 13 m/s shown in figure 4.23. Coherence between  $u-p$  is generally lower than for  $v-p$  and the phase between  $u-p$  has no discernible order to it.

Spatial plots of rms vorticity and the mean energy production term are shown in figure 6.46. In the vorticity plot, two bands of vorticity are seen near the upstream edge, the upper corresponding to the free shear layer, and the lower corresponding to where the fluid

diverted from the boundary layer is injected into the cavity. These two streams appear nearly equal in strength and continue along the length of the opening. By contrast, in the vorticity plot for the air injection, shown in figure 6.31, the vorticity near the upstream edge is much weaker and is not equal for the upper and lower streams. Further downstream, the upper band of vorticity appears to gain strength. The difference between the external fluid injection case and the boundary layer diverted fluid injection case is that the fluid injection condition is a resonant sheartone, while the diversion condition is not. Thus, the vorticity in the fluid injection case is associated with the discrete vortex shedding which is generating the cavity tone. The vorticity in the diversion case is associated with the shear layer but is not sufficiently organized to excite cavity resonance.

## 6.5 Comparison of Techniques Investigated

The control techniques discussed above may be compared in terms of, first, their effect on the sheartones and cavity tones in the cavity pressure spectra, and second, the mechanisms that cause them to be effective. The effect on tones in the pressure spectra is considered in terms of how the Strouhal number of the tones is affected and how the level of the peak resonance is affected. In examining the mechanisms by which these techniques are effective, primary consideration is given to the phase speed at which the vortices convect along the cavity opening.

### 6.5.1 Comparison of Cavity Pressure Results

It is surprising to note that based on the cavity pressure results, boundary layer diversion shows greater similarity to the fence than to air injection in its effect on the Strouhal number behavior of sheartones. Both the fence and diversion reduce the Strouhal number of speed dependent tone so that peak resonance occurs at a higher speed. Both also reduce the level of the peak resonance. However, diversion is noticeably more effective, reducing both the Strouhal number and the level of peak resonance by a greater amount.

Air injection, which might have been expected to work in a manner similar to boundary layer diversion, had no observable effect on the free stream velocity at which peak excitation

occurred. No statement may be made about its effect on Strouhal number of non-resonant sheartones, since none were observed. Air injection itself was a major source of broadband noise, and likely would make any sheartones unobservable. However, since the speed at which peak resonance occurred was unchanged by air injection, it is likely that if non-resonant sheartones were present, but not detected, their Strouhal numbers were unaltered by air injection.

The fact that the frequency of the cavity resonance tone with injection present still increased slightly with increasing  $U_0$  suggests that the feedback mechanism for the resonating condition still operates with air injection present. But it is possible that injection destroys the feedback mechanism that produces sheartones.

It was shown in the discussion in Chapter 3 that at low Mach numbers, Strouhal number is proportional to  $U_c/U_0$ . Based on that discussion, it is worth investigating whether the reduced Strouhal numbers seen with the fence and with diversion are due to the effect of those devices on the average convective velocity of vortices in the opening. Table 6.1 is a list of the mean convection velocity over the measured region of the cavity opening. The convective velocity with boundary layer diversion is about 0.6 times that of the uncontrolled  $U_c$ . This is similar to the difference in Strouhal number, where diversion reduces Strouhal number to about 0.5 times its uncontrolled value.

For the fence, however, this similarity between reduction in Strouhal number and reduction in convection velocity is not seen. In fact, with the fence,  $U_c$  increases to about 1.2 times the uncontrolled value, while Strouhal number is reduced to about 0.8 times the uncontrolled value. These results suggest that, at least for the fence, the lower Strouhal number of the sheartones is not explained by a lower convection velocity. The lower convection velocity may explain the lower Strouhal number seen with boundary layer diversion, however, the fence results suggest that it is possible that some other explanation applies.

Table 6.1: Mean Convection Velocity

Cavity Configuration	$U_c$
Uncontrolled	0.39
Fence	0.49
Air Injection	0.40
Boundary Layer Diversion	0.23

### 6.5.2 Comparison of Phase

As was done in section 4.3.4, phase between v-p along the path of maximum vorticity was extracted for the cavity tone with the  $\frac{1}{4}$ " fence, with 4.6 SCFM of air injection, and with boundary layer diversion, as discussed above. In figure 6.47, these are compared with data for the uncontrolled cavity tone at 30 m/s. Recall that the uncontrolled tone had the highest level; the air injection reduced the level by about 12 dB with regions of negative energy production reduced in magnitude, but still present; the  $\frac{1}{4}$ " fence reduced the level by about 15 dB, and resulted in no regions of negative energy production; finally, boundary layer diversion completely eliminated the cavity resonance, reducing the level of the first speed dependent tone by greater than 40 dB. Now, note that with increasing reduction of the cavity tone, we see in the phase plot increasing value of the phase across the opening of the cavity. Also note the decrease in slope between the uncontrolled case and the controlled cases. This suggests a relationship between the phase between v-p and the strength with which the cavity tone is excited. A possible explanation for this may be related to the Nelson's model described in Chapter 5. It was seen there that at cavity resonance, the phase between v-p controlled the timing of the vortex shedding at the upstream edge. Altering this phase would alter that timing and result in weaker coupling between the vortex shedding process and interaction of the vortex near the downstream edge of the opening.

The phase speed curves based on the phase curves shown in figure 6.47 were calculated as described in Chapter 4 and are shown in figure 6.48. Observe here the region  $0.7 < x/L < 0.9$ . With no control, this region corresponds to a significant deceleration of the vortex as it convects along the opening. With increasing amounts of reduction of the cavity tone level, the slope increases, until finally, the slope corresponding to boundary layer diversion shows a significant acceleration in this region. Based on these results, successful control of cavity resonance is associated with increasing the acceleration of the convected vortex as it approaches the downstream edge of the opening. This observation makes sense when considered with the approach of Tang and Rockwell (1983). In their model, the feedback process is based on a dipole source at the downstream edge due to the interaction between the vortex and that edge. If the vortex is accelerating rather than decelerating, it

may no longer be interacting with that edge, or may be doing so more weakly. This would result in a reduction of strength of the cavity resonance.

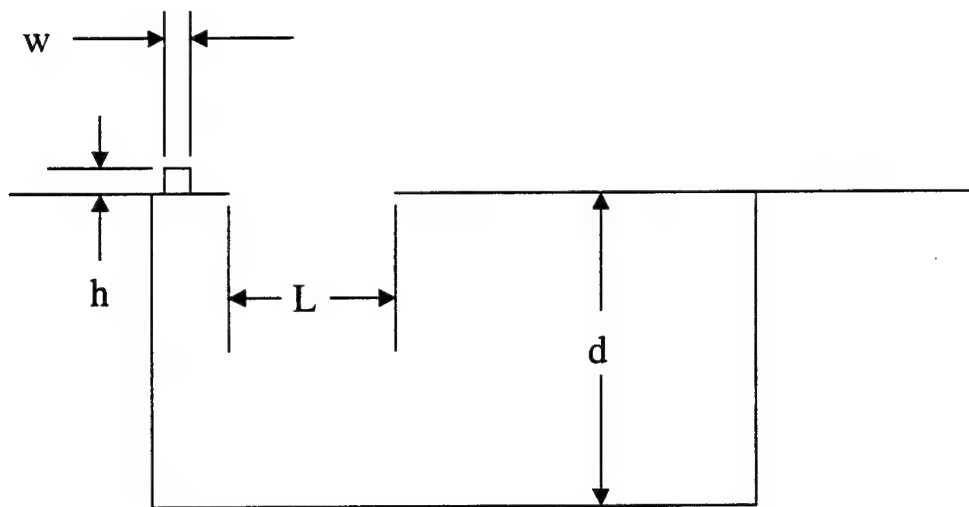


Figure 6.1: Schematic of cavity with fence installed

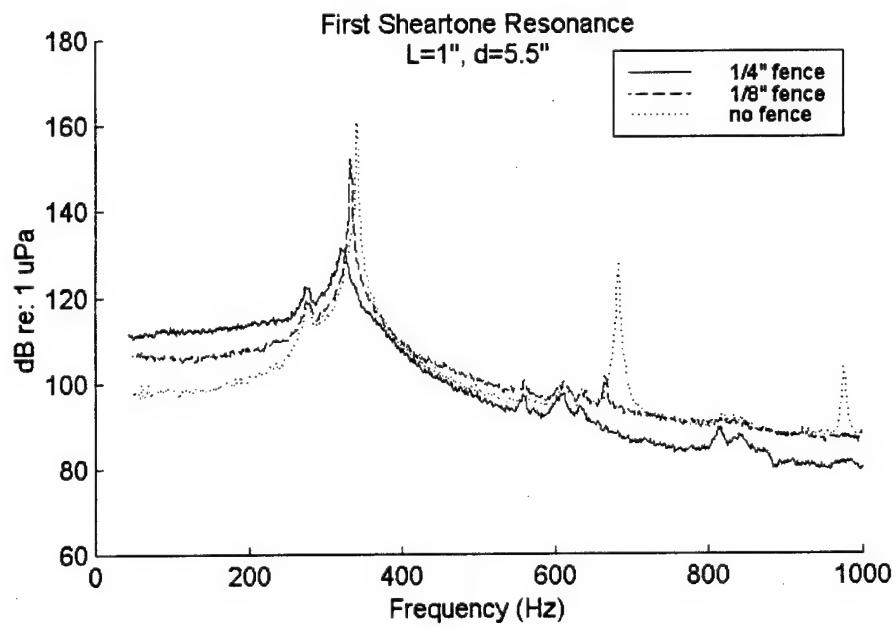


Figure 6.2: Cavity pressure spectra at 30 m/s for configuration 2d  
 with  $\frac{1}{4}"$  fence,  $\frac{1}{8}"$  fence, and no fence

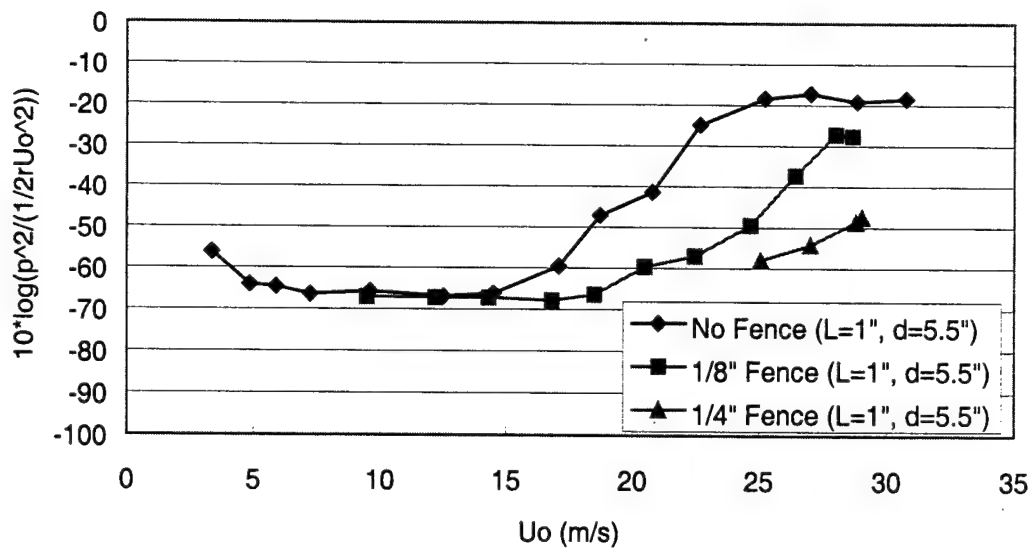


Figure 6.3: Comparison of normalized level of first sheartone for cavity configuration 2dd with  $\frac{1}{4}$ " fence,  $\frac{1}{8}$ " fence, and no fence

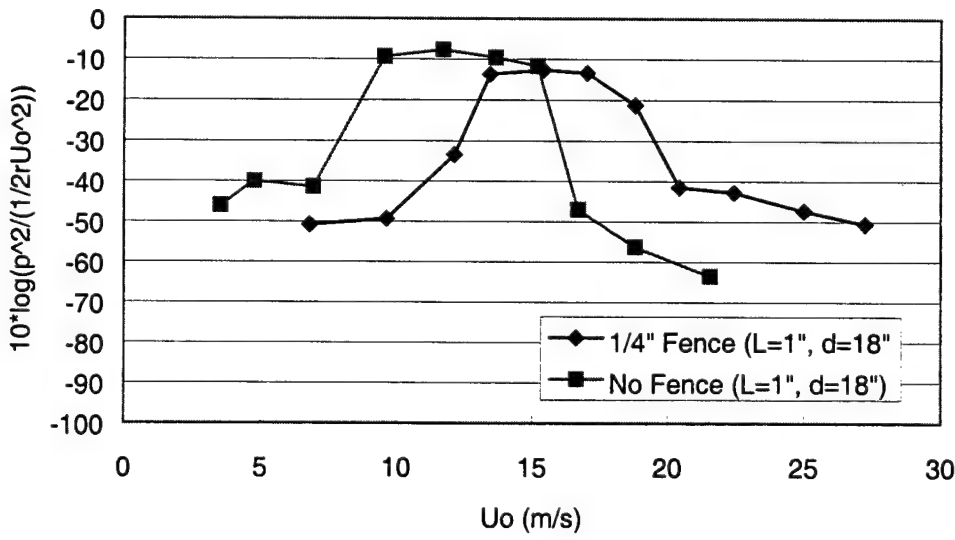


Figure 6.4: Comparison of normalized level of first sheartone for cavity configuration 2d with  $\frac{1}{4}$ " fence and no fence

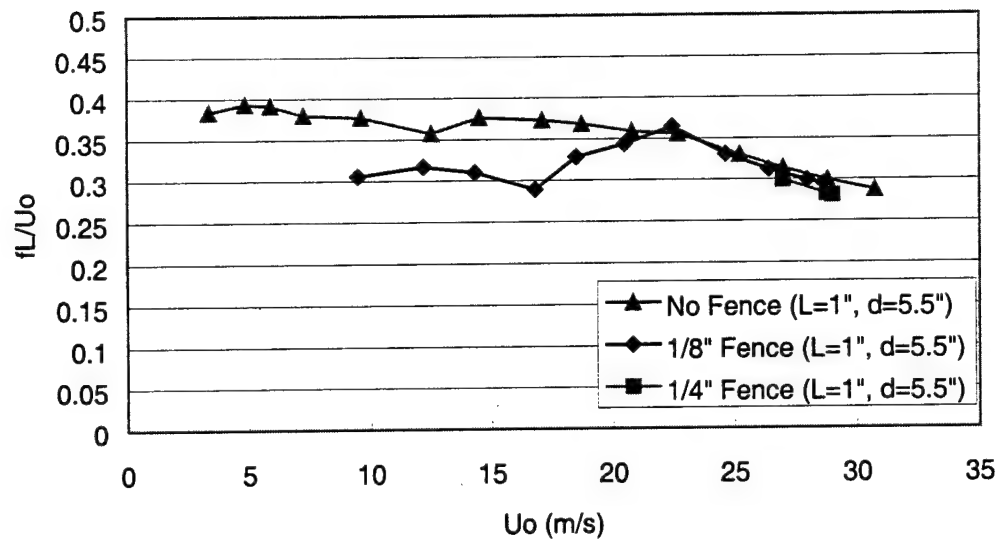


Figure 6.5: Comparison of Strouhal number of first shear tone for cavity configuration 2d  
with  $\frac{1}{4}$ " fence,  $\frac{1}{8}$ " fence and no fence

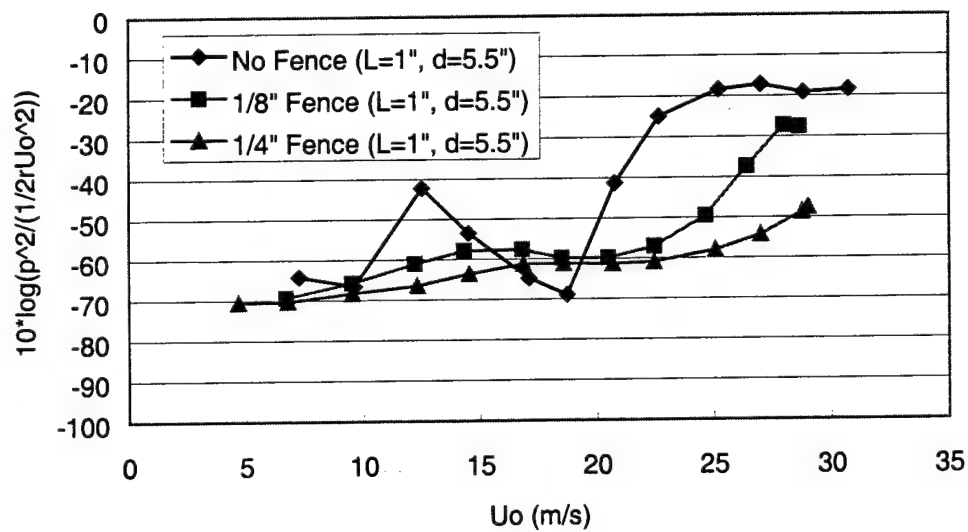


Figure 6.6: Comparison of normalized level of Helmholtz resonance cavity tone for cavity configuration 2d with  $\frac{1}{4}$ " fence,  $\frac{1}{8}$ " fence, and no fence

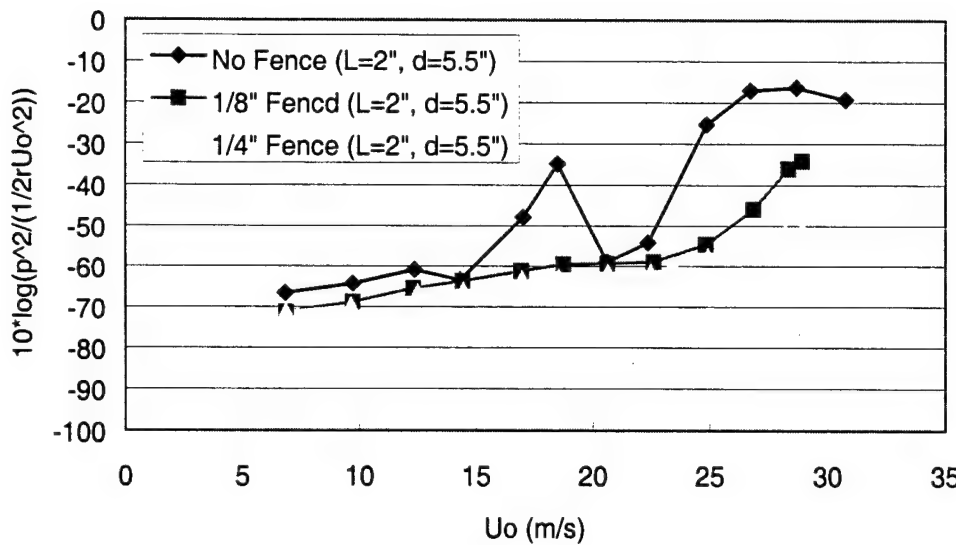


Figure 6.7: Comparison of normalized level of Helmholtz resonance cavity tone for cavity configuration 4d with  $\frac{1}{4}$ " fence,  $\frac{1}{8}$ " fence, and no fence

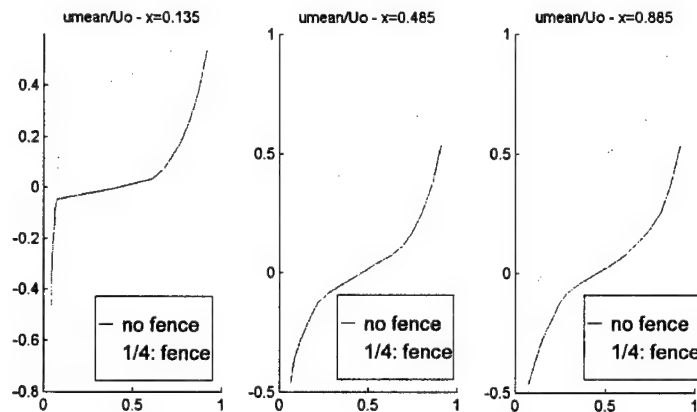


Figure 6.8: Comparison of streamwise mean velocity profiles at 30 m/s for configuration 2d with and without  $\frac{1}{4}$ " fence

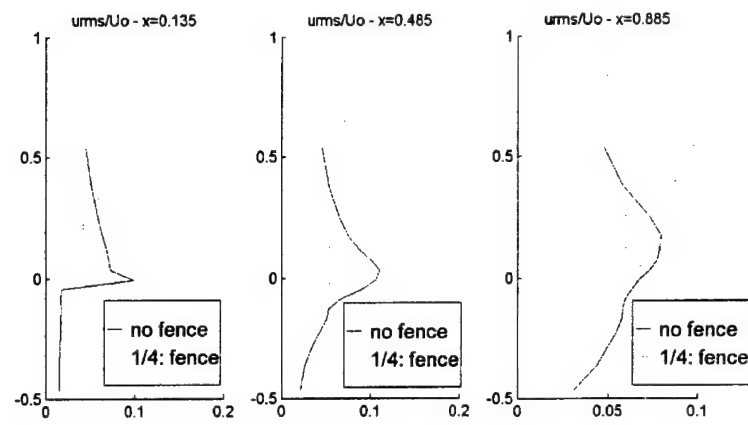


Figure 6.9: Comparison of streamwise turbulence intensity profiles at 30 m/s for configuration 2d with and without  $\frac{1}{4}$ " fence

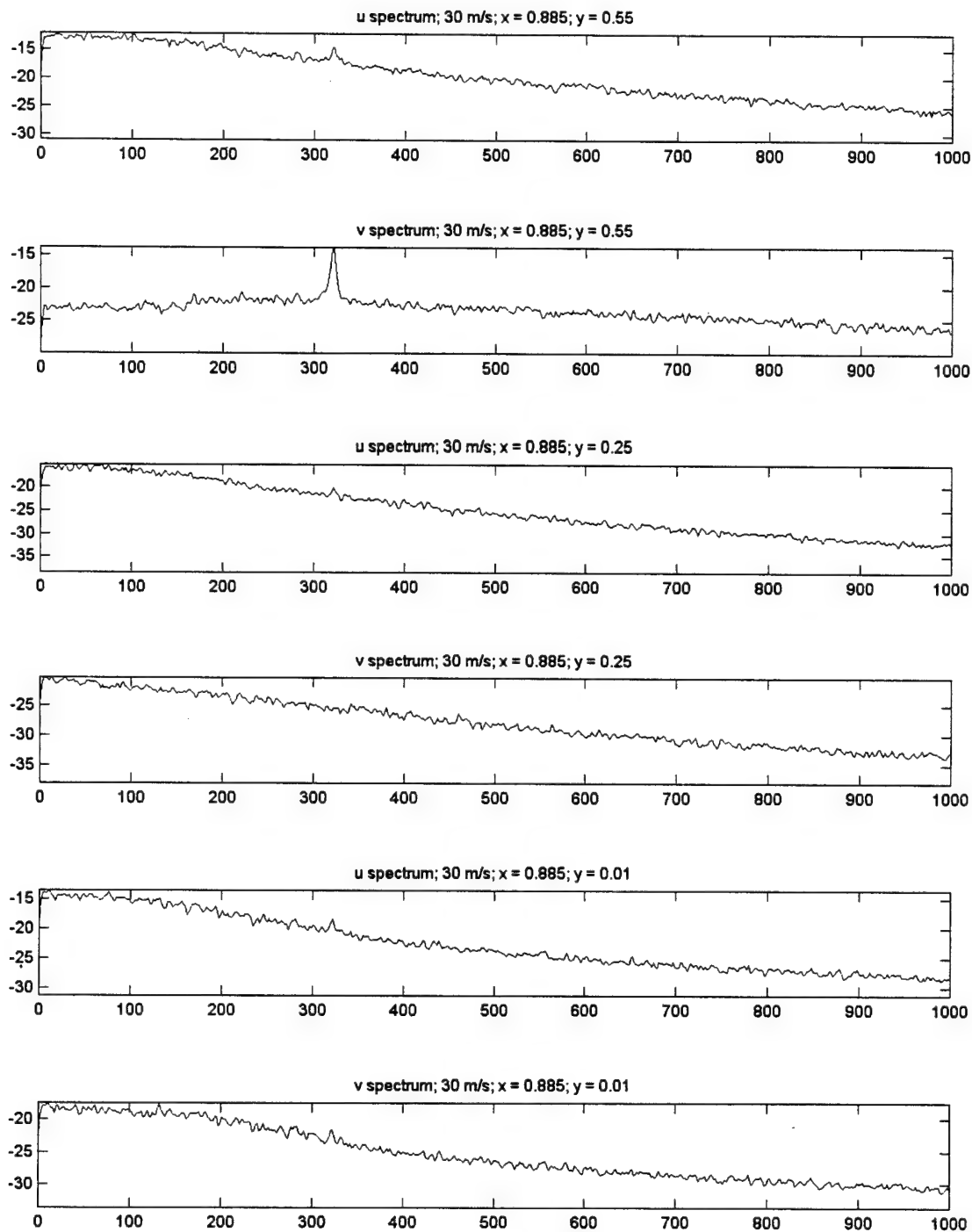


Figure 6.10: Velocity spectra at 30 m/s at 2 locations for configuration 2d with  $\frac{1}{4}$ " fence

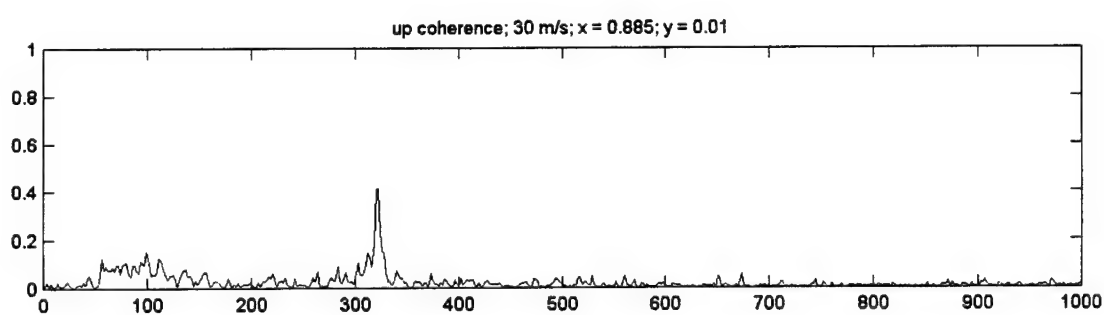
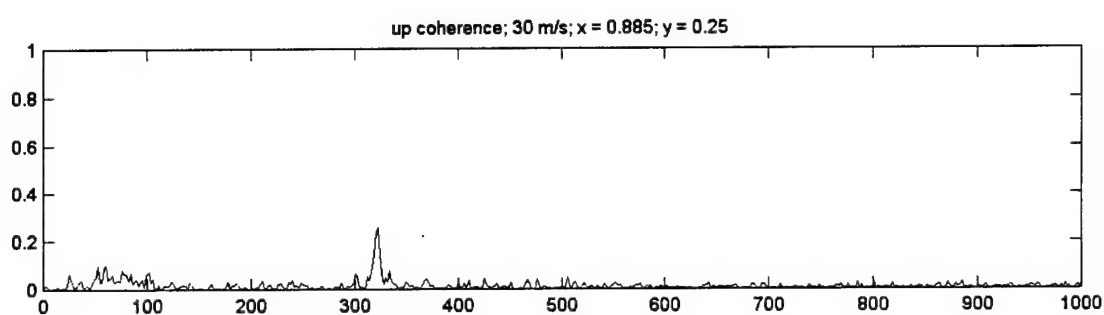
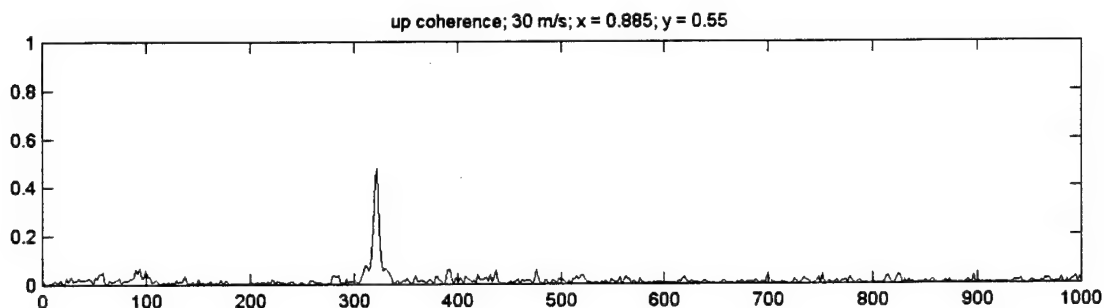


Figure 6.11: Coherence between u-p at 30 m/s for 3 locations for configuration 2d with  $\frac{1}{4}$ " fence

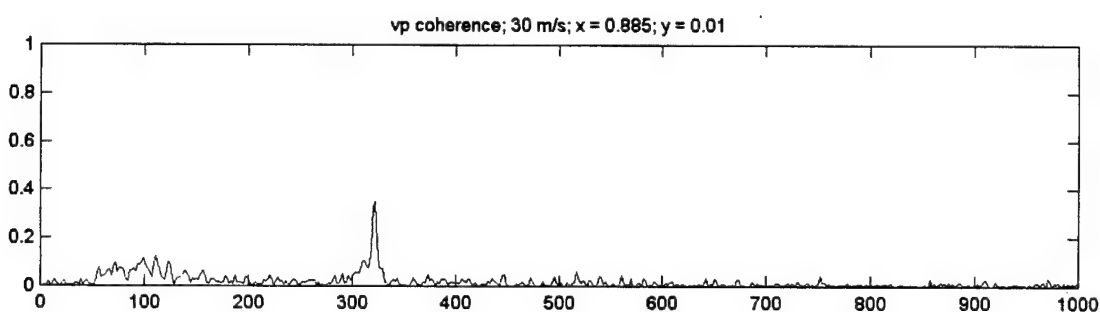
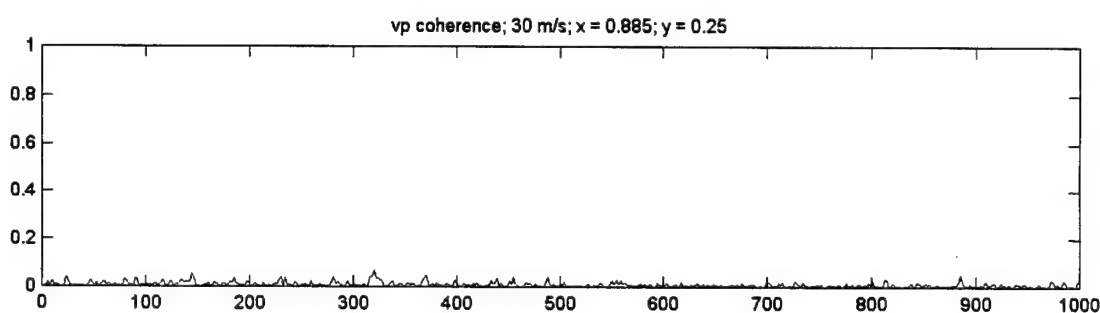
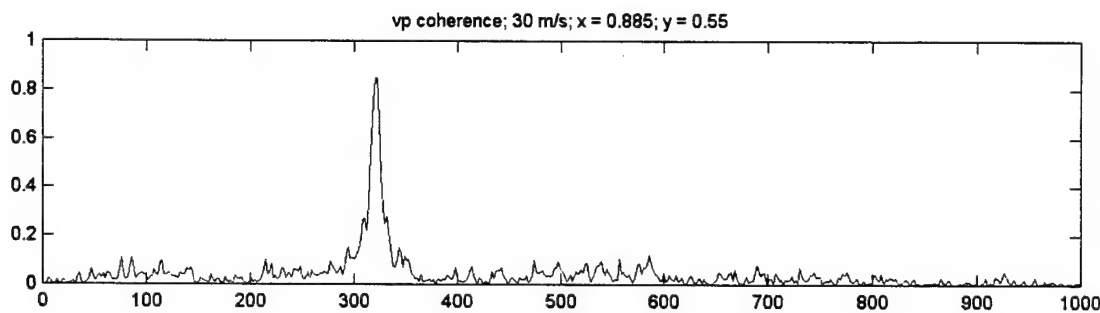


Figure 6.12: Coherence between v-p at 30 m/s for 3 locations for configuration 2d with  $\frac{1}{4}$ " fence

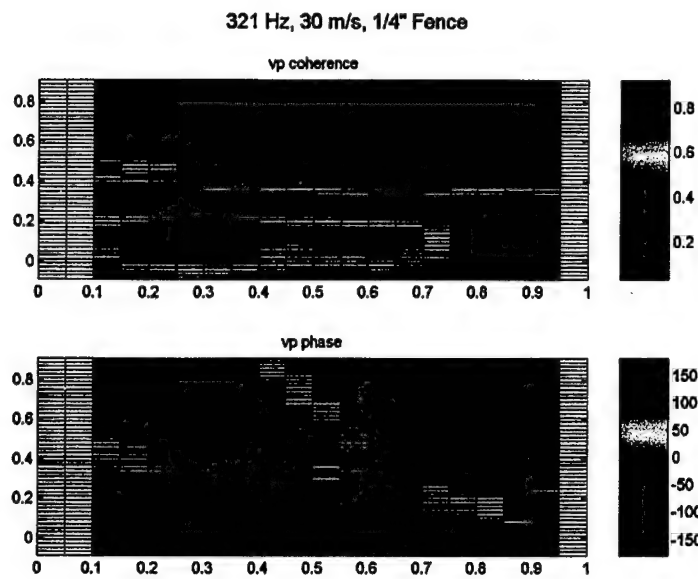


Figure 6.13: Spatial plot of phase and coherence between v-p of first sheartone resonance at 30 m/s for configuration 2d with  $\frac{1}{4}$ " fence

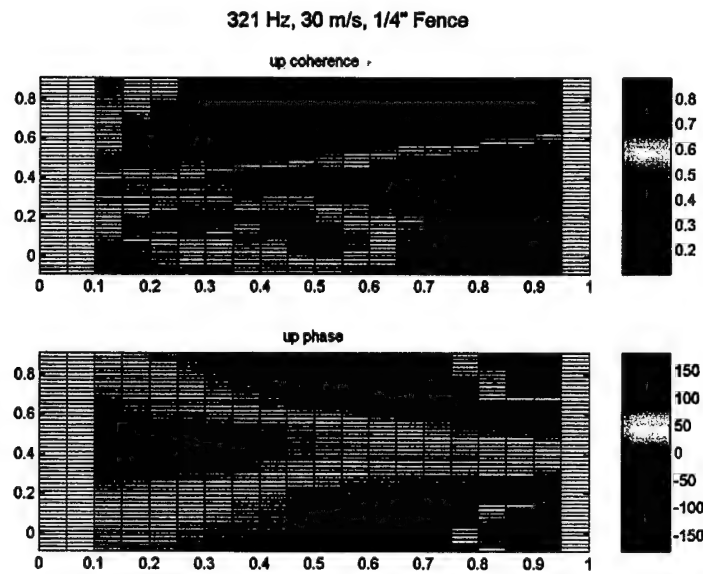


Figure 6.14: Spatial plot of phase and coherence between u-p of first sheartone resonance at 30 m/s for configuration 2d with  $\frac{1}{4}$ " fence

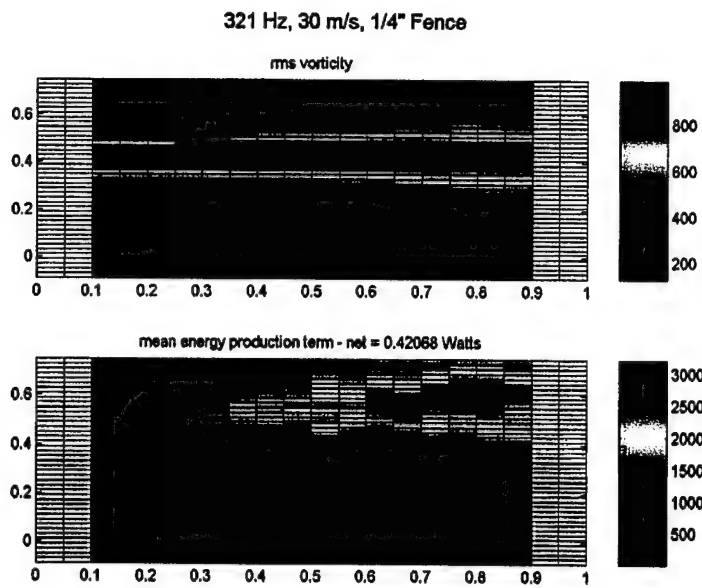


Figure 6.15: Spatial plot of rms vorticity and mean energy production term of first sheartone resonance at 30 m/s for configuration 2d with 1/4" fence

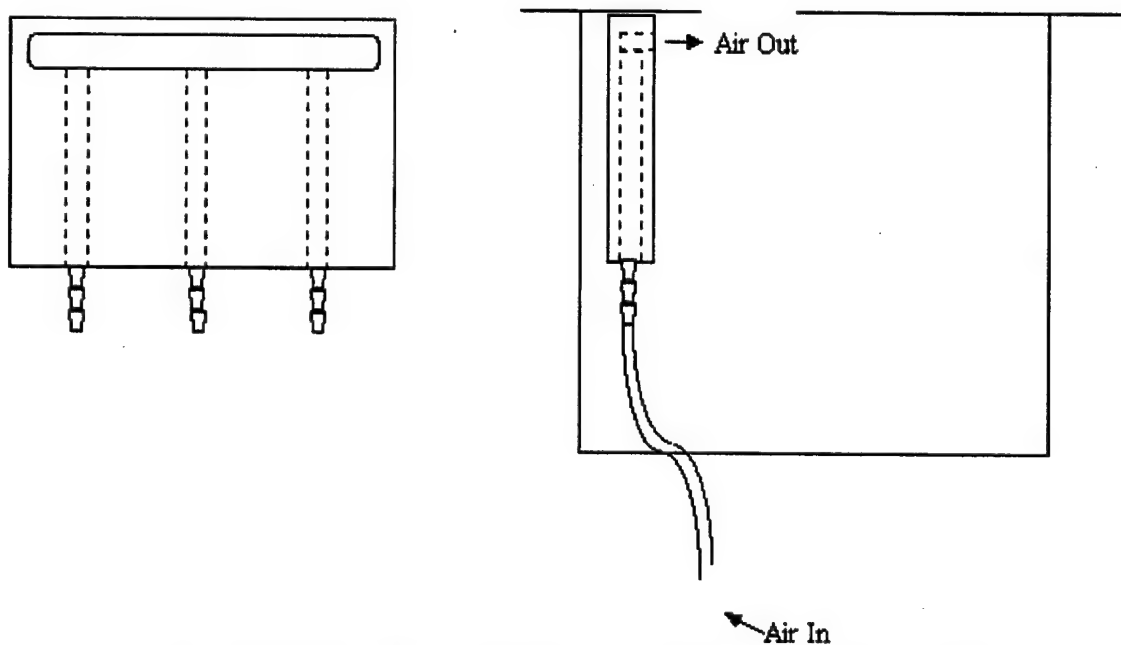


Figure 6.16: Configuration and drawing of air injection manifold

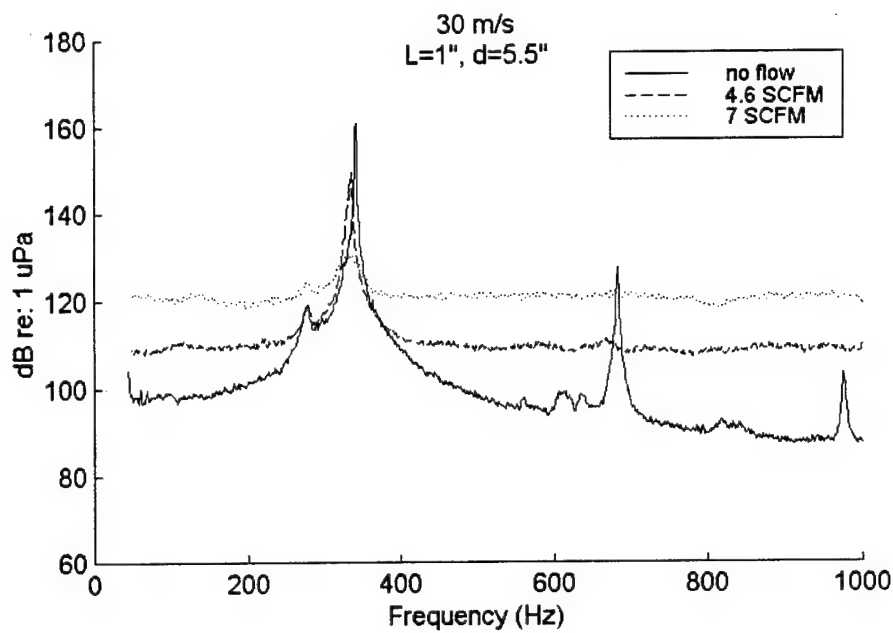


Figure 6.17: Cavity pressure spectra at 30 m/s for configuration 2d, with 0, 4.6, and 7 SCFM fluid injection

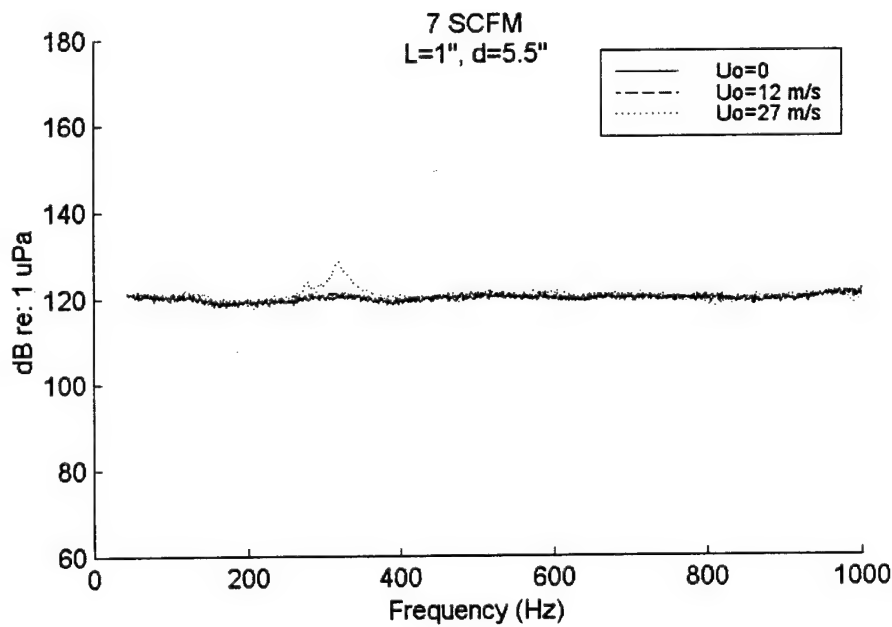


Figure 6.18: Cavity pressure spectra for configuration 2d, with 7 SCFM fluid injection at 0, 12, and 27 m/s.

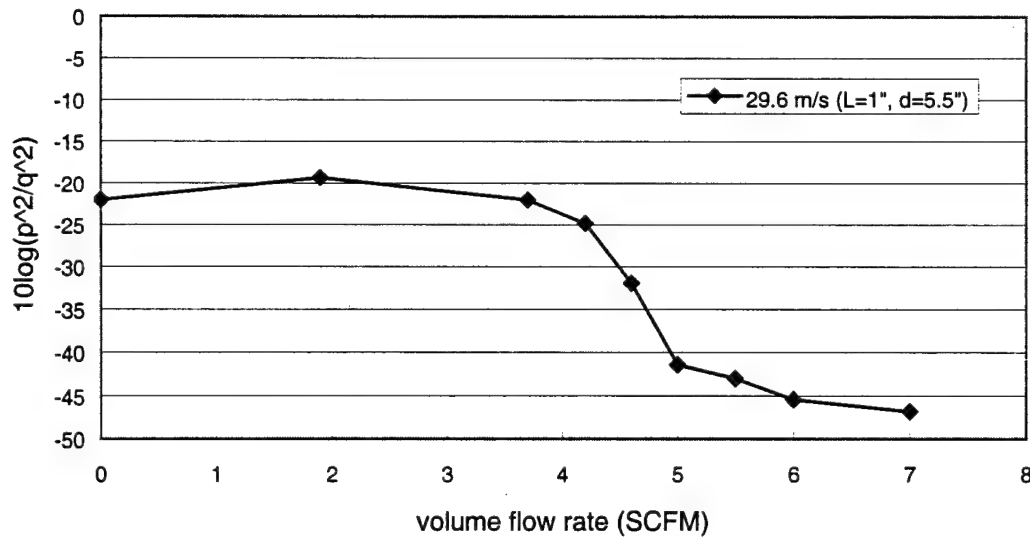


Figure 6.19: Normalized level of Helmholtz resonance at 30 m/s for cavity configuration 2d as a function of fluid injection rate

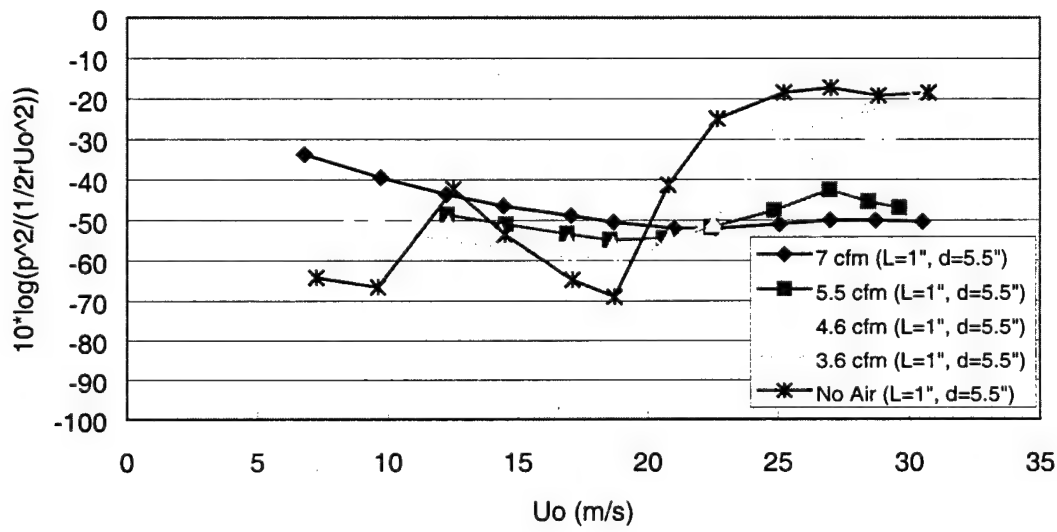


Figure 6.20: Normalized level of Helmholtz resonance for cavity configuration 2d at 5 values of fluid injection rate

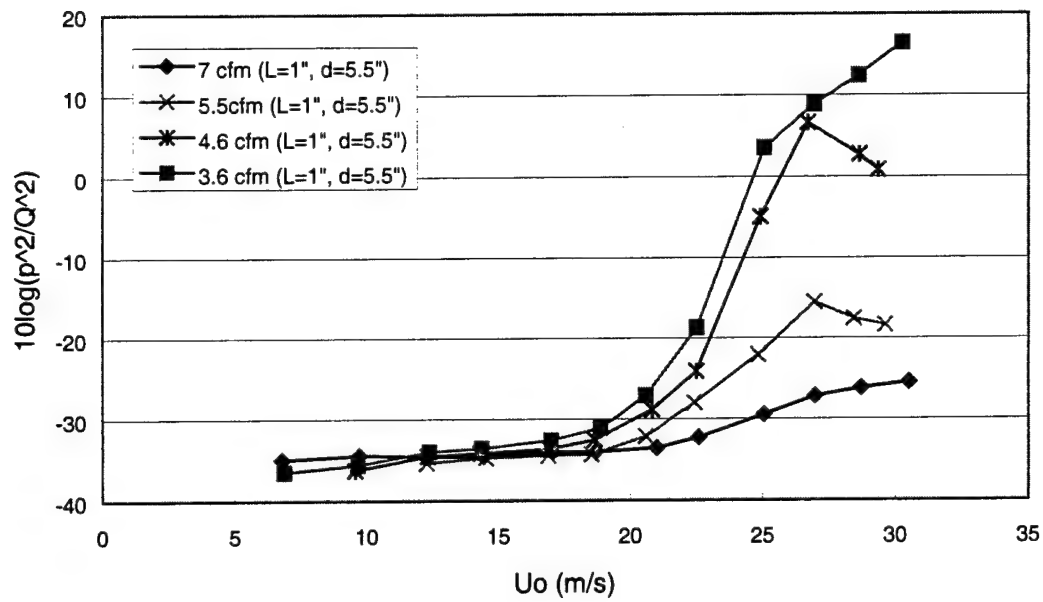


Figure 6.21: Flow-rate normalized level of Helmholtz resonance for cavity configuration 2d  
at 5 values of fluid injection rate

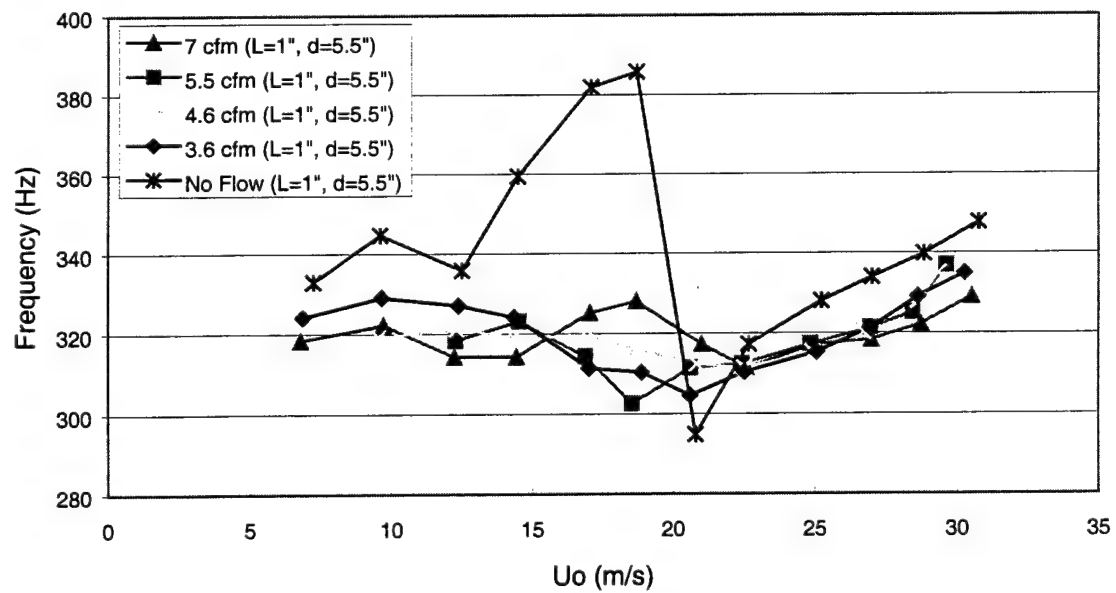


Figure 6.22: Frequency of Helmholtz resonance for cavity configuration 2d at 5 values of  
fluid injection rate

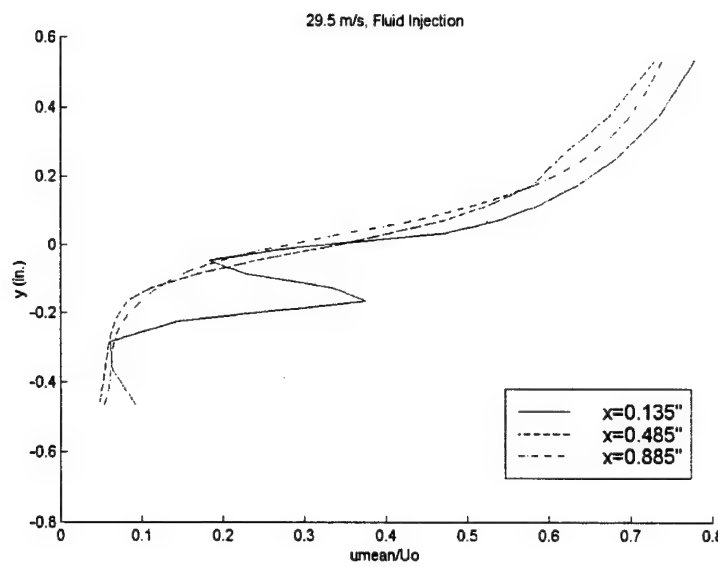


Figure 6.23: Streamwise mean velocity profile at 29.5 m/s for configuration 2d with 4.6 SCFM air injection at 3 streamwise locations

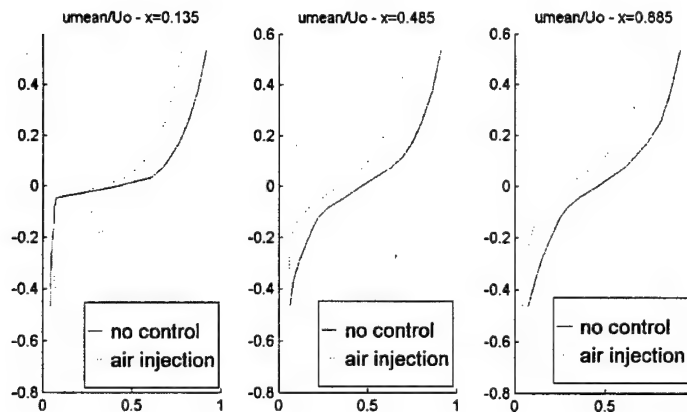


Figure 6.24: Comparison of streamwise mean velocity profiles at 30 m/s for configuration 2d with and without 4.6 SCFM air injection

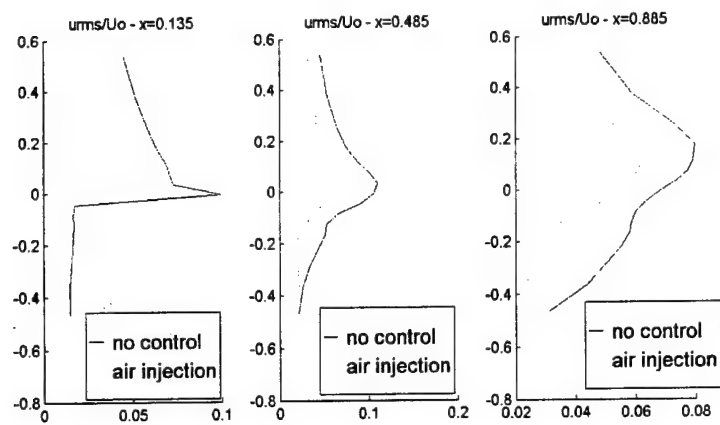


Figure 6.25: Comparison of streamwise turbulence intensity profiles at 30 m/s for configuration 2d with and without 4.6 SCFM air injection

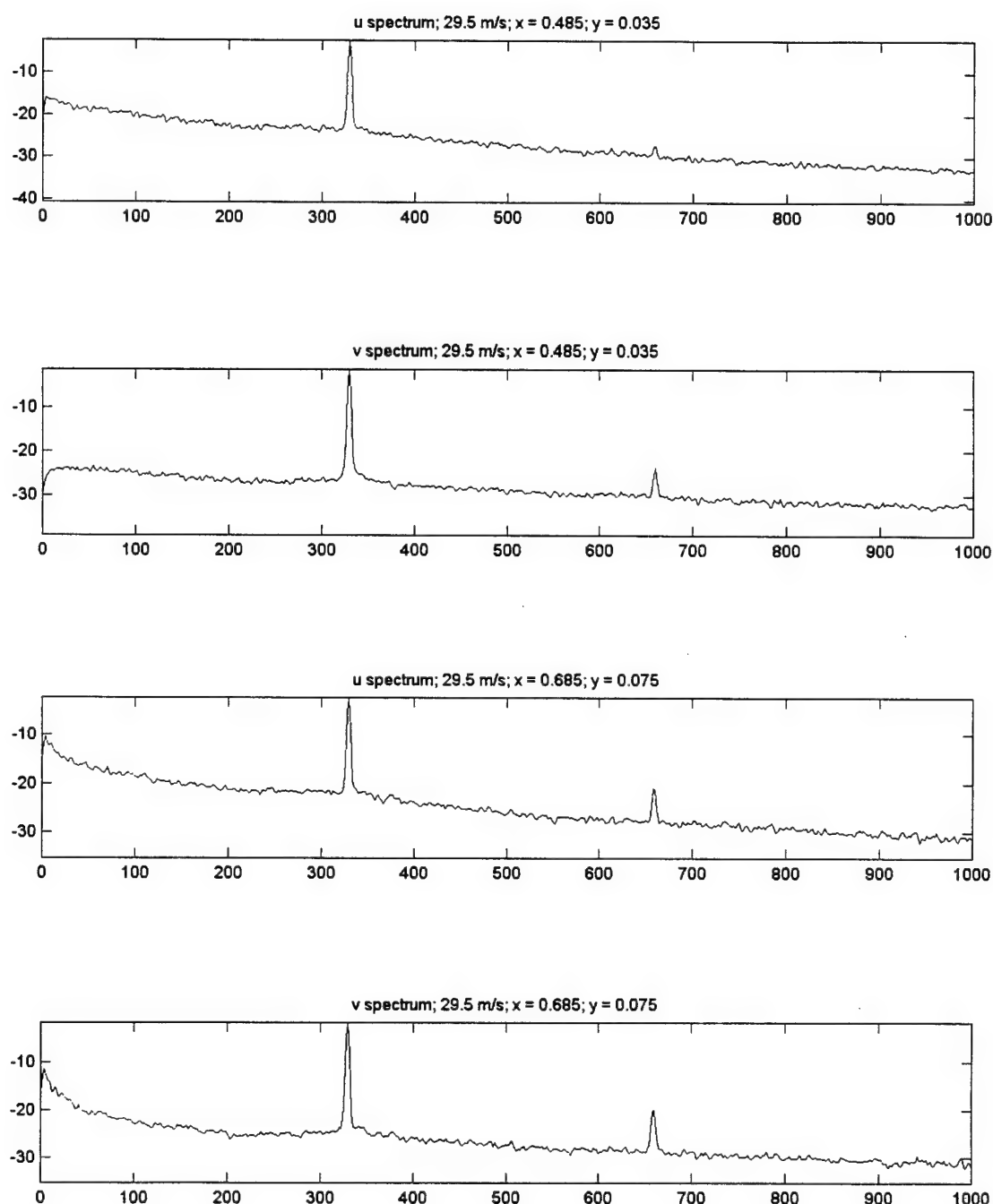


Figure 6.26: Velocity spectra at 29.5 m/s at 2 locations for configuration 2d  
with 4.6 SCFM air injection

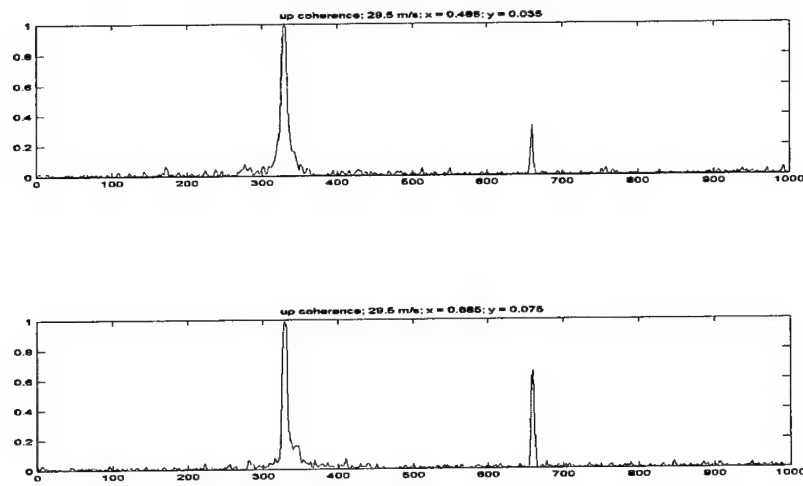


Figure 6.27: Coherence between u-p at 29.5 m/s for 2 locations for configuration 2d  
with 4.6 SCFM air injection

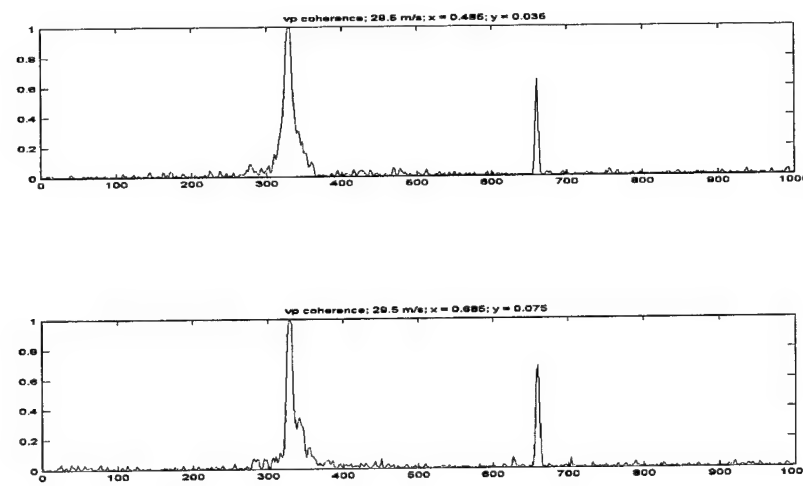


Figure 6.28: Coherence between v-p at 29.5 m/s for 2 locations for configuration 2d  
with 4.6 SCFM air injection

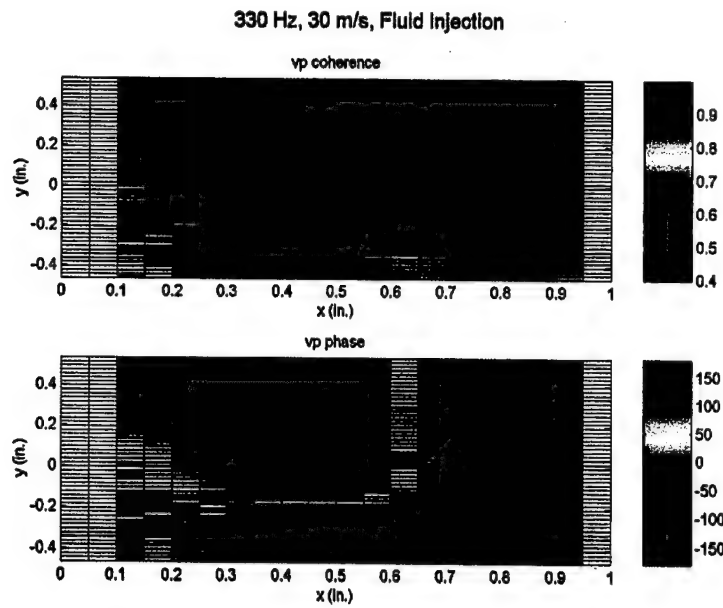


Figure 6.29: Spatial plots of phase and coherence between v-p of first sheartone resonance at 29.5 m/s for configuration 2d with 4.6 SCFM air injection

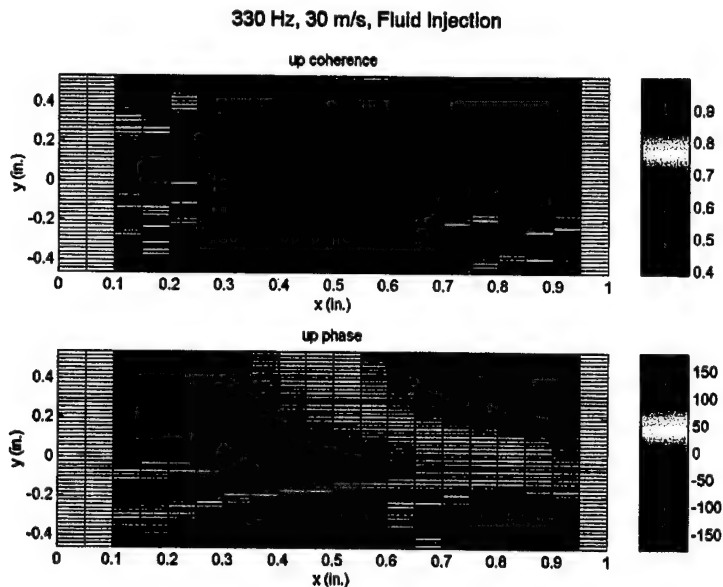


Figure 6.30: Spatial plots of phase and coherence between u-p of first sheartone resonance at 29.5 m/s for configuration 2d with 4.6 SCFM air injection

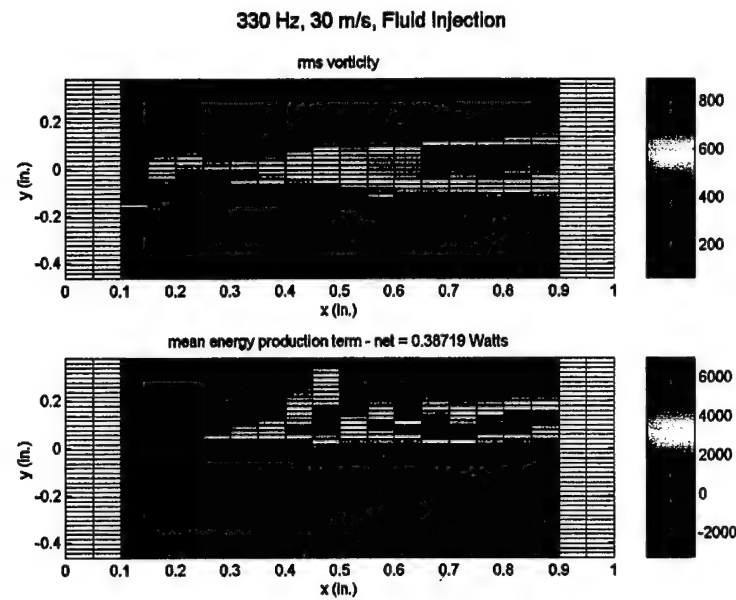


Figure 6.31: Spatial plots of rms vorticity and mean energy production term of first sheartone resonance at 29.5 m/s for configuration 2d with 4.6 SCFM fluid injection

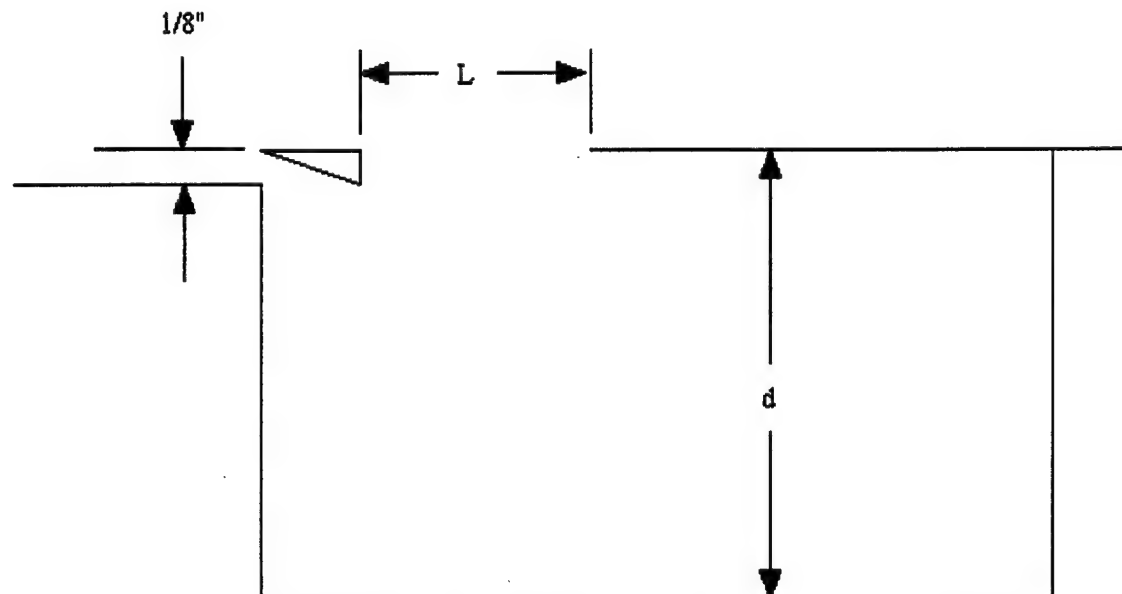


Figure 6.32: Schematic of boundary layer diversion implementation

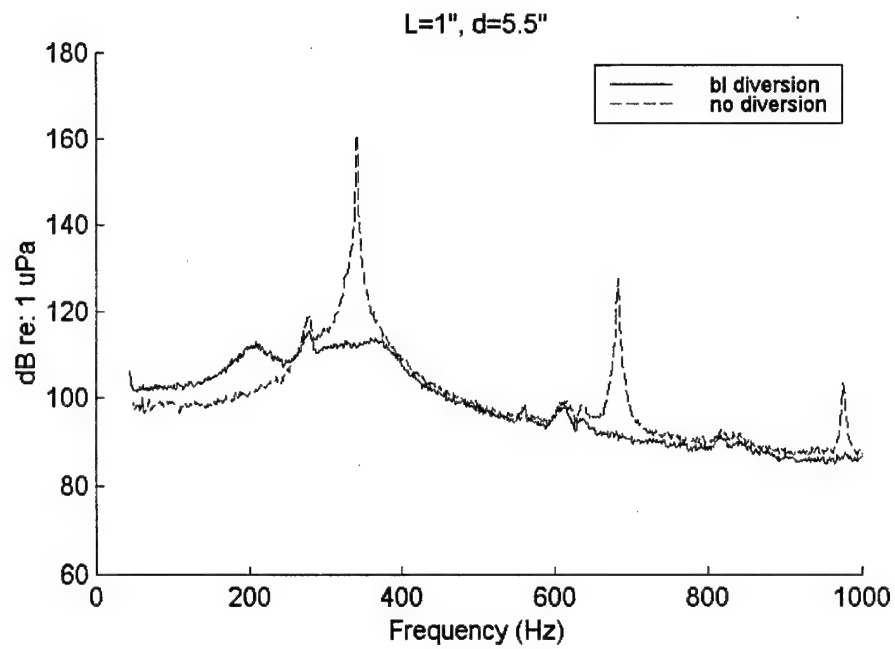


Figure 6.33: Cavity pressure spectra at 29 m/s for configuration 2d, with and without boundary layer diversion

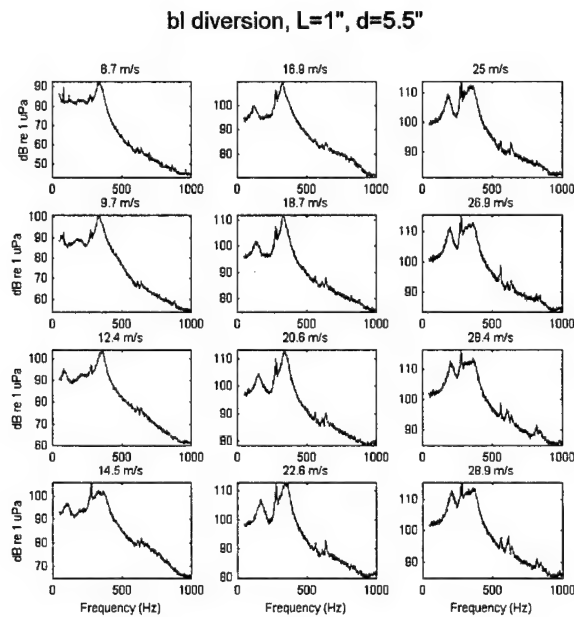


Figure 6.34: Cavity pressure spectra at 12 speeds for configuration 2d, with boundary layer diversion

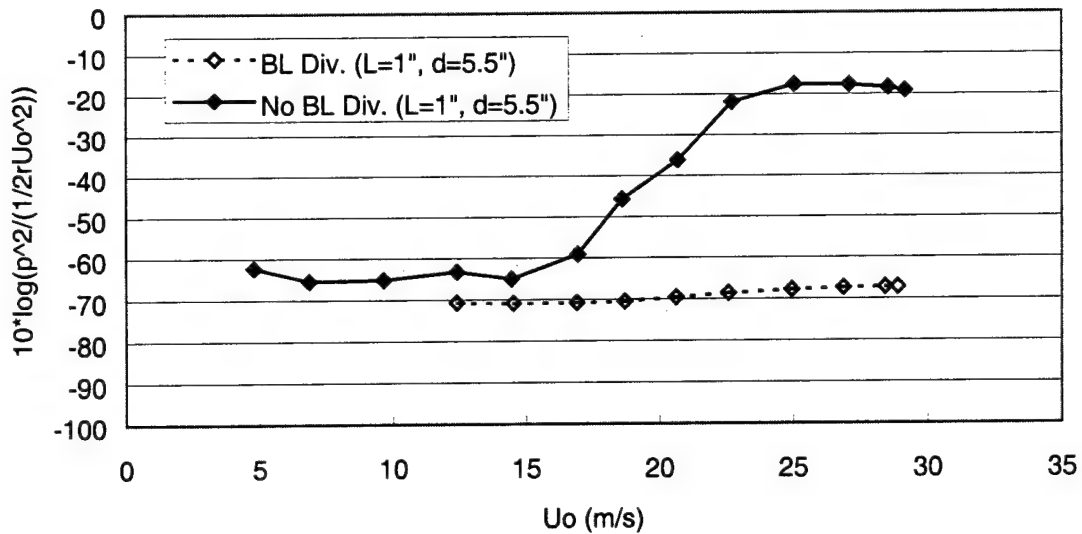


Figure 6.35: Comparison of normalized level of first sheartone for cavity configuration 2d with and without boundary layer diversion

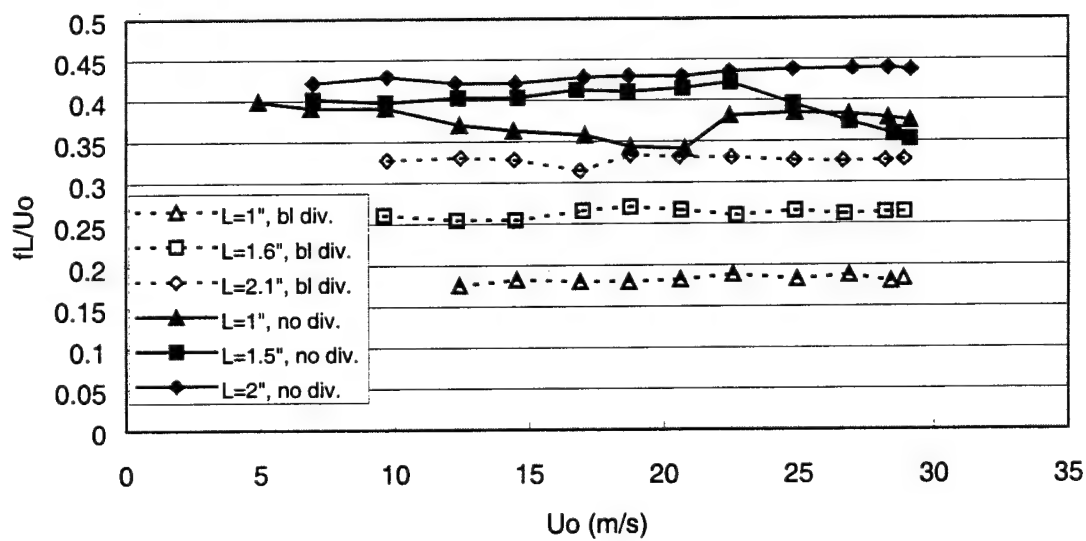


Figure 6.36: Comparison of Strouhal numbers of first sheartone for deep cavity ( $d=5.5"$ ) at various values of  $L$  with and without boundary layer diversion

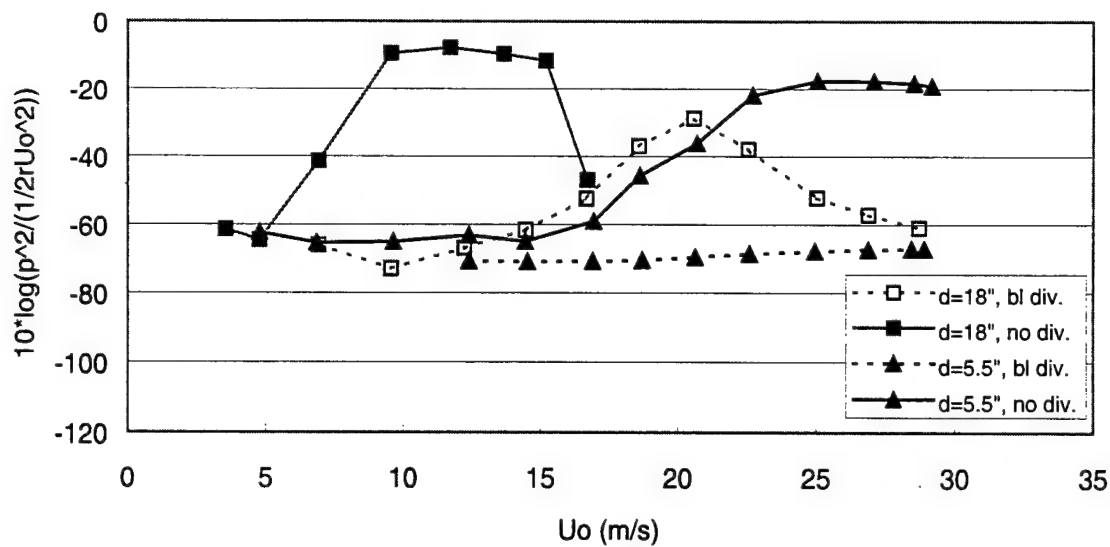


Figure 6.37: Comparison of normalized level of first sheartone for cavity configurations 2d and 2dd with and without boundary layer diversion

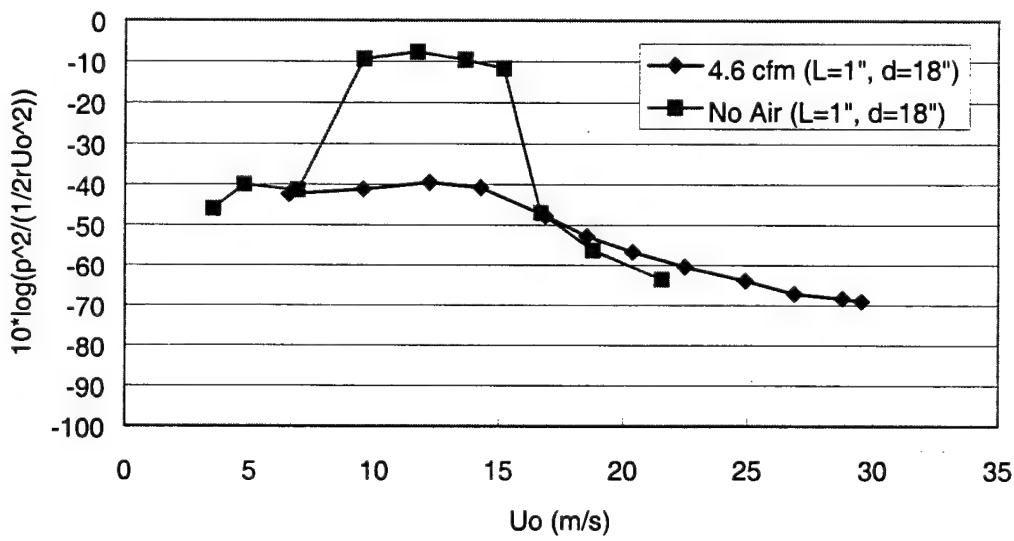


Figure 6.38: Comparison of normalized level of Helmholtz resonance tone for cavity configuration 2dd with and without 3.6 SCFM air injection

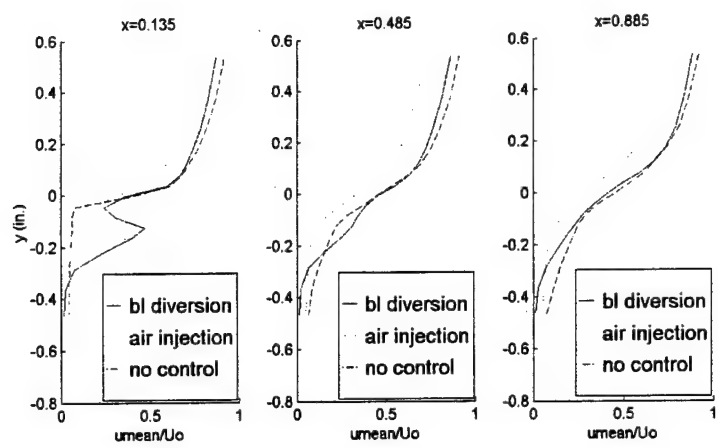


Figure 6.39: Comparison of streamwise mean velocity profiles at 30 m/s for configuration 2d with boundary layer diversion and with 4.6 SCFM air injection

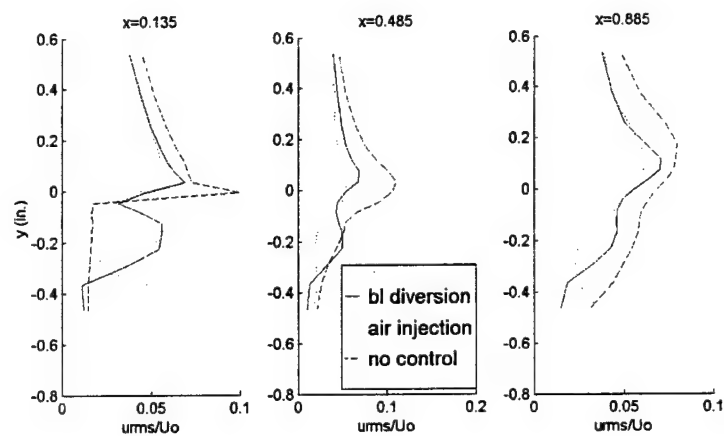


Figure 6.40: Comparison of streamwise turbulence intensity profiles at 30 m/s for configuration 2d with boundary layer diversion and with 4.6 SCFM air injection

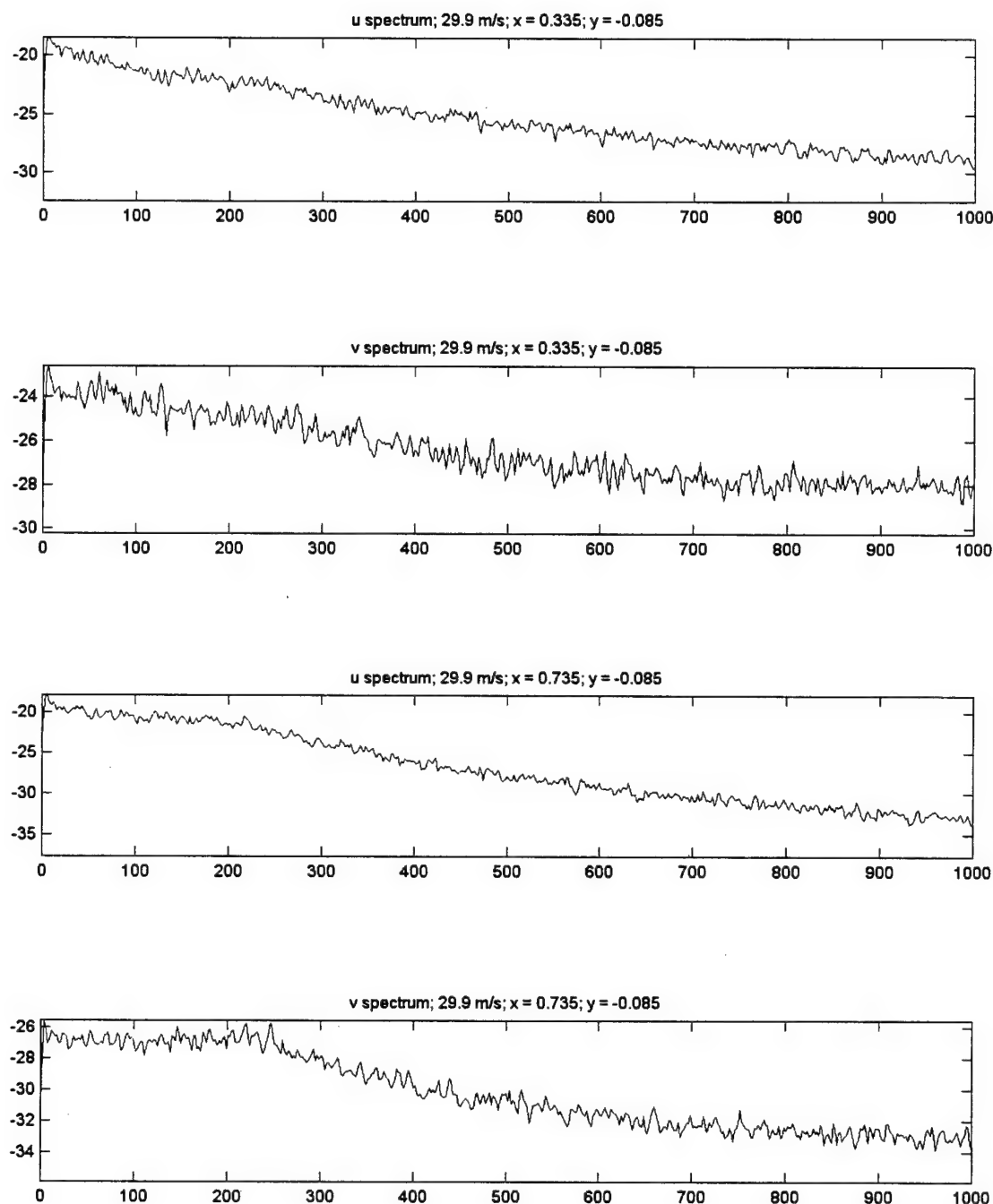


Figure 6.41: Velocity spectra at 29.9 m/s at 2 locations for configuration 2d  
with boundary layer diversion

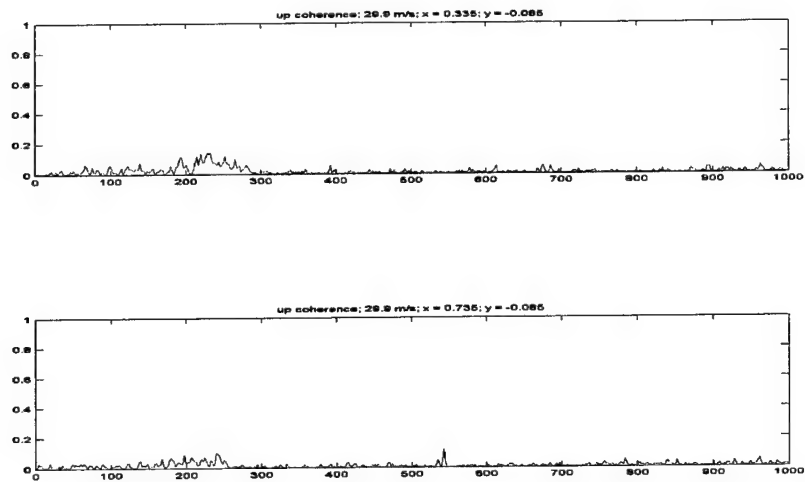


Figure 6.42: Coherence between u-p at 29.9 m/s at 2 locations for configuration 2d  
with boundary layer diversion

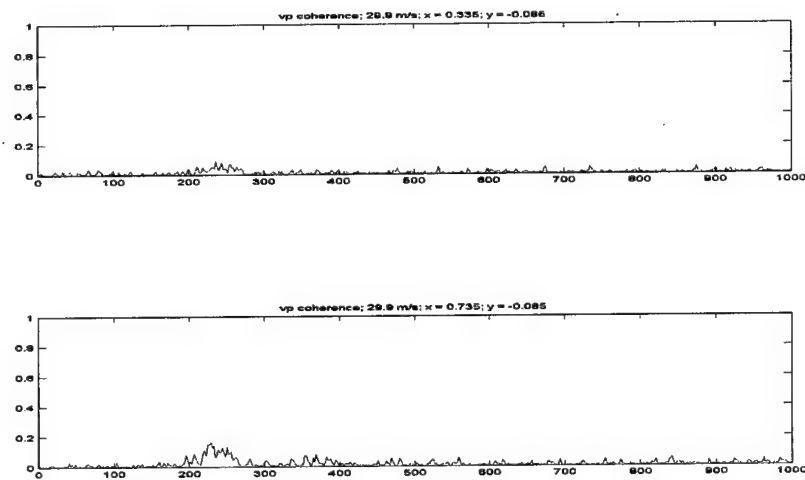


Figure 6.43: Coherence between v-p at 29.9 m/s at 2 locations for configuration 2d  
with boundary layer diversion

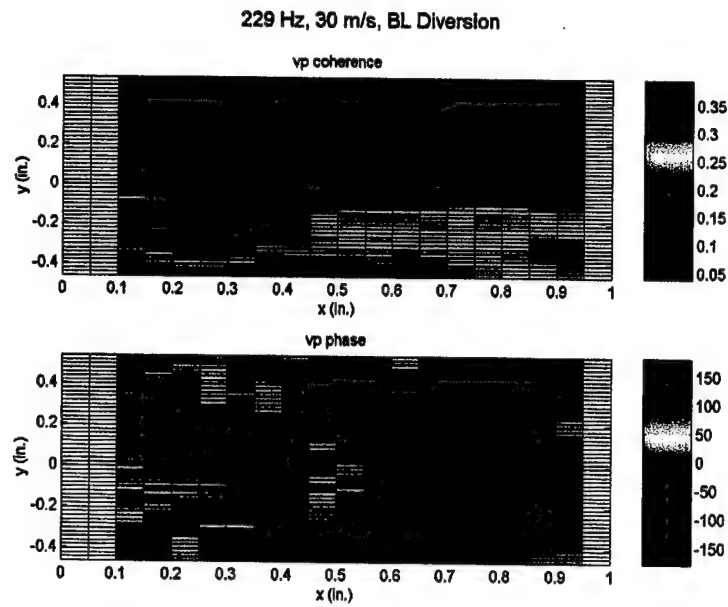


Figure 6.44: Spatial plots of phase and coherence between v-p of first sheartone at 29.9 m/s for configuration 2d with boundary layer diversion

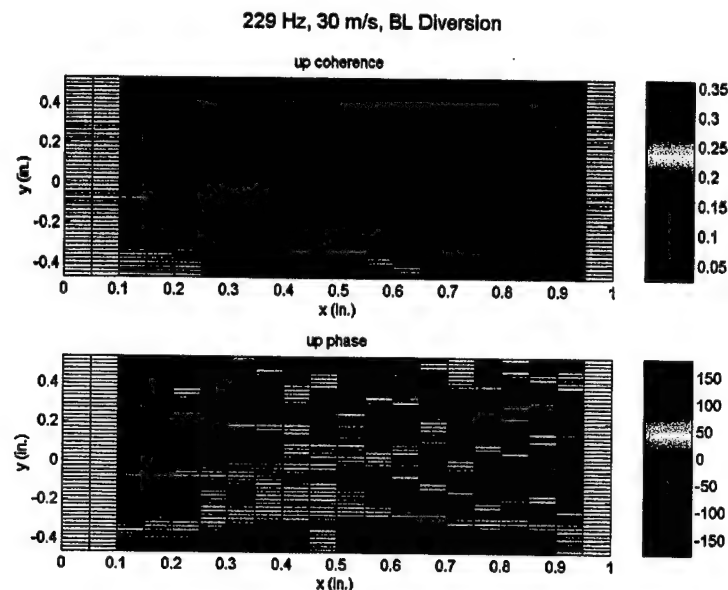


Figure 6.45: Spatial plots of phase and coherence between u-p of first sheartone at 29.9 m/s for configuration 2d with boundary layer diversion

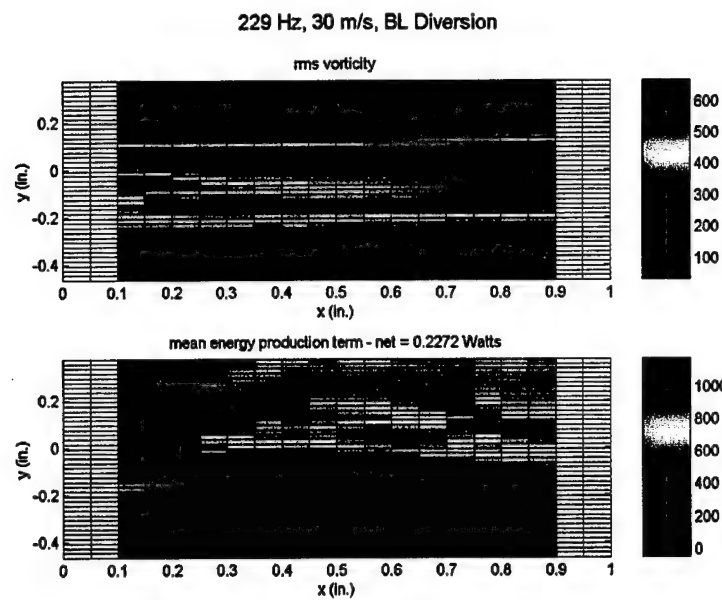


Figure 6.46: Spatial plots of rms vorticity and mean energy production term of first sheartone at 29.9 m/s for configuration 2d with boundary layer diversion

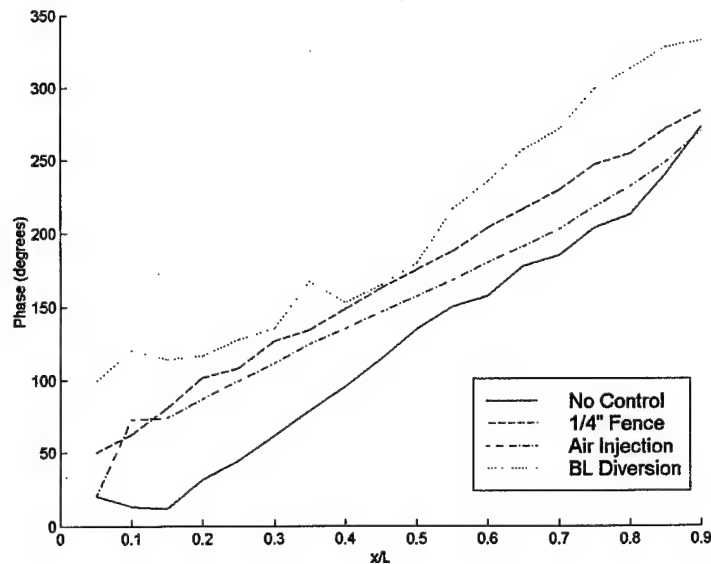


Figure 6.47: Phase between v-p along vortex path of first sheartones for configuration 2d with boundary layer diversion, 4.6 SCFM air injection,  $\frac{1}{4}$ " fence, and no control

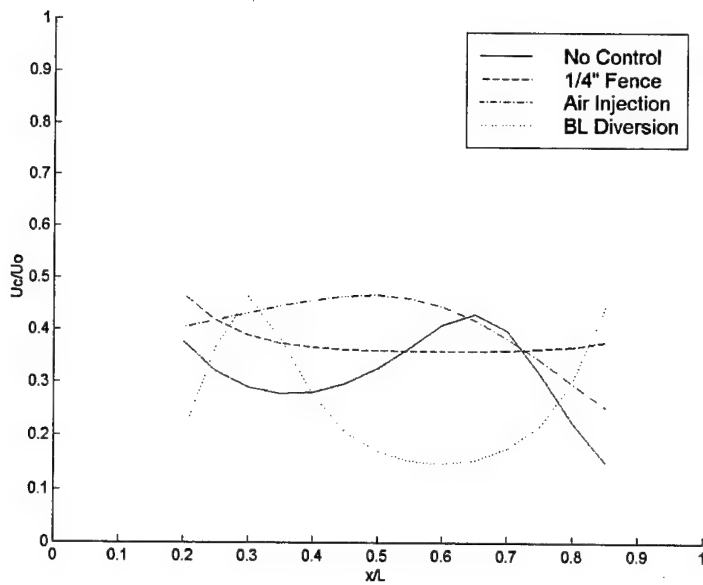


Figure 6.48: Convection velocity of vortex of first sheartones for configuration 2d with boundary layer diversion, 4.6 SCFM air injection,  $\frac{1}{4}$ " fence, and no control

## 7. Summary and Conclusions

### 7.1 Summary

The goal of this research was to enhance the current understanding of mechanisms governing flow-induced cavity resonance so that techniques for controlling it could be developed or improved. The specific objectives were first, to discern distinct features of sheartones in the cavity opening under both non-resonant and resonant conditions, and second, to determine what features of the flow are associated with effective control. To accomplish these objectives, extensive data were obtained of cavity pressure fluctuations over a broad speed range and cavity parameters. Also, the correlation between the velocity field in the cavity opening and the cavity pressure was obtained for select speeds and configurations. The results of these experiments are summarized.

#### Sheartone Behavior

Grazing flow over a cavity opening results in speed dependent tones. These tones, referred to as sheartones, are produced by discrete vortices shed from the upstream edge of the opening. They are generally observable in the cavity pressure spectra at speeds where their frequency is below that of the cavity resonance.

Cavity pressure was measured over a range of speeds and for various cavity configurations. At low speed, first and second sheartones were observed in the cavity pressure spectra for many of the configurations tested. The first sheartone corresponds to the presence of one vortex in the cavity opening, while the second sheartone corresponds to two vortices and has a frequency greater than, but less than two times, the first. As the grazing flow speed is increased, the first and second sheartones increase in frequency. When the frequency of the second sheartone approaches the cavity resonance frequency, the second sheartone becomes coupled to the cavity resonance and becomes a cavity tone. The level of the tone then begins to increase rapidly with speed. When the speed has increased sufficiently that the frequency of the tone is greater than the resonant frequency of the cavity, the level decreases rapidly to near its original level. The process is repeated at still

higher speeds when the frequency of the first sheartone approaches the cavity frequency and becomes resonant.

These observations were quantified by studying the non-dimensional level and the non-dimensional frequency, or Strouhal number,  $fL/U_0$ , of the tones as a function of speed. Both of these quantities are constant as a function of speed prior to the sheartone becoming coupled to the cavity frequency. The Strouhal number of the sheartone prior to its becoming coupled to the cavity frequency is also independent of the cavity, but does scale on  $(\theta/L)^{-1/7}$ .

The flow field in the cavity opening and its correlation to the cavity pressure was also measured. Velocity spectra and coherence between the velocity components and cavity pressure showed significant correlation between the cavity pressure and the flow field in the opening. The high levels of coherence supported the use of the phase between the quantities at the tonal frequencies.

The spatial distribution of the phase between the velocity components and the cavity pressure at the frequency of the cavity tone confirmed that flow in the opening was consistent with the understanding of it as a series of vortices shed periodically from the upstream edge. The phase between  $v-p$  was used to calculate the convection velocity of the vortices as they move across the opening. Convection velocity as a function of streamwise location was examined for first and second sheartones at several speeds. These data suggest that resonant sheartones may be distinguished from non-resonant sheartones by the presence of a local minimum in the convection velocity in the region  $0.2 < x/L < 0.5$ .

Some features of the model of flow-excited cavity resonance given by Nelson, et al. were reviewed. Of particular interest is the energy production term, which relates the interaction between the fluctuating vorticity and the fluctuating velocity in the opening of the cavity. Regions of positive and negative energy production in the opening of a resonating cavity predicted by the model were confirmed by comparison to the measured energy production term of a resonant first sheartone. The energy production term was also measured for a resonant second sheartone and for a non-resonant cavity tone. The distributions of energy production in these cases were similar to each other, but different from that of the resonant first sheartone. The distinction between resonant sheartones with and without a significant region of negative energy production is important. The vorticity

distribution suggests that it is related to the magnitude and phase of the fluctuating vorticity in the opening. The phase relationship between the vortex shedding and the cavity pressure observed by Nelson was also compared to the current data. Good agreement was seen for the resonant first sheartone.

### Cavity Resonance Control Techniques

The behavior of sheartones and how they become coupled to a cavity resonance have been studied by analyzing measurements of cavity pressure over a range of speeds and configurations and by examining the correlation between the cavity pressure and the flow field in the cavity opening at selected conditions. The analysis techniques used and the understanding gained from these studies were used to investigate techniques for controlling cavity resonance.

Three different cavity control devices were tested: a boundary layer fence, air injection at the upstream edge of the opening, and a device for diverting fluid from the boundary layer into the cavity at the upstream edge. Measurements of cavity pressure over the speed range of the tunnel were made for these techniques. In addition, flow velocity-cavity pressure correlations at the speed corresponding to the maximum resonance of the uncontrolled cavity were also obtained.

The results of cavity pressure measurements with the boundary layer fence installed showed that the fence was effective at reducing the cavity resonance level. It was effective primarily because it lowered the Strouhal number of the non-resonant sheartones, delaying resonance to higher speeds. A slight reduction in the level of the resonant tone at the speed where resonance did occur was also seen.

The boundary layer diversion technique was more effective than the boundary layer fence in reducing the cavity resonance. This technique lowered the Strouhal number of the non-resonant tones by a greater amount than the fence, delaying resonance to correspondingly higher speeds. Boundary layer diversion also produced a much greater reduction in the level of the resonant tone at the speed where resonance did occur.

Air injection was also effective in reducing the level of cavity resonance. However, it did not have the effect of delaying resonance to a higher speed. The reduction in the resonance level was a function of the flow injection rate. At low flow rates, a small increase

in the cavity resonance level was seen. Injection at high rates produced a significant decrease in the level. In between, the level as a function of fluid injection rate showed a critical region, in which a small change in the flow rate made a large difference in the level of the cavity tone.

The cavity pressure-flow field correlation was measured using fluid injection at a rate in the middle of the critical region. The distribution of the energy production term for this condition was similar to that of the uncontrolled resonance but with a lower magnitude for the region of negative energy production. This suggested that the critical region corresponds to a transition from an energy production term distribution with negative and positive regions of roughly equal magnitude to one with no negative region.

Phase between velocity and pressure and the convection velocity calculated from it were compared for the three techniques tested. The comparison showed that successful control is associated with an increase in the phase between the out-of-plane velocity fluctuations in the cavity opening and cavity pressure. Successful control is also associated with a change from deceleration to acceleration of the vortex as it approaches the downstream edge of the opening.

### Accomplishments

Prior measurements of cavity pressure over a range of speeds and for different cavity configurations have been made by DeMetz and Farabee (1978) and Elder, et al. (1977), among others. Pressure measurements made as part of this research served to validate and consolidate the work of these researchers. This work was extended by measurements made with the cavity removed. The results of these measurements helped to establish the scaling between the boundary layer thickness and the Strouhal number of non-resonant sheartones.

The only previous attempt at a detailed measurement of the flow field in the cavity opening and its correlation to the cavity pressure fluctuations was made by Nelson, et al. (1981, 1983). Their results were limited to the case of a first sheartone excited cavity resonating at its maximum level. Their findings were useful in defining some of the features of the fluid-acoustic interactions in a resonant cavity.

In this investigation, correlations between the flow field and cavity pressure were obtained at a speed corresponding to the second sheartone excited resonance and for a non-

resonant speed, as well as for the first sheartone excited resonance. These measurements were also performed for cavities with various control techniques implemented. The data were used to calculate the convection velocity of the discrete vortices associated with sheartones as they convect along the opening. The behavior of the convection velocity as a function of streamwise distance was compared for the various conditions tested and the features distinguishing the conditions described. These findings provided new insight into the mechanisms governing flow-induced cavity resonance. The use of the same data to measure the energy production term in the cavity opening also provided new insight. A comparison of the conditions tested suggested a distinction among cavity tones based on the distribution of their energy production term.

Three different control techniques were tested as part of this research. The boundary layer diversion technique was developed as part of this effort and was shown to be effective. Tests of the two other techniques, the fence, and fluid injection at the upstream edge, have been reported before, however little effort was made to explain their effectiveness. In this research, measurements of the cavity pressure as a function of speed, as well as correlations between the flow field and the cavity pressure helped show the effect of the fence and boundary layer diversion on the Strouhal number of the sheartones. The effect of the fluid injection rate was also explored.

## 7.2 Conclusions

In this research, an enhanced understanding of the mechanisms governing flow-induced cavity resonance was sought. This was done so that techniques for controlling the resonance could be developed or improved.

Resonant sheartones, or cavity tones, are distinguished from non-resonant sheartones by the feedback mechanisms controlling the vortex shedding from the upstream edge. It has been previously established that the feedback mechanism for non-resonant sheartones does not involve the cavity, while the feedback for cavity tones does involve the resonant response of the cavity. This was confirmed during this investigation.

Some conclusions about sheartone behavior were drawn from the use of phase between the wall-normal velocity in the cavity opening and the cavity pressure. The phase was used to calculate the convection velocity of vortices as they convect along the opening. Comparisons of this velocity as a function of streamwise location for different uncontrolled conditions show that resonant sheartones may be distinguished from non-resonant sheartones by the presence of a local minimum in the convection velocity in the region  $0.2 < x/L < 0.5$ . Also, the results of these calculations with various control techniques implemented show that successful control is associated with the acceleration of the vortex as it approaches the downstream edge of the opening. For the uncontrolled resonance, the vortex decelerates as it approaches the downstream edge. It is thought that the reduction of the resonance level for a vortex that is accelerating, rather than decelerating, as it approaches the downstream edge, may be due to its no longer interacting with that edge, or doing so more weakly.

Measurements of the distribution of the energy production term in the cavity opening lead to the conclusion that an important difference appears to exist among resonant sheartones. The distribution for the first sheartone-driven cavity tone showed a significant region of negative energy production, as well as a larger region of positive energy production. For a second sheartone driven cavity tone, as well as for a first sheartone driven cavity tones where the resonance level is reduced by the use of a fence, the negative region is not seen. Also, it was seen that, when using fluid injection to control cavity resonance, increasing the fluid injection rate is associated with a transition from a distribution with a negative region to a distribution with no negative region. Resonant sheartones with the negative energy production region are associated with tones having the highest normalized level. Where no negative region is seen, the sheartone is still coupled to the Helmholtz resonance, but the normalized levels are lower.

These findings suggest some fundamental difference between cavity tones with and without the region of negative energy production. The difference appears to be related to the phase and amplitude of the fluctuating vorticity near the upstream edge of the opening, and suggests that the strongest resonant response is associated with the highest levels of vorticity occurring near the upstream edge.

In addition to the established control techniques of the boundary layer fence and fluid injection at the upstream edge of the cavity, a new control technique was developed and tested. A vane was used to divert fluid from the boundary layer upstream of the opening into the cavity at the upstream edge. This technique was referred to as boundary layer diversion. Measurements of cavity pressure as a function of speed for all three techniques showed that the fence and boundary layer diversion reduced the Strouhal number of non-resonant sheartones in the cavity opening, thus delaying resonance to higher speeds. Both techniques also reduced the maximum level of the tone when resonance was achieved. However, boundary layer diversion was significantly more effective than the fence, both at reducing Strouhal number, and at reducing the resonance level.

The identification of cavity resonance with variations in the convective velocity of vortices in the shear layer, and the classification of resonant tones based on their energy distribution, are important findings that, it is hoped, will lead to improved techniques for controlling flow-induced cavity resonance in the future. The development of the boundary layer diversion technique and the behavior of the established control techniques are findings that can be useful in the practical implementation of these cavity resonance control in present day designs.

### **7.3 Suggestions for Future Research**

In this research, the features of resonant and non-resonant sheartones have been examined and the effectiveness of various control techniques has been explored. Part of the motivation for this research is the improvement of current control techniques and the establishment of new control techniques. Several possibilities for future research are suggested by the current results.

The current research was based in part on measurements of the flow velocities made using a constant temperature anemometer with an x-wire probe. The resolution and extent of flow field measurements that could be made this way were limited. Other methods of measuring the velocity field, such as laser doppler velocimetry, may allow the flow field to

be measured with greater resolution and over a greater spatial extent. The use of flow visualization may also be helpful, and should be considered.

These techniques should be used to further explore the feedback mechanisms controlling cavity resonance. It was shown that cavity tones could be classified based on the presence of a negative region of energy production in the cavity opening. The local variations in the convection velocity were also shown to be important. Additional work should be done to determine how these results fit into a theoretical framework and how they may apply to control of cavity resonance. Computational fluid dynamics should also be considered for this purpose.

Practical application of the control techniques tested would benefit from an understanding of the scaling behavior of both these techniques. Two fence heights were tested and the higher was found to be more effective. However, scaling laws relating the fence height, opening length, boundary layer thickness to the performance are needed. Fluid injection was tested for a range of injection rates. A modest attempt was made to relate these rates to the grazing flow speed. Further work in this area is also required. Finally, the boundary layer diversion technique was tested for one value of the displacement of the diverting vane from the upstream flow surface. This value was selected based on its relationship to the boundary layer thickness. Additional work should be done to determine the scaling relationship among the height of the diverter, the boundary layer thickness, and the opening length.

It may also be desirable to apply the knowledge gained from this investigation and from any further investigations to improving the understanding and effectiveness of active feedback control techniques. These techniques have been used with some success, but might benefit from an improved understanding of how they work.

## Appendix 1 - Frequency And Level Of Speed Dependent Tones

Configuration 2d (L=1", d=5.5")				
v (m/s)	f1 (Hz)	L1	f2 (Hz)	L2
4.8	77.1	-62.3	142.6	-69.8
6.8	108.4	-65.4	193.4	-71
9.6	147.5	-65.1	277.5	-63.9
12.4	183.6	-63.2	335	-45.6
14.4	209	-65	357.4	-55.8
16.9	258.8	-59.1	375	-65
18.6	271.5	-45.8	380.8	-68.8
20.7	301.8	-36.2		
22.7	317.4	-21.9		
25.0	326.2	-17.6		
27.1	333	-17.7		
28.5	338.8	-18.4		
29.2	341.8	-19.2		
Configuration 3d (L=1.5", d=5.5")				
v (m/s)	f1 (Hz)	L1	f2 (Hz)	L2
4.9	52.7	-56.5	101.6	
6.9	74.2	-56.6	136.7	-69.1
9.6	100.6	-56.1	194.3	-68.1
12.3	129.9	-54.2	240	-70
14.3	150.4	-50.3	277.3	-60.1
16.9	178.7	-42	332	-49.8
18.6	187.5	-47.1	358.4	-33.7
20.6	188.5	-46.4	377	-22.2
22.4	205.1	-58.2	387.7	-22.4
25.1	265.6	-30.9	407.2	-57.1
27.1	286.1	-31.7	425.8	-64.3
28.4	296.9	-29.2		
29.1	305.7	-26.9		
Configuration 4d (L=2", d=5.5")				
v (m/s)	f1 (Hz)	L1	f2 (Hz)	L2
5.0	42	-56.4	77.1	-65.4
6.8	57.6	-55.7	100.6	-67.8
9.8	82	-55.4	147.5	-68.8
12.3	104.5	-54.9	195.3	-67.4
14.4	120.1	-51.6	222.7	-65.8
16.8	141.6	-49	265.6	-61
18.8	159.2	-46.9	293	-57
20.6	176.8	-42.5	323.2	-53.7
22.4	186.5	-50.5	352.5	-36.8
25.0	194.3	-44.9	388.7	-21.9
26.9	201.2	-61	399.4	-17.6
28.5	217.8	-63.9	407.2	-17.8
29.1			411.1	-18.2
Configuration 1d (L=0.5", d=5.5")				
v (m/s)	f1 (Hz)	L1	f2 (Hz)	L2
4.9	120.1	-68.5		
6.9	189.4	-64.9		
9.7	264.6	-59		
12.3	291	-36.1		
14.4	303.7	-24.3		
16.9	311.5	-24.3		
18.6	319.3	-42.6		
20.8	323.2	-57.5		
22.5	323.2	-61.1		
24.9				
27.0				

Configuration 2s (L=1", d=2.75")				
v (m/s)	f1 (Hz)	L1	f2 (Hz)	L2
4.9	77.1	-59.6	135.7	-67.7
6.9	105.5	-60.5	190.4	-70.4
9.6	148.4	-61.3	279.3	-65.7
12.4	180.7	-61.7	369.1	-69.2
14.4	206	-63.2	427.7	-63.1
17.1	240.2	-61.3	478.5	-29.3
18.8	253.9	-63.1	494.1	-21.4
20.8	279.3	-62	510.7	-25.4
22.5	336.9	-54.2	524.4	-49
24.9	377	-39.7	521.5	-63.7
26.9	405.3	-29.8		
28.3	421.9	-25.7		
29.2	430.2	-22.5		
Configuration 3s (L=1.5", d=2.75")				
v (m/s)	f1 (Hz)	L1	f2 (Hz)	L2
4.9	51.8	-51.8	91.8	-64.1
6.9	73.2	-52.2	137.7	-66.8
9.6	100.6	-53.7	196.3	-69.3
12.4	130.8	-54	240	-70
14.6	154.3	-56.9	279.3	-64.7
16.8	181.6	-61.7	347.7	-74.4
18.7	201.2	-62.1	386.7	-67.4
20.7	225.6	-63.3	440.4	-62.8
22.5	249	-62.7	475.6	-53.8
24.8	257.8	-60.1	514.6	-21.8
26.9	263.7	-42.2	526.4	-19.4
28.5	268.8	-49.5	535.2	-17.6
29.1	269.5	-53.2	538.1	-17.9
Configuration 4s (L=2", d=2.75")				
v (m/s)	f1 (Hz)	L1	f2 (Hz)	L2
4.8	42	-51	75.2	-61.8
6.9	57.6	-51.8	104.5	-64.4
9.7	82	-51.3	153.3	-65.8
12.3	101.6	-53.2	188.5	-67.2
14.5	120.1	-55.1	228.5	-68
17.0	143.6	-53.8	279.3	-65
18.7	158.2	-53.6	287.1	-67.9
20.7	174.8	-51.9	326.2	-67
22.5	192.4	-51.6	354.5	-65.7
24.8	213.9	-50.2	405.3	-63.1
27.0	233.4	-46.2	435.5	-57.8
28.3	245.1	-44.8	464.8	-53.4
29.2	251	-43.8	476.6	-48.3
Configuration 1s (L=0.5", d=2.75")				
v (m/s)	f1 (Hz)	L1	f2 (Hz)	L2
4.7	127	-66.7		
6.8	184.6	-66.6		
9.7	258.8	-67.5		
12.4	337.9	-62.3		
14.4	382.8	-46.4		
17.0	407.2	-21.5		
18.7	418.9	-22.3		
20.7	435.5	-21.9		
22.5	445.3	-21.8		
24.8	460	-26		
26.8	470.7	-42.8		
28.4	477.5	-53.2		
29.2				

## Bibliography

Bendat, J.S. and Peirsol, A.G. 1980. *Engineering applications of correlation and spectral analysis*. New York : John Wiley & Sons.

Bruggemann, J.C., Vellekoop, J.C., and van der Knaap, F.G.P. 1991. Flow excited resonance in a cavity covered by a grid: theory and experiments. *NCA-Vol. 11/FED-Vol. 130, Flow Noise Modeling, Measurement, and Control ASME*.

Bruggemann, J.C., Looijmans, K.N.H., Golliard, J. 1997. Broadband and tonal noise of flow excited cavities. *AD-Vol. 53-1, Fluid-Structure Interaction, Aeroelasticity, Flow-Induced Vibration and Noise Volume I ASME* : 373-380.

Cattafesta, L.N., Garg, S., Choudari, M., and Li, F. 1997. Active control of flow-induced cavity resonance. *AIAA Paper No. 97-1804*.

Chase, D.M. 1987. The character of the turbulent wall pressure spectrum at subconvective wavenumbers and a suggested comprehensive model. *JSV 12* : 125-147.

DeMetz, F.C. and Farabee, T.M. 1977. Laminar and turbulent shear flow-induced cavity resonances. *AIAA Paper No. 77-1293*.

Doak, P.E. 1974. Acoustic, thermal and turbulent energy density and linear momentum density relationships and fluxed in fluctuating flows. *Proceedings of the Eighth International Congress on Acoustics, Contributed Papers, Volume II* : p. 532.

Dunham, W.H. 1962. Flow-induced cavity resonance in viscous compressible and incompressible fluids. *4<sup>th</sup> Symposium of Naval Hydrodynamics Vol. 3*.

Elder, S.A. 1978. Self-excited depth-mode resonance for a wall-mounted cavity in turbulent flow. *JASA 64* : 877-890.

Elder, S.A., Farabee, T.M., and DeMetz, F.C. 1982. Mechanisms of flow-excited cavity tones at low Mach numbers. *JASA 72* : 532-549.

Ethembaoglu, S. 1973. On the fluctuating flow characteristics in the vicinity of gate slots. Division of Hydraulic Engineering, University of Trondheim, Norwegian Institute of Technology.

Farabee, T.M. 1986. An experimental investigation of wall pressure fluctuations beneath non-equilibrium turbulent flows. *David Taylor Naval Ship Research and Development Center Technical Report DTNSRDC-86/047*.

Heller, H.H. and Bliss, D. 1975. The physical mechanism of flow-induced pressure fluctuations in cavities and concepts for their suppression. *AIAA Paper No. 75-491*.

Ho, C.-M. and Huerre, P. 1984. Perturbed free shear layers. *Annual Review of Fluid Mechanics 16* : 365-424.

Howe, M.S. 1979. Attenuation of sound in a low Mach number nozzle flow. *JFM 91* : 209-229.

Howe, M.S. 1980. The dissipation of sound at an edge. *JSV* 70 : 407-411.

Kammeyer, M.E. 1995. *An experimental investigation of organized turbulent motions and wall-pressure fluctuations in complex flows*. PhD thesis, The Catholic University of America.

Kassab, S.Z., Derksen, R.W., and Azad, R.S. 1985. Remarks on stem configuration of X-array hot-wire probes. *Dantec Information No. 01*.

Kestens, T. and Nicoud, F. 1998. Active control of an unsteady flow over a rectangular cavity. *AIAA Paper No. 98-2348*.

Kinsler, L.E., Frey, A.R., Coppens, A.B., and Sanders, J.V. 1982. *Fundamentals of acoustics*. New York : John Wiley & Sons.

Komerath, N.M., Ahuja, K.K., and Chambers, F.W. 1987. Prediction and measurement of flows over cavities – a survey. *AIAA Paper No. 87-0166*.

Kook, H. and Mongeau, L. 1997. Analytical model for the periodic pressure fluctuations induced by flow over a cavity. *AD-Vol. 53-1, Fluid-Structure Interaction, Aeroelasticity, Flow-Induced Vibration and Noise Volume I* : 361-372.

Mast, T.D. and Pierce, A.D. 1995. Describing-function theory for flow excitation of resonators. *JASA* 97 : 163-172.

Mendoza, J.M. and Ahuja, K.K. 1996. Cavity noise control through upstream mass injection from a coanda surface. *AIAA Paper No. 96-1767*.

Michalke, A. 1965. On spatially growing disturbances in an inviscid shear layer. *JFM* 23 : 521-544.

Mongeau, L., Kook, H., and Franchek, M.A. 1998. Active control of flow-induced cavity resonance. *AIAA Paper No. 98-2349*.

Nelson, P.A., Halliwell, N.A., and Doak, P.E. 1981. Fluid dynamics of a flow excited resonance, Part I: Experiment. *JSV* 78 : 15-38.

Nelson, P.A., Halliwell, N.A., and Doak, P.E. 1983. Fluid dynamics of a flow excited resonance, Part II: Flow acoustic interaction. *JSV* 91 : 375-402.

Raman, G., Raghu, S., and Bencic, T.J. 1999. Cavity resonance suppression using miniature fluidic oscillators. *AIAA Paper No. 99-1900*.

Rockwell, D. and Knisely, C. 1979. The organized nature of flow impingement upon a corner. *JFM* 93 : 413-432.

Rockwell, D. and Naudascher, E. 1978. Review – self-sustaining oscillation of flow past cavities. *Journal of Fluids Engineering* 100 : 152-165.

Rossiter, J.E. 1964. Wind tunnel experiments on the flow over rectangular cavities at subsonic and transonic speeds. *RAE Tech. Rep. 64037*.

Russell, S.J. 1997. *Wall pressure signatures of organized turbulent notions*. PhD thesis, The Catholic University of America.

Sarno, R.L. and Franke, M.E. 1990. Suppression of flow-induced pressure oscillations in cavities. *AIAA Paper No. 90-4018-CP*.

Sarohia, V. and Massier, P.F. 1977. Control of cavity noise. *Journal of Aircraft* 14 : 833-837.

Schlichting, H. 1968. *Boundary layer theory*. New York: McGraw-Hill.

Shaw, L. 1998. Active control for cavity acoustics. *AIAA Paper No. 98-2347*.

Shaw, L.L. 1979. Suppression of aerodynamically induced cavity pressure oscillations. *JASA* 66 : 880-884.

Sunyach, M. and Ffowcs-Williams, J.E. 1986. The active suppression of oscillation in flow-excited cavities. *C.R. Acad. Sc. Paris, t. 303, Serie II*, no. 12.

Tam, C.K.W. and Block, P.J.W. 1978. On the tones and pressure oscillations induced by flow over rectangular cavities. *JFM* 89 : 373-399.

Tang, Y.-P. and Rockwell, D. 1983. Instantaneous pressure fields at a corner associated with vortex impingement. *JFM* 126 : 187-204.

Wyganski, I.J. and Petersen, R.A. 1987. Coherent motion in excited free shear flows. *AIAA Journal* 25 : 201-213.

Zoccola, P.J. 1999. Suppression of acoustic cavity resonance induced by fluid flow. U.S. Patent Application. Navy Case No. 79767.

## Distribution

<i>Copies</i>	<i>Copies</i>
<b>DoD</b>	
CHIEF OF NAVAL RESEARCH ATTN DR ALBERT TUCKER BALLSTON CENTRE TOWER ONE 800 NORTH QUINCY ST ARLINGTON VA 22217-5660	1 DR FILIPPO GAVELLI DEPT OF MECH ENG CATHOLIC UNIVERSITY WASHINGTON DC 20064
CHIEF OF NAVAL RESEARCH ATTN DR KAM NG BALLSTON CENTRE TOWER ONE 800 NORTH QUINCY ST ARLINGTON VA 22217-5660	1 DR YUN FAN HWANG APPLIED RESEARCH LAB PENN STATE UNIVERSITY STATE COLLEGE PA 16804
CHIEF OF NAVAL RESEARCH ATTN DR L P PURTELL BALLSTON CENTRE TOWER ONE 800 NORTH QUINCY ST ARLINGTON VA 22217-5660	1 DR GERALD LAUCHLE APPLIED RESEARCH LAB PENN STATE UNIVERSITY STATE COLLEGE PA 16804
CHIEF OF NAVAL RESEARCH ATTN DR EDWIN ROOD BALLSTON CENTRE TOWER ONE 800 NORTH QUINCY ST ARLINGTON VA 22217-5660	1 DR M S HOWE COLLEGE OF ENGINEERING BOSTON UNIVERSITY 110 CUMMINGTON ST BOSTON MA 02215
COMMANDER NAVAL SEA SYSTEMS COMMAND ATTN MR RICHARD TADDEO 2531 JEFFERSON DAVIS HIGHWAY ARLINGTON VA 22242-5160	1 DR SHERYL GRACE COLLEGE OF ENGINEERING BOSTON UNIVERSITY 110 CUMMINGTON ST BOSTON MA 02215
COMMANDER US AIR FORCE RESEARCH LAB ATTN DR LEONARD SHAW 2145 5 <sup>TH</sup> ST WRIGHT PATTERSON AFB OH 45433	1 DR J FOSS DEPT OF MECH ENG MICHIGAN STATE UNIVERSITY EAST LANSING MI 48824
DEFENSE TECHNICAL INFORMATION CENTER 8725 JOHN KINGMAN ROAD SUITE 0944 FORT BELVOIR VA 22060-6218	1 DR J M MENDOZA NASA Langley Research Center HAMPTON VA 23681-2199
<b>NON-DoD</b>	
DR MARIO CASARELLA DEPT OF MECH ENG CATHOLIC UNIVERSITY WASHINGTON DC 20064	1 DR KRISHAN AHUJA SCHOOL OF AEROSPACE ENGINEERING GEORGIA INSTITUTE OF TECHNOLOGY ATLANTA GA 30332-0150
DR J STEVEN BROWN DEPT OF MECH ENG CATHOLIC UNIVERSITY WASHINGTON DC 20064	1 PROF DONALD ROCKWELL DEPT OF MECH ENG LEHIGH UNIVERSITY BUILDING NO 19 BETHLEHEM PA 18015
	1 DR MARTIN POLLOCK LOCKHEED MARTIN PO BOX 1072 SCHENECTADY NY 12301-1072

## Distribution

	<i>Copies</i>		<i>Copies</i>
MR DAVID PRATT ELECTRIC BOAT CORP 75 EASTERN POINT RD GROTON CT 06340	1	72      Shang 7204    Rumerman 722     Leibolt 725     Farabee 725     Antonides	1 1 1 1 1
MR GARY COOPER ELECTRIC BOAT CORP 75 EASTERN POINT RD GROTON CT 06340	1	725    Bowers 725    Cummings 725    Cole 725    Gershfeld 725    Grega	1 1 1 1 1
MR KEVIN SMITH NEWPORT NEWS SHIPBUILDING 4101 WASHINGTON AVENUE NEWPORT NEWS VA 23607	1	725    Hemingway 725    Kim 725    Leibolt 725    Lewis 725    Maga	1 1 1 1 1
MR DOUGLAS WASSON RAYTHEON CORPORATION A402 7700 ARLINGTON BLVD FALLS CHURCH VA 22042	1	725    Mathews 725    Minniti 725    Noll 725    Rappl 725    Roth 725    Santiago	1 1 1 1 1 1
<b>Non-DoD - EXCONUS</b>		725    Whipple	1
DR PHILIP NELSON UNIVERSITY OF SOUTHAMPTON ISVR HIGHFIELD SOUTHHAMPTON S0171BJ GREAT BRITAIN	1	725    Wojno 725    Young 725    Zoccola 741    Russell 3442   TIC	1 1 1 1 30 1 1

DR JAN BRUGGEMANN TNO-INSTITUTE OF APPLIED PHYSICS PO BOX 155 2600 AD DELFT THE NETHERLANDS	1
---	---

### **NSWC, CARDEROCK DIVISION INTERNAL DISTRIBUTION**

Code	Name	Copies
0112	Barkyoumb	1
50	Morgan	1
5200	Griffin	1
70	Covich	1
701	Smith	1
7015	Fisher	1
702	Strasberg	1
703	Maidanik	1
7051	Blake	1
7052	Feit	1
7053	Liu	1
712	Thompson	1
712	Pfeifer	1